



MONASH University

Computational Modelling of Friction Stir Processing

Timothy Fagan

This thesis submitted in fulfilment of the requirements for the degree of

Doctor of Philosophy

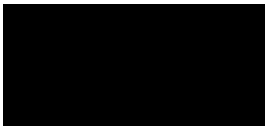
September 2015

© The author 2015. Except as provided in the Copyright Act 1968, this thesis may not be reproduced in any form without the written permission of the author.

I certify that I have made all reasonable efforts to secure copyright permissions for third-party content included in this thesis and have not knowingly added copyright content to my work without the owner's permission.

Declaration

I, **Timothy Fagan**, declare that this thesis, submitted in fulfilment of the requirements for the award of Doctor of Philosophy, in the department of Mechanical and Aerospace Engineering, Monash University is entirely my own work unless otherwise referenced or acknowledged. This thesis includes no material which has been submitted for the award for any other degree or diploma in any university.



Timothy Fagan

Abstract

Friction Stir Processing (FSP) is a new and exciting processing technique to locally modify the grain structure and improve mechanical properties of metals. Numerical modelling of the process will allow for improved understanding of the deeply complex thermo-mechanical processes that occur within this seemingly simple technique. An accurate numerical model will increase understanding of the process and reduce the number of experimental trials required to achieve the desired result.

In FSP, a cylindrical non-consumable tool, generally consisting of a pin and shoulder, is rotated and plunged into the surface of a metal workpiece. The larger diameter shoulder prevents the surface of the metal workpiece from flowing outwards, while the specially designed pin induces a stirring action, producing a combination of frictional and adiabatic heating allowing the metal to flow around the pin from the advancing side to the retreating side. Localised severe plastic deformation occurs generally resulting in grain refinement. It is the grain refinement that has attracted the attention of many researchers and prompted development of numerical models.

The typical numerical methods applied in literature rely on Eulerian or Lagrangian meshes which struggle to overcome large mesh deformation and track material history respectively. In addition, phenomenological models are generally applied which do not have a physical basis. To this end, this work will implement a particle based numerical method with a physically based constitutive law. The proposed three-dimensional fully-coupled thermo-mechanical model is able to concurrently determine the temperature field, material flow and microstructure evolution dependent on the processing conditions of FSP.

The results of the complete model agree well with experimental thermocouple measurements, material flow and microstructure development.

Contents

Declaration	i
Abstract	ii
Contents	iii
List of Figures	vi
List of Tables	xi
Acknowledgements	xii
Symbols	xiii
Publications	xv
1 Introduction	1
1.1 Background and Motivation	1
1.2 Research Overview and Objectives	3
1.3 Chapter Outline	3
2 A Review of Friction Stir Processing	5
2.1 Background Information	5
2.1.1 Introduction to the Process	5
2.1.2 Characteristics and Novel Aspects of Friction Stir Processing	9
2.1.3 Superplasticity	10
2.1.4 Improvement of Cast Components	11
2.1.5 Surface Composites	12
2.1.6 Room-Temperature Formability	13
2.1.7 Enhancement of Powder Processed Alloys	13
2.1.8 Friction Stir Channeling	14
2.1.9 Summary	15
2.2 Numerical Modelling of FSP	16
2.2.1 Numerical Methods Overview	16
2.2.2 The Challenges of Modelling FSP	19
2.2.3 Large Deformation and Material Flow	20
2.2.4 Grain Size Evolution	25
2.2.5 Boundary Conditions	27
2.2.6 Modelling Fast Tool Rotation / Slow Tool Translation	32
2.3 Concluding Remarks	33

3	The Material Point Method	35
3.1	Introduction	35
3.2	The Governing Equations	35
3.3	Discretisation	36
3.3.1	Weak Form of the Governing Equations	36
3.3.2	Shape Functions	37
3.3.3	Derivation of the discretised Form of the Governing Equations	39
3.4	Constitutive Model in the Context of Large Deformation	42
3.4.1	Hyperelasticity	42
3.5	Forces and Contact Between Bodies	47
3.5.1	Contact Detection	47
3.5.2	Contact Treatment	49
3.5.3	Calculation of the Surface Normal	50
3.6	The MPM Incremental Update	50
3.6.1	Incremental Update	51
3.7	Conclusion	53
4	Thermal Modelling of Friction Stir Processing	55
4.1	Introduction	55
4.2	Description of the Thermal Model	55
4.2.1	Modelling the FSP Tool as a Moving Heat Source	56
4.2.2	Thermal Losses	57
4.3	Experimental Method	59
4.4	Boundary Conditions used in Modelling FSP	61
4.4.1	Heat Generation	61
4.4.2	Thermal Losses	63
4.5	Comparison of Experiment with the Obtained Thermal Model of FSP	65
4.5.1	Resulting Temperature Field	65
4.6	Conclusion	70
5	Thermo-mechanical Modelling of Friction Stir Processing	71
5.1	Introduction	71
5.2	Description of the Thermo-mechanical Model	72
5.2.1	Constitutive Law	72
5.2.2	Calculation of Heat Generation	73
5.2.3	Establishing the Mechanical Boundary Conditions	74
5.3	Implementing Effective Mass Scaling to Reduce Computation Time	77
5.3.1	The Limiting Condition on the Timestep	77
5.3.2	The Effect of Mass Scaling on the Kinetic Energy of the Workpiece	78
5.3.3	The Effect of Mass Scaling on Material Displacement in the Workpiece	80
5.3.4	The Effect of Mass Scaling on the Temperature of the Workpiece	80
5.3.5	Summarising the Effect of Mass Scaling on Simulation of FSP	85
5.4	Comparison of Experiment with the Obtained Thermo-mechanical Model of FSP	85
5.4.1	Resulting Temperature Field	85
5.4.2	Resulting Material Flow	94
5.5	Conclusion	112
6	Modelling of FSP with a Dislocation-Density Based Material Model	114
6.1	Introduction	114
6.2	Dislocation-Density Based Microstructure Model	114

6.2.1	Brief Description of the Model	114
6.2.2	Flow Stress According to the Two-Phase Model	115
6.2.3	Calibration of the Two-Phase Model to FSP Conditions for Copper and AA5005	117
6.3	Establishing the Boundary Conditions for the Microstructure FSP Model	127
6.3.1	Thermal Loss to the Backing Plate and Surrounding Air	127
6.3.2	Friction Coefficient Between Tool and Workpiece - AA5005	128
6.4	Comparison of Experiment with the Obtained Dislocation-Density Based Model of FSP	130
6.4.1	Resulting Temperature Field	130
6.4.2	Resulting Material Flow	137
6.4.3	Resulting Microstructure	151
6.4.4	Conclusion	158
7	Conclusions and Future Work	159
7.1	Conclusions	159
7.2	Outlook	160
	BIBLIOGRAPHY	162
	Appendices	171
A	Full Resolution EBSD Images	172
B	Aluminium Alloy 5005 Workpiece Dimensions and Properties	175

List of Figures

1.1	Computer generated image (CGI) of copper plate under Friction Stir Processing.	2
2.1	Schematic of Friction Stir Processing.	5
2.2	Traverse section of processed workpiece (with pin) [6] and pinless FSP [4]. . . .	7
2.3	Example cross-section FSP zone transitions [7].	7
2.4	Thermal conditions of FSP.	8
2.5	Example surface appearance after FSP. Also indicated is the distance between the bands: δ , which is approximately equal to the translational velocity divided by the rotational speed, V/ω	9
2.6	Cross section micrograph highlighting material flow and flash formed during FSSW [11].	9
2.7	Friction Stir Processed Aluminium Alloy exhibiting superplasticity [13].	10
2.8	Examples of cast-metal products that could benefit from post-processing with FSP. [21, 22]	11
2.9	Example interface between surface composite formed by FSP and substrate/base material [38].	12
2.10	Example cross-section of the processed zone of a surface composite formed by FSP [34].	13
2.11	Enhanced bending after application of FSP to tensioned side (top) [40].	13
2.12	Improvement in particle distribution and homogenization [46]. Left) as-sintered, right) after FSP (same scale).	14
2.13	FSP conducted upon a powder processed composite [46] and an aluminium alloy [48] resulting in cavities/wormholes indicated by the arrows.	15
2.14	Left) A channel fabricated using friction stir channeling technique [50], right) cross-sectional image of a channel [49].	15
2.15	Large deformation of mesh in impact simulation.	18
2.16	a) Example of material flow after partial passage of friction stir tool, b) CT scan of workpiece showing scatter of processed copper tracer material. [60]	21
2.17	Material flow (visualised by velocity vectors) around two different pin styles [64].	21
2.18	a-b) Material flow around a two-dimensional pin [68] c-d) Material flow around a three-dimensional tool [48] (top and side view).	22
3.1	GIMP shape function in one dimension for unit cell size.	39
3.2	Schematic of contacting MPM material particles over background grid. Highlighted nodes indicate inactive (grey), single (blue/red) and multi-material (purple) nodes.	48
3.3	Flow chart of MPM update during one timestep.	54
4.1	Left) tool dimensions, right) experimental set-up.	60

4.2	Schematic of plate with marked (+) thermocouple positions, T1-T3. The dimensions of the trapezoidal cavity are also shown.	61
4.3	Experimental tensile test data for 0.2% yield stress vs. temperature for OFHC copper [150] fitted with a 4 Parameter Logistic (4PL) regression curve. Also shown is the tensile strength vs. temperature for C11000 H02 copper [150] with a fitted 4PL regression curve.	62
4.4	The experimental temperature over time for thermocouples 1-3 (cavity 1) with separated processing and cooling phase for reference.	63
4.5	Plot of dT/dt vs $(T_{\text{room}} - T_{\text{body}})$ for the cooling phase of cavity 1, with a fitted linear function shown.	64
4.6	Temperature profile predicted by the thermal model over time for T1, T2 and T3.	65
4.7	Temperature profile predicted by the thermal model over time for T1, T2 and T3 compared against experiment.	66
4.8	Temperature 1mm below the surface at times of a) 10s, b) 25s, c) 40s. Left image is the temperature across the slice, right is the temperature across each line on the advancing, centre and retreating sides.	68
4.9	Temperature profile over time for T1, T2 and T3 for both the lumped backing plate convection coefficient and BPC + Air Convection.	69
4.10	Temperature profile 1mm below the surface for both the lumped backing plate convection coefficient and BPC + Air Convection, 40 seconds into the simulation.	70
5.1	Initial set-up of numerical model.	72
5.2	Plot of experimentally determined coefficient of friction over time (10s) for translation speed of 120mm/min.	75
5.3	Kinetic energies over the first 20 seconds of simulation for $\chi_{\text{ms}} = 10^4$ to $\chi_{\text{ms}} = 10^7$	78
5.4	The kinetic energy and 1% of internal energy for mass scaling of (left) $\chi_{\text{ms}} = 10^8$, and (right) $\chi_{\text{ms}} = 10^7$	79
5.5	Plane section 10 seconds into simulation at the tool / workpiece interface. Axis orientation as shown for reference. Processing in the positive x-direction.	79
5.6	Material displacements at the tool/workpiece interface 10 seconds into the simulation for mass scaling factors of 10^4 , 10^5 , 10^6 and 10^7	81
5.7	Material flow around the tool at a range of mass scaling factors (10 seconds into the simulation); from left to right, $\chi_{\text{ms}} = 10^4$, $\chi_{\text{ms}} = 10^5$, $\chi_{\text{ms}} = 10^6$ and $\chi_{\text{ms}} = 10^7$	82
5.8	Average temperature for the copper plate over the first 20 seconds of simulation for $\chi_{\text{ms}} = 10^4$ to $\chi_{\text{ms}} = 10^7$	82
5.9	Temperature followed by equivalent stress at the tool/workpiece interface 10 seconds into the simulation for mass scaling factors of 10^4 , 10^5 , 10^6 and 10^7	83
5.10	Surface area used for calculating the average temperature over both area and time, slices (blue, red, green) are 0mm, 1mm and 2mm from the surface, respectively.	83
5.11	The average temperature over time and area for $\chi_{\text{ms}} = 10^4$ and $\chi_{\text{ms}} = 10^7$ at depths of 2mm, 1mm and at the surface of the copper plate.	84
5.12	Temperature profile over time for thermocouple locations T1, T2 and T3.	86
5.13	Temperature profile over time for thermocouple locations T1, T2 and T3 compared with experiment.	87
5.14	Temperature 1mm below the surface at times of a) 10s, b) 25s, c) 40s. Left image is the temperature across the slice, right is the temperature across each line on the advancing side, retreating side, and the central line.	88

5.15	Comparison of temperature profiles over time for T1, T2 and T3 predicted by thermo-mechanical model and purely thermal model.	89
5.16	Comparison of temperature profiles over time predicted by the thermo-mechanical model (Johnson-Cook), purely thermal model and experiment for a) T1, b) T2 and c) T3.	91
5.17	Temperature at locations 1mm below the surface across each line on the a) Advancing Side b) Centre Line, c) Retreating Side.	92
5.18	Left) Experimental tensile test data for yield stress vs. temperature for copper [150], Right) Johnson-Cook model for $T = 1000\text{K}$ and $\dot{\epsilon} = 8.33 \times 10^{-5} \text{ s}^{-1}$	93
5.19	a) Strain map and b) temperature field for an area the size of the tool / work-piece interface as the tool passes across it ($t = 15$ seconds).	93
5.20	Copper flashing after processing (experimental and numerical) shown by a) Advancing side - Experiment (processing direction to the left), b) Advancing Side - Numerical, and c) Retreating side - Experiment (processing direction to the right), d) Retreating side - Numerical. Note that the thermocouple holes were machined on the other side to the simulation for this particular plate. . .	95
5.21	Overlaid images of simulation and experimental results according to processing side, top) advancing side flash, bottom) retreating side flash. The dark shadow shows the experimental flashing.	96
5.22	Series of particles used for tracking pathlines.	98
5.23	View of completed particle paths. Viewing angle clockwise from top left) top view (parallel projection), aerial view (perspective), processing direction view (perspective).	99
5.24	Side view (perspective) with each particle line shown individually. Processing direction indicated by positive x-direction.	101
5.25	Initial set-up of simulation with seeded particles for pathline tracking (coloured by strata).	102
5.26	The initial state of particles for subsurface tracking at a depth of 1-2mm. . . .	108
5.27	View of completed subsurface particle paths. Viewing angle clockwise from top left: top view (parallel projection), aerial views (perspective), processing direction view (perspective).	109
5.28	Final material flow into cavity 1.	110
5.29	The three cavity orientations with material filling as shown for experiment and simulation.	111
5.30	Material displacement and velocity at the tool interface for left) $t=15\text{s}$ and right) $t=40\text{s}$	112
6.1	Flow stress response for two-phase model at low strain rate and room temperature compared against experiment (in compression and torsion) [157, 158].	118
6.2	Flow stress response for original model at various temperatures and a strain rate of $\dot{\epsilon} = 1\text{s}^{-1}$. Experimental data sourced from $T=298\text{K}, 542\text{K}$ [159], $T=773\text{K}, 1123\text{K}$ [160].	120
6.3	Fitted curve for calibration of temperature dependent α^*	120
6.4	Flow stress response for calibrated two-phase model at various temperatures and a strain rate of $\dot{\epsilon} = 1\text{s}^{-1}$	121
6.5	Flow stress and temperature response at $T=298\text{K}$ and $\dot{\epsilon} = 1\text{s}^{-1}$	121
6.6	Comparison of both models to experimental compression tests at 773K . Experimental data sourced from [160].	122
6.7	Comparison of both models to experimental compression tests at 1123K . Experimental data sourced from [160].	122

6.8	Fitted curve for calibration of temperature dependent α^* for aluminium alloy 5005.	123
6.9	Flow stress response for calibrated two-phase model at a range of temperatures and strain rates of $\dot{\epsilon} = 0.25s^{-1}$ and $\dot{\epsilon} = 1s^{-1}$. Experimental data sourced from: $\dot{\epsilon} = 0.25s^{-1}$ [161] and $\dot{\epsilon} = 1s^{-1}$ [162].	124
6.10	Flow stress and temperature response at $T = 293K$ and $\dot{\epsilon} = 1s^{-1}$	124
6.11	Comparison of two-phase model to experimental compression tests at 573K. Experimental data sourced from [161].	125
6.12	Comparison of two-phase model to experimental compression tests at 653K. Experimental data sourced from [161].	125
6.13	Comparison of two-phase model to experimental compression tests at 723K. Experimental data sourced from [161].	126
6.14	Experimental cooling phase (for the copper workpiece) plotted with a fitted exponential decay curve, equation (6.16).	127
6.15	Plot of dT/dt vs $(T_{room} - T_{body})$ to determine the rate of change for substitution into equation (4.10).	128
6.16	Plot of experimentally determined coefficient of friction over time ($\sim 4s$) for a translation speed of 120mm/min for AA5005.	129
6.17	Temperature profiles over time with the Dislocation-Density based material model, for T1, T2 and T3 compared against experiment (for the copper workpiece).	130
6.18	Temperature 1mm below the surface at times of a) 10s, b) 25s, c) 40s. Left image is the temperature across the slice, right is the temperature across each line on the advancing, centre and retreating sides (for the copper workpiece).	131
6.19	Comparison of temperature profiles over time for T1, T2 and T3 predicted by all three developed models a) two-phase and thermal model, b) two-phase and Johnson-Cook thermo-mechanical model (for the copper workpiece).	133
6.20	Comparison of temperature profiles over time predicted by the two-phase model, Johnson-Cook model, thermal model and experiment for a) T1, b) T2 and c) T3 (for the copper workpiece).	134
6.21	Temperature 1mm below the surface across each line on the a) Advancing Side b) Centre Line, c) Retreating Side for all three models (for the copper workpiece).	135
6.22	Source of thermal energy (%) in FSP of copper for the two-phase model and the Johnson-Cook thermo-mechanical model.	136
6.23	Copper flashing after processing (experimental and numerical) shown by a) Advancing side - Experiment (processing direction to the left), b) Advancing Side - Numerical, and c) Retreating side - Experiment (processing direction to the right), d) Retreating side - Numerical. Note that the thermocouple holes were machined on the other side to the simulation for this particular plate.	138
6.24	Overlaid images of simulation and experimental results according to processing side, top) advancing side flash, bottom) retreating side flash. The dark shadow shows the experimental flashing.	139
6.25	View of completed particle paths. Viewing angle clockwise from top left) top view (parallel projection), aerial view (perspective), processing direction view (perspective).	140
6.26	Overlay of material particles (black) and the generated surfaces for the JC model and two-phase model (cavity 3).	147
6.27	Final material flow into cavity 1.	148
6.28	Cavity filling for the experiment and both thermo-mechanical models, Johnson-Cook and two-phase.	149

6.29	Cross-section material flow analysis.	150
6.30	Material displacement and velocity at the tool interface for left) $t=15s$ and right) $t=40s$	151
6.31	Average grain size at a slice 65mm into the plate (parallel to processing direction) for a) Copper and b) AA5005. Points on the advancing side, centre and retreating side are plotted against their distance from the bottom.	152
6.32	Cross-section EBSD data for copper and AA5005.	154
6.33	Stir zone of the processed copper coloured by average grain size.	156
6.34	The inverted copper workpiece, which combined with the scale shows the depth of the stir zone from the surface.	156
6.35	Processed copper that experiences temperatures greater than 748K during processing.	156
6.36	The stir zone of the processed copper (transparent blue) compared to the region that experiences temperatures greater than 748K (orange).	157
6.37	EBSD plane (green) lies in the region experiencing annealing temperatures (yellow).	157
1	Copper workpiece at a slice 65mm into the plate (parallel to processing direction); a) Band contrast map - high angle boundaries ($>15^\circ$) in red, LAGB in black ($>2^\circ$); b) Inverse pole figure orientation map - high angle grain boundaries ($>15^\circ$) in black, LAGB in grey ($>2^\circ$).	173
2	AA5005 workpiece at a slice 65mm into the plate (parallel to processing direction); a) Band contrast map - high angle boundaries ($>15^\circ$) in red, LAGB in black ($>2^\circ$); b) Inverse pole figure orientation map - high angle grain boundaries ($>15^\circ$) in black, LAGB in grey ($>2^\circ$).	174
3	Schematic of AA5005 plate with marked (+) thermocouple positions, T1-T3, although note that the thermocouple results for AA5005 are not reported in this thesis.	175

List of Tables

2.1	Calibration methodology used by Wang et al. [122].	31
4.1	The three cavity orientations with tool processing direction as shown by the arrow.	60
4.2	Copper plate and tool steel material parameters (used in calculation of the global convective coefficient, \bar{h}_c , and thermal coefficient, g , accounting for heat loss into the tool).	61
4.3	Copper plate material parameters (used in calculation of the global convective coefficient, \bar{h}_c).	62
5.1	Johnson-Cook parameters for copper [151].	73
5.2	Temporal averages of the friction coefficient for Tests 1-4 at speeds of 60mm/min and 120mm/min.	75
6.1	Model parameters for Copper [101, 157].	119
6.2	Values used for calculation of global convective coefficient, \bar{h}_c , for copper. . . .	128
6.3	Values used for calculation of global convective coefficient, \bar{h}_c , for AA5005. . .	128
6.4	Temporal averages of the friction coefficient for Tests 1-6 at speeds of 120mm/min for AA5005.	129
6.5	Approximate percentage of material filling for each cavity in the experiment and both thermo-mechanical models, Johnson-Cook and two-phase (to two significant figures).	148
6.6	Comparison of the resulting grain size in the SZ for the experiment and two-phase model. Note that the experimental data is taken from the retreating side of the workpiece, and the two-phase model predicts an average grain size.	153
1	Two-phase model parameters for AA5005.	176

Acknowledgements

Firstly, I would like to express my deep and sincere gratitude to my three supervisors; Raafat Ibrahim, Vincent Lemiale and Yuri Estrin. Their guidance has been extremely precious and much of what I have learned over the past few years has been enabled by their support.

Raafat has been tremendous support, both through finding financial assistance and offering me the opportunity to undertake this project. A gentle and kind man, his ability to explain research in a simple and understandable way is inspiring and I hope has 'rubbed off' in my own work.

Whenever I had a problem or issue with my work, a meeting with Vincent always gave me greater incite and clarity on the problem at hand, and despite all the commitments of the CSIRO, he has always made himself available. His generosity and kindness will always be remembered.

In Yuri I have been extremely lucky to have such a kind and well learned man oversee this work. His expertise in concepts of materials science has been invaluable, and throughout my candidature his comments have always been constructive and insightful. His ability to break down a problem and critically analyse different aspects is a skill I have tried to emulate.

This research would not have been possible without generous financial support from several institutions, which I gratefully acknowledge: the Departmental Scholarship from the Mechanical Engineering Department who also supported my trip to the International Conference on Computational Methods (ICCM) on the Gold Coast. The Departmental Scholarship from the Department of Materials Engineering who also assisted in funding my visit to New Zealand for the International Conference in Processing and Fabrication of Advanced Materials (PFAM). Finally, the Australian CSIRO, who not only provided a top-up scholarship but also gave me access to world-class resources for conducting my research.

I'd like to express my sincere gratitude to my colleagues: Yogita Ahuja, who helped in conducting the experimental work. Her positive attitude and energy was inspiring. My thanks to both Ehsan Bafekrpour and Derek Lok who were both able to provide experimental guidance and help during particular stages of the project, which was much appreciated. I'm also grateful to John Mikhail who provided some of the experimental materials. Finally to Yuanshen Qi of the Materials Engineering Department for his assistance acquiring the EBSD images.

My thanks go to the staff of the Mechanical Engineering workshop and in particular Hugh Venables, who provided technical assistance for many of the experiments.

This thesis would not have been possible without the support and love of my family. Their encouragement and patience has been enormous, my parents, Elton and Glenda, my brother and sister in-law, Christopher and Julie, and my sister, Sarah.

Symbols

Symbol	Description
a	Scalar a
\mathbf{a}	Tensor a , which can be of any order, for example first order (vector)
$\mathbf{a} \cdot \mathbf{b}$	Dot product of vectors a and b , also called first order vector contraction
$\mathbf{a} : \mathbf{b}$	Dot product of tensors a and b , also called second order tensor contraction
∇	Gradient operator
Δ	Increment or difference operator
t	Time (s)
u	Position (m)
v	Velocity (m/s)
a	Acceleration (m/s ²)
V	Volume (m ³)
S	Surface area (m ²)
p	Momentum (kg-m/s)
f	Force (N)
m	Mass (kg)
ρ	Density (kg/m ³)
T	Temperature (K)
k	Thermal conductivity (W/m-K)
C_p, C_v	Specific heat capacity (J/Kg-K)
α_t	Coefficient of thermal expansion
q	Volumetric thermal energy (source) (W/m ³)
dq	Increment of energy flux (W/m ²)
E_{HF}	Thermal flux from input power (W/m ²)
E_f	Thermal energy from friction (J)
E_p	Volumetric thermal energy from plastic dissipation (J/m ³)
J	Heat flux (W/m ²)
g	A thermal energy coefficient (corresponds to loss at interface)
η	A thermal energy coefficient (plastic work dissipated as heat)
h_c	Convection coefficient (W/m ²)
Q	Power or thermal energy (W)
M	Torque (Nm)
r	Distance or displacement (m)
ω	Angular velocity (rad/s)
\mathbf{R}	Rotation matrix

Symbol	Description
E	Young's modulus (GPa)
G	Shear modulus (MPa)
ν	Poisson's ratio
σ	Stress (MPa)
σ_K	Kirchoff stress (MPa)
τ	Shear stress (MPa)
τ^r	Resolved shear stress (MPa)
ϵ	Strain
$\dot{\epsilon}$	Strain rate (s^{-1})
γ	Shear strain
$\dot{\gamma}$	Shear strain rate (s^{-1})
F	Deformation gradient
B	left Cauchy-Green strain
I	Strain invariant
P	Pressure (MPa)
W_e	Elastic strain energy density function
J	Normalised volume change
Λ_{res}	Extension due to free thermal expansion
α	Internal hardening variable
\mathbf{b}	Body force (N)
α	Material constant
$\rho_{w,c,t}$	Dislocation density for cell wall, cell interior and total, (m^{-2})
m, n	Strain rate sensitivity parameters in two-phase model
α^*, β^*, k_o	Material parameters for two-phase model
f	Volume fraction of dislocation density within the cell walls
d	Average grain size (m)
K	Proportionality constant
M_T	Taylor factor
b	Burgers vector
w	Weighting function
S_{ip}	GIMP shape function
χ_p	Characteristic particle function for particle 'p'
N_i	Standard MPM grid shape function for node 'i'
\hat{n}	Unit vector in normal direction
\hat{t}	Unit vector in tangential direction
μ	Coefficient of (Coulomb) friction
$T1, T2, T3$	Thermocouple 1,2,3
χ_{ms}	Mass scaling factor
R_b	Rigid bias factor

Publications

Fagan, T., Lemiale, V., Ibrahim, R. & Estrin, Y. A Thermal Model of Friction Stir Processing Using a Particle Based Method in Proceedings of the 4th International Conference on Computational Methods (2012).

Fagan, T., Das, R., Lemiale, V. & Estrin, Y. Modelling of equal channel angular pressing using a mesh-free method. *Journal of Materials Science* 47, 4514–4519 (2012).

Fagan, T., Das, R., Lemiale, V., Ibrahim, R. & Estrin, Y. Application of Smoothed Particle Hydrodynamics to the Simulation of Equal Channel Angular Pressing in Proceedings of the 19th International Conference on Processing and Fabrication of Advanced Materials (Auckland, New Zealand, 2011).

Islam, S., R.Ibrahim, Das, R. & Fagan, T. Novel approach for modelling of nanomachining using a mesh-less method. *Applied Mathematical Modelling* 36, 5589–5602 (2012).

Islam, S., R.Ibrahim, Das, R. & Fagan, T. Understanding of nanomachining using Smoothed Particle Hydrodynamics in Proceedings of the 19th International Conference on Processing and Fabrication of Advanced Materials (Auckland, New Zealand, 2011).

Chapter 1

Introduction

1.1 Background and Motivation

The industry value added (IVA) by the manufacturing sector was just under \$98b in the 2012-2013 Australian financial year [1], for which the fabricated metal product manufacturing sector contributed roughly 10%. As a critical component of our economy, the growth and success of this sector is vital for the continuing wealth of this nation.

There is however, great pressure from low-labour cost countries to manufacture products at lower cost, and without drastically reducing labour expenses, the viability of manufacturing in Australia and other western countries relies on improving current processing technologies. Adoption of new manufacturing techniques can mean an edge over competition and reduction in processing costs and material wastage. It is vital then that new technologies and processes be discovered, developed and understood through research.

An exciting and promising new fabrication technology is Friction Stir Processing (FSP). Adapted by Mishra et al. [2] from the more well known Friction Stir Welding (FSW), FSP is characterised by the ability to improve localized mechanical properties in metals through modification of their microstructure. Indeed, microstructural features, most notably grain size for polycrystalline materials, are one of the key factors affecting nearly all aspects of the physical and mechanical behaviour of polycrystalline metals, as well as their chemical and biochemical response to the surrounding environment. As such, the search for the next level of metal processing technologies has led many to develop processes that focus on microstructure modification and grain size refinement.

Although there exist a number of processes that aim to improve mechanical properties through various methods of grain refinement, such as processes of severe plastic deformation (SPD), powder processing and electrodeposition, FSP is a relatively new technique that brings a host of advantages and opportunities. The process aims to reduce the grain size locally, rather than through the bulk of the specimen and is relatively independent of component size or shape. Rather than attempt to modify the entire domain, a stirring action is applied locally to the material, and through mechanical work, the grain size is reduced increasing the strength and ductility of the processed area.

The ability to process a localized area means that it can be used to locally modify microstructure without destroying previous fabrication, while simultaneously improving formability to enhance further post-processing. It offers a number of unique processing characteristics that are very attractive to a range of manufacturing environments.

Friction Stir Processing is still a new technology, and although it has been attracting greater research over the last decade, it has seen limited uptake by industry. The complexity of the material response to FSP is also an issue, as subtle processing changes can result in considerable variation in resultant properties. Computer modelling, when used in conjunction with experiments, offers the ability to develop new processing technologies in a much more effective way; and this depth of understanding is what will allow the technique to develop and industrial opportunities to become more apparent. This justifies the need for a reliable numerical model to be initially validated against experimental results, and subsequently used for further investigation.



Figure 1.1: Computer generated image (CGI) of copper plate under Friction Stir Processing.

A number of numerical models have been developed for FSP, with varying complexity, but very few are able to predict the resulting microstructure. As a key characteristic of the process and determining factor in so many material attributes, prediction of the grain size is crucial for modelling of FSP - for its continuing development and ability to support experimental work.

In addition to the grain size, another aspect that requires special consideration in FSP modelling, is the presence of very large deformation. Typical methods such as the Finite Element Method (FEM) applied in a Lagrangian framework struggle to maintain accuracy without remeshing - a computationally expensive solution to excessive mesh deformation. Applied in an Eulerian framework, the FEM is able to avoid the large deformation problem, but capturing surfaces and material history is also much more difficult. Gaining greater and greater popularity are the particle or meshless methods. These particle based numerical methods provide an avenue to analyse material response in a Lagrangian framework without the problems of excessive mesh distortion. There have been no models proposed to date using a particle based method to simulate FSP.

Friction Stir Forming (FSF), a new area of research, is a specific application of FSP to the manufacture of composite materials [3]. By a small modification to the tool, in addition to microstructure refinement, the thermomechanical process forms a mechanical interlock between two materials. This process thus has the ability to rapidly form composite materials, through a single pass of the tool.

1.2 Research Overview and Objectives

The aim of this project is to develop a numerical model that relates the external process variables of FSP, such as tool rotation rate and penetration depth, to resulting microstructure and mechanical properties of processed FCC metals.

To achieve this, a particle based numerical method is combined with a physically based material model. The application of a particle based numerical method will enable comprehensive analysis of material and surface flow due to the ability to capture large deformation and natural handling of free surfaces. The physically-based material model, in the context of a thermal and mechanical problem, will enable a material response dependent not only on the temperature, deformation and deformation-rate, but also upon the evolution of the underlying microstructure developed during FSP.

Such a comprehensive and inherently physically based approach represents a major step forward for the numerical modelling of FSP.

In summary the research objectives are:

- 1: The development of a full three-dimensional thermo-mechanical model of FSP within a particle based numerical framework, capable of predicting the effect of each of the experimental parameters.
- 2: Application of a physically based constitutive law able to capture the resulting temperature, material flow and microstructure for processed metals.
- 3: Validation of the model against experimental results, including temperature profiles, material flow and microstructure development. In this thesis I will focus on pure copper with additional microstructure validation including aluminium alloy 5005.

In addition to the research objectives above, the numerical model will be developed in the context of FSF. Although a secondary material will not be used to form a composite, the model will be developed with a pinless tool. Occasionally used in FSP, the pinless tool is necessary in FSF. This will be discussed further in the following chapter. The focus of this thesis however, is the parent process FSP.

1.3 Chapter Outline

The thesis is divided into 7 chapters. As a general overview, the first chapter introduces the modelling of FSP, providing necessary background information and discussing the FSP modelling field as it is in literature. Following this is a detailed description of the numerical method chosen for this thesis. Subsequent chapters develop the numerical model, each building on the previous chapter. The final chapter discusses the significance of this work and further aspects that could be developed in the future.

- 1: The present chapter provides the reader with the basic overview and motivation for this research, outlining the aims and expectations of the work.
- 2: Chapter 2 is split into two sections, the first provides a detailed background of FSP. The second presents the modelling of FSP as it currently stands in literature. The background information will include a detailed explanation of the process along with benefits and applications. The modelling review will focus on the methods used to model

particular aspects of FSP, including the thermal field, material flow and microstructure. Comparing the existing models in literature, the importance of a meshfree model of FSP that can predict the evolution of temperature, material flow and microstructure, will be established.

- 3: Chapter 3 discusses the particle based numerical method utilized for modelling FSP in this work. It will provide background information necessary to understand how a numerical model for FSP can be developed. The chapter will outline the governing equations of the Material Point Method (MPM), followed by their discretization for solution over discrete points. The constitutive model in the context of large deformation will then be discussed followed by the description of how forces and contact between bodies is handled in MPM. Finally the full MPM update algorithm will be presented.
- 4: Chapter 4 begins the process of developing a model of FSP. It begins by describing each of the components necessary for the thermal model of FSP. It includes the description of an analytical solution for the heat source and thermal boundary conditions such as thermal losses. This is then followed by describing the experimental work undertaken to validate the numerical model. The resulting thermal field is compared to the experimental results.
- 5: In Chapter 5 the thermal model is refined by adding the mechanical component of FSP. This allows for more complex boundary conditions based on interaction between the tool and workpiece and thus more accurate portrayal of the experimental procedure. The constitutive law applied will be the Johnson-Cook flow law, and the analysis now includes temperature and material flow resulting from frictional contact and plastic deformation.
- 6: In Chapter 6 a dislocation-density based constitutive law is introduced. This enables the model to predict the evolution of the underlying microstructure of the processed material. The physically based law replaces the previously applied empirical relationship. The results will now include microstructure evolution, with comparison to the experimental results for both copper and aluminium alloy 5005.
- 7: Finally chapter 7 provides a discussion of the overall work, followed by a statement on the contribution to the field and future outlook.

Chapter 2

A Review of Friction Stir Processing

2.1 Background Information

2.1.1 Introduction to the Process

In FSP, a cylindrical non-consumable tool, generally consisting of a pin and shoulder, is rotated and plunged into the surface of a metal workpiece. The larger diameter shoulder prevents the surface of the metal workpiece from flowing outwards, while the specially designed pin induces a stirring action, producing a combination of frictional and adiabatic heating allowing the metal to flow around the pin from the advancing side to the retreating side. Localised severe plastic deformation occurs generally resulting in grain refinement. A backing plate serves to remove excess heat from the system. Figure 2.1 below shows a schematic of the process.

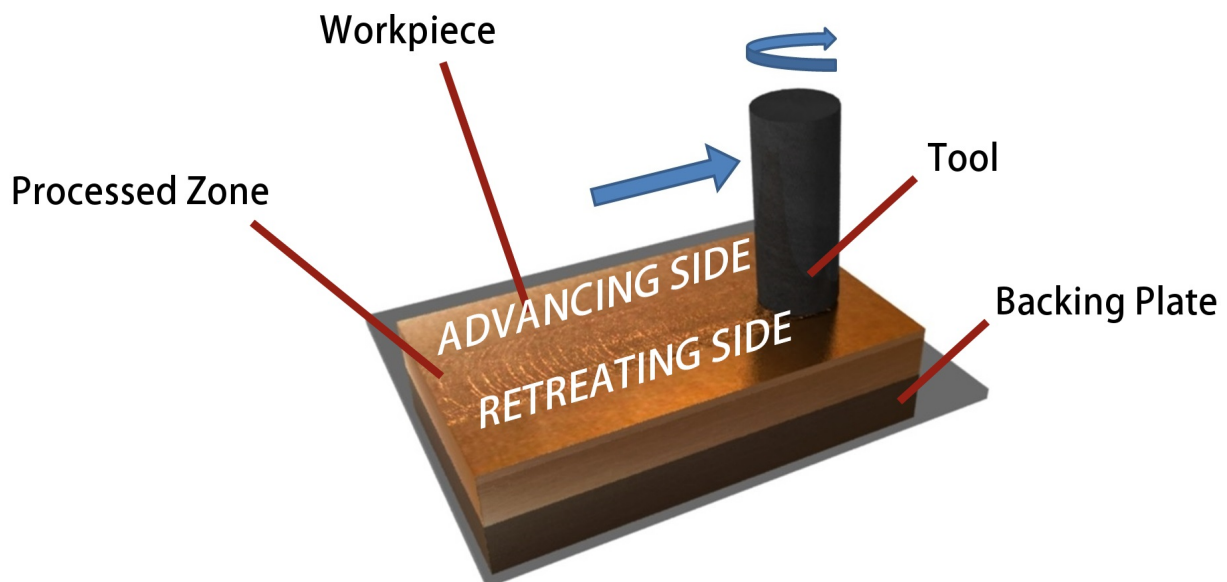


Figure 2.1: Schematic of Friction Stir Processing.

The tool is comprised of a shoulder and pin, although sometimes just the shoulder is used (pinless). Both tools modify the surface microstructure, however the depth of modification is reduced without the pin. In the case of thin plates the pin is often not needed [4]. The same pinless approach can be applied to thicker plates where only surface processing is required.

This can be particularly useful in the development of hybrid composite materials, where composites are formed through mechanical interlocking of adjacent materials. Removing the pin allows the surfaces to form a mechanical joint while simultaneously avoiding damage to either material. As discussed in the Introduction (chapter 1) this has been termed Friction Stir Forming [3] and is a new area of research.

Two terms often used in this field, are 'advancing' and 'retreating' sides. These are dependent on the rotational direction of the tool and its traverse direction. The advancing side experiences both tool rotation and translation in the same direction. The retreating side experiences tool rotation in the opposite direction from the traverse direction. The two sides can therefore experience differing thermo-mechanical effects.

Heating is produced within the workpiece by two mechanisms, the plastic deformation of the material generates heat that is released volumetrically, and sliding contact between the tool and the workpiece induces a frictional heat. The localised heating, generally up to 90-95% of the melting temperature, softens the material around the pin and shoulder, allowing the tool rotation and translation to move the material to the rear. The position of the shoulder prevents the movement of material above the workpiece surface, thus with no loss of material, the processed workpiece has the same cross sectional shape as in its initial condition.

FSP has distinct advantages compared to other metal working techniques [5]:

- 1: It is a short route, solid state, one step technique that achieves microstructural refinement.
- 2: The resulting microstructure and mechanical properties can be adjusted depending on tool design and process parameters.
- 3: The depth of processing can be adjusted by the height of the pin, ranging from several hundred micrometres to tens of millimetres. This is in contrast to many of the processing methods which refine the bulk microstructure.
- 4: It is a "green" technology, energy-efficient, without harmful gases or noise, and no consumable components.
- 5: There is no modification to the original shape of the processed component. Many of the established processes to induce grain refinement, such as Equal Channel Angular Pressing and High Pressure Torsion, require specific geometries to enable processing.

There are specific regions of the cross-sectional processed zone often referred to in literature. The area the pin and shoulder pass through, often called the stir zone (SZ) or nugget, has the greatest level of plastic deformation and thus grain refinement. The thermo-mechanically affected zone (TMAZ) is where movement of the pin and shoulder deforms and heats the material but to a smaller degree than the stir zone. The heat affected zone (HAZ) experiences a purely thermal impact, which depending on the process conditions can result in modification of the microstructure in a similar way to annealing. The base or parent metal (BM/PM) extends beyond this heat affected zone, and is essentially unaffected. These zones are illustrated in Figure 2.2. Note that the precise change in microstructure will be dependent on both the material and processing conditions applied. Figure 2.3 shows further examples and illustrates that sometimes not all zones are present, with direct transition between the stir zone and base material in some cases.

The material movement around the pin is complex, owing to pin design, and the variability of processing parameters, generating gradients in strain, temperature and strain rate. The

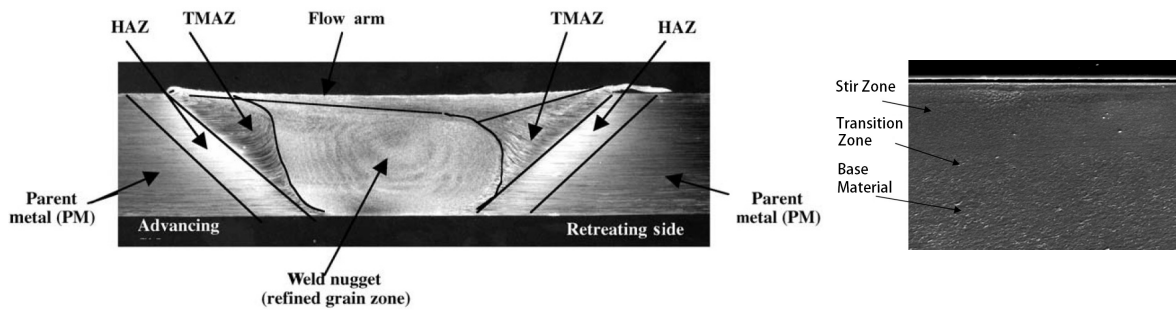


Figure 2.2: Traverse section of processed workpiece (with pin) [6] and pinless FSP [4].

resulting microstructure through the SZ and TMAZ reflect these different thermomechanical histories and is not homogeneous.

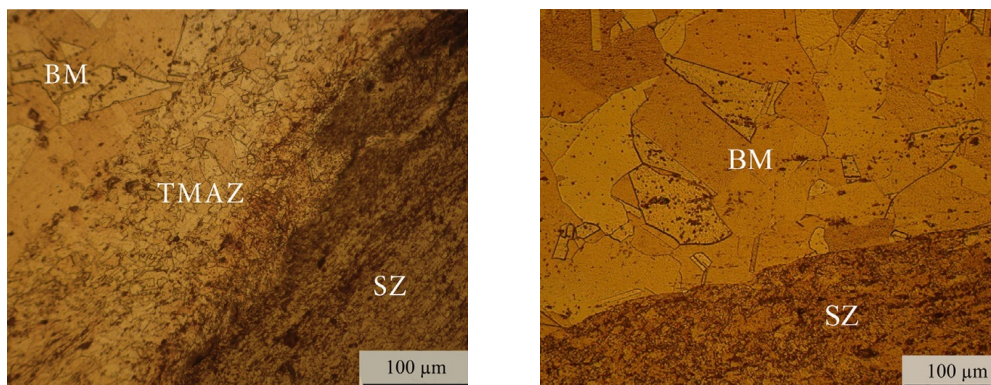


Figure 2.3: Example cross-section FSP zone transitions [7].

Thus evolution of grain size during processing is complex and in addition the processes that occur at the microstructure scale are different for some metals. For example, alloys have a strong dependence on precipitate evolution, but pure metals do not.

The unique combination of characteristics that FSP exhibits:

- 1: Low amount of heat generated (below melting)
- 2: Severe plastic flow of material
- 3: Extreme grain refinement in the stir zone
- 4: Healing of flaws and casting porosity
- 5: Random misorientation of grain boundaries in the stir zone
- 6: Mechanical mixing of the surface and subsurface layers

Drawbacks of FSP include:

- 1: Variation in workpiece shape or dimension typically requires altering processing parameters for ideal performance. The thermo-mechanical process is quite complex and the relationship between input parameters and the final material properties is not clear. This makes it difficult to correctly process newly designed workpieces without significant testing.
- 2: Following from the previous point, varying processing parameters can have a significant impact on the resulting properties of the processed workpiece. This process therefore requires high accuracy and consistency in implementation.

The study of the process can be broken into two major components of work, which are the thermal and mechanical.

2.1.1.1 Thermal Work

In FSP the heat is generated by a combination of friction and plastic dissipation during deformation of the metal. Which of these two mechanisms for heat generation is dominant depends on the contact condition between the two surfaces, which can be sticking, sliding or alternating between both of these. These conditions in turn are dependent on the process parameters, material properties, and the tool geometry.

As the temperature of the thermo-mechanically worked metal rises, the metal softens, torque is reduced, and less heat is imparted to the metal via mechanical work. This self-regulation of heat generation tends to stabilize temperatures and keep processing conditions in the solid state. Under these circumstances the stick/slide condition (also called stick/slip) could be in oscillation [8]. For modelling, this complicated set of boundary conditions is often enforced by choosing a contact condition which produces temperatures matching experimental results. This will be explained and discussed further in the numerical modelling section. However there are a number of thermal considerations within FSP, and these are illustrated in Figure 2.4.

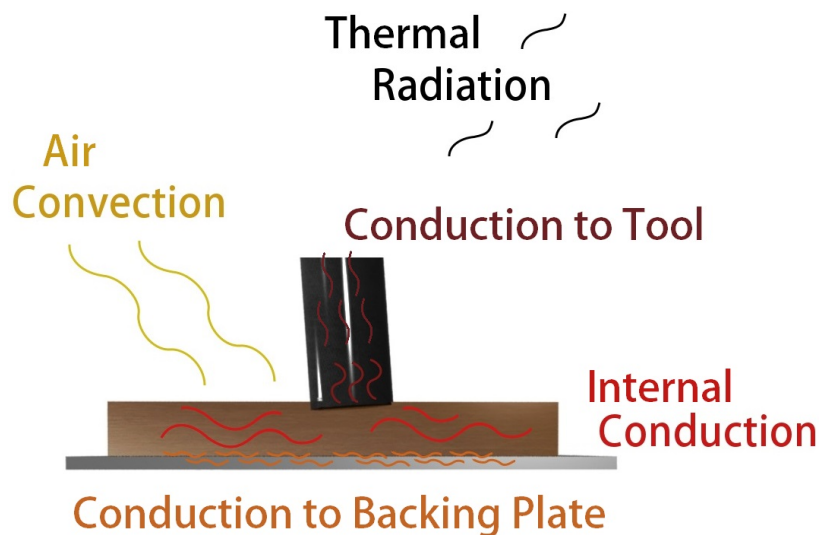


Figure 2.4: Thermal conditions of FSP.

As shown in Figure 2.4, the work carried out by the tool generates heat which is passed through the system in three ways. Conduction occurs within the workpiece and through the boundary between the workpiece and backing plate, and into the backing plate. Heat is also transferred by conduction into the tool. Convection occurs between the workpiece and the surrounding air, and to a much smaller degree thermal radiation is present. The latter is generally ignored during modelling, but conduction and to a lesser extent convection play an important role in determining the thermal condition of the workpiece [9].

2.1.1.2 Mechanical Work

There is a significant mechanical load applied to the material during FSP, with large plastic deformation and material stirring resulting in fine grains. The process parameters coupled with

the tool design control the volume of metal heated and subsequent portion swept behind the tool.

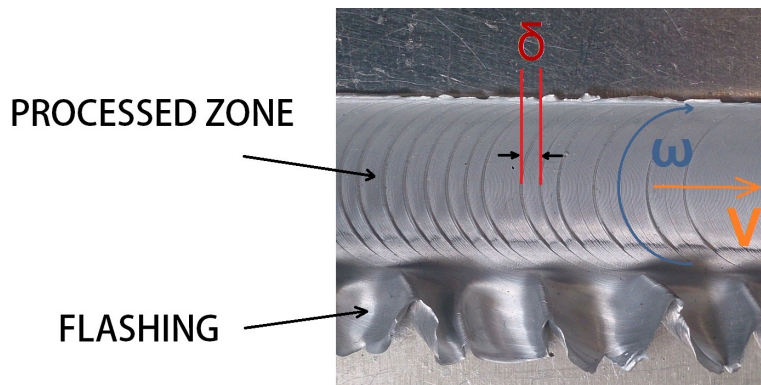


Figure 2.5: Example surface appearance after FSP. Also indicated is the distance between the bands: δ , which is approximately equal to the translational velocity divided by the rotational speed, V/ω .

The material swept behind the tool is deposited in bands, and the length between each band is estimated as the longitudinal distance the tool travels during one rotation [10], shown in Figure 2.5. The figure also shows the often present flashing, which occurs along the edge of where the tool shoulder passes. In an investigation of material flow during Friction Stir Spot Welding (FSSW), Zeng et al. [11] observed multiple modes of flashing behaviour. Figure 2.6 shows an example of material flow and flashing around the edge of the tool, similar with that expected during FSP.

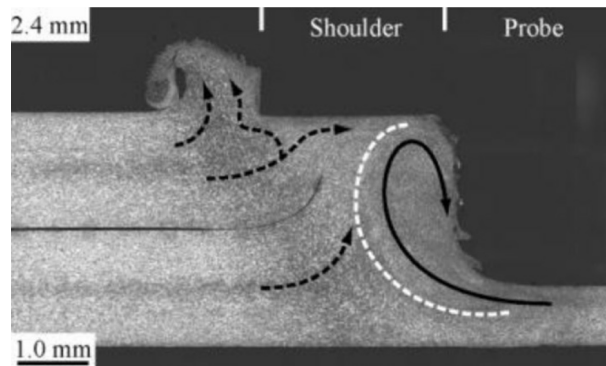


Figure 2.6: Cross section micrograph highlighting material flow and flash formed during FSSW [11].

The next section will go into detail on the specific characteristics and novel aspects of FSP.

2.1.2 Characteristics and Novel Aspects of Friction Stir Processing

FSP was first developed as a generic tool for materials processing and modification. Initially proposed by Mishra et al. [2] as a means of developing high strain rate superplasticity in aluminium alloys, it has since been shown to extend to a large range of metals and alloys, with benefits including increased strength, fatigue life and ductility. It has been identified as a solution to a number of manufacturing problems and basis for new manufacturing techniques. Some of the benefits and applications of FSP include:

- 1: Superplasticity

- 2: Improvement of cast components
- 3: Manufacture of surface composites through insertion of metallic powders
- 4: Enhancement of room temperature formability
- 5: Enhancement of Powder Processed Alloys
- 6: Creation of mid-section channels

These will be discussed in more detail below.

2.1.3 Superplasticity

Superplasticity refers to the ability in metals to attain very high levels of ductile behaviour, and in general shows high uniform elongation when pulled in tension, while maintaining a stable microstructure. In practice, metals exhibiting superplasticity are able to be formed and processed at a faster rate compared to their non-superplastic counterparts.

The characteristics owing to this behaviour are a fine grain size, typically less than 10 - 15 μm , and thermal stability of the fine microstructure at elevated temperatures. Obtaining these qualities has been an elaborate multi-step process previously, but FSP has been shown as a viable and simpler alternative. As mentioned in the previous section, Mishra et al. [12] showed that superplasticity was achievable in an aluminium alloy via FSP. Further research [13, 14] showed that Al-4Mg-1Zr alloy and 7075Al alloy could similarly exhibit high strain-rate superplasticity after processing.

Figure 2.7 shows example tension tests upon an FSP'd aluminium alloy conducted by Ma et al. [13].

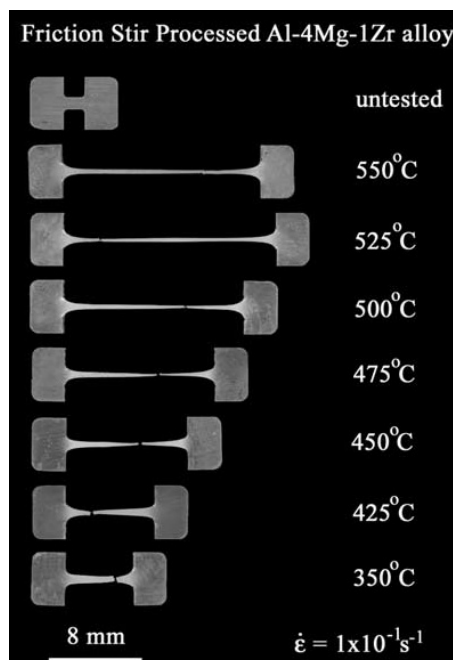


Figure 2.7: Friction Stir Processed Aluminium Alloy exhibiting superplasticity [13].

More recent work has focussed on achieving greater homogeneity through the workpiece via implementation of multipass FSP [15].

2.1.4 Improvement of Cast Components

Die castings are made by the rapid injection of molten metal into metal molds under high pressure. The procedure is relatively efficient and effective in mass production. However, casting defects can occur, such as porosity and cold flake. These casting defects are introduced during the casting process. Molten metal is poured into a sleeve and then injected into a mold by a plunger. While the molten metal resides in the sleeve, the molten metal in contact with the surface of the sleeve can cool and solidify. As the material is pushed into the mold, this solidified layer can be scraped off, broken up, and pushed in to form part of the cast structure. These small impurities embedded within the cast material reduce the strength of the final product. Similarly the presence of porosity can reduce fatigue life as these concentrate stress. Typically this requires testing to determine if the cast product is free of defects [16], and if present the product is re-smeled and cast again. Post processing by FSP however, could provide an alternative solution to re-casting with the added benefit of localised property enhancement.

In one of the most widely used alloys in the aircraft and automotive industries, Ma and Mishra showed the complete removal of porosity in cast A356 aluminium via FSP [17]. In the specific area of cold flake removal, Nakata et al. determined that FSP can eliminate the cold flakes as well as uniformly disperse secondary particulate in aluminium alloys [18]. In the cast aluminium alloy A206, most often used in gear housings, cylinder heads and turbines, Kapoor et al. noted improved fatigue life, life to crack initiation, increased UTS and ductility [19]. In an investigation into a cast aluminium alloy (A390) applied to heavy wear applications such as pistons, cylinder blocks and compressors, Mahmoud observed healing of cavities, refinement of coarse eutectic and dendritic structures, higher hardness values and improved wear resistance [20].



Figure 2.8: Examples of cast-metal products that could benefit from post-processing with FSP. [21, 22]

As well as cast aluminium, Cao et al. found significant increase in ductility in both cast and wrought aluminium alloys [23]. In further work on cast aluminium alloys, Weglowski found decrease in porosity and microstructure refinement in aluminium alloy AlSi9Mg [24]. Song et al. found improved resistance to corrosion and cavitation erosion [25].

In maritime applications, cast nickel-aluminium-bronze alloys are widely used in thick sections, and the fabrication of these large products results in coarse grain sizes ($\sim 1\text{mm}$), resulting in poor mechanical properties. Oh-ishi et al. determined that FSP can be applied to selectively improve the mechanical properties of these structures [26]. The authors found higher strength and ductility in the stir zone, and further improvement with multiple passes.

Although often overlooked in favour of more advanced alloys, cast iron can similarly benefit from FSP. Fujii et al. conducted FSP on cast iron and found a range of benefits including

higher hardness and lower distortion [27]. Noting the expense of commonly used cast irons, Imagawa et al. conducted FSP on ferritic flake graphite cast iron. Generally unused due to its poor mechanical properties, this material is relatively inexpensive and the improvement in surface hardness could enable wider applications [28].

In summary FSP can improve service performance of cast metal components and it could enable replacement of wrought metal components with cheaper to produce cast components, where selective property enhancement in specific locations is achieved through post-process FSP.

2.1.5 Surface Composites

Metal-matrix composites (MMCs) can exhibit higher strength, higher elastic moduli and improved resistance to wear, creep and fatigue, compared to their non-reinforced counterparts. However, these bulk structures can suffer from a great loss of ductility, and the additive itself can be expensive. Applying a composite surface layer can create favourable properties on the surface, such as increased hardness and wear resistance, while retaining much of the base materials ductility, and at reduced material cost compared to their bulk alternatives. FSP offers a cost-effective means of producing surface composites.

Mishra et al. first attempted to form a surface composite via FSP with ceramic particles embedded into an aluminium substrate [29]. Since the success of this first trial, many composites have been fabricated via FSP and reported in literature [7, 30–37]. Typically the additive is in the form of a ceramic or metallic powder applied to the surface of the metal substrate. Figure 2.9 shows an example composite layer formed above the base metal [38].

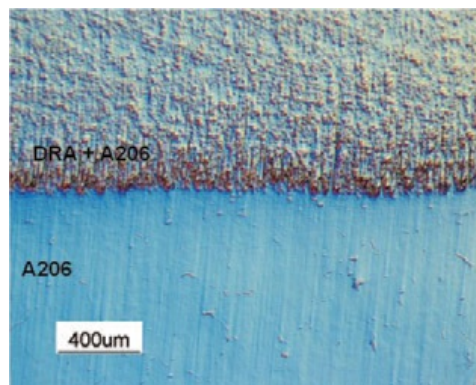


Figure 2.9: Example interface between surface composite formed by FSP and substrate/base material [38].

For proper mixing and homogeneous distribution of the added material, the method of initial distribution of the additive is significant. Methods have included using a pre-mixed surface coating containing the additive material [29], grooves along the processing direction filled with particulate [30], distributed drilled holes filled with powder [7, 34], air plasma spraying of powder upon the substrate surface [32], and direct injection of powder through a hollow and pinless FSP tool [36]. Figure 2.10 shows an example cross-section of the processed zone of a surface composite formed by FSP.

Some other investigations include effects of tool traverse and rotational speed [34], groove parameters for particulate [35, 37], and multiple FSP passes (Anvari et al. were able to drastically increase the tensile strength of their Al-Cr-O surface composite [33]).

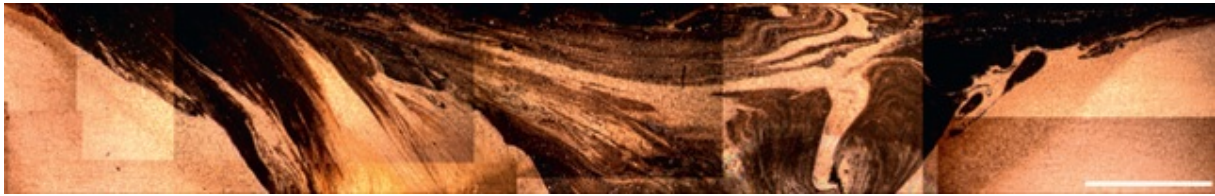


Figure 2.10: Example cross-section of the processed zone of a surface composite formed by FSP [34].

Sun et al. [38] investigated surface composites formed with aluminium alloys often used in casting. In their investigation, the authors observed higher ductility and strength resulting from the near complete elimination of porosity, also noting that their findings are significant for manufacturing of diesel engines and other critical and high integrity components.

Akramifard et al. [7] developed a metal-matrix composite with a copper substrate where surface hardness increased two-fold and wear resistance improved.

2.1.6 Room-Temperature Formability

Development of superplasticity via FSP requires through-thickness processing, however formability of large structures can be increased by local surface application of FSP. It can be used to enhance both the high-temperature and room-temperature formability - the fine-grain microstructure created during processing enables enhanced bending, torsion, compression and tension [39]. It is ideal in applications where certain sections of the structure will be manipulated, as FSP can be carried out at local areas and over a defined path. Figure 2.11 shows an aluminium alloy in bending after application of FSP to one side.

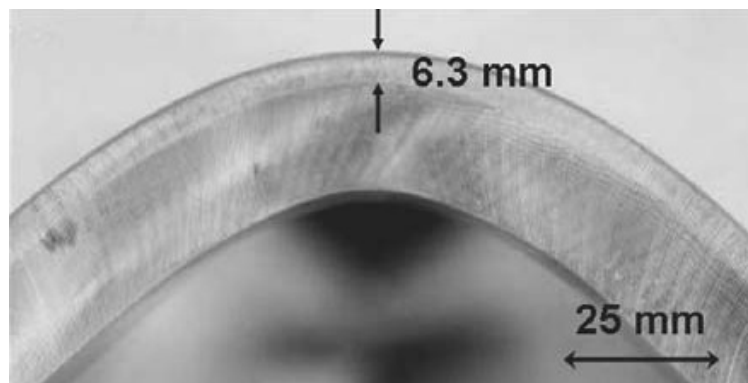


Figure 2.11: Enhanced bending after application of FSP to tensioned side (top) [40].

Although up to 37% lighter than the widely used aluminium alloys, with high strength to weight ratios, excellent castability and recyclability, one of the limitations for the increased use of magnesium alloys is their formability. Thus much of the recent work focussed on increasing formability through FSP has been conducted on Magnesium alloys, for example Mg AZ31 [41–43].

2.1.7 Enhancement of Powder Processed Alloys

Powder metallurgy is a widely used fabrication method for producing metal-matrix composites. Three stages usually make up the process - blending of the powders (generally

metal/ceramic), pressing or cold compaction, and then sintering. An efficient means of producing bulk composites, powder metallurgy has some disadvantages including porosity and segregation or clustering of the reinforcing particles from the matrix particles. Degradation of the mechanical properties results. FSP can be applied post-fabrication to remove some of these defects.

Liu et al. showed that increased yield strength could be achieved through FSP of their carbon-nanotube/aluminium composites [44, 45]. Izadi et al. found improved microhardness and particle distribution with elimination of porosity [46]. Zhang et al. noticed improved strength and ductility due to the refinement of coarse particle clusters [47]. Figure 2.12 shows how particle clustering can be reduced and greater homogeneity of the reinforcing and matrix material achieved [46].

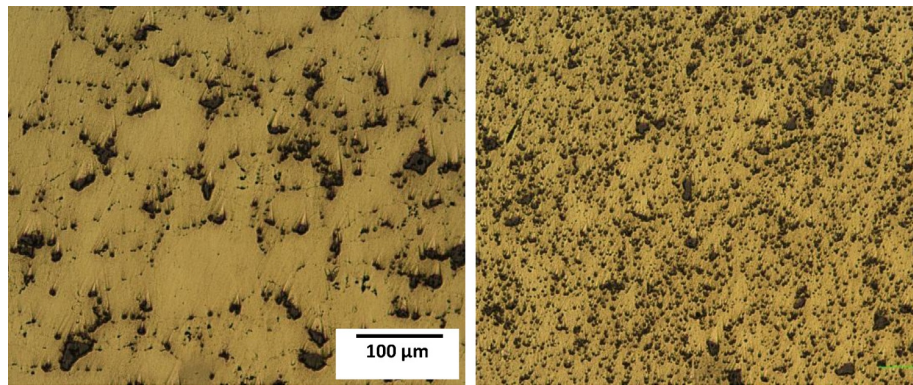


Figure 2.12: Improvement in particle distribution and homogenization [46]. Left) as-sintered, right) after FSP (same scale).

2.1.8 Friction Stir Channeling

One of the possible flaws generated in FSP is a cavity where the material is not completely filled in behind the tool. Figure 2.13 highlights this quite well with a cross-section of a processed region.

Defects such as these are detrimental to the improvement in mechanical properties that is often sought. However, in the field of friction stir channeling (FSC), Balasubramanian et al. [49] has suggested that designing specifically for a continuous wormhole or channel can be extremely useful. Heat exchangers are typically fabricated from joining multiple tubes, or by independently fabricating and joining fluid channels. By modifying the process parameters of FSP, fabrication of heat exchangers is possible in a single step. This is done by creating continuous, integral channels in a monolithic plate with one FSP pass. Generally in FSP, researchers are tweaking the process parameters, such as traverse speed, rotation rate, pin depth and tool shape, to avoid any wormhole or voids occurring, but in this case the creation of a wormhole is essential. The process parameters themselves are what make FSC possible. Figure 2.14 shows a fabricated channel and an example view through the cross-section of a channel.

The main difference in processing for FSC is that the profiled tool is rotated in such a way that the material flows upwards towards the tool shoulder. Secondly, an initial clearance is provided between the top of the plate and the tool shoulder - room for material from the base of the pin to flow into.

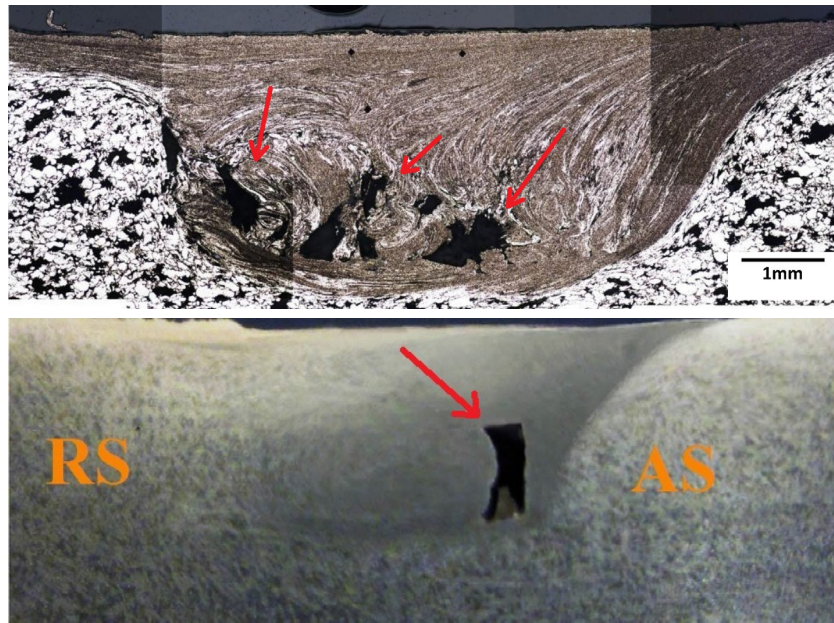


Figure 2.13: FSP conducted upon a powder processed composite [46] and an aluminium alloy [48] resulting in cavities/wormholes indicated by the arrows.

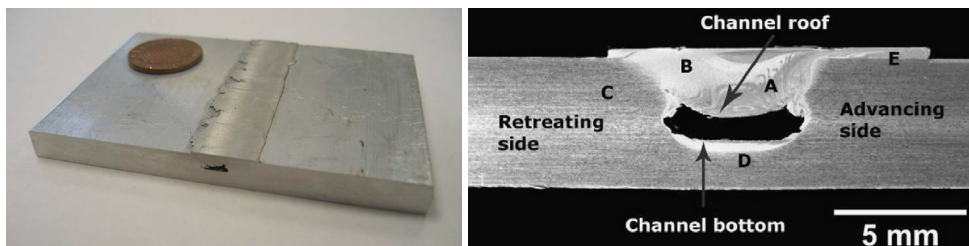


Figure 2.14: Left) A channel fabricated using friction stir channeling technique [50], right) cross-sectional image of a channel [49].

Balasubramanian et al. showed that channels could be achieved in both curved and linear profiles and that the channel volume could be controlled through manipulation of process parameters [49]. They found the channel size increased with both an increase in the traverse speed and decrease in rotational rate. The hydraulic diameters of the channels formed varied from 0.2mm to 1.2mm, classifying them as minichannels. In following works by the same group [50, 51], they attempted to develop a relationship between the processing conditions (tool rotation rate, traverse speed and plunge depth) and the resulting channel area and shape. The force on the pin was also studied, and a relationship found between the position of the net force on the tool and the condition of the channel produced. Such information could eventually be useful in a control-feedback system, where monitoring of the processing conditions such as tool pressure, combined with manipulation of the tool parameters, can simultaneously control creation of channels (FSC) or avoidance of wormholes (FSP).

2.1.9 Summary

The physical convenience of FSP is an attractive quality - actual implementation can be very quick in industrial settings, and the previous sections have highlighted how varied and widely applicable FSP can be to modern manufacturing. However, due to the complex relationship between the processing parameters and final properties of a given processed metal, deter-

mining the correct parameters to use for a particular application can be a time consuming task.

Deeper understanding may shed more light on the process and enable faster uptake by industry. However, this understanding can be difficult to gain with the experimental tools available. Computation allows for great detail and powerful observation - it is possible to look into the various parameters and their respective effects on the final mechanical properties. Many phenomena, for example plastic dissipation or heat loss, can even be isolated to observe their specific impact. There are difficulties in numerical modelling however, and these are discussed below.

2.2 Numerical Modelling of FSP

Computational simulations play a very active role in developing new material processing technologies. The ability to run many simulations in parallel make it an efficient way to discover new information. A limited number of models have been developed in FSP over the past decade, but many more so in Friction Stir Welding, of which FSP is a derivative.

There is one difference between the conditions for Friction Stir Processing and Friction Stir Welding. In FSW, being a welding technique, the processed material is initially in two parts. The stirring action actually combines the two pieces together. In FSP, the stirring action is used only to manipulate the microstructure. As the precise difference in response between these two processes is not clear, the review will be focussed on those papers researching FSP, and supplemented by work from FSW where applicable. By far, most research has gone into FSW, and there is sufficient similarity between the two processes that inclusion of these works will be beneficial.

A similar analogy can be applied for the many other processes that are derivatives of FSW or FSP. FSW is the most well known, but others include Friction Stir Spot Welding (FSSW) [52], where the process includes only the plunge stage of FSW (no translation) and as the name suggests is used to create spot welds. Friction Stir Forming (FSF) uses the material flow aspect of FSP to create a mechanical interlock between two materials [3]. Direct Friction Stir Processing (DFSP) modifies the FSP tool for application to surface composites [36].

With that said, below is a review of the current state of modelling in Friction Stir Processing. Many good reviews have been published to date, for example [5, 40], this one will focus on the numerical aspects of the published models rather than their specific results. Initially however, the basics of numerical modelling will be described.

2.2.1 Numerical Methods Overview

This subsection gives an overview of the methodology to create a numerical simulation. Insight into this area will make the subsequent sections easier to follow.

From the physical phenomena, mathematical models are developed in the form of governing equations with boundary conditions and/or initial conditions. These are often in the form of a set of ODE's, PDE's, or integrals. The initial conditions and boundary conditions allow these to be solved for the field variables in space and/or time.

When the problem cannot be solved according to a closed-form (analytical) solution, generally due to the complexity of the geometries, loads or boundary conditions, a numerical

solution is needed.

The way that this is done, is through domain discretisation, where the problem geometry is subdivided or discretized into smaller discrete areas/volumes, and form the framework for the solution. This framework is generally a mesh or grid, made up of interconnecting grid nodes. The grid nodes are the locations where the field variables are evaluated, and give an insight into the material behaviour as a whole. Its accuracy is obviously dependent on the size of the cells/distance between the nodes.

The numerical discretisation is referring to changing the continuous form of the governing equations to discrete or discontinuous representations. This allows the problem to be solved over the mesh or nodes.

All this must then be translated into a computer code, where factors such as accuracy, efficiency (speed, storage), and robustness (consistency, ability to handle errors) become important.

The physical phenomena that can be modelled are infinite, and an important aspect of numerical modelling is adapting the method to the problem that is to be solved. Fundamental to this, is the frame used for describing material motion.

There are two fundamental frames for describing material motion, the Eulerian and Lagrangian description. To help describe each, a common analogy is that of water flowing through a channel. If a temperature sensor is placed on the inner channel wall, we could track the temperature data of many water particles as they passed that point. In another type of analysis, we could allow a sensor to flow with the water, tracking the temperature of just local particles, but continuously, as they flow through the channel. The first case is analogous to the Eulerian framework, the second to Lagrangian. With each, we gain a picture of the problem from a different perspective.

When a fixed mesh is used and particles pass through it, this is considered an Eulerian analysis. If the mesh distorts with the material, this is a Lagrangian analysis. Another way of approaching Lagrangian analysis is without a mesh at all, whereby the particles are free to move around without relying on a rigid connectivity to their immediate neighbours.

Each of these techniques has advantages and disadvantages, which will be discussed below.

2.2.1.1 Lagrangian Grid-based Methods

Advantages of Lagrangian grid-based methods

- i) No convective terms - In Lagrangian analysis, there are no convective terms in the related PDE's, so numerical diffusivity is reduced.
- ii) Traceable history of variables at material points - As the mesh distorts with the same material points, gaining the history of the field variables is relatively direct.
- iii) Applying boundary conditions is straightforward - The grid nodes can be placed at boundaries and material interfaces. The boundary conditions at free surfaces, material interfaces and moving boundaries are automatically imposed, tracked and determined by the movement of these nodes.
- iv) Complex bodies are solvable - An irregular mesh can be applied for complicated geometries.

- v) Minimised computation time – The grid is only applied to the problem domain, minimising nodal calculations as deformation or motion does not require the use of a grid extending beyond the problem geometry.

Disadvantages of Lagrangian grid-based methods

However, for large material deformations, the mesh can become distorted and entangled which leads to inaccurate solutions or error. Figure 2.15 highlights this problem with the simulation of a high velocity particle impact modelled in the FEM package, Marc Mentat.

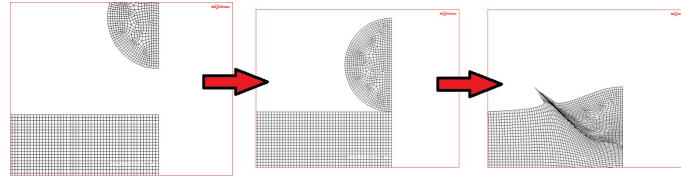


Figure 2.15: Large deformation of mesh in impact simulation.

One method to overcome this is to apply re-meshing, where a new undistorted mesh is overlaid on the old distorted mesh, so that the following-up computation is performed on the new undistorted mesh. The new elements gain the physical properties of the old cells by calculating the mass, momentum and energy transport in an Eulerian description. However, this procedure can be very time consuming and accuracy of material history can also be reduced due to interpolation of data between the new and old mesh. There is also great technical difficulty in applying this solution for 3D problems.

2.2.1.2 Eulerian Formulations

Advantages of Eulerian formulations

Large deformations and mixing - As the mesh is fixed throughout, and the material is able to flow across it, there are no problems associated with large deformation or heavy mixing. This has made this approach ideal for modelling fluid flow problems.

Disadvantages of Eulerian formulations

- i) Difficult to track material properties – As the information is stored on grid points, tracking field variables for individual particles is very difficult.
- ii) Difficult to determine material boundaries, free surfaces and material interfaces – as the Eulerian method determines the mass, momentum and energy flux across cell boundaries, it is difficult to determine the material boundaries, interfaces and free surfaces.
- iii) Larger grid required – the grid needs to cover all regions that the material can possibly flow, hence it can be many times larger than the material domain by itself, which when it comes to computation requires more time to solve.

It would be ideal to combine the strengths of these formulations, and to a degree this has been applied by the Arbitrary Lagrangian Eulerian method. It allows a Lagrangian analysis to be carried out, but when large deformation begins, there is a re-meshing stage, which can mean a new mesh the same as the original shape (as in the typical re-meshing scheme) or a new mesh with a more advantageous shape. This still maintains the same limitations as re-meshing however, but does allow wider problems to be solved, such as combined fluid and solid problems. An alternative solution is the mesh-free particle based methods.

2.2.1.3 Mesh-free Particle Methods

Another way of approaching the discretisation of the material domain is to do so with discrete particles, rather than a mesh. The material particles are not interconnected, and the field variables are evaluated on the particles, in the same way as they are solved on the nodes or gauss points of a Lagrangian analysis.

Advantages of mesh-free Particle Methods

- i) Large deformation - The problem domain is discretized into particles without fixed connectivity, allowing for large deformations.
- ii) Particle motion traceability - The ability to trace the motion of the particles means dealing with free surface problems, involving moving interfaces and boundaries, relatively easy.
- iii) Traceable particle history - Time history of field variables is also possible for any particle in the material.

Disadvantages of mesh-free Particle Methods

- i) Neighbour searching often required - As the nodal connectivity is not established for particle based methods, there is a need to determine the particles within an 'influencing zone' when approximating the governing equations. As neighbouring particles can change over time, this can be a computationally time intensive job.
- ii) Unbalanced particles - When solving over a particle domain, a lack of data points in a particular region can contribute to inaccurate interpolations and divergence of the solution.

For details of mesh-free fundamentals, see references [53, 54].

2.2.2 The Challenges of Modelling FSP

FSP is a complex process - the combination of high speed rotation, comparatively slow traversal speed, high temperatures, and large deformation create modelling challenges. The phenomena contributing to the computational difficulties will be discussed below.

Very large plastic deformation: This can result in overly deformed meshes and has encouraged most to approach the problem with Eulerian methods.

Flashing on the surface: Free surface deformation can be difficult for Eulerian methods to solve as surfaces are not inherently tracked. The severe deformation leading to flashing similarly makes it extremely difficult for a Lagrangian mesh to capture.

Boundary Conditions: A number of the parameters in FSP are difficult to quantify without other testing. The friction coefficient between the tool and the workpiece has so far been difficult to determine, with approximations often being used. Also the rate of heat exchange between the workpiece and the backing plate can vary depending on the experimental conditions. A combination of these factors means accurate modelling is difficult without some form of calibration.

High tool rotation/slow tool translation: The combination of high speed forces and a comparatively slow overall process time introduces a problem for numerical simulation. Two common formulations for integration of the PDE's exist, in general these are an explicit scheme, where integration is based on a time increment and a rate of change, and

an implicit scheme, where integration is less dependent on small timesteps, however this calculation is more computationally expensive. Generally quasi-static problems are solved using an implicit algorithm while dynamic problems are easier to approach with an explicit algorithm. In the case of FSP, the combination of very high dynamics induced by the tool rotation, with the comparatively slow overall processing time means that selecting a time marching scheme is not trivial.

Complex grain size evolution: The change in the microstructure is very much dependent on the thermal field and material deformation. Thus modelling of grain size requires a non-trivial interdependence of these three fields (including the current state of the microstructure itself).

Some of the methods used to handle these complex problems in literature will be discussed in the following sections.

2.2.3 Large Deformation and Material Flow

FSP generates large amounts of material flow and plastic deformation. In a review of material flow in FSW, Reynolds expressed the importance of studying it, expressing that the real driver for studying material flow is to elucidate accurate strain and temperature histories for the material being processed. It is only with this information in hand that microstructure prediction can be made, or intelligent decisions made on how to modify processing conditions to achieve microstructure goals [55]. Thus many researchers have undertaken the study of material flow. Common in experimental research studies is the use of tracer material to analyse the flow of material during processing. A brief review of these results will help to quantify the type of material flow that can be expected.

Shi et al. applied SiC tracer particles to observe flow around the FSP tool [56]. By observing the post processed specimens at transverse locations they were able to deduce the path the initial particles had travelled. A greater number of studies have also been conducted in FSW - in an early investigation, Colligan embedded small steel spheres in the workpiece to act as tracer material [57]. By halting the process mid-way, Colligan was able to analyse the movement of the tracer around the tool. Similarly, by placing small amounts of AA5454 at various locations in AA2195, Seidel and Reynolds were able to analyse the flow of material around the tool and through the plate [58]. Guerra et al. placed a strip of copper along the centre-line of an AA6061 weld, combining this with a process 'freeze' where the rotation and translation of the tool is stopped part-way through welding [59]. The authors were able to analyse material flow on both advancing and retreating sides of the tool, concluding that each have very different thermo-mechanical histories and properties. Schmidt et al. introduced a thin copper strip into the processing/welding line and through computer tomography (CT) were able to extract excellent visual data of the flow around the tool [60]. Some of their findings are reproduced in Figure 2.16. These studies in general provide excellent insight into material flow during processing, however the introduction of foreign material into the process arguably effects the material flow itself. Without the need for introduction of foreign matter, and powerful visualization tools, computational models have the potential to excel at analysis of material flow.

In modelling material flow, the numerical method applied needs some way of dealing with large deformation, in FSP this has generally been through Eulerian models. Routinely used in computational fluid dynamics, this method has generally been favoured in modelling of friction stir processes as they can handle the large material deformations.

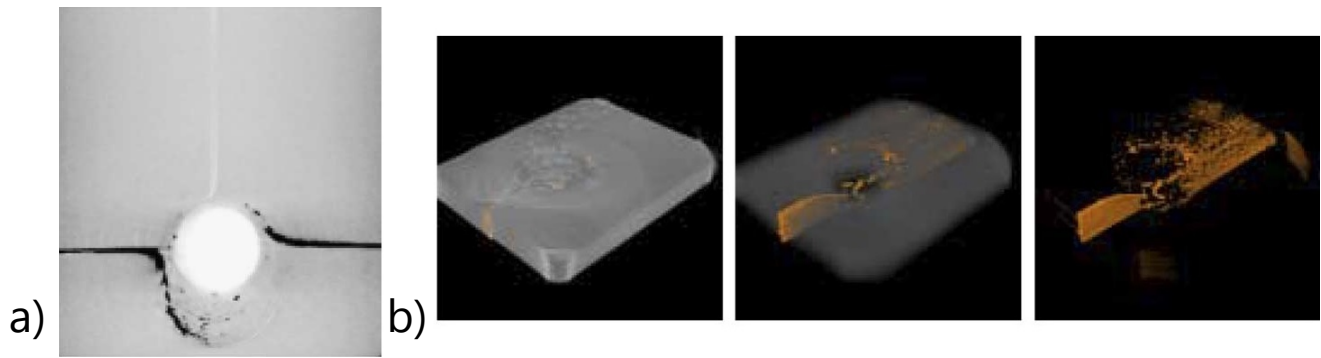


Figure 2.16: a) Example of material flow after partial passage of friction stir tool, b) CT scan of workpiece showing scatter of processed copper tracer material. [60]

Aljoaba et al. developed an FSP model using an Eulerian method - within this framework the authors were able to make predictions for the velocity field and strain rate around the tool, as well as the temperature field, dynamic viscosity, and microstructure [61]. This was followed by another work investigating the effect of coolant through the backing plate, and its effect on the resulting material flow around the tool and microstructure of the workpiece [62].

In another model, Nassar et al. [63] investigated the effect of localised melting and material flow during FSP. They were able to observe the flow behaviour around the tool for partially melted workpiece material. Other works have involved analysis of material flow around various tool profiles, in order to optimise material flow [64–66]. Figure 2.17 shows an example of material flow predicted with CFD around two tool profiles.

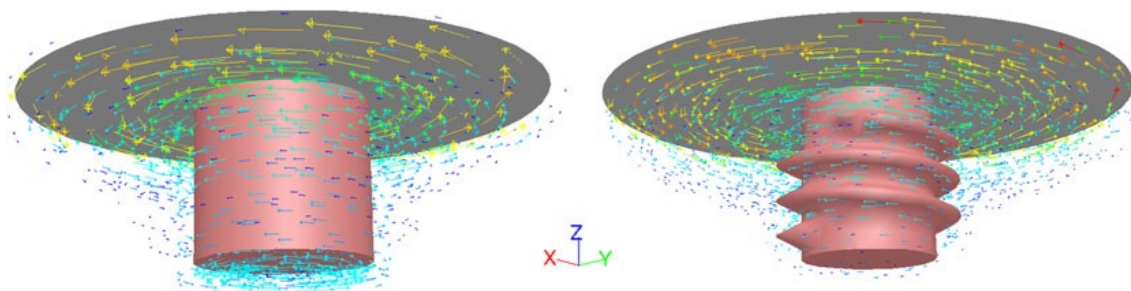


Figure 2.17: Material flow (visualised by velocity vectors) around two different pin styles [64].

Although Eulerian methods do very well with computing material flow within the workpiece, they have difficulty computing material surfaces and preventing the formation of partially filled elements. Tracking material history is also a problem - they do very well computing flow around the tool for example, but cannot follow the path of material from its initial position to its final state. An alternative approach is the Lagrangian methods of solid mechanics. However, although the mesh based methods, and in particular FEM, are well proven tools for solid mechanics problems, their drawbacks are significant and cannot be overlooked when applied to the modelling challenges of FSP; i) the fixed mesh does not allow material mixing within an element and ii) the large strain/deformation that occurs during FSP creates mesh entanglement and error prone results. Due to these challenges, an adapted FEM method applying remeshing has often been used as an alternative.

One example of this is the Arbitrary Lagrangian Eulerian (ALE) Method, which uses a mesh combining both aspects of the Lagrangian and Eulerian formulation - the mesh on the material boundaries can move with the material to track the boundaries and interfaces, while the mesh inside the material can move and reshape itself to optimize the shape of the elements,

essentially remeshing when needed.

A number of studies have been conducted with the ALE formulation. Schmidt and Hattel developed an early fully coupled 3D analysis of FSW applying the ALE method [67]. They were able to observe void formation, and draw conclusions on the parameters effecting the deposition of workpiece material around the tool. Zhang et al. developed a series of solid mechanics-based FE solutions beginning with a two-dimensional model of FSP. The authors analysed advancing and retreating material flow around a circular pin [68], see Figure 2.18 for an example of the authors' particle tracking for material flow analysis. This is similar to the two-dimensional model developed by Mukherjee et al. [69]. Zhang's model was later developed into three dimensions, similarly including particle tracking for flow analysis [70].

In a series of articles, Grujicic et al. applied the ALE formulation to FSW of aluminium alloys [71–73]. Their latter work focussed on material flow and also provided a brief overview of experimental/visualization studies to date. They investigated the effect of process parameters including weld pitch, tool tilt-angle, and shoulder/pin diameter, on the material flow, by tracking the movement of an initial sub-volume of the workpiece.

Another ALE model, Tutunchilar et al. used Deform-3D software with remeshing to model FSP [48]. They observed material flow for a number of points during the simulation. They were able to predict the shape of the stir zone based on the final resting position of nodes initially in-front of the pin and also observe material flow around the pin on the advancing, centre and retreating sides; however they did not look at material flow on the surface of the material.

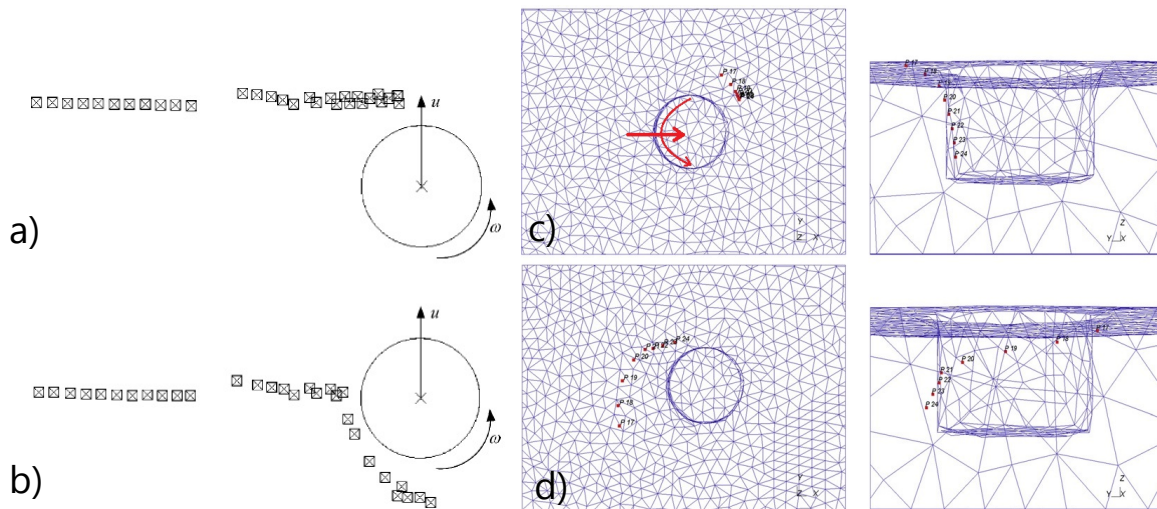


Figure 2.18: a-b) Material flow around a two-dimensional pin [68] c-d) Material flow around a three-dimensional tool [48] (top and side view).

In a recent study also conducted with the ALE formulation, a model for material deformation during FSW was developed, and they did study flashing on the surface, achieving qualitative agreement with their experiments [74].

One of the downsides of the ALE method is that remeshing is computationally expensive, and interpolation of nodal data during this stage can introduce errors. In addition, there is often the need for a separate algorithm to track the position of material interfaces.

Particle methods on the other hand, are able to inherently track material surfaces without the need for any additional algorithm. The need for remeshing is also alleviated as the particles

are not inter-connected. With this in mind, a number of modellers in various fields have begun to apply particle based numerical methods to solid mechanics problems.

A mesh-free particle method in general refers to a class of methods that define a set of discrete particles to represent the state of a system and to record its movement. Each particle can either be directly associated with one discrete physical object (such as a grain within a grain hopper or grain of sand on a beach) or as a part of a continuum problem domain, where the sum of particles make up the whole specimen.

There are many variations that have been created over the past few decades, with some being evolutions of previous formulations. Many of them continue to be actively developed for adoption to new problems and for removal of previous limitations. However, there has been no work in the literature that has applied a meshless or particle method to FSP. In the related field of FSW, in 2006 Tartakovsky et al. were the first to apply a particle method [75]. The authors developed a two-dimensional model using the Smoothed Particle Hydrodynamics (SPH) method. One of the oldest and most famous of the particle methods, it was originally created for modelling astrophysical phenomena [76, 77], and has since been adapted for a range of problems in fluid mechanics and more recently solid mechanics [78].

By colouring the material particles with two separate shades, Tartakovsky et al. was able to analyse material flow and mixing around the two-dimensional pin. Pan et al. [79] built on the previous work of Tartakovsky et al. by incorporating an effective viscosity into a three-dimensional SPH model, where the flow stress and effective viscosity are strain rate and temperature dependent.

Yoshikawa et al. applied the moving particle semi-implicit (MPS) method to model FSW, adopting an Eulerian formulation to model material flow [80]. The MPS method is another particle method and allows for the simulation of free surfaces, capturing processing effects such as flash. Investigating welding of dissimilar metals, they studied mixing of two separate plates by observing particle flow around a tool. This was followed by an investigation into the effect of tool angle on material flow [81].

In an analysis of friction stir spot welding (FSSW), which is essentially the plunge and withdrawal phase of FSP with the additional function of lap joining, Hirasawa et al. applied the MPS method to observe the effect of tool geometry on the plastic flow [82]. Studying numerous pin styles, they were able to identify and reproduce the hook like flow of material around the tool shoulder, and isolate their more desirable tool shape - in the triangular pin with concave shoulder. However, their model is decoupled, first computing the temperature field followed by the plastic deformation, which limits dependency on these two variables during the deformation. They also rely on a pre-determined yield stress vs. temperature curve for determining the onset of plastic deformation.

Due to the numerous advantages presented by particle methods, one such method will be applied to FSP in this work. However there are a number of particle methods to choose from. Apart from SPH and MPS, other particle methods include the Discrete Element Method (DEM), which has been used for simulation of soils and sands, where each particle represent one object, be it a grain or soil particle. The Element Free Galerkin (EFG) method [83] has been widely used to solve solid mechanics problems; based on the Diffuse Element Method it uses a background mesh for integration. Comparison to FEM has shown that the method is better able to handle large deformations [84].

With the advantage of only a local background mesh for integration, the Meshless Local Petrov-Galerkin (MPLG) [85] has been applied to the problems of beam and plate structures, fluid flows, and other mechanics problems. The Particle-in-Cell (PIC) method developed by

Harlow in the 60's, has been used primarily in the fluid mechanics field and more recently in plasma simulation.

The Material Point Method (MPM) is an extension of the Particle-in-Cell method from fluid mechanics to solid mechanics. It has been shown to be well suited to large strain engineering problems [86]. The author describes MPM as having a number of advantages over the traditional finite element method, and many of these are shared with other particle based methods.

- i) The problem of mesh distortion characteristic of Lagrangian FEM is eliminated.
- ii) The problem of free surface is easy to solve.
- iii) The problem of flow around an obstacle is easy to solve as in the case of an Eulerian formulation.
- iv) The problem of self-contact is solved automatically, there is no penetration of particles because the velocities of the material point are calculated by interpolation of nodal values defined on the background Eulerian mesh.
- v) The boundary conditions can be applied easily as in the case of FEM.
- vi) External forces and other boundary conditions can be applied at nodes of the computational mesh or on the material points, whichever is more appropriate for the problem.
- vii) Adding material points during calculations is relatively easy, this is needed in for example, filling a silo.
- viii) The finite element method can be modified for the material point method relatively easily. One major reason for this is that the gauss points in FEM serve as the material points in MPM, but with the additional freedom that they are not fixed in space within the mesh element.

The main drawbacks, the author argues, are that the stability for time integration depends on a critical value for the time increment, and this value can be significantly smaller than in the case of FEM. However, this can be alleviated by adding more material points - although it should be noted that more material points increases the number of necessary computations, or as more and more researchers are integrating into their codes, implementing the method such that it can run in parallel.

As many of the particle based numerical methods have been successfully applied to solid mechanics problems, one of the criteria for modelling selection becomes the ease with which one can use the method itself; and there are many freely available codes on the internet for SPH and MPM. A list of SPH codes available online can be found in [87]. For MPM there is NairnMPM [88] and Uintah [89]. As these are robust codes with user communities and resources for support, it makes sense to use one of these methods for modelling of FSP.

In a study by Ma et al., the authors consider the numerical advantages and disadvantages of both MPM and SPH as applied to hypervelocity (or high strain rate) impact problems [90]. They note a number of these:

- i) The critical time step is determined by the smallest smoothing length in SPH, and by the background mesh size (constant) in MPM. The smoothing length in SPH varies with particle distances, and under compression the particles can move closer together, significantly increasing the number of required time steps. This means that SPH can take longer than MPM to solve the same problem.

- ii) The integration over the support domain in SPH is converted into a summation of a limited number of particles. Under tension, there may be insufficient particles to serve as sampling points for the integration to ensure stability. On the other hand, the additional component of the background grid in MPM, serves to reduce this occurrence: where the grid nodes serve as field nodes to construct the approximation functions of the field variables, and the particles serve as sampling points for integration. As there are many more material points than grid nodes, the numerical instability arising from a lack of sampling points is more often avoided.
- iii) In both MPM and SPH, particles are free to move, and as such the risks involved with mesh based methods such as mesh entanglement are avoided. However, as mentioned above, nodal connectivity must be determined to evaluate field variables at each timestep. In SPH this requires a neighbour search algorithm, such as a tree-like search; in MPM the nodal connectivity is defined by the regular background grid, which does not change with time. The advantage of a background grid becomes obvious in this instance.
- iv) For convergence in a numerical method, the shape function employed must achieve a certain degree of consistency, that is interpolation between objects such as particles and nodes should introduce minimum error. In the case of unbalanced particles contributing to a required summation, this condition may not be met. This can occur when solving for particles at or near the boundary of the problem domain or when there is irregularly distributed particles. Both of these problems can occur in the original formulation of SPH - solutions have been developed although at the cost of computational efficiency.

A number of advantages for MPM over SPH have been highlighted above for hypervelocity impacts, most of which would be shared between different problems. The objective of this research is not to re-develop a new code, for obvious efficiency reasons, but to investigate the application of a particle or mesh-free method to the challenging problem of FSP. In literature, there is a freely available and open-source MPM code that has been used to model severe plastic deformation, "NairnMPM" [88]. Thus this software and method have been tested in the context of large deformation and in particular for contact, as this was one of the focusses of the article [91]. The open-source license of NairnMPM means that material models and any necessary components can be added as needed to the software. For these reasons MPM is an ideal candidate for modelling of FSP and has been selected for this work.

In summary, the various models in literature have been able to capture many aspects of material flow, however the limitation of Eulerian based FE models to capture free surfaces means they cannot observe processing effects such as flashing or track particular material points from start to finish. The ALE models developed are able to track the material movement, but at the expense of remeshing. The particle models developed so far have been able to observe more detailed material flow through particle analysis, however none have been applied to FSP.

In this work a particle method will be employed within a solid mechanics framework. This enables the tracking of free surfaces and material flow, combined with material history tracking for each particle. The next section will discuss the significance of microstructure modelling in FSP.

2.2.4 Grain Size Evolution

As one of the key outcomes of FSP, grain refinement is a major focus of experimental research, both developing it and observing what effects it has on the mechanical and other

properties of the material, however this has not translated significantly into the modelling of FSP - possibly due to its complexity.

Yazdipour et al. used an analytical model to analyse the effect of cooling rate on the stir zone grain size of AA5083 [92]. Similarly, Hofmann et al. used experimentally determined thermal history in an analytical relationship to predict the final grain diameter of pure aluminium after FSP [93].

Some models apply an empirical relationship with calibration to determined grain size profiles [61, 62]. A popular method of introducing a grain size dependent on processing conditions is through the Zener-Hollomon parameter.

Buffa and Fratini developed a series of models, the first of which applied an empirical relationship for the grain size according to strain, strain-rate and temperature [94]. In later work the authors applied a neural network to further enhance the analytical model [95]. Other work compared two analytical models, one incorporating the often applied Zener-Hollomon parameter [96]. They found that exclusion of effective plastic strain in the latter analytical case resulted in poorer characterisation of the grain size.

Another approach is to use an empirical constitutive law and apply an additional softening component. One such model is that applied by Grujicic et al. [71, 72] who modified the Johnson-Cook material model. They argue that although the effect of high temperatures on promoting plastic deformation via thermal activation is taken into account, annealing is not considered, and these conditions promote material softening. They obtained reasonably good quantitative agreement, however one drawback of modifying a strain hardening model like this is that there is no information regarding the microstructure of the material. Physically based models on the other hand can account for evolution of the underlying grain structure.

Although no physically based models have been applied to FSP, arguably one of the most advanced models in FSW literature is that provided by Simar et al. [97]. Focussed on the FSW of 6xxx series aluminium alloys, it includes a microstructure evolution model and a microstructure based strength and strain hardening model. However precipitation plays a dominant role in microstructure evolution of 6xxx series aluminium alloys, and the applied microstructure based models rely on this fact - as such they are not appropriate for FCC metals and non age-hardenable alloys where precipitation hardening does not occur.

A model developed by Robson et al. [98] accounted for grain refinement due to plastic shear and grain growth due to strain rate and temperature. They separate the evolution of grain size into the larger diameter grain boundary and internal subgrains. The grain boundary diameter decreases based on increasing plastic shear strain (as a fraction of the original grain size). The subgrain diameter is dependent on the calibrated Zener-Hollomon parameter, increasing with temperature and decreasing with strain rate. These two parameters in competition determine the final grain size.

Gao et al. developed a FE model for FSSW of aluminium with a physically based constitutive law [99]. Although they found reasonable agreement in the stir zone, grain refinement in other areas was not calculated.

The hardening and softening of the workpiece material is governed by microstructural evolution, thus a constitutive model must allow for dependence on microstructure. Although which mechanisms involved are dominant for each process is still unclear, modelling the evolution of microstructure with a physically based model can help to identify these. When empirical relationships are applied, they do not have the physical basis to supply this additional information.

In 1998, Estrin et al. proposed a dislocation-based model for all hardening stages in large strain deformation [100]. This model was extended to three-dimensional modelling in 2002 [101]. The model allows for the tracking of dislocation density and provides a response variable that describes the grain size (or dislocation cell size) based on the variation in dislocation density. It was formulated to be applied to processes that incur severe plastic deformation, and makes assumptions based on this.

The model assumes the formation of a dislocation cell consistent with the early stages of dynamic recovery or recrystallisation, commonly cited processes during FSP [102, 103]. The model considers the cell or grain to be made of two phases; a cell wall and cell interior, each with its own dislocation density. These two distinct dislocation densities are the internal variables of the model.

The strength of this physically-based microstructure model is that it can be incorporated into a numerical framework that operates at the continuum level, and through the material constitutive behaviour provide information at a microscopic level (microstructure). Successfully applied to the SPD process ECAP for both copper and aluminium [104, 105], it is an excellent candidate for a physically based constitutive model for FSP.

2.2.5 Boundary Conditions

To accurately model FSP, a number of boundary conditions must be determined. These can be generalized to heat generation, heat loss and friction or contact conditions. In the literature, various assumptions are made and these will be summarised below.

2.2.5.1 Heat Generation

Heat is generated by two mechanisms in FSP, plastic deformation of the processed material, and frictional sliding of the tool upon the workpiece. The precise contribution of each is challenging to quantify, and various values have been suggested in literature. For example Zhang et al. calculated over 85% resulting from frictional heating [106], and Zhang and Chen calculated 81.5% from frictional heating [107]. In general, all agree that the majority of heat is generated through frictional contact.

Early models of FSP were analytical and based around the thermal field. Initially the heat generated was simplified to a point source moving in a line [108, 109]. These were extended into solutions for 2D and 3D moving heat sources [110, 111]. Another more recent example is the full transient solution to the temperature field in FSW provided by Haghpanahi et al., where the authors made use of Green's function [112]. They were able to reproduce the results provided by their FEM solution in roughly 1/5th the time, with good agreement in both the position and time domain of the temperature distribution. In contrast, the initial numerical models simply fitted the input thermal energy to produce the necessary temperature distributions [113].

A very popular alternative approach has since been to approximate the heat generation by assuming an analytical function based on the input power passing from the tool to the plate. This has seen use both in fully analytical models and in numerical models [114, 115]. Dependent upon the assumed contact condition, the model applies either a heat resulting from the work of plastic deformation or that from the work of friction. If the contact condition is assumed to be sticking, the torque produces a stress in the material that is assumed to be

τ_{\max} , and combined with the rotation rate becomes a thermal energy due to plastic work. Alternatively, if a sliding condition is assumed, the thermal energy is dependent on the contact pressure and the coefficient of friction.

The drawback for this model is that calibration is required, as various parameters are not fully known, such as the percentage of heat lost to the tool, the precise friction coefficient or yield strength for example.

Khandkar et al. proposed a thermal energy input based on the power from the tool [115]. This input power can be related to a uniform shear stress at the interface of the tool and workpiece (if the sticking condition is assumed):

$$P_{av} = M_{tot} \omega \quad (2.1)$$

$$M_{tot} = \int (\tau r)(2\pi r)dr \quad (2.2)$$

where P_{av} is the average power input from the tool, M_{tot} is the total torque, ω is the rotational speed of the tool, τ is the uniform shear stress and r is the radius. Then the thermal energy into the workpiece can be calculated from:

$$q = \frac{P_{av}r}{\frac{2}{3}\pi r_s^3 + 2\pi r_p^2 h} \quad (2.3)$$

such that the average input power from the tool P_{av} , applied at a radius of r , is distributed uniformly across the surface of the interface between the tool and workpiece. Here q is the heat flux (W/m^2) applied to workpiece at the interface of the tool, r is the distance of the particle relative to the vertical axis of the tool, r_s is the shoulder radius, r_p is the pin radius, and h is the height of the pin.

This can be re-written in terms of the uniform shear stress:

$$q = \tau \omega r \quad (2.4)$$

This approach has been adopted by many modellers as it allows for temperature dependence of the shear stress. Colegrove et al. [66] applied a fully sticking assumption although suggested that this leads to an overestimation of the heat generation.

Schmidt and Hattel [114] investigated partial sticking/sliding. Furthering the input torque based model from Khandkar et al. they introduced a refinement which included the temperature dependent flow stress of the material in the torque based power function. This has the tendency to reduce the thermal energy input as the material approaches melting and the shear strength reduces to zero. This has been used by a number of researchers since, for example Zhang et al. [116] applied the same assumption, using the following relationship for the shear stress:

$$\tau_{\max} = \min(\mu P, \frac{\sigma_y(T)}{\sqrt{3}}) \quad (2.5)$$

where μ is the friction coefficient, P is the axial pressure applied on the welding tool, $\sigma_y(T)$ is the yield stress at the current temperature, T . The latter relation between shear and yield stress is found by comparing von Mises yield criterion in uniaxial tension and pure shear. This temperature dependent yield stress can be determined from experimental yield stress vs. temperature curves, as many authors have applied [117–119], or calculated within the numerical model itself according to the constitutive model (if it includes temperature dependence of stress).

In a similar style to the assumption of a temperature dependent yield stress, Hamilton et al. argued that the earlier numerical models did not account for the slip that occurs as the workpiece temperature approaches the solidus temperature, and the interface between the tool and the workpiece softens - resulting in an over-prediction of the maximum temperature. The researchers thus incorporated a variable friction coefficient, reducing its value depending on the energy per unit length of the weld.

If we convert Equation 2.4 to a sliding condition, we get the following relationship to the thermal load:

$$q = \mu P \omega r \quad (2.6)$$

which is equivalent to:

$$q = \frac{\mu N \omega r}{S_{wt}} \quad (2.7)$$

where N is the normal force applied by the tool to the workpiece, and S_{wt} is the contact surface area between the tool and workpiece.

If the velocity of the workpiece is known, one has:

$$q = \frac{\mu N (v_t - v_w)}{S_{wt}} \quad (2.8)$$

where $(v_t - v_w)$ is also known as the slip rate, as defined by Schmidt et al. [114]. If unknown, a coefficient for the dimensional slip rate, δ , can be applied and calibrated, as applied by Zhang et al. [116], or similarly as Bastier et al. (2006) did through variation of v_w at the tool workpiece interface in their CFD model.

$$\delta = \frac{v_w}{v_t} = 1 - \frac{\dot{\gamma}}{\dot{\gamma}_t} \quad (2.9)$$

$$q = \frac{(1 - \delta) \mu N \omega r}{S_{wt}} \quad (2.10)$$

If the assumption of a partial sticking and partial sliding condition is applied, the heat flux function can now take into account both work due to plastic deformation and friction, by including both functions with the coefficient, δ , as applied in these references [114, 118]. As the velocity of the workpiece material approaches that of the tool, the energy due to friction drops off and is fully calculated due to plastic deformation. Similarly, as the workpiece velocity approaches zero (stationary), the thermal energy is fully calculated from the frictional contact

condition. This is possible as the contact condition is assumed an average over the interface between the tool and workpiece.

Few models have deviated from the analytical function for heat generation, however some of the solid mechanics based models have applied a heating term from calculated plastic dissipation [71, 72]. In this research, a more sophisticated function based on the calculated interaction between the tool and workpiece will be applied. Not only does this simplify any calibration but also naturally handles differences in temperature due to the advancing and retreating sides.

The contact condition will not be an average across the tool interface, but determined for each particle based on the interaction with the tool and a friction coefficient. This removes the need for an analytical function completely. Note that although in this research the friction coefficient will be constant, this value could be made a function of particle state, such as temperature, in the future.

2.2.5.2 Heat Loss

The removal of heat is also a very important aspect of modelling FSP. In terms of heat loss to the tool, in their model of FSW, Darvazi et al. included a coefficient representing the proportion of thermal energy transferred into the workpiece [120]. Their fraction was estimated using a relation for steady state one-dimensional heat transfer.

$$g = \frac{J_W}{J_W + J_T} = \frac{\sqrt{(k\rho C_p)_W}}{\sqrt{(k\rho C_p)_W} + \sqrt{(k\rho C_p)_T}} \quad (2.11)$$

where g is the coefficient representing the proportion of energy transferred into the workpiece within their heat generation term, J represents the heat flux, k the thermal conductivity, C_p the specific heat capacity, ρ the density, and the subscripts W and T refer to the workpiece and tool respectively.

The backing plate is the largest heat sink in the system and an important factor in controlling the flow of heat through the workpiece. There are generally two approaches to modelling the loss of heat through the backing plate. The first is to include a backing plate in the model, however this increases computation time and requires use of a contact gap conductance between the two materials. The simplest method is to assume convective heat loss across the bottom surface of the workpiece. The use of a convection coefficient was first applied by Khandkar et al. [115], and has since been applied by many modellers [118, 121].

In addition to convection coefficients, Khandkar et al. [115] also modelled a variable contact conductance at the bottom side of the plate, varying the value according to the tool position and shoulder radius. A similar assumption was made more recently by Wang et al. [122].

Apart from heat loss through the backing plate, typical convective values across the surface of the plate for heat loss to the surrounding atmosphere are $15 - 30 \text{ W/m}^2\text{K}$. Radiation in the context of FSW/P is typically neglected due to its minimal impact.

2.2.5.3 Thermal Calibration

Fitting of variables or parameters is a necessary part of the vast majority of the models in literature. Various methods of calibration are applied and these are explained below.

Using experimental curves from friction welding of steel bars, Arora and Nandan et al. [118, 123] applied a friction coefficient that varied from the pin to the edge of the shoulder according to a velocity relation.

$$\mu_f = \mu_o \exp^{-\delta \frac{\omega}{\omega_o} \frac{r}{r_s}} \quad (2.12)$$

where μ_o is the highest value of the friction coefficient and ω_o is the reference value for the tool rotational speed.

The friction coefficient is often linked to heat generation, for example Frigaard et. al. used a calibrated friction coefficient adjusted against the maximum temperature so as to prevent melting [124]. As the value of the friction coefficient is unlikely to be constant, and it is a difficult value to determine, it is often used to aid calibration. In the fluid models of FSW/P the velocity of the material at the tool interface is often calibrated by the same method. These two methods are strongly related, as the friction coefficient directly effects the velocity imparted to the workpiece from the tool rotation.

Most authors admit there is not a straightforward way to determine the friction coefficient. This creates the need for approximation or as some have done, an average value based on those used in other models presented in literature [125].

In general, the application of the uniform shear stress models can be less accurate towards the stir zone because there is a lack of clarity on where the heat is produced - assumptions are made that for example all the input energy (torque) is distributed around the tool surface, but some of this energy will be volumetric from plastic dissipation. Wang et al. investigated the interface condition with six different models, looking at the effect of the slip or sliding boundary condition, the contact shoulder radius ratio (CSSR) and a softening regime [122]. The CSSR is a method developed to address the issue of excessive heat developed under each interface condition. It reduces the effective amount of tool shoulder in contact with the workpiece, increasing from zero at the inner edge of the shoulder to 100% at the outer edge. Essentially this is a calibration mechanism. In addition, as in most of the models, they applied a universal slip coefficient - the authors note that this is unlikely to be the case in practice with macrosections of the processed material often showing little deformation underneath the periphery of the shoulder. This suggests that use of a contact shoulder ratio is useful, however, arguably better would be to remove the assumption of an average heat flux, and instead introduce natural determination of contact. The heat flux can then be applied naturally depending on whether contact is occurring or not, and in what degree. This would also alleviate the loss of accuracy in the stir zone. Table 2.1 shows the steps Wang et al. carried out in calibrating their models.

Step	Calibration
1.	Assume backing plate coefficients
2.	Calibrate CSSR for sticking model
3.	Use same CSSR and calibrate θ for sliding model

Table 2.1: Calibration methodology used by Wang et al. [122].

In this work, the thermal load is applied according to the work done by both plastic deformation and frictional contact, however it does not assume a global contact condition across all surfaces, but rather relies on the contact algorithm within MPM to determine how and

where contact occurs. This allows for a dynamic prediction of heat generation, applied to each particle within the simulation.

The product of the stress on each particle and the strain rate is used to determine the component of plastic energy dissipated as heat. This means that there is no initial assumption required for the dissipation ratio between friction and plastic dissipation, rather it is naturally handled according to the conditions of the process, the contact algorithm and the prescribed friction coefficient. The latter coefficient to be determined according to classical friction testing methods. The experimental temperature profiles will be used to calibrate for the heat loss through the backing plate. This will essentially remove all free parameters in the model.

2.2.6 Modelling Fast Tool Rotation / Slow Tool Translation

2.2.6.1 Integration Scheme

With tool rotation speeds in the order of 400-1200rpm and tool translation speeds of around 1mm/s - 4mm/s, FSP's variation in dynamics is large, creating large gradients of strain rate and temperature. This contrast introduces a problem for numerical simulation due to the nature of PDE integration in a numerical model. The choices are limited however. Most of the models in literature apply an explicit scheme to model the process, and some an implicit algorithm. Both have advantages and drawbacks that have been handled in different ways in the literature.

The explicit scheme is very much time step dependent, as the value of field variables at the next time step is directly related to those of the current step. Small step size is crucial to maintain accuracy of the integrated value - a step size too great results in poor accuracy and error. The key advantage of the explicit scheme is that it can be very quick to solve certain problems (often ones involving high speed), while also being very accurate, provided the time step restrictions are satisfied.

An implicit scheme is unconditionally stable, and thus can be run over larger time steps without loss in accuracy. However the solution procedure is more complex, and generally is a longer process than the simple explicit integration. However, with highly dynamic problems, larger timesteps can lead to a lack of convergence and error.

2.2.6.2 Dealing with the Drawbacks in an Explicit Integration Scheme

Due to the restriction on the maximum size of the timestep, the number of iterations required by an explicit integration scheme can be large - leading to very long computation time. To reduce the number of iterations, the natural time of the simulated event can be decreased, or the step size can be increased. These two approaches infer different considerations. To reduce the natural time of the event, the simulation size can be reduced or the loading speed can be increased. Both Zhang et al. [74] and Ulysse [126] applied FSW to reduced plate sizes in order to minimize computation time, but this is perhaps an impractical solution. In fact one plate was reduced to $3 \times 1.5 \times 0.2 \text{ cm}^3$. An increase in loading speed is useful when the rate of deformation is not important, when for example the constitutive model is rate-independent. A simple way to apply this is to artificially increase the velocity of the tool for example.

The alternative approach, increasing the timestep, is accomplished by manipulating the variables that condition the maximum timestep. The Courant condition describes the maximum

time to accurately capture the stress wave as it moves from one cell or node to the next in a deforming material [127]. It is described in equation (2.13) below.

$$\Delta t_{\max} = \frac{d}{c_d} \quad (2.13)$$

where d is the cell size or distance between nodes, and c_d is the speed of the stress wave through the material. For an elastic material in MPM the stress wave speed, c_d , is shown in equation (2.14):

$$c_d = \sqrt{\frac{K + \frac{4G}{3}}{\rho}} \quad (2.14)$$

Using this definition, it can be seen that decreasing the stress wave speed can also reduce the restriction on the timestep, and this can be done by artificially increasing the density. This is termed mass scaling and has been applied in the literature to a number of models in Friction Stir techniques.

Schmidt et al. [67] used mass scaling in their ALE explicit code to model FSW. Grujicic et al. applied mass scaling to their ALE explicit code in FEM, increasing their timestep from $\Delta t = 1 \times 10^{-7} \text{s}$ to $\Delta t = 1 \times 10^{-3} \text{s}$. They ensured that the ratio of the kinetic energy over the internal energy was always below 1%, which is recommended to avoid alteration of the mechanical solution. They argued that use of such a mass scaling algorithm does not alter the amount of heat generated by dissipation of plastic deformation work and frictional slip. Also they noted that the thermal stable time increment was still greater than their adjusted mechanical stable time increment. Zhang et al. applied a mass scaling factor of 10^7 [70] in their 3D ALE simulation of FSW.

Mass scaling and its effect on FSP within a particle method will be further investigated in this research.

2.3 Concluding Remarks

The Finite Element Method (FEM) has been developed for static and dynamic, linear and non-linear stress analysis of solids, structures and fluids. Its wide application to many engineering problems has seen it develop into a robust and commercially viable problem solving tool for solid mechanics. However, a number of limitations exist when transferred to problems of large deformation, the major one being mesh distortion or entanglement. It is clear that the calculated solutions will then become inaccurate. However this is where the mesh-free/particle based methods shine. Some of the advantages of MPM over other particle based methods such as SPH were discussed (section 2.2.3). These in combination with a freely available, tested, open-source MPM solver (NairnMPM) present a compelling choice for the particle based numerical method. As such the particle based MPM will be applied to model FSP in this research.

Although a limited number of particle methods have been applied to the problem of Friction Stir Welding, none have been used in Friction Stir Processing. Even in the case of FSW, the applications have been limited in some way, for example with two-dimensional analysis or use of non-physical material laws. It is now generally recognised that the microstructure plays

a significant role in the behaviour of metals and, therefore, the developed model should be microstructure based. The constitutive law selected is an advanced hardening law for FCC metals that includes temperature and strain-rate dependence, while also tracking the evolution of dislocation densities allowing for observation of microstructure within a continuum framework.

The most commonly applied approach to calculate heat generation during FSP has been through an analytical relationship based on input power from the tool. In this work, the thermal load will be applied in two separate components, i) according to the work done through friction and ii) the work done through plastic deformation (dissipated as heat). Both will be dependent on material contact and external loads calculated during the simulation.

Within the limited choices for an integration scheme, an explicit algorithm will be applied, with an available solution to excessive computation time in mass scaling.

This research will focus on the development of a model of FSP that will study the relationship between external variables and response variables, such as temperature profiles, strain rate, strain, and subsequent microstructure evolution. The model will provide a predictive capability for the resultant properties, at the desired location. To achieve this goal, the model will combine a thermo-mechanical description of the process, with a physical description of the mechanical response of the material able to estimate the change in microstructure under the thermo-mechanical loading of FSP. With comparison to literature, this represents one of the most advanced models of Friction Stir Processing currently available.

Chapter 3

The Material Point Method

3.1 Introduction

In the previous chapter the numerical models presented in the literature were discussed. Although many models have been developed, very few incorporate a particle based numerical method. The aim of this chapter is to present the numerical method applied in this work, the Material Point Method (MPM) in greater detail. It will include the major components of the method - such as how the governing equations are maintained over the grid and particles, the material formulation and plasticity, how contact is handled, and finally the incremental update structure of MPM.

The MPM is the latest in an evolving set of particle-in-cell (PIC) methods used to solve engineering problems. It is derived from another PIC method with the acronym FLIP, originally developed to solve fluid flow problems [128]. The MPM iteration of the PIC method allows for handling of material strength and stiffness, which is necessary to solve problems in the field of solid mechanics. The underlying structure and distinguishing feature of a PIC method is the synchronous use of essentially two meshes, one a material or Lagrangian mesh, the other a spatial or Eulerian mesh defined over the computational domain. By mapping or transferring data between the two meshes, numerical dissipation due to advection usually associated with an Eulerian method is avoided, and mesh distortion associated with a Lagrangian method is also alleviated.

The following section will describe the Material Point Method applied in this research. The method is continuing to be updated and refined over time, but what is below is consistent with the original method published by Sulsky et al. in a series of papers from 1994 [129–131], unless otherwise noted.

The software used for this research has been developed by John Nairn at Oregon State University [132]. Over the past 15 years or so it has developed into a robust and efficient MPM code. Some of the formulations described here are based from the notes provided online and released with this software [88].

3.2 The Governing Equations

Below are the governing equations that need to be solved. The conservation of mass implies the following continuity equation:

$$\frac{d\rho}{dt} + \rho \nabla \cdot \mathbf{v} = 0 \quad (3.1)$$

Here ρ is the density, ∇ is the gradient operator and $\nabla \cdot \mathbf{v}$ is the divergence of the vector field \mathbf{v} , where \mathbf{v} is the velocity. The conservation of momentum (also called the equation of motion) implies that:

$$\rho \mathbf{a} = \nabla \cdot \boldsymbol{\sigma} + \rho \mathbf{b} \quad (3.2)$$

where \mathbf{a} is the acceleration vector, $\boldsymbol{\sigma}$ is the Cauchy stress tensor, and \mathbf{b} is the specific body force.

To complete the description of the continuum, a relationship is needed between the strain and the stress of the material. In this work this is determined according to a hyperelastic formulation, and is described in detail in section 3.4 below.

The heat equation can be written as follows:

$$\nabla \cdot \mathbf{k} \nabla T + q = \rho C_p \frac{\partial T}{\partial t} \quad (3.3)$$

where \mathbf{k} is the thermal conductivity tensor, T is the temperature, q is the heat source, C_p is the specific heat capacity and t is time.

3.3 Discretisation

3.3.1 Weak Form of the Governing Equations

The set of governing equations or PDE's with boundary conditions is called the strong form of the problem. The weak form is the variational statement of the problem, in which these equations are integrated against a test function, $w(\mathbf{x})$, where $\mathbf{x} = \mathbf{x}(x, y, z)$ is a position vector. This reduces the accuracy of the solution but also leads to the problem being solvable in a discrete manner.

The conservation of mass is satisfied implicitly by leaving discrete particle masses unchanged throughout the computation. However to allow for evolution of particle momenta over time, the discrete version of the equation of motion must be solved. The weak form of the equation of motion (equation 3.2 above) can be written as:

$$\int_{\Omega} (\rho \mathbf{a} - \nabla \cdot \boldsymbol{\sigma} - \rho \mathbf{b}) w(\mathbf{x}) \, dV = 0 \quad (3.4)$$

where the domain is given by the symbol Ω and is divided into N_p sub-domains or particle domains, Ω_p . The subscripts p and i refer to particle and nodes respectively, and V is the volume of the domain. Similarly the weak form of the heat equation is:

$$\int_{\Omega} \left(\nabla \cdot \mathbf{k} \nabla T + q(\mathbf{x}) - \rho C_p \frac{\partial T}{\partial t} \right) w(\mathbf{x}) \, dV = 0 \quad (3.5)$$

3.3.2 Shape Functions

The projection of particle data onto the computational grid requires the use of weighting functions, also called shape or interpolation functions. A characteristic function is chosen to represent the particles, $\chi_p(\mathbf{x})$, and a shape function as a basis of support on the computational nodes, $N_i(\mathbf{x})$. The generalised shape functions are found from the convolution of these two functions.

The differences between schemes for calculating $\chi_p(\mathbf{x})$ distinguishes one MPM method from another. In the original MPM [129, 130], the particle characteristic function was formed from a Dirac delta function, as such the particle was idealised as a point mass. The general interpolation material point method (GIMP) introduced a volumetric particle domain [133]. By integrating the shape function over particle volumes rather than points, the grid shape functions are smoothed, increasing support. One important consequence of this is that a particle which lies coincident with a grid node will not interpolate data exclusively to that vertex, or suddenly change nodal contribution as it crosses a cell boundary, improving performance in large deformations.

The shape functions and shape function gradients are defined from the current particle positions relative to the background grid. From the definition of the generalised shape functions [133]:

$$S_{ip}(\mathbf{x}) = \frac{1}{V_p} \int_{\Omega_p} \chi_p(\mathbf{x}) N_i(\mathbf{x}) \, dV \quad (3.6a)$$

$$\nabla S_{ip}(\mathbf{x}) = \frac{1}{V_p} \int_{\Omega_p} \chi_p(\mathbf{x}) \nabla N_i(\mathbf{x}) \, dV \quad (3.6b)$$

where $S_{ip}(\mathbf{x})$ is the generalised (GIMP) shape function for particle p at node i , and Ω_p is the particle domain. The particle characteristic function is taken as:

$$\chi_p(\mathbf{x}) = \chi_p^x(x) \chi_p^y(y) \chi_p^z(z) \quad (3.7)$$

and in one dimension, $\chi_p(\mathbf{x})$ is of the form:

$$\chi_p^x(x) = H[x - (x_p - L_p)] - H[x - (x_p + L_p)] \quad (3.8)$$

where x_p is the material particle position, $H[x]$ is the Heaviside step function (1 for $x > 0$, zero for $x < 0$), and L_p is the particle radius or half the particle domain - hence $\chi_p(\mathbf{x})$ is equal to 1 within the particle domain and zero otherwise.

For a uniform structured grid the nodal basis function is generally in the form of a tent function (in one dimension):

$$N_i^x(x) = \begin{cases} 1 + \frac{x-x_i}{h} & -h < x - x_i < 0 \\ 1 - \frac{x-x_i}{h} & 0 < x - x_i < h \\ 0 & \text{otherwise} \end{cases} \quad (3.9)$$

where h is the cell or element length and x_i is the nodal position. Then as $\chi_p(\mathbf{x})$ is equal to 1 within the particle domain, the integration for the generalised shape functions is simplified to (in one dimension):

$$S_{ip}^x(x_p) = \frac{1}{L_p} \int_{x_p-L_p}^{x_p+L_p} N_i^x(x) dx \quad (3.10a)$$

$$\nabla S_{ip}^x(x_p) = \frac{1}{L_p} \int_{x_p-L_p}^{x_p+L_p} \nabla N_i^x(x) dx \quad (3.10b)$$

Integrating the nodal basis function over the particle domain, dividing by the length of the particle domain, and accounting for overlap yields the smoothed or generalised shape functions:

$$S_{ip}^x(x_p) = \begin{cases} \frac{(h+L_p+(x_p-x_i))^2}{4hL_p} & -h-L_p < x_p-x_i \leq -h+L_p \\ 1 + \frac{(x_p-x_i)}{h} & -h+L_p < x_p-x_i \leq -L_p \\ 1 - \frac{(x_p-x_i)^2+L_p^2}{2hL_p} & -L_p < x_p-x_i \leq L_p \\ 1 - \frac{(x_p-x_i)}{h} & L_p < x_p-x_i \leq h-L_p \\ \frac{(h+L_p-(x_p-x_i))^2}{4hL_p} & h-L_p < x_p-x_i \leq h+L_p \\ 0 & \text{otherwise} \end{cases} \quad (3.11a)$$

$$\nabla S_{ip}^x(x_p) = \begin{cases} \frac{h+L_p+(x_p-x_i)}{2hL_p} & -h-L_p < x_p-x_i \leq -h+L_p \\ \frac{1}{h} & -h+L_p < x_p-x_i \leq -L_p \\ -\frac{(x_p-x_i)}{hL_p} & -L_p < x_p-x_i \leq L_p \\ -\frac{1}{h} & L_p < x_p-x_i \leq h-L_p \\ -\frac{h+L_p-(x_p-x_i)}{2hL_p} & h-L_p < x_p-x_i \leq h+L_p \\ 0 & \text{otherwise} \end{cases} \quad (3.11b)$$

where $S_{ip}(\mathbf{x}_p) = S_{ip}^x(x_p)S_{ip}^y(y_p)S_{ip}^z(z_p)$, and can be given the simpler notation S_{ip} . The GIMP shape function in one dimension is plotted in Figure 3.1.

In this approach the particle domain is assumed to remain undeformed, only translating with the particles. Although there has been some research into developing shape functions based

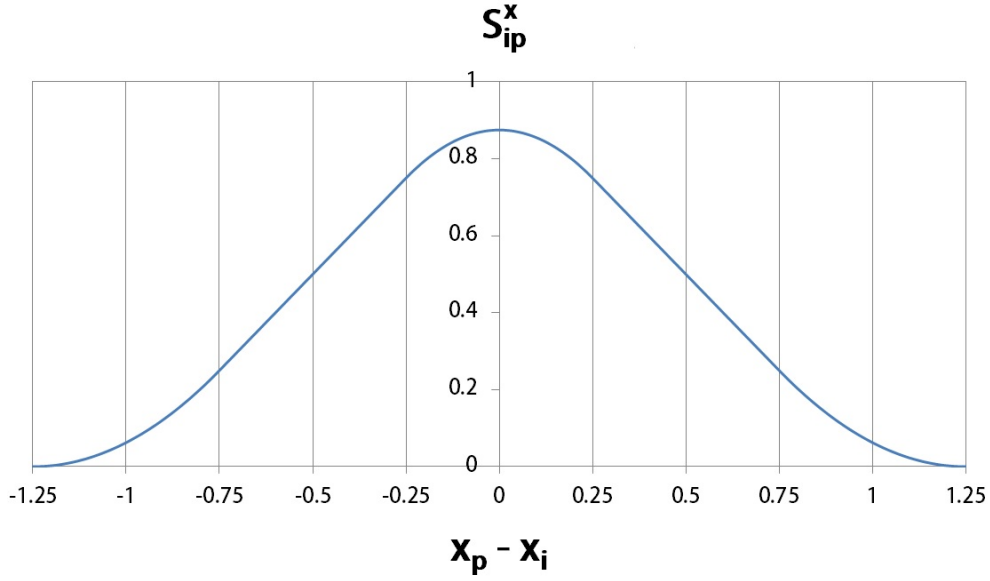


Figure 3.1: GIMP shape function in one dimension for unit cell size.

on a deformed particle domain, the most popular technique referred to as convected particle domain interpolation (CPDI) [134–136], this strategy is more computationally expensive. This work will implement the standard GIMP shape functions with the assumption of a uniform particle domain.

3.3.3 Derivation of the discretised Form of the Governing Equations

3.3.3.1 Equation of Motion

Continuing from the weak form of the equation of motion given in section 3.3.1, applying a vector identity to the stress term results in:

$$(\nabla \cdot \boldsymbol{\sigma}) \cdot \mathbf{w}(\mathbf{x}) = \nabla \cdot (\boldsymbol{\sigma} \cdot \mathbf{w}(\mathbf{x})) - (\nabla \mathbf{w}(\mathbf{x})) : \boldsymbol{\sigma} \quad (3.12)$$

Equation (3.4) becomes:

$$\int_{\Omega} \mathbf{w}(\mathbf{x}) \rho \mathbf{a} - \nabla \cdot (\boldsymbol{\sigma} \cdot \mathbf{w}(\mathbf{x})) + (\nabla \mathbf{w}(\mathbf{x})) : \boldsymbol{\sigma} - \mathbf{w}(\mathbf{x}) \rho \mathbf{b} \, dV = 0 \quad (3.13)$$

And rearranged:

$$\int_{\Omega} \mathbf{w}(\mathbf{x}) \rho \mathbf{a} \, dV = \int_{\Omega} \nabla \cdot (\boldsymbol{\sigma} \cdot \mathbf{w}(\mathbf{x})) - (\nabla \mathbf{w}(\mathbf{x})) : \boldsymbol{\sigma} + \mathbf{w}(\mathbf{x}) \rho \mathbf{b} \, dV \quad (3.14)$$

Then using the divergence theorem:

$$\int_{\Omega} \nabla \cdot (\boldsymbol{\sigma} \cdot \mathbf{w}(\mathbf{x})) \, dV = \int_{\delta\Omega} (\boldsymbol{\sigma} \cdot \mathbf{w}(\mathbf{x})) \cdot \hat{\mathbf{n}} \, dS \quad (3.15)$$

where $\hat{\mathbf{n}}$ is the unit vector outwardly normal to $\delta\Omega$, equation (3.14) becomes:

$$\int_{\Omega} w(\mathbf{x}) \rho \mathbf{a} \, dV = \int_{\delta\Omega} w(\mathbf{x}) \tau \, dS - \int_{\Omega} \nabla w(\mathbf{x}) : \boldsymbol{\sigma} \, dV + \int_{\Omega} w(\mathbf{x}) \rho \mathbf{b} \, dV \quad (3.16)$$

where τ is the traction vector on the surface $\delta\Omega$, defined by $\tau = \boldsymbol{\sigma} \cdot \hat{\mathbf{n}}$.

Equation (3.16) can be discretised by solving over the particle domain, Ω_p , and applying the particle and nodal basis functions, where the continuous representation of particle and grid data respectively can be written as [129, 133]:

$$f(\mathbf{x}) = \sum_p f_p \chi_p(\mathbf{x}) \quad (3.17a)$$

$$g(\mathbf{x}) = \sum_i g_i N_i(\mathbf{x}) \quad (3.17b)$$

Thus for the variables in equation (3.16):

$$\rho \mathbf{a} = \sum_p \rho_p \mathbf{a}_p \chi_p(\mathbf{x}) \quad (3.18a)$$

$$\boldsymbol{\sigma} = \sum_p \boldsymbol{\sigma}_p \chi_p(\mathbf{x}) \quad (3.18b)$$

$$\rho \mathbf{b} = \sum_p \rho_p \mathbf{b}_p \chi_p(\mathbf{x}) \quad (3.18c)$$

$$w(\mathbf{x}) = \sum_i w_i N_i(\mathbf{x}) \quad (3.18d)$$

$$\nabla w(\mathbf{x}) = \sum_i w_i \nabla N_i(\mathbf{x}) \quad (3.18e)$$

where $w_i = w(\mathbf{x}_i)$, which results in:

$$\begin{aligned} \int_{\Omega_p} \left(\sum_i w_i N_i(\mathbf{x}) \sum_p \rho_p \mathbf{a}_p \chi_p(\mathbf{x}) \right) dV &= \int_{\delta\Omega} \left(\left(\sum_i w_i N_i(\mathbf{x}) \right) \tau \right) dS \\ &\quad - \int_{\Omega_p} \left(\sum_i w_i \nabla N_i(\mathbf{x}) \cdot \sum_p \boldsymbol{\sigma}_p \chi_p(\mathbf{x}) \right) dV \\ &\quad + \int_{\Omega_p} \left(\sum_i w_i N_i(\mathbf{x}) \sum_p \rho_p \mathbf{b}_p \chi_p(\mathbf{x}) \right) dV \end{aligned} \quad (3.19)$$

Bringing the integrals inside the summations and introducing a particle volume term, V_p :

$$\begin{aligned}
\sum_i \sum_p \left(w_i V_p \rho_p \mathbf{a}_p \frac{1}{V_p} \int_{\Omega_p} \chi_p(\mathbf{x}) N_i(\mathbf{x}) dV \right) &= \sum_i \left(\int_{\delta\Omega} (w_i N_i(\mathbf{x})) \tau dS \right) \\
&\quad - \sum_i \sum_p \left(w_i V_p \boldsymbol{\sigma}_p \cdot \frac{1}{V_p} \int_{\Omega_p} \chi_p(\mathbf{x}) \nabla N_i(\mathbf{x}) dV \right) \\
&\quad + \sum_i \sum_p \left(w_i V_p \rho_p \mathbf{b}_p \frac{1}{V_p} \int_{\Omega_p} \chi_p(\mathbf{x}) N_i(\mathbf{x}) dV \right)
\end{aligned} \tag{3.20}$$

where $V_p = (1 + \epsilon_{xx,p})(1 + \epsilon_{yy,p})(1 + \epsilon_{zz,p})^{m_p/\rho_p}$ is the particle volume. Then by introducing the GIMP shape functions (equation 3.6a and 3.6b), this is simplified to:

$$\begin{aligned}
\sum_i \sum_p (w_i V_p \rho_p \mathbf{a}_p S_{ip}) &= \sum_i \left(\int_{\delta\Omega} (w_i N_i(\mathbf{x})) \tau dS \right) \\
&\quad - \sum_i \sum_p (w_i V_p \boldsymbol{\sigma}_p \cdot \nabla S_{ip}) \\
&\quad + \sum_i \sum_p (w_i V_p \rho_p \mathbf{b}_p S_{ip})
\end{aligned} \tag{3.21}$$

and as w_i must be arbitrary:

$$\sum_p (V_p \rho_p \mathbf{a}_p S_{ip}) = \int_{\delta\Omega} N_i(\mathbf{x}) \tau dS - \sum_p (V_p \boldsymbol{\sigma}_p \cdot \nabla S_{ip}) + \sum_p (V_p \rho_p \mathbf{b}_p S_{ip}) \tag{3.22}$$

where the first term is the rate of change of momentum or impulse, $\dot{\mathbf{p}}_i$, and is equal to the traction, internal and body forces, respectively:

$$\dot{\mathbf{p}}_i = \mathbf{f}_i^{\text{tractions}} + \mathbf{f}_i^{\text{internal}} + \mathbf{f}_i^{\text{body}} \tag{3.23}$$

3.3.3.2 Heat Equation

Following the same procedure used for the equation of motion, the discrete version of the heat equation, (3.5), becomes:

$$\frac{dT_i}{dt} = - \sum_p (V_p \mathbf{k} \nabla T_p \cdot \nabla S_{ip}) + \sum_p (V_p q_p S_{ip}) + \int_{\delta\Omega} (N_i(\mathbf{x}) \mathbf{k} \nabla T) \cdot \hat{\mathbf{n}} dS \tag{3.24}$$

The individual terms within equation (3.24) take into account (from left to right) conduction, volumetric heat sources (such as that from plastic dissipation), and surface fluxes (such as convection and thermal energy released from friction). Where $\mathbf{k} \nabla T \cdot \hat{\mathbf{n}}$ in the last term of equation (3.24) can be replaced by a heat-flux boundary condition. Note that this equation

gives the nodal temperature, which is preferably used in temperature dependent constitutive laws as it gives a better representation of the temperature field avoiding possible fluctuations within grid cells [136].

3.4 Constitutive Model in the Context of Large Deformation

3.4.1 Hyperelasticity

FSP involves large plastic strains therefore the usual assumptions of small strain plasticity no longer holds. Different formulations are available to extend plasticity to the case of finite strains. In this work, a hyperelastic model is considered which relies upon the definition of the strain energy density function, which assumes different forms according to the material or class of materials studied. In the case of isotropic materials, the strain energy density function depends upon the strain invariants.

An important part of the hyperelastic material definition, is the deformation gradient, \mathbf{F} . It contains all information about the local deformation in the solid, and can be used to form many other strain quantities. The deformation gradient is used to separate rigid body translations and rotations from deformations, which are the source of stresses. It is defined as follows:

$$\mathbf{F} = \begin{bmatrix} 1 + \epsilon_{xx} & 1/2(\gamma_{xy} - \omega_{xy}) & 1/2(\gamma_{xz} - \omega_{xz}) \\ 1/2(\gamma_{xy} + \omega_{xy}) & 1 + \epsilon_{yy} & 1/2(\gamma_{yz} - \omega_{yz}) \\ 1/2(\gamma_{xz} + \omega_{xz}) & 1/2(\gamma_{yz} + \omega_{yz}) & 1 + \epsilon_{zz} \end{bmatrix} \quad (3.25)$$

where ϵ , γ and ω are the strain, shear strain and rotation on the particle.

3.4.1.1 Multiplicative Decomposition of the Deformation Gradient

For small deformations, the strain tensor is additively partitioned into elastic and plastic components:

$$\epsilon = \epsilon^e + \epsilon^p \quad (3.26)$$

where ϵ , ϵ^e and ϵ^p represent the total, elastic and plastic strain tensors respectively. This is accurate when the deformation is small allowing the higher order terms of the strain tensor to be safely ignored. For large or finite deformation however, the higher order terms cannot be ignored, and the partition for plasticity takes place through a multiplicative decoupling of the deformation gradient:

$$\mathbf{F} = \mathbf{F}^e \mathbf{F}^p \quad (3.27)$$

where \mathbf{F}^e and \mathbf{F}^p are the elastic and plastic components of the deformation gradient.

3.4.1.2 Hyperelastic Strains

Following standard conventions in continuum mechanics [137], the left Cauchy-Green strain tensor is defined according to the deformation gradient:

$$\mathbf{B} = \mathbf{F}\mathbf{F}^T \quad (3.28)$$

where \mathbf{B} is the (Eulerian) elastic left Cauchy-Green strain tensor. Note that only the elastic tensor is required for the current formulation.

3.4.1.3 Update of the Deformation Gradient

With hyperelastic materials, the full incremental deformation gradient is used, and is defined as [136]:

$$\frac{d\mathbf{F}}{dt} = \nabla \mathbf{v} \cdot \mathbf{F} \quad (3.29)$$

where $\nabla \mathbf{v}$ is the current velocity gradient. With a constant velocity gradient, the exact solution for the deformation gradient, \mathbf{F} , is:

$$\mathbf{F}^{k+1} = e^{(\Delta t \nabla \mathbf{v})} \mathbf{F}^k = d\mathbf{F} \cdot \mathbf{F}^k \quad (3.30)$$

where Δt is the timestep and $\Delta t \nabla \mathbf{v} = \nabla \mathbf{u}$ is the displacement gradient. To find the exponential of the matrix a Cayley-Hamilton expansion method is applied [138].

$$d\mathbf{F} = e^{(\Delta t \nabla \mathbf{v})} = e^{(\nabla \mathbf{u})} = \sum_{i=0}^{i_{\max}} \frac{(\nabla \mathbf{u})^i}{i!} \approx \mathbf{I} + \nabla \mathbf{u} + \frac{(\nabla \mathbf{u})^2}{2} \quad (3.31)$$

where the minimum recommended value for i_{\max} is 2 [136]. Then the update for the particle deformation gradient simply requires the current particle deformation gradient and the particle displacement gradient:

$$\nabla \mathbf{u}_p = \Delta t \sum_i \mathbf{v}_i \nabla \mathbf{S}_{ip} \quad (3.32)$$

$$\mathbf{F}^{k+1} = \left(\mathbf{I} + \nabla \mathbf{u}_p + \frac{(\nabla \mathbf{u}_p)^2}{2} \right) \mathbf{F}^k \quad (3.33)$$

3.4.1.4 Hyperelastic Stress

For the elastic stress response, a Neo-Hookean strain energy density function is applied [139].

$$W_e = \frac{K}{2} \left(\frac{1}{2} (J^2 - 1) - \ln J \right) + \frac{G}{2} \left(\frac{I_1}{J^{2/3}} - 3 \right) \quad (3.34)$$

The elastic strain energy density function, W_e , is dependent on the small-strain bulk modulus, K , small-strain shear modulus G , normalised volume change $J = \det \mathbf{F} = V/V_0$, and stress invariant I_1 , where the invariant I_1 is the trace of the elastic left Cauchy-Green strain tensor, $\text{Tr}(\mathbf{B})$:

$$I_1 = \text{Tr}(\mathbf{B}) = B_{xx} + B_{yy} + B_{zz} \quad (3.35)$$

The Cauchy stress (or true stress) is found by differentiation of the elastic strain energy density function (3.34):

$$\boldsymbol{\sigma} = \frac{J_{\text{res}} G}{3J^{2/3}} \left(\mathbf{B} - \frac{I_1}{3} \mathbf{I} \right) + K(J-1)\mathbf{I} \quad (3.36)$$

where J_{res} is a term accounting for thermal expansion:

$$J_{\text{res}} = \Lambda_{\text{res}}^3 = \left[e^{(\alpha_t dT)} \right]^3 \approx (1 + \alpha_t dT)^3 \quad (3.37)$$

and Λ_{res} is the extension due to free thermal expansion, α_t is the coefficient of thermal expansion and dT is the increment of temperature (assumed to be small in the approximation). During calculation, the Kirchoff stress tensor is used, and is related to the Cauchy stress tensor through the normalised volume change:

$$\boldsymbol{\sigma} J = \boldsymbol{\sigma}_K \quad (3.38)$$

In addition, the state of the material deformation must be determined - whether elastic or elastic/plastic.

3.4.1.5 Plasticity

In order to adjust for any plastic deformation, the radial return algorithm is used. Here a classic Mises-Huber yield condition is applied given in terms of the Kirchoff stress tensor:

$$f(\boldsymbol{\sigma}_K, \alpha) = \|\text{dev}[\boldsymbol{\sigma}_K]\| - \sqrt{2/3} [\sigma_y + K(\alpha)] \leq 0 \quad (3.39)$$

where σ_y is the initial yield stress, $K(\alpha)$ is a non-linear hardening function, and α is a non-negative function of the amount of plastic strain, also called an internal hardening variable. The hardening function applied, $K(\alpha)$, varies in this work and will be defined in later chapters. The typical assumption for α in metal plasticity is:

$$\dot{\alpha} = \sqrt{2/3} \lambda \quad (3.40)$$

where λ is the scalar plastic multiplier. The yield condition determines the state of deformation in the material, whether elastic or elastic/plastic:

$$f^{\text{trial}}(\boldsymbol{\sigma}_K, \alpha) \begin{cases} \text{if } f \leq 0 & \text{elastic deformation only} & \Delta\lambda = 0 \\ \text{if } f > 0 & \text{elastic and plastic deformation} & \Delta\lambda > 0 \end{cases}$$

where f^{trial} is the trial or test function initially calculated based on an assumed elastic response.

Trial Functions:

The following trial functions are applied to test for plasticity:

$$\mathbf{s}_{n+1}^{\text{trial}} = J_{\text{res}} \mathbf{G} \text{dev} [\bar{\mathbf{B}}_{n+1}^{\text{trial}}] \quad (3.41)$$

where \mathbf{s} is the deviatoric Kirchoff stress tensor, and $\bar{\mathbf{B}} = \mathbf{B}/J^{2/3}$. The trial \mathbf{B} can be written as:

$$\mathbf{B}_{n+1}^{\text{trial}} = \mathbf{dF} \mathbf{B}_n \mathbf{dF}^T \quad (3.42)$$

where \mathbf{dF} is the incremental deformation gradient for this time step and \mathbf{B}_n is the previous step elastic left Cauchy-Green strain tensor. The expansion of $\mathbf{s}_{n+1}^{\text{trial}}$ for x, y and z is:

$$\begin{aligned} s_{xx}^{\text{trial}} &= \frac{J_{\text{res}} \mathbf{G}}{3J^{2/3}} (2B_{xx}^{\text{trial}} - B_{yy}^{\text{trial}} - B_{zz}^{\text{trial}}) \\ s_{yy}^{\text{trial}} &= \frac{J_{\text{res}} \mathbf{G}}{3J^{2/3}} (2B_{yy}^{\text{trial}} - B_{xx}^{\text{trial}} - B_{zz}^{\text{trial}}) \\ s_{zz}^{\text{trial}} &= \frac{J_{\text{res}} \mathbf{G}}{3J^{2/3}} (2B_{zz}^{\text{trial}} - B_{xx}^{\text{trial}} - B_{yy}^{\text{trial}}) \\ s_{xy}^{\text{trial}} &= \frac{J_{\text{res}} \mathbf{G}}{J^{2/3}} B_{xy}^{\text{trial}} \\ s_{xz}^{\text{trial}} &= \frac{J_{\text{res}} \mathbf{G}}{J^{2/3}} B_{xz}^{\text{trial}} \\ s_{yz}^{\text{trial}} &= \frac{J_{\text{res}} \mathbf{G}}{J^{2/3}} B_{yz}^{\text{trial}} \end{aligned}$$

The pressure term, P , is given by:

$$P = -K(J - 1) \quad (3.43)$$

The trial α is

$$\alpha_{n+1}^{\text{trial}} = \alpha_n \quad (3.44)$$

With these relations, the trial function is checked to see the state of deformation occurring for this timestep on the particle.

If $f^{\text{trial}} \leq 0$:

The deformation is within the yield surface and elastic. The trial values of the left Cauchy-Green deformation tensor and deviatoric stress tensor can be saved to the particle:

$$\mathbf{B}_{n+1} = \mathbf{B}_{n+1}^{\text{trial}} \quad (3.45)$$

$$\mathbf{s}_{n+1} = \mathbf{s}_{n+1}^{\text{trial}} \quad (3.46)$$

If $f^{\text{trial}} \geq 0$:

If f^{trial} is greater than zero, elastic and plastic deformation are occurring - consequently the contribution of plastic deformation must be determined. Below the plastic corrector is added to the trial elastic functions.

$$\mathbf{B}_{n+1} = \mathbf{B}_{n+1}^{\text{trial}} - \frac{2\Delta\lambda I_1 \hat{\mathbf{n}}_{n+1}}{3J^{2/3}} \quad (3.47)$$

$$\mathbf{s}_{n+1} = \mathbf{s}_{n+1}^{\text{trial}} - 2\Delta\lambda \bar{G} \hat{\mathbf{n}}_{n+1} \quad (3.48)$$

where

$$\bar{G} = \frac{J_{\text{res}} G I_1}{3J^{2/3}} \quad (3.49)$$

and

$$\hat{\mathbf{n}}_{n+1} = \frac{\mathbf{s}_{n+1}}{\|\mathbf{s}_{n+1}\|} = \frac{\mathbf{s}_{n+1}^{\text{trial}}}{\|\mathbf{s}_{n+1}^{\text{trial}}\|} \quad (3.50)$$

Thus the only variable remaining to determine is the plastic multiplier, $\Delta\lambda$, and this is found by ensuring the stress state lies on the yield surface during plastic flow. The following equation can be derived from equation (3.48):

$$\|\mathbf{s}_{n+1}\| = \|\mathbf{s}_{n+1}^{\text{trial}}\| - 2\Delta\lambda \bar{G} \quad (3.51)$$

Then using equation (3.51), equation (3.39) can be re-written according to the trial stress and the incremented hardening variable.

$$f(\boldsymbol{\sigma}_K, \alpha) = \|\mathbf{s}_{n+1}^{\text{trial}}\| - \sqrt{2/3} \sigma_y - \left[\sqrt{2/3} K(\alpha_n + \sqrt{2/3} \Delta\lambda) + 2\bar{G} \Delta\lambda \right] = 0 \quad (3.52)$$

As the function $f(\boldsymbol{\sigma}_K, \alpha)$ must equal zero, $\Delta\lambda$ can be solved by the iterative Newton-Raphson method:

$$\Delta\lambda^{k+1} = \Delta\lambda^k - \frac{f(\Delta\lambda^k)}{f'(\Delta\lambda^k)} \quad (3.53)$$

where

$$f(\Delta\lambda^k) = \|\mathbf{s}_{n+1}^{\text{trial}}\| - \sqrt{2/3} \sigma_y - \left[\sqrt{2/3} K(\alpha_n + \sqrt{2/3} \Delta\lambda^k) + 2\bar{G} \Delta\lambda^k \right] \quad (3.54)$$

$$f'(\Delta\lambda^k) = -2\bar{G} - 2/3 K'(\alpha_n + \sqrt{2/3} \Delta\lambda^k) \quad (3.55)$$

$$K'(\alpha_n + \sqrt{2/3} \Delta\lambda^k) = \frac{K(\alpha_n + \sqrt{2/3} \Delta\lambda^k) - K(\alpha_n)}{\Delta t} \quad (3.56)$$

$$\Rightarrow \alpha^{k+1} = \alpha^0 + \sqrt{2/3} \lambda^{k+1} \quad (3.57)$$

Once the increment of plastic flow is determined, the stress and strain can be updated on the particle (equations 3.47 and 3.48), and the deformation update is complete.

3.5 Forces and Contact Between Bodies

Many solid mechanics problems involve contact between multiple materials - in the case of FSP there is the tool and the workpiece for example. When objects come into contact, new loads and forces must be recognised, if not problems such as non-physical interpenetration can occur. This requires proper handling of contact conditions. Furthermore, as friction is a very important aspect of FSP, detection of contact and its implementation has a crucial role to play.

Typically, particle methods are seen as having "contact for free" [91], as they do not require special contact elements as in purely Lagrangian finite element methods, or predefined surfaces. This section will discuss the background of contact detection and the implementation within MPM.

3.5.1 Contact Detection

The set of algorithms that control contact within MPM have been termed "multimaterial" MPM [140]. The methodology has been previously described in the literature [91, 140, 141] and will be summarised here. In general, the goal of multimaterial MPM is to detect contact-ing materials and adjust for any consequential changes to momentum and forces. The steps involved in this are described below.

In this set of methods, contact is determined on the background grid rather than the particles themselves. As discussed in the previous sections, at each timestep, data is passed between the particles and the background grid in order to carry out grid based or particle based operations. In multimaterial MPM, each material extrapolates variables to its own field on the nodes of the background grid. Those nodes that have more than one material must be checked for contact.

Figure 3.2 shows a schematic of two materials that must be checked for contact. The material points are represented as circles, blue (material 1) and red (material 2). The nodes are located at the intersections of the background grid elements. The nodes tending towards the middle (purple) have particles from both materials within their adjacent cells and are the contact nodes. All others are either single material (red/blue) as they contain one material, or inactive (grey) due to no material points.

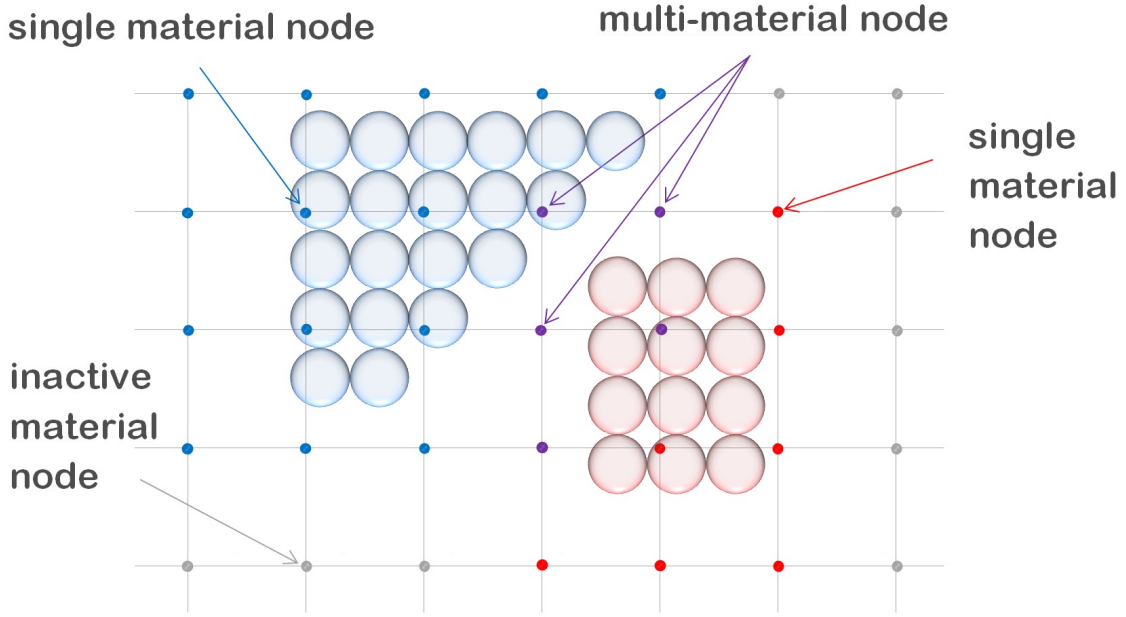


Figure 3.2: Schematic of contacting MPM material particles over background grid. Highlighted nodes indicate inactive (grey), single (blue/red) and multi-material (purple) nodes.

In the case of two materials coming into contact, the contact node will gain the extrapolated nodal velocities for each material, \mathbf{v}_a and \mathbf{v}_b and a body surface normal, $\hat{\mathbf{n}}$, defined as positive when directed from material a to b. This normal vector can be calculated and is discussed further below (section 3.5.3).

3.5.1.1 Contact Tests

There are two conditions that need to be met for contact to have deemed to occur. The first was proposed by Bardenhagen et al. [142], and determines whether the two materials are moving towards each other.

$$\text{Check 1)} \quad \Delta \mathbf{v}_i \cdot \hat{\mathbf{n}} = (\mathbf{v}_b - \mathbf{v}_a) \cdot \hat{\mathbf{n}} < 0 \quad (3.58)$$

where $\Delta \mathbf{v}_i$ is the velocity difference between the two materials and $\hat{\mathbf{n}}$ is the body surface normal. It is not sufficient on its own, however, as this condition can detect contact too soon.

The second test proposed by Lemiale et al. [91], is based on extrapolated material positions, and is satisfied when:

$$\text{Check 2)} \quad \Delta \mathbf{x}_i \cdot \hat{\mathbf{n}} = (\mathbf{x}_b - \mathbf{x}_a) \cdot \hat{\mathbf{n}} < 0.8\Delta h \quad (3.59)$$

where \mathbf{x}_i are the extrapolated particle positions, $0.8\Delta h$ is a fraction of the element length. It represents an approximation of two materials in contact according to GIMP extrapolation of two materials precisely in contact [91]. Note that using a cell criterion means that the method is resolution independent. Material positions on the nodes are found by an average grid extrapolation:

$$\mathbf{x}_i = \frac{\sum_{p \in j} m_p \mathbf{x}_p S_{ip}}{\sum_{p \in j} m_p S_{ip}} \quad (3.60)$$

Satisfying both these conditions confirms two materials are moving towards each other and are close enough for contact to occur.

3.5.2 Contact Treatment

Once contact is detected, the nodal momenta are adjusted to implement the chosen contact physics. Consider two materials, a and b, with nodal velocities on the same (multi-material) node of \mathbf{v}_a and \mathbf{v}_b . The centre of mass velocity is given by:

$$\mathbf{v}_c = \frac{m_a \mathbf{v}_a + m_b \mathbf{v}_b}{m_a + m_b} \quad (3.61)$$

where m_a and m_b are the masses for the two materials. Next, define $\Delta \mathbf{p}_a$ as the momentum change required on material a for its velocity to change from \mathbf{v}_a to \mathbf{v}_c or

$$\mathbf{v}_a + \frac{\Delta \mathbf{p}_a}{m_a} = \mathbf{v}_c \quad \text{which means} \quad \Delta \mathbf{p}_a = -m_a(\mathbf{v}_a - \mathbf{v}_c) \quad (3.62)$$

Substitution of \mathbf{v}_c defined in Equation (3.61) leads to:

$$\Delta \mathbf{p}_a = -m_a \mathbf{v}_a + m_a \frac{m_a \mathbf{v}_a + m_b \mathbf{v}_b}{m_a + m_b} = \frac{m_a \mathbf{p}_b - m_b \mathbf{p}_a}{m_a + m_b} \quad (3.63)$$

where \mathbf{p}_a and \mathbf{p}_b are the nodal momenta for the two materials.

When one of the bodies is rigid, contact is implemented by considering the rigid particles to have infinite mass. In this limit, the rigid material velocity defines the center of mass velocity: $\Delta \mathbf{p}_a = m_a \mathbf{v}_b - \mathbf{p}_a$ and $\Delta \mathbf{v} = \Delta \mathbf{p}_a / m_a$ where \mathbf{v}_b is the tracked rigid material velocity. All other contact methods are identical to deformable material contact, except that the position of the rigid particles is found by volume-weighted averaging instead of mass-weighted averaging, and no momentum change is applied to the rigid particles.

To avoid interpenetration of material points, the momentum of each material point is adjusted to that of the centre-of-mass momentum on the node. The momentum change for material a to adjust to the centre-of-mass momentum is $\Delta \mathbf{p}_a = \mathbf{p}_c - \mathbf{p}_a$.

With the assumption of a stick condition, the momentum change of $\Delta \mathbf{p}_a$ is applied to material a. These momenta changes correspond to normal and tangential forces of

$$\mathbf{f}_n = \frac{(\Delta \mathbf{p}_a \cdot \hat{\mathbf{n}})}{\Delta t} \hat{\mathbf{n}} \quad \text{and} \quad \mathbf{f}_t = \frac{(\Delta \mathbf{p}_a \cdot \hat{\mathbf{t}})}{\Delta t} \hat{\mathbf{t}} \quad (3.64)$$

where Δt is time step and $\hat{\mathbf{t}}$ is unit vector in the tangential direction of motion. The positive normal contact force is then $\mathbf{f}_n = -(\Delta \mathbf{p}_a \cdot \hat{\mathbf{n}}) / \Delta t$ and the positive sliding force is $\mathbf{f}_t = (\Delta \mathbf{p}_a \cdot \hat{\mathbf{t}}) / \Delta t$.

If $|\mathbf{f}_t| < \mu |\mathbf{f}_n|$, the objects will stick. Otherwise, the object is sliding and the tangential force is converted into a frictional force, $\mu |\mathbf{f}_n|$, but the objects still stick in the normal direction.

$$\mathbf{f}_t = (\mu |\mathbf{f}_n|) \hat{\mathbf{t}} \quad (3.65)$$

3.5.3 Calculation of the Surface Normal

Both contact detection and changes in momenta depend on the surface normal. During the MPM phase to extrapolate particle data to the grid, volume gradients are also extrapolated.

$$\sum_p V_p \nabla S_{ip} = \nabla V_i \quad (3.66)$$

Initially, the typical implementation of MPM selected the surface normal from the maximum mass gradient of the two contacting materials, however this method does not account for contact between materials with different densities or between deformable and rigid materials [140]. Thus the volume gradient is generally used to determine the surface normal [143]. The contact method implemented here takes the surface normal vector as:

$$\mathbf{n} = \max\left(\nabla V_a, \nabla V_b\right) \quad (3.67)$$

where the vector \mathbf{n} is found from the maximum volume gradient of the two contacting materials. The normal unit vector, $\hat{\mathbf{n}}$, is found by normalizing \mathbf{n} .

When rigid particles are used, the volume gradient at contact nodes near these particles can give more reliable results for the surface normal compared to a deforming non-rigid material [91, 140]. Thus, in these cases the normals calculated from the rigid materials should be preferred over the volume gradient from the deformable material, whose volume gradient will fluctuate in regions of high deformation. For these cases a rigid bias factor is introduced, R_b , and the contact normal calculation becomes:

$$\mathbf{n} = \max\left(\nabla V_a, R_b \nabla V_b\right) \quad (3.68)$$

where body b is the rigid material. Thus the normal is taken from the rigid material unless the volume gradient for the deformable material is R_b times higher. A finite R_b is preferred over an infinite value to protect against nodes with a near zero gradient from the rigid material [91]. In FSP, large material deformation at the contact interface (between the tool and workpiece) encourages calculating the surface normal from the rigid tool material, and thus the use of a rigid bias factor.

In summary, one of the great features of this set of contact methods is its efficiency - it scales linearly with the number of particles as there is no need for pairwise comparison of velocities or momentum, rather the background grid handles the contact detection in a single sweep. It also removes the need for additional contact elements and predefinition of the contact surface.

3.6 The MPM Incremental Update

This section will outline and summarise the step by step state update for the MPM. Before the process begins, the problem geometry is discretised into particles that reside on a background computational mesh. The particles or material points are assigned material properties

such as mass and elastic stiffness. Boundary and initial conditions are also created upon the material points and/or background grid, such as initial velocities or temperatures.

In the following description, let k define the current timestep, e.g. \mathbf{v}^k is the current velocity vector and \mathbf{v}^{k+1} is the vector for the next time step. In the original MPM description, the choice of when to update the stress could lead to either dissipation or increase in energy, and potential instabilities [144]. To resolve this, the update is carried out twice during each timestep resulting in an average value being applied [143].

3.6.1 Incremental Update

1) At the beginning of the timestep, all data resides on the particles (rather than the background grid). The shape functions and shape function gradients are determined from the current particle positions relative to the background grid (equations 3.6a and 3.6b), and are used throughout the timestep.

2) Next the nodal momentum, mass and temperature is calculated from the extrapolated particle data:

$$\mathbf{p}_i^k = \sum_p \mathbf{p}_p^k S_{ip}^k = \sum_p m_p \mathbf{v}_p^k S_{ip}^k \quad (3.69)$$

$$m_i^k = \sum_p m_p S_{ip}^k \quad (3.70)$$

$$T_i^k = \sum_p T_p S_{ip}^k \quad (3.71)$$

The volume gradient is also needed for use in the contact algorithm:

$$\nabla V_i^k = \sum_p V_p^k \nabla S_{ip}^k \quad (3.72)$$

3) Next a check for contact is done (section 3.5.1), then if contact is occurring, the nodal momenta is adjusted and contact forces calculated (section 3.5.2). Any friction resultant thermal energy is stored for use in the later thermal calculation.

4) Any nodal based boundary conditions, such as displacement or velocity conditions, can now be applied to the nodes.

5) In order to calculate an average stress and deformation over the time step, the particle stress and deformation gradient are first calculated here. In the hyperelastic formulation, each time the stress and strain is calculated the following procedure is used.

The particle deformation gradient, \mathbf{F}_p , is updated from the nodal displacement gradient (section 3.4.1.3). The particle temperature is extrapolated directly from the nodes. The temperature increment (required for residual stresses) is calculated based on the current and previously extrapolated temperature.

$$T_p = \sum_i T_i S_{ip} \quad (3.73)$$

$$dT = T_p^k - T_p^{k-1} \quad (3.74)$$

The procedure to determine the stress then follows the description of the hyperelasticity section above (section 3.4.1), where the material hardening is calculated by the desired constitutive law. At the end of the stress update the plastic dissipation is stored for use in the thermal calculation.

6) The nodal forces (internal, external and traction) are calculated from equation 3.22. If there are nodes with fixed displacements the total forces for that node are set to zero to prevent any acceleration being applied.

7) The nodal momenta can then be determined based on the acting nodal forces:

$$\mathbf{p}_i^{k'} = \mathbf{p}_i^k + \Delta t \mathbf{f}_i^{\text{total}} \quad (3.75)$$

8) The particles' position, velocity and temperature are now updated, where the nodal temperature increment is calculated according to section 3.3.3.2 and includes the thermal energy dissipated from plastic deformation and friction:

$$\mathbf{x}_p^{k+1} = \mathbf{x}_p^k + \Delta t \sum_i \frac{\mathbf{p}_i^{k'} S_{ip}^k}{m_i^k} \quad (3.76)$$

$$\mathbf{v}_p^{k+1} = \mathbf{v}_p^k + \Delta t \sum_i \frac{\mathbf{f}_i^{\text{total}} S_{ip}^k}{m_i^k} \quad (3.77)$$

$$T_p^{k+1} = T_p^k + \Delta t \sum_i \frac{dT_i}{dt} S_{ip} \quad (3.78)$$

9) The new particle velocities are again extrapolated to the grid to give a revised set of nodal momenta, the temperature is also extrapolated again for use in the constitutive model (the extrapolated nodal temperature gives more consistent results than the current particle temperature). The nodal displacement is also calculated for use in contact detection. As the same shape functions are used, the nodal mass and volume will remain unchanged.

$$\mathbf{p}_i^{k''} = \sum_p m_p \mathbf{v}_p^{k+1} S_{ip}^k \quad (3.79)$$

$$T_i^{k'} = \sum_p T_p^{k+1} S_{ip}^k \quad (3.80)$$

$$\mathbf{u}_i^{k'} = \sum_p \mathbf{u}_p^{k'} S_{ip}^k \quad (3.81)$$

9) Check for contact as the particles now have updated positions and velocities.

10) Determine the particle deformation gradient (the nodal velocities have been updated), and particle stress once more.

11) The material history and all information are now stored on the particles. The mesh can be reset (discarded) and the next step may begin at **(1)**, with $k = k + 1$.

Figure 3.3 shows the description summarised into a flow chart.

3.7 Conclusion

In this chapter the formulation of MPM has been discussed. The strong form of the governing equations was presented, followed by the weak form and discretisation for solving over the discretised (particle and nodal) domain. The generalised GIMP shape functions, an improvement on the original MPM shape functions, were also presented. The constitutive model was discussed in the context of large deformation. A hyperelastic formulation was shown with a description of the method for determining plasticity. The forces and contact between different bodies was discussed - crucial for correct tool and plate interaction in FSP. The detection of contact, including contact tests, was followed by contact treatment. The method for calculating the surface normal for contact treatment was also shown. The means by which MPM updates all the relevant quantities and variables was discussed in the final section.

With this relatively complete description of MPM, the development of the FSP model can now begin. The next chapter will present the thermal model of FSP.

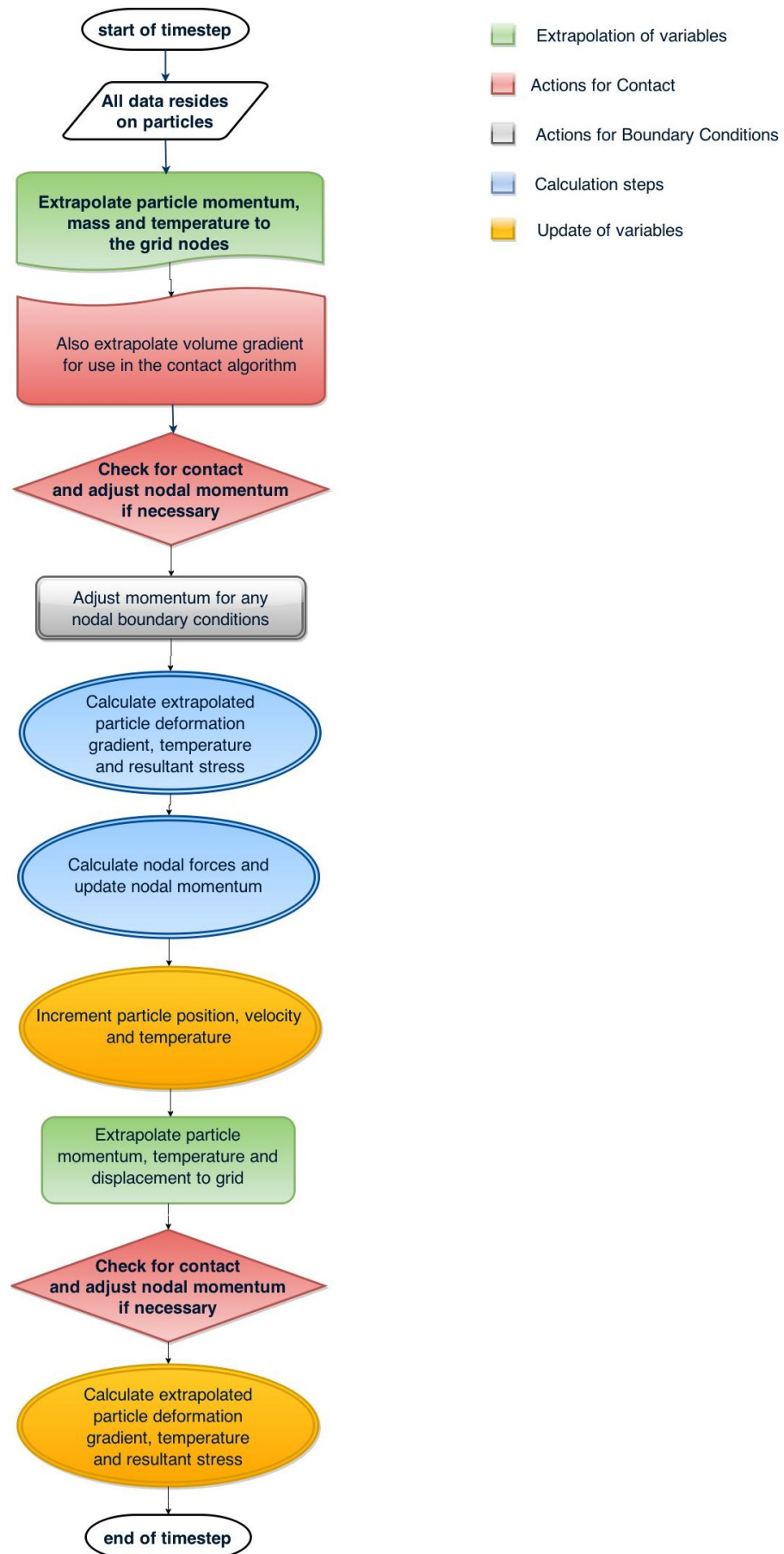


Figure 3.3: Flow chart of MPM update during one timestep.

Chapter 4

Thermal Modelling of Friction Stir Processing

4.1 Introduction

In the previous chapter the formulation of MPM was discussed. In this chapter, a purely thermal model of FSP will be developed within this framework.

Note that in the previous chapters the importance of the meshless technique to modelling large deformation problems has been discussed, however only the thermal model is presented here, which excludes any mechanical calculation. Therefore the strength of MPM compared to FEA or other mesh based techniques will not be apparent. A complete thermo-mechanical model will be presented in the next chapter however.

The thermal response is a major component of FSP, as the thermal field will contribute to the microstructure evolution, which itself is a key parameter determining the final strength and ductility of the processed material. In addition, the thermal field affects the strength and flow of the processed material. For these reasons, purely thermal models have been presented from around the inception of FSW and FSP, and continue to be published even recently [117, 119, 145].

This chapter begins by discussing the development of the numerical model - the method for calculation of heat generation, its implementation as a moving heat source, and thermal losses to the backing plate, surrounding air, and tool. In order to validate the developed numerical models, the next section describes the experimental work that has been undertaken. In the final sections, the precise boundary conditions are determined for these experiments, and the results of this initial stage of thermal modelling are presented.

4.2 Description of the Thermal Model

A number of boundary conditions (BCs) are applied to model FSP. In a purely thermal model this is limited to heat generation from the moving tool and heat loss to the surroundings. The method for determining these parameters is explained in detail below.

4.2.1 Modelling the FSP Tool as a Moving Heat Source

4.2.1.1 Heat Generation

The generation of heat is a result of frictional contact between the tool and workpiece and plastic dissipation. From the relation between power, torque, force and stress, the following relationships can be defined:

$$dQ = \omega dM = \omega r dF = \omega r \tau dS \quad (4.1)$$

where dQ is an increment of energy or power, dM is an increment of torque, r is the radial distance from a centre where the increment of force, dF , is acting, and τ is the average assumed shear stress over the increment of area dS [114].

Thus an increment of energy flux, dq (W/m^2), can be determined from rotational speed, radial distance and shear stress:

$$dq = \frac{dQ}{dS} = \omega r \tau \quad (4.2)$$

This analytical relationship can be utilised in the modelling of a heat source for FSP as it defines a thermal energy increment for any point on the surface of the plate in contact with the rotating tool.

Determining the rotational speed and radial distance for FSP is straightforward, however the shear stress is more complex and has typically been calculated according to the contact condition between the tool and workpiece in literature [146]. If we assume the workpiece material is fully sticking to the tool, the shear stress is equivalent to the shear stress at yielding for the workpiece material, τ_y . If alternatively we assume sliding (frictional contact), the shear stress can be estimated using a friction model such as Coulomb's law ($\tau_f = \mu P$, where μ is the coefficient of friction and P is the normal pressure). However, the most likely condition is a combination of sticking and sliding, and this is supported by the observation of banding in microstructure due to differences in strain rate resulting from fluctuating contact conditions [8]. A combination of the two contact conditions estimates partial sticking/sliding by incorporating a fraction, c , of each $\tau = c\tau_f + (1 - c)\tau_y$.

For simplification and as an initial starting point, this model assumes a full sticking condition at the interface between the tool and workpiece, and has been applied in recent publication [147]. In purely thermal models such as this one, a popular approach to determine the shear yield stress in literature has been to make use of experimentally determined yield stress vs temperature curves [117, 119]. This allows the model to determine stress (based on these curves) as a function of the current thermal conditions of the workpiece. Equation 4.2 can be redefined as:

$$dq = \omega r \frac{\sigma_y(T)}{\sqrt{3}} \quad (4.3)$$

where the relation between the stress and shear stress is simply $\tau = \sigma / \sqrt{3}$, from comparison of the von Mises yield criteria in uniaxial tension and pure shear.

In this way, the temperature is self-regulated in the processing zone, because a rise in temperature implies a drop in yield stress, which in turns reduces the heat flux experienced at that point.

4.2.1.2 Moving Heat Source

In this model, the physical tool is replaced by a moving surface heat flux boundary condition. The tool angle, concave interface and penetration depth are ignored in favour of a simple circular heat flux applied on the surface. It is a function dependent on temperature, position and time.

$$E_{HF} = \omega r_p \frac{\sigma_y(T)}{\sqrt{3}} \quad : r_p < r_s \quad (4.4)$$

where E_{HF} is the prescribed surface heat flux, r_s is the shoulder radius and r_p is the particle radius from the tool centre, calculated from

$$r_p(x_p, y_p, t) = \sqrt{((x_p - x_o) - v_T t)^2 + (y_p - y_o)^2} \quad (4.5)$$

where v_T is the translational speed of the tool, x_o and y_o are the initial central positions of the tool in x and y , and the subscript p refers to the current particle being evaluated. The requirement that $r_p < r_s$ ensures that the heat flux is only applied to particles beneath the calculated position of the tool.

4.2.2 Thermal Losses

4.2.2.1 Thermal Loss to the Backing Plate and Surrounding Air

To model the loss of heat into the backing plate, rather than add the backing plate material itself and an interfacial conduction coefficient (as some researchers have done [79, 148]), a convection coefficient is added to the bottom surface of the workpiece. Replacing the backing plate and interfacial conduction coefficient with only a convection coefficient allows the computation time to be reduced while maintaining the same number of calibrated coefficients.

Two assumptions are made, that the convection coefficient on the bottom surface is constant throughout and after processing, and that the backing plate convection coefficient can represent all heat loss - including air convection on each of the other surfaces and heat transfer into the backing plate. With this understanding, the experimental data can be used to determine a lumped backing plate convection coefficient. During cooling (after the tool has left the plate), the temperature steadily decreases over time, and this curve can be used to determine an average convection coefficient.

Recalling the heat equation for 3D heat flow in an isotropic solid:

$$\nabla \cdot k \nabla T + q = \rho C_p \frac{\partial T}{\partial t} \quad (4.6)$$

where k is the thermal conductivity (W/mK), T is the temperature (K), q is a source term (heat generated per unit volume) (W/m³), ρ is the material density (kg/m³), C_p is the specific heat capacity (J/kg-K) and t is the time (s). If we assume homogeneous temperature distribution through the workpiece during cooling (when there is no heat input), this relation can be simplified and applied to the case of a cooling copper plate:

$$q = \rho C_p \frac{dT}{dt} \quad (4.7)$$

In the case of our cooling workpiece, in the absence of any heating component, q becomes equivalent to the rate of thermal energy loss for the plate. If we assume all losses are through convection, the rate of heat loss experienced by the workpiece can be calculated as follows:

$$qV = Q = h_c S (T_{\text{body}} - T_{\text{room}}) \quad (4.8)$$

where V is the volume of the body (m³), h_c is the convection coefficient (W/m²), S is the surface area (m²), Q is a thermal energy (W), T_{body} is the current temperature of the body and T_{room} is the room temperature. Combining Equations 4.7 and 4.8 yields:

$$\rho C_p V \frac{dT}{dt} = h_c S (T_{\text{body}} - T_{\text{room}}) \quad (4.9)$$

Thus an average convection coefficient can be approximated from the rearranged equation:

$$\bar{h}_c = \frac{\rho C_p V}{S} \frac{\frac{dT}{dt}}{(T_{\text{body}} - T_{\text{room}})} \quad (4.10)$$

Given this function, the average convection coefficient, \bar{h}_c , can be determined for our workpiece: ρ and C_p will be the density and specific heat capacity for copper, while V and S the volume of the workpiece and surface area exposed to the backing plate respectively. The relation $\frac{\frac{dT}{dt}}{(T_{\text{body}} - T_{\text{room}})}$ can be determined through analysis of recorded cooling temperatures.

4.2.2.2 Thermal Loss to the Tool

As mentioned in the literature review, chapter 2, in their model of FSW, Darvazi et al. included a coefficient representing the proportion of thermal energy transferred into the workpiece [120]. Their fraction was estimated using a relation for steady state one-dimensional heat transfer, which is presented in the work of Carslaw and Jaeger [149].

At the interface of the two dissimilar materials (1 and 2), equal temperature and flux across the boundary are assumed:

$$T_1 = T_2 \quad \& \quad k_1 \frac{\partial T_1}{\partial x} = k_2 \frac{\partial T_2}{\partial x} \quad \text{at the interface, } x=0 \quad (4.11)$$

Based on these initial boundary conditions, a relationship for the heat flux, J , into each material can be found.

$$\frac{J_1 \kappa_1^{1/2}}{k_1} = \frac{J_2 \kappa_2^{1/2}}{k_2} \quad (4.12)$$

where J_1 and J_2 represent the heat flux into each material respectively, ($J_1 + J_2 = J_{\text{total}}$), and κ is the diffusivity of the material ($\kappa = k/\rho C_p$). Rearranging equation (4.12) for the ratio of the flux J_1 over J_2 :

$$\frac{J_1}{J_2} = \frac{\kappa_2^{1/2} k_1}{\kappa_1^{1/2} k_2} \quad (4.13)$$

Then the ratio of the heat flux into one material, J_1 , with respect to the total flux gives:

$$\frac{J_1}{J_1 + J_2} = \frac{k_1 \kappa_2^{1/2}}{k_2 \kappa_1^{1/2} + k_1 \kappa_2^{1/2}} \quad (4.14)$$

which rearranged and written in terms of the FSP workpiece and tool becomes that shown in equation (2.11).

Additionally, as there is no tool in the model, but rather a moving surface heat flux, the analytical heat source function (equation 4.3) is multiplied by the energy fraction for copper.

$$E_{\text{HF}} = g \omega r \frac{\sigma_y(T)}{\sqrt{3}} \quad (4.15)$$

where E_{HF} is the prescribed surface heat flux and g is the fraction of energy conducted into the copper workpiece.

This concludes the set of boundary conditions required for the thermal model. In the next sections the experimental method will be discussed, followed by calibration of the model to the experiment.

4.3 Experimental Method

For the purpose of validation, FSP was conducted upon copper plates (C11000 Electrolytic tough pitch copper, temper H02). Figure 4.1 (right) shows an image of the experimental set-up with annotations. The copper plates were processed with between two and three K-type thermocouples. Temperatures were recorded at three positions along the plate (locations shown in Figure 4.2). Trapezoidal cavities were initially machined into the centre of the plates in order to observe material flow into these regions (this will be explored in chapter 5). A mild steel backing plate was positioned between the copper workpiece and the machining bench. Four clamps were used to hold the copper workpiece in place.

The pinless tool (shown to the left in Figure 4.1) was rotated 3° away from the traverse direction, and maintained a penetration depth of 0.05mm measured from the leading edge throughout processing. The traversal speed was 1.8mm/s and rotational speed 970rpm. A schematic of the workpiece is shown in Figure 4.2. The location of the thermocouples is given by the red crosses and the dimensions of the trapezoidal cavity are shown. Table 4.1 shows

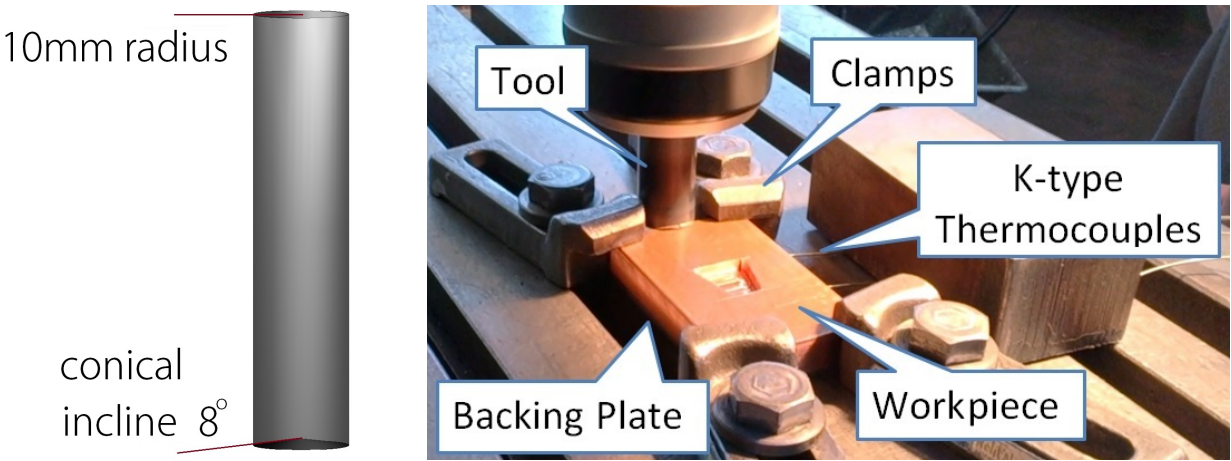


Figure 4.1: Left) tool dimensions, right) experimental set-up.

the three orientations of trapezoidal cavity processed in this work, where each is centred about the middle of the plate (which is also the location of T2 as shown by Figure 4.2).

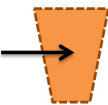
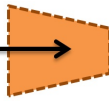
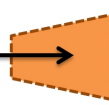
Cavity	1	2	3
Orientation			

Table 4.1: The three cavity orientations with tool processing direction as shown by the arrow.

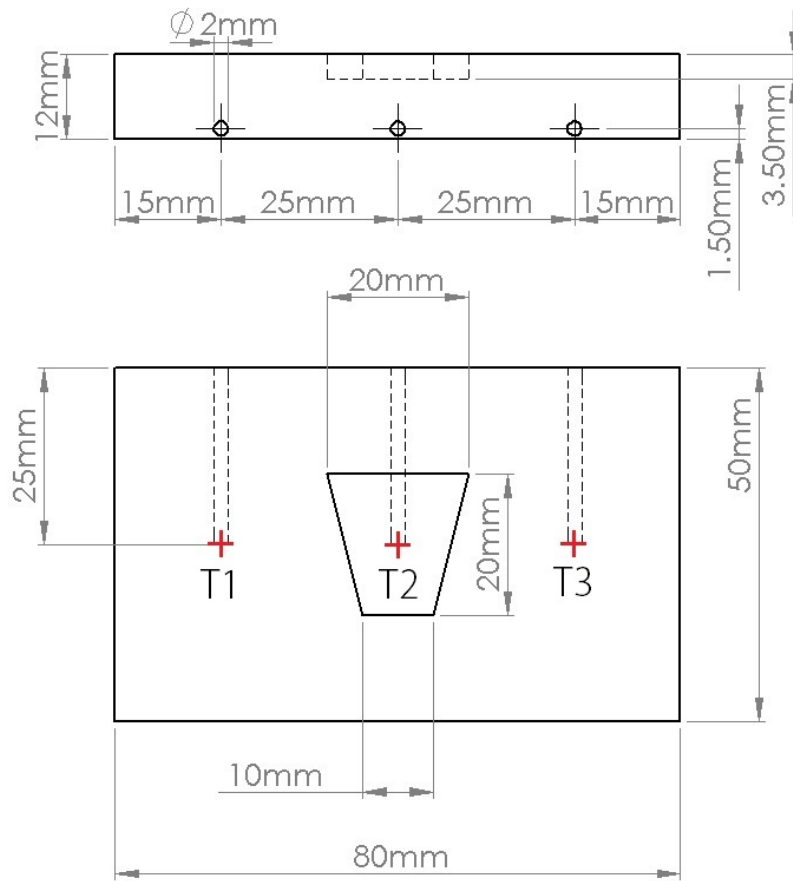


Figure 4.2: Schematic of plate with marked (+) thermocouple positions, T1-T3. The dimensions of the trapezoidal cavity are also shown.

The results of the experimental work will be presented in conjunction with the relevant numerical results. The following section describes the calibration of the numerical model.

4.4 Boundary Conditions used in Modelling FSP

Following from the numerical methodology described above, section 4.2, the following section will describe the appropriate values found for the given experimental conditions.

4.4.1 Heat Generation

The workpiece has thermal properties for copper, as defined in Table 4.2, and consists of 388,968 particles with a particle separation of 0.5 mm.

	ρ (kg/m ³)	C_p (J/kg-K)	k (W/mK)
Copper	8960	386	391
Tool	7800	14.4	460

Table 4.2: Copper plate and tool steel material parameters (used in calculation of the global convective coefficient, \bar{h}_c , and thermal coefficient, g , accounting for heat loss into the tool).

	V (m ³)	S (m ²)
Copper	4.671×10^{-5}	0.004

Table 4.3: Copper plate material parameters (used in calculation of the global convective coefficient, \bar{h}_c).

4.4.1.1 Temperature Dependent Yield Stress

The temperature dependence of the yield stress in copper is shown in Figure 4.3.

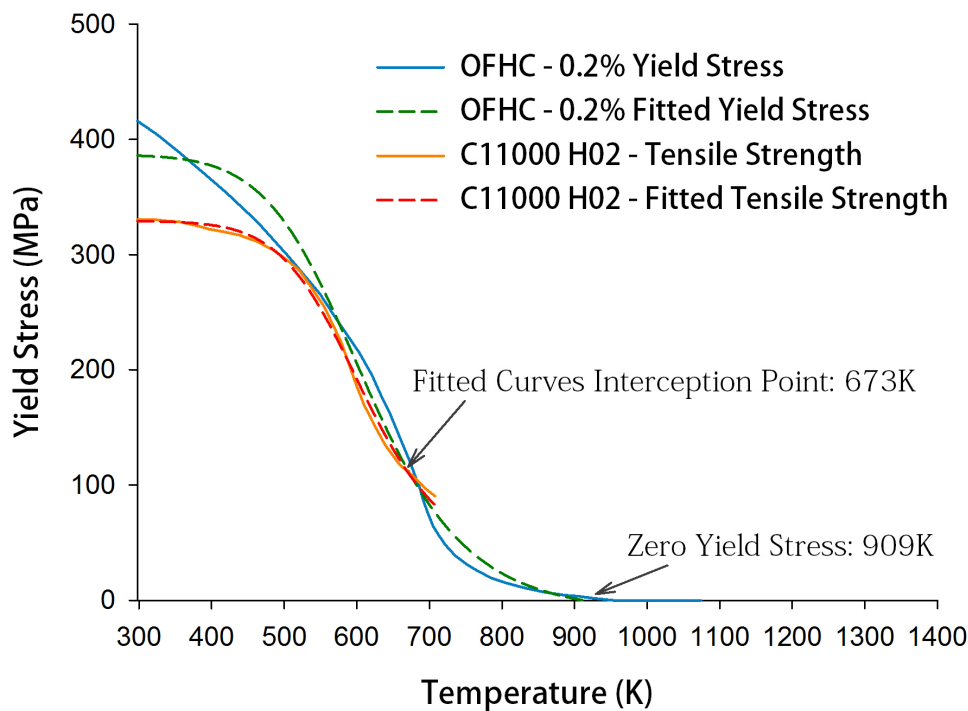


Figure 4.3: Experimental tensile test data for 0.2% yield stress vs. temperature for OFHC copper [150] fitted with a 4 Parameter Logistic (4PL) regression curve. Also shown is the tensile strength vs. temperature for C11000 H02 copper [150] with a fitted 4PL regression curve.

Due to the lack of experimental yield stress vs temperature data for C11000 H02 copper, an OFHC yield stress curve is assumed. However, given that the tensile strength data available for C11000 H02 is less than the yield stress of OFHC copper for most of its presented range, a hybrid function is applied. Both curves are shown in Figure 4.3. At room temperature, the yield stress of C11000 H02 copper is within ~15% of its tensile strength, thus the tensile strength is a better approximation for the yield stress of the material in its initial range. The unavailable data at higher temperatures is approximated by the OFHC yield stress data. The two experimental curves also presented in Figure 4.3 are fitted with a 4 Parameter Logistic (4PL) nonlinear regression model (shown in equation (4.16)). This model most aptly reflected the data. This allows the temperature dependent shear yield stress to be replaced by a hybrid function, shown in equation (4.17).

$$\sigma_y(T) \approx \sigma_{\min} + \frac{\sigma_{\max} - \sigma_{\min}}{1 + (T/EC50)^{-H_s}} \quad (4.16)$$

$$\sigma_y(T) = \begin{cases} 32.6 + \frac{329.2 - 32.6}{1 + (T/608.4)^{10.55}} & : 293 < T \leq 673 \\ -12.2 + \frac{386.7 + 12.2}{1 + (T/612.7)^{8.71}} & : 673 < T \leq 909 \\ 0 & : T > 909 \end{cases} \quad (4.17)$$

4.4.2 Thermal Losses

4.4.2.1 Backing Plate Convection Coefficient

Figure 4.4 shows the experimental temperature profiles for cavity 1 (table 4.1). The processing and cooling phase have been separated by a vertical line that indicates the moment when the back edge of the tool leaves the workpiece. The overlapping temperature profiles during the cooling phase indicate that our assumption of a homogeneous temperature in the plate is reasonable.

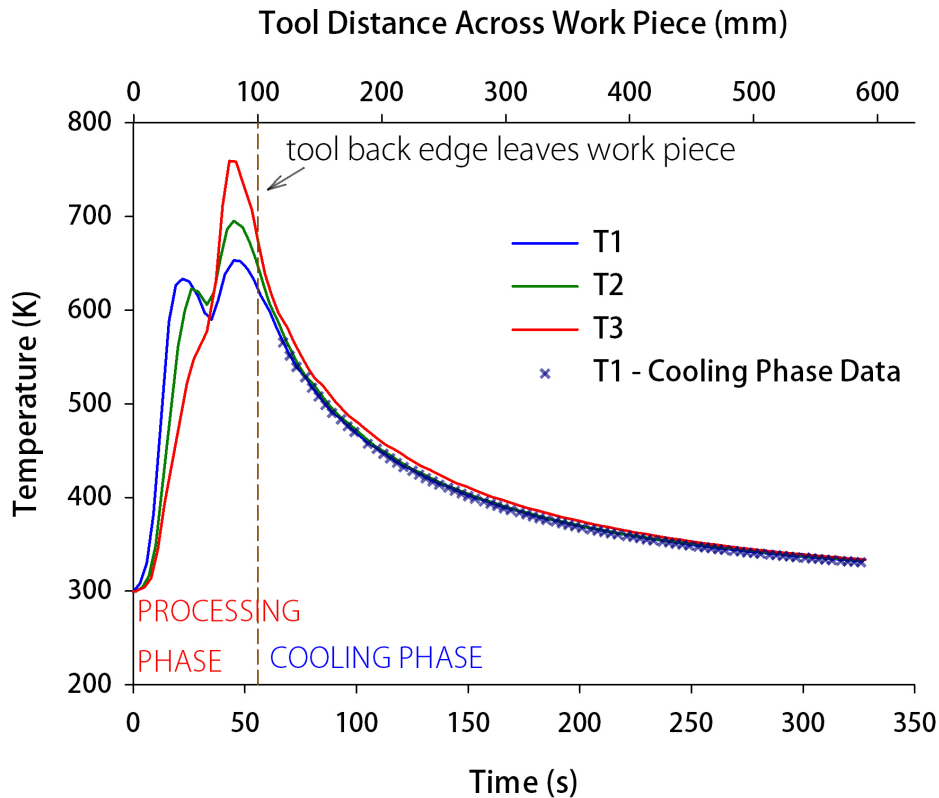


Figure 4.4: The experimental temperature over time for thermocouples 1-3 (cavity 1) with separated processing and cooling phase for reference.

To calculate the rate of change of the temperature with respect to time, in this instance the approach has been to rely on the recorded temperatures at each increment of time.

$$\frac{dT}{dt} = \frac{T_c - T_p}{t_c - t_p} \quad (4.18)$$

$$T_{\text{body}} - T_{\text{room}} = \left(\frac{T_c + T_p}{2} \right) - T_{\text{room}} \quad (4.19)$$

where T_c , T_p , t_c and t_p are the current and previous temperature and time recorded respectively, as shown by the blue crosshairs in Figure 4.4.

Figure 4.5 shows the trend observed between the rate of change of the temperature of the plate, dT/dt , and the temperature difference of the plate relative to the room, $(T_{\text{body}} - T_{\text{room}})$ for Thermocouple 1 (cavity 1). Cooling phase data is taken from 65 seconds which is when the rear of the tool is well past the edge of the plate. A least squares regression analysis yields a trend line as shown, whose gradient is the relation $(dT/dt)/(T_{\text{body}} - T_{\text{room}})$, needed for equation (4.10).

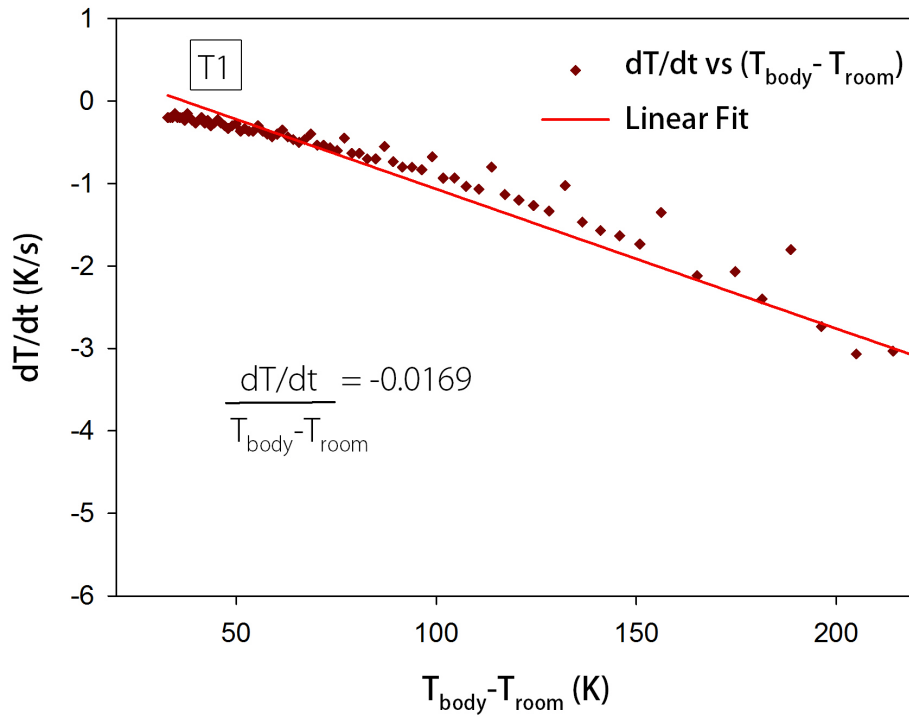


Figure 4.5: Plot of dT/dt vs $(T_{\text{room}} - T_{\text{body}})$ for the cooling phase of cavity 1, with a fitted linear function shown.

Applying this fitting to T1, T2, T3 yielded gradients of -0.0169, -0.0179, -0.0174 respectively, and thus an average value of -0.0174. This slope is substituted into Equation (4.10) along with the material parameters for the copper plate (showed in Table 4.2 and 4.3) to determine a global value for \bar{h}_c , -700 W/m²K in this case. Note that derivation of this coefficient is explored further in chapter 6.

4.4.2.2 Coefficient for Heat Loss into the Tool

For the conditions of this experiment, the values for the parameters of equation (2.11) are shown in Table 4.2. The derived fraction for thermal energy passed to the copper workpiece is 0.836.

In summary the previously described boundary conditions allow for the modelling of the thermal response of the workpiece according to the experimental conditions. It is important to note that all parameters have been identified, leaving no free parameter to be adjusted to match the experimental results. The results are presented in the following section.

4.5 Comparison of Experiment with the Obtained Thermal Model of FSP

4.5.1 Resulting Temperature Field

4.5.1.1 Comparison of Calculated Temperature Profile with the Experimental Result

Figure 4.6 shows the resulting temperature profiles for thermocouple positions T1, T2 and T3. The vertical dashed lines highlight notable positions of the tool relative to the plate during processing, linking them to the corresponding times that they occur.

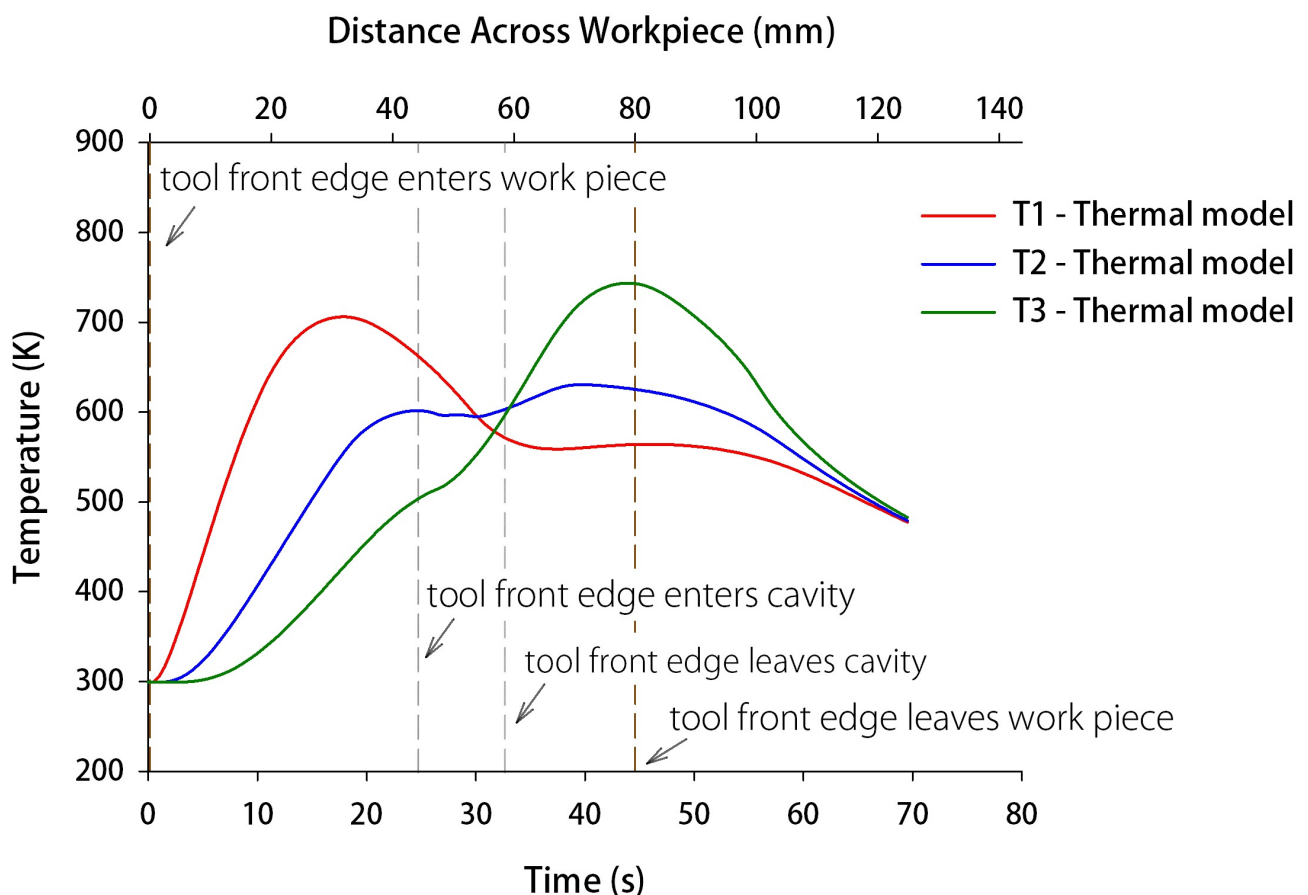


Figure 4.6: Temperature profile predicted by the thermal model over time for T1, T2 and T3.

The model predicts a drop in temperature for all thermocouples as the tool passes over the cavity, and similarly cooling after the tool leaves the workpiece. Compared against the experimental temperature readings shown in Figure 4.7, the overall trend is captured reasonably well at all three locations. T1 (thermocouple 1) in red over-predicts the initial peak by about

11%, and under-predicts the secondary peak by approximately 14%. The rate of heat loss for T1 seems slightly too high, similarly with T2 and T3. For thermocouple T2, there is an under-prediction of both peaks (by about 4% and 10%). Thermocouple T3 shows a less drastic loss in temperature as the tool passes through the cavity, and the secondary peak error is less than 2%.

The temperatures are initially overpredicted, but as the simulation progresses and the plate heats up, the peak temperatures close to the tool become quite reasonable (see first peak for T2 and second peak for T3). The tendency to underpredict the temperature as the tool moves away (secondary peak T1 and T2) may be due to a larger backing plate convection coefficient than is realistic. This will be investigated again in chapter 6. Furthermore, the large switch from over-prediction to under-prediction seen for T1, may be due to the trend observed in the stress vs. temperature curve applied to determine the heat flux - as seen in Figure 4.3, a higher temperature corresponds to a lower yield stress, thus an over-prediction in temperature will be followed by a comparatively lower thermal input. Therefore correction of the over-prediction for the initial peak could level out the following under-prediction for the secondary peak.

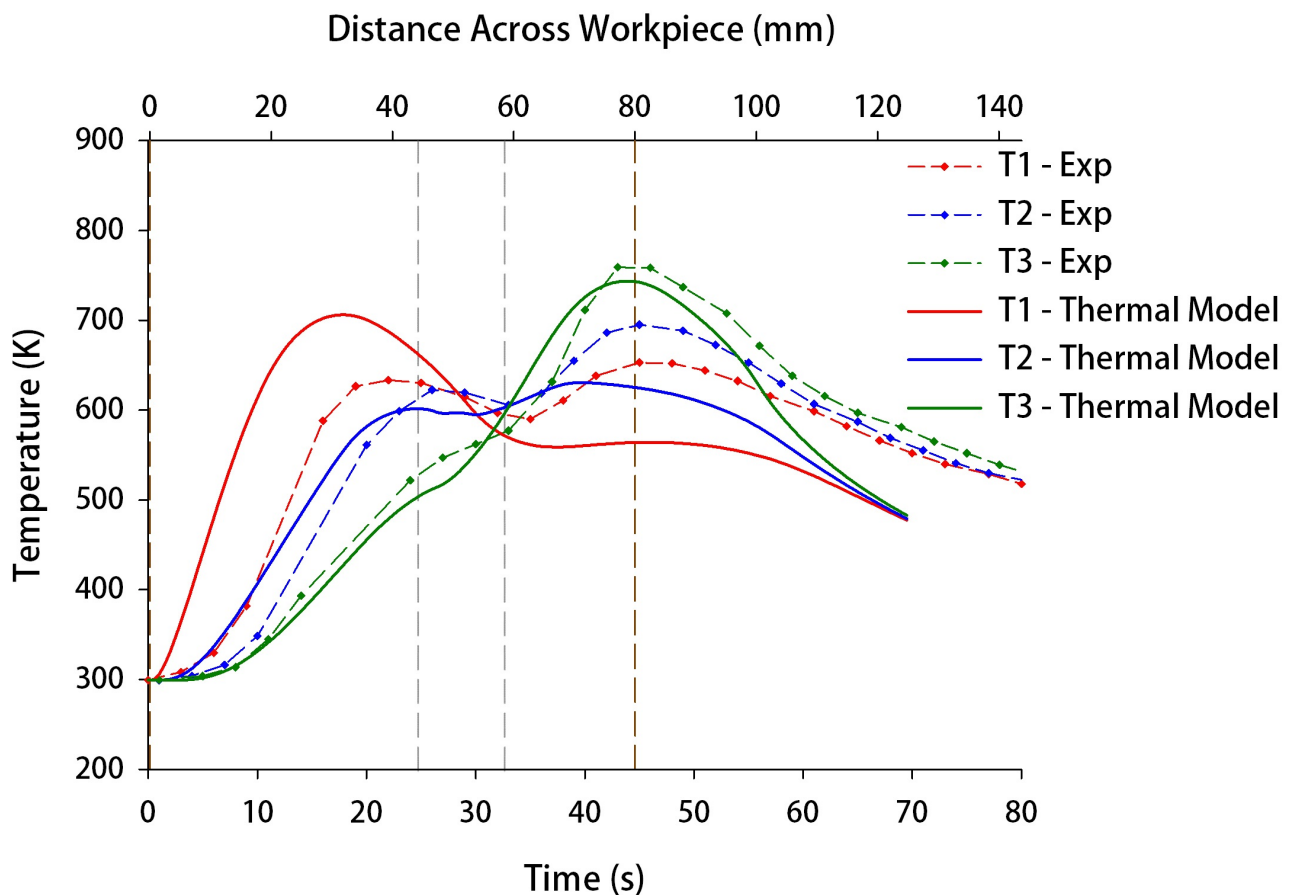


Figure 4.7: Temperature profile predicted by the thermal model over time for T1, T2 and T3 compared against experiment.

4.5.1.2 Analysis of Surface Temperature

Figure 4.8 (left) shows the temperature across the entire face of the plate, 1mm below the surface. Figure 4.8 (right) shows the temperature along the three parallel lines across the plate, at a depth of 1mm from the surface. The three lines represent areas corresponding to the advancing side, retreating side and centre line. The advancing and retreating lines run along the edge of the tool, that is they are 10mm either side of the centre line of the plate. The temperature scale has a maximum set at the melting temperature of copper (1356K). The figure is split into three moments in time - 10, 25 and 40 seconds. In the plots, the position of the front and rear of the tool are indicated by the dashed horizontal lines.

The figure in general shows that the peak temperatures are located along the centre line underneath the tool. In addition, the advancing and retreating sides have very similar profiles. This is because there is nothing in the formulation to account for the effect of the difference in advancing and retreating velocities on the flow stress, and thus any subsequent difference in heat generation. There are some differences as the tool passes over the cavity, and this is due to the trapezoidal shape.

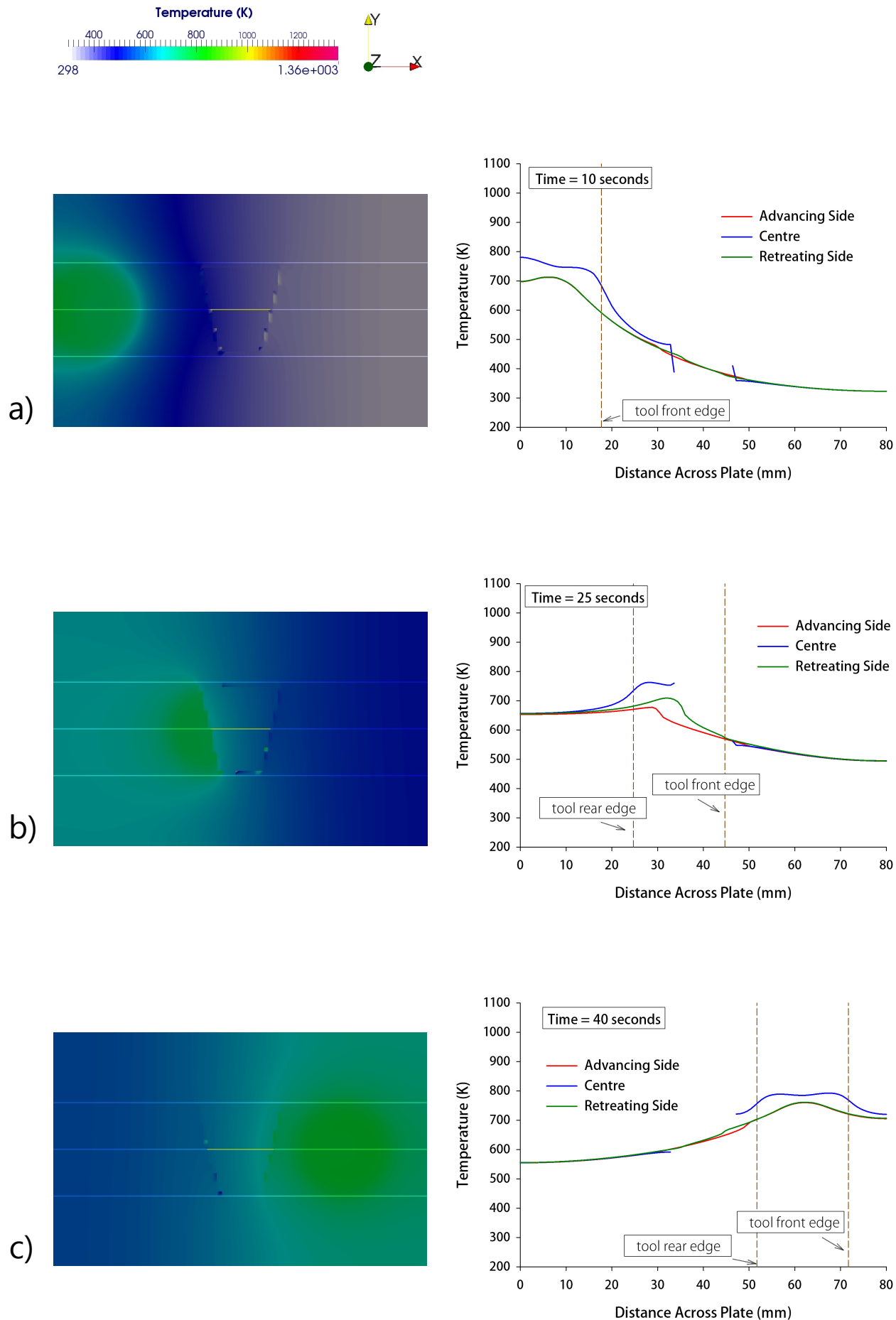


Figure 4.8: Temperature 1mm below the surface at times of a) 10s, b) 25s, c) 40s. Left image is the temperature across the slice, right is the temperature across each line on the advancing, centre and retreating sides.

4.5.1.3 The Effect of Air Convection on Calculated Thermal Profiles

The assumption of a lumped backing plate convection coefficient allows for the removal of heat loss boundary conditions on other surfaces (such as air convection boundary conditions). Although these convection losses are easily implemented in a thermal model, some inconsistency can arise when particles are free to move, for two reasons - as the boundary condition is applied to nodal positions, displaced particles may not have the same convective value, also the surface of the top layer is difficult to define after processing. However, the effect of a lumped convection coefficient has not been tested - and this is the purpose of this section. Figure 4.9 shows temperature at each of the thermocouple positions for a lumped convection boundary condition versus the same simulation run with a (reduced) backing plate convection coefficient and air convection ($15\text{W/m}^2\text{K}$) on each of the other surfaces. The total rate of thermal energy loss is the same for each simulation, as determined from experimental data.

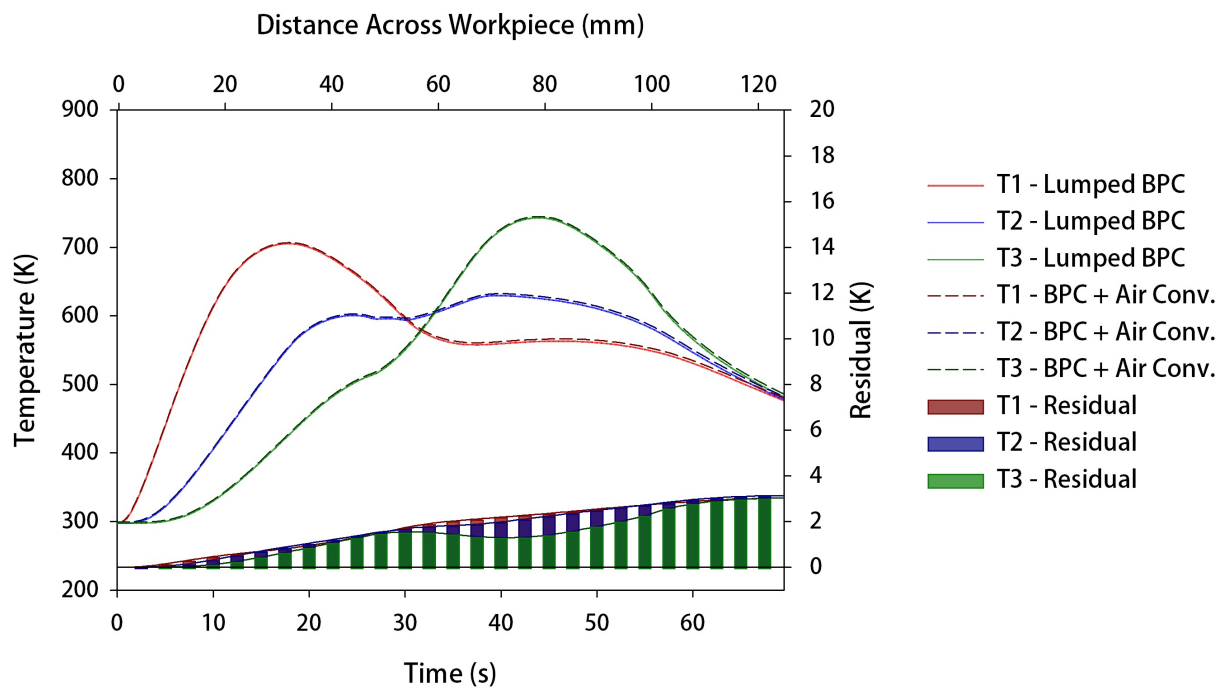


Figure 4.9: Temperature profile over time for T1, T2 and T3 for both the lumped backing plate convection coefficient and BPC + Air Convection.

Figure 4.9 shows that the effect of the lumped backing plate convection coefficient is negligible at the thermocouple locations. The difference in Kelvin (shown by the residual), ranges up to $\sim 3^\circ\text{K}$ for each location over the simulation.

Similarly, Figure 4.10 compares surface temperature profiles 1mm below the surface for the advancing side, centre and retreating side. It shows temperature differentials of up to $\sim 2^\circ\text{K}$, and given the magnitude of temperatures confirms that the assumption of a lumped heat loss at the backing plate is reasonable.

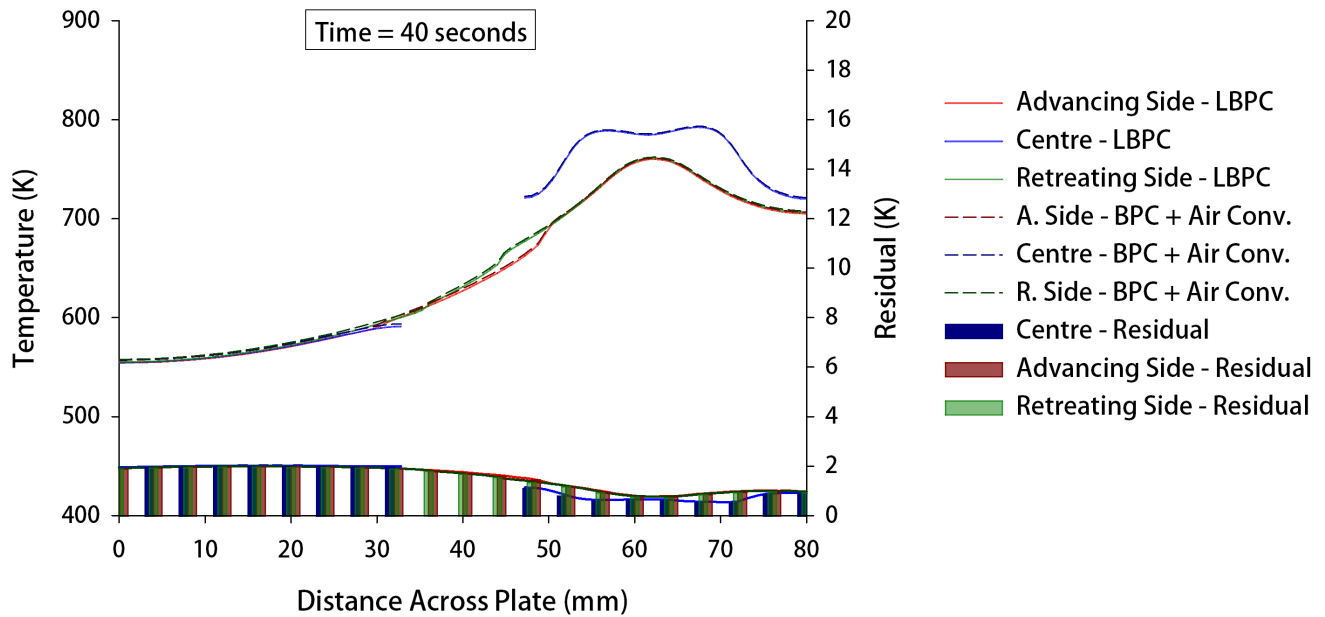


Figure 4.10: Temperature profile 1mm below the surface for both the lumped backing plate convection coefficient and BPC + Air Convection, 40 seconds into the simulation.

4.6 Conclusion

In this chapter, an MPM model of FSP heat transfer was described. The heat input was imposed by moving a self-regulating heat source achieved by a temperature dependent shear stress. The other sources of heat transfer were modelled by means of convective boundary conditions and energy loss coefficients. The results obtained with the calibrated shear stress model agree well with the experimental data, demonstrating that the model can be used to gain insights into FSP.

The model was checked to observe the effect of air convection and a lumped backing plate convection coefficient. It was found that air convection had negligible impact on the temperature profiles in comparison to a lumped heat loss through the backing plate. Thus a lumped backing plate convection coefficient will be applied in each of the FSP models.

Although the thermal model makes adequate predictions for the thermal response, it provides no information on the mechanical behaviour of the material, including the ability to resolve differences in temperature between the advancing and retreating sides. In the next chapter, the model will be expanded to incorporate a coupled thermo-mechanical model - taking advantage of MPM's particle based formulation and natural management of large deformations. This will enable more sophisticated thermal boundary conditions based on the mechanical interaction between the workpiece and the tool, and also provide the basis for analysis of flashing and cavity flow, in addition to the thermal field.

Chapter 5

Thermo-mechanical Modelling of Friction Stir Processing

5.1 Introduction

In the previous chapter, a thermal model of FSP was presented. In this chapter, the thermal model will be further developed into a fully coupled thermo-mechanical model, thus allowing for more accurate and detailed simulations - vital if optimisation and faster experimental results at reduced cost is to be achieved.

The generation of heat will no longer be reliant on a calibrated shear stress, but rather due to the combined effect of frictional contact and plastic dissipation, in part determined from a constitutive law. The coupling between the thermal and mechanical solution means that the effects of temperature as well as strain and strain rate can be analysed concurrently.

As an initial starting point for determining the material behaviour, the Johnson-Cook constitutive model will be used, which has been applied previously for simulation of FSP [67]. Widely applied to many solid mechanics problems, it is a natural choice for comparison to more complex material models. This constitutive model will determine the stress field resulting from the mechanical forces, which in turn is used to calculate the thermal response due to friction and plastic deformation.

The addition of a mechanical component also means more processing conditions can be investigated, for example tool angle and penetration depth. These processing parameters will now have a direct impact on the thermal and mechanical response. This addition requires introduction of mechanical boundary conditions, which will be discussed.

The chapter begins by discussing the numerical model, the applied constitutive law, how thermal energy caused by friction and plastic deformation is calculated, and the additional boundary conditions. Following from this is an investigation into the effect of mass scaling on FSP. Finally the outcomes of the thermo-mechanical model are presented in terms of both temperature and material flow.

5.2 Description of the Thermo-mechanical Model

In the numerical model, the workpiece is defined as an elastoplastic solid and the tool as a rigid body. The rigid tool has the same dimensions as the experimental tool (see Figure 4.1), but the concave face has been ignored and a simpler flat surface assumed. Figure 5.1 shows the model as defined in NairnMPM. The red particles define the copper plate and the blue particles the rigid tool. The model incorporates the initial tool angle of 3° . The entire simulation consists of 391,576 particles with a particle separation of 0.5 mm. The constitutive law and a detailed explanation of the boundary conditions can be found in the following sections.

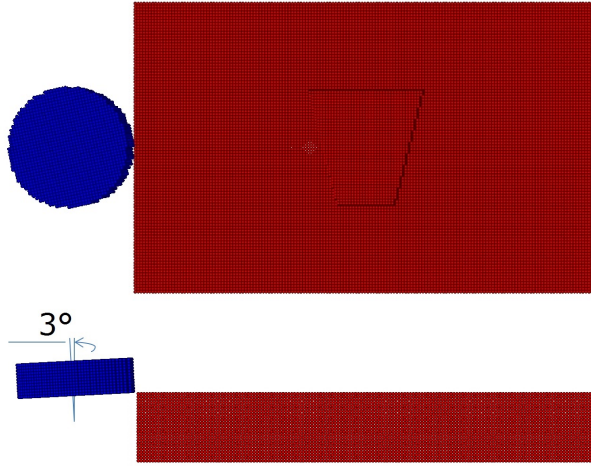


Figure 5.1: Initial set-up of numerical model.

5.2.1 Constitutive Law

5.2.1.1 Johnson-Cook Model

As mentioned in the literature review, this constitutive model was originally developed [151] as a material model easily implemented into numerical computations, also incorporating strain, strain rate and temperature dependence.

$$\sigma_y = (A + B(\bar{\epsilon}^p)^n) \left(1 + C \ln \frac{\dot{\epsilon}^p}{\dot{\epsilon}_0} \right) \left(1 - \left(\frac{T - T_{\text{room}}}{T_{\text{melt}} - T_{\text{room}}} \right)^m \right) \quad (5.1)$$

where σ_y is the flow stress, $\bar{\epsilon}^p$ is the equivalent von Mises plastic strain, $\dot{\epsilon}^p$ is the equivalent von Mises plastic strain rate, $\dot{\epsilon}_0$ is the normalising or reference strain rate, T is the current material temperature. A is the initial yield stress of the undeformed material, B and n are material constants describing the strain hardening, while C provides the material sensitivity to plastic strain rate. The last term in equation (5.1) represents the temperature dependence with T_{melt} and T_{room} denoting the melting temperature and room temperature, respectively.

The parameters applied are shown in Table 5.1.

Parameter	Copper
Density, ρ (kg/m ³)	8960
Young's modulus, E (GPa)	124
Poisson's ratio, ν	0.34
A (MPa)	90
B (MPa)	292
n	0.31
C	0.025
m	1.09
Reference strain rate, $\dot{\epsilon}_0$ (s ⁻¹)	1
Melting temperature, T_{melt} (K)	1356
Room temperature, T_{room} (K)	298

Table 5.1: Johnson-Cook parameters for copper [151].

5.2.2 Calculation of Heat Generation

5.2.2.1 Heat Dissipation Resulting from Frictional Contact Between FSP Tool and Work-piece

As an alternative to the analytical function based on input power for heat generation (see Chapter 4), a friction heating law can be used to determine the heat input as a result of the frictional contact between the tool and the workpiece. In order to fully describe this, it is important to know how contact is controlled in MPM, as this provides the framework within which frictional heating is implemented.

This has been explained in a previous chapter (see Chapter 3), recall that with the assumption of a sticking condition, normal and tangential forces are:

$$\mathbf{f}_n = \frac{(\Delta \mathbf{p}_a \cdot \hat{\mathbf{n}})}{\Delta t} \hat{\mathbf{n}} \quad \text{and} \quad \mathbf{f}_t = \frac{(\Delta \mathbf{p}_a \cdot \hat{\mathbf{t}})}{\Delta t} \hat{\mathbf{t}} \quad (5.2)$$

where Δt is time step and $\hat{\mathbf{t}}$ is unit vector in the tangential direction of motion. The positive normal contact force is then $\mathbf{f}_n = -(\Delta \mathbf{p}_a \cdot \hat{\mathbf{n}})/\Delta t$ and the positive sliding force is $\mathbf{f}_t = (\Delta \mathbf{p}_a \cdot \hat{\mathbf{t}})/\Delta t$.

If Coulomb friction is assumed, then for $|\mathbf{f}_t| < \mu |\mathbf{f}_n|$ the objects will stick. Otherwise, the object is sliding and the tangential force is converted into a frictional force, $\mu |\mathbf{f}_n|$, keeping in mind the objects still stick in the normal direction.

$$\mathbf{f}_t = (\mu |\mathbf{f}_n|) \hat{\mathbf{t}} \quad (5.3)$$

The energy thus converted into heat (applied when $|\mathbf{f}_t| > \mu |\mathbf{f}_n|$) is therefore:

$$E_f = |\mathbf{f}_t \cdot (\mathbf{v}_o - \mathbf{v}_i)| \Delta t \quad (5.4)$$

where E_f is the total thermal energy from friction (J), \mathbf{f}_t is the tangential contact force, and \mathbf{v}_o and \mathbf{v}_i represent the velocity of the tool and workpiece, respectively, in the sliding direction. The temperature increment can then be determined according to equation (5.5):

$$\Delta T = \frac{|\mathbf{f}_t \cdot (\mathbf{v}_o - \mathbf{v}_i)|}{\rho C_v} \Delta t \quad (5.5)$$

where ΔT is the temperature increment, ρ is the material density and C_v its specific heat capacity.

5.2.2.2 Heat Dissipation Resulting from Plastic Deformation of the FSP Workpiece

Due to the large material deformation and forces applied during FSP, heat resulting from plastic deformation cannot be ignored. The relation for the volumetric thermal energy resulting from plastic deformation, E_p (J/m^3), is shown in equation (5.6).

$$E_p = \eta \boldsymbol{\sigma} : \dot{\boldsymbol{\epsilon}} \Delta t \quad (5.6)$$

where $\dot{\boldsymbol{\epsilon}}$ is the strain rate tensor and η is the coefficient characterising the fraction of plastic work dissipated as heat. It is generally accepted that approximately 90% of the energy dissipated during plastic deformation is transformed into thermal energy [126], the remaining 10% being stored within the material in the form of defects such as dislocations. From the relation for thermal energy resulting plastic deformation, the change in temperature can be determined from the material properties, as shown in equation (5.7).

$$\Delta T = \eta \frac{\boldsymbol{\sigma} : \dot{\boldsymbol{\epsilon}}}{\rho C_v} \Delta t \quad (5.7)$$

5.2.3 Establishing the Mechanical Boundary Conditions

As explained in the previous chapters, a number of boundary conditions (BCs) are applied to model FSP. The mechanical boundary conditions, not discussed in the previous thermal model chapter, are explained in detail below.

5.2.3.1 Friction Coefficient Value for the Tool and Workpiece

In previously published work, a friction coefficient has been chosen that lies within the reasonable range of known metal to metal contact coefficients [114]. In this work, this estimation of a constant friction coefficient will be guided by experiment. A series of observations were made with the coefficient of friction tester, Model C0008, from IDM Instruments Pty Ltd. The copper and tool steel material were machined to the required geometries and forces calculated for translational movement of one material upon the other. From this data the coefficient of friction was determined.

Tool steel was machined into a block, such that it could be mounted onto a copper plate. The copper plate was moved while the steel block was held in place and the force of resistance upon the steel block was measured. Two different translational speeds were applied, 60mm/min and 120mm/min. The result for 10 seconds of runtime for the 120mm/min are shown in Figure 5.2.

Temporal averages of the friction coefficient for each run are shown in Table 5.2.

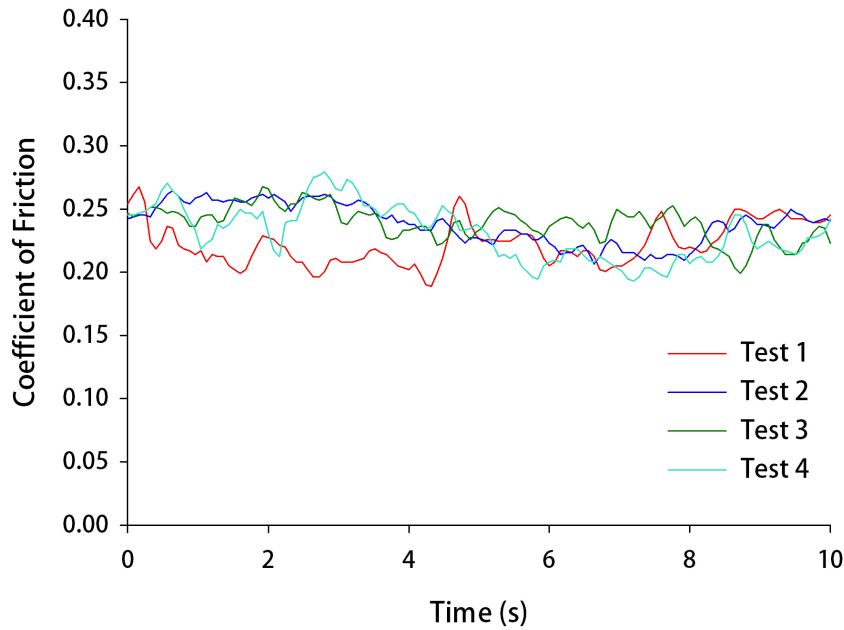


Figure 5.2: Plot of experimentally determined coefficient of friction over time (10s) for translation speed of 120mm/min.

Speed	Test 1	Test 2	Test 3	Test 4	Average
60mm/min	0.21	0.22	0.24	0.23	0.23
120mm/min	0.22	0.25	0.22	0.22	0.23

Table 5.2: Temporal averages of the friction coefficient for Tests 1-4 at speeds of 60mm/min and 120mm/min.

The average for both speeds is 0.23, and the coefficient applied in this work was rounded to 0.2. It is noted that an improvement could be made by conducting a sensitivity analysis of the coefficient of friction upon the numerical model, and should be applied in future work.

5.2.3.2 Clamping

Two boundary conditions are applied to the bottom surface of the workpiece. The first is to model the fixing created by the clamps, the second to reproduce the loss of heat into the backing plate. The latter has been explained in the previous chapter.

To avoid movement of the copper plate during processing, an acceleration condition is applied to its bottom layer of material points. This boundary condition overrides any calculated acceleration from loads or forces. This is achieved simply by assigning those particles an initial velocity of zero, and then an acceleration of zero at each time-step.

5.2.3.3 Tool Angle and 3D Rotation

During FSP, a rotating tool traverses the workpiece, providing the energy for the thermo-mechanical processes that take place, simultaneously ensuring no material leaves the plate

surface. To avoid build up of material and high torque on the tool axis, the tool is initially rotated 3° away from the processing direction.

On a technical note, as the tool angle is small relative to the grid or cell size, it is better to define the tool particles in a vertical position, and apply a translation to the rigid body during the simulation. This initial rotation for the tool position is implemented via a velocity term as a function of position and time. With a vertical tool, the initial tool rotation is in two dimensions, the vertical plane (z) and the plane parallel to the processing direction (x). The applied velocity is a function of the radial distance from the centre and the angular velocity, which split into their two components in x and z are as follows:

$$v_x = r_x \omega = (x - x_0) \omega \quad (5.8)$$

$$v_z = r_z \omega = (z - z_0) \omega \quad (5.9)$$

where ω is in radians per second.

The tool rotation during processing occurs on the rotated tool axis and is not perpendicular to the global axis in x or z. The rotation about an axis specified by a unit vector, \hat{u} , can be defined as follows:

$$\mathbf{R} = \begin{bmatrix} \cos\theta + u_x^2(1 - \cos\theta) & u_x u_y(1 - \cos\theta) - u_z \sin\theta & u_x u_z(1 - \cos\theta) + u_y \sin\theta \\ u_y u_x(1 - \cos\theta) + u_z \sin\theta & \cos\theta + u_y^2(1 - \cos\theta) & u_y u_z(1 - \cos\theta) - u_x \sin\theta \\ u_z u_x(1 - \cos\theta) - u_y \sin\theta & u_z u_y(1 - \cos\theta) + u_x \sin\theta & \cos\theta + u_z^2(1 - \cos\theta) \end{bmatrix}$$

where $\hat{u} = u_x + u_y + u_z$ and $u_x^2 + u_y^2 + u_z^2 = 1$

As there is no change in the y component of the axis of rotation, the rotation matrix simplifies to:

$$\mathbf{R} = \begin{bmatrix} \cos\theta + u_x^2(1 - \cos\theta) & -u_z \sin\theta & u_x u_z(1 - \cos\theta) \\ u_z \sin\theta & \cos\theta & -u_x \sin\theta \\ u_z u_x(1 - \cos\theta) & u_x \sin\theta & \cos\theta + u_z^2(1 - \cos\theta) \end{bmatrix}$$

Although this provides the rotational velocity, implemented in an incremental update, it results in the growth of small errors over time and expansion of the rigid body. There is a simple way to overcome this, which is to use an "effective velocity" rather than the instantaneous tangential velocity. This transforms the velocity into essentially a position update.

Looking at the problem in two-dimensions, if a particle's position relative to a centre point is $(x - x_0, y - y_0) = (r \cos \theta, r \sin \theta)$, the end position after an increment of rotation would be $(r \cos(\theta + d\theta), r \sin(\theta + d\theta))$, where the increment $d\theta = 2\pi\omega\Delta t$. The effective velocity is then calculated with:

$$v_{\text{eff}} = \frac{r}{\Delta t} (\cos(\theta + d\theta) - \cos \theta, \sin(\theta + d\theta) - \sin \theta) \quad (5.10)$$

where r is the radial distance. If we were looking at translation in the x and y direction, this would become:

$$v_x = \frac{1}{\Delta t}((x - x_0)(\cos(2\pi\omega\Delta t) - 1) - (y - y_0)\sin(2\pi\omega\Delta t)) \quad (5.11)$$

$$v_y = \frac{1}{\Delta t}((x - x_0)\sin(2\pi\omega\Delta t) - (y - y_0)(\cos(2\pi\omega\Delta t) - 1)) \quad (5.12)$$

Thus the above rotation matrix can be modified for an effective velocity update.

$$\begin{bmatrix} v_{x,eff} \\ v_{y,eff} \\ v_{z,eff} \end{bmatrix} = \begin{bmatrix} \cos\theta + u_x^2(1 - \cos\theta) - 1 & -u_z\sin\theta & u_x u_z(1 - \cos\theta) \\ u_z\sin\theta & \cos\theta - 1 & -u_x\sin\theta \\ u_z u_x(1 - \cos\theta) & u_x\sin\theta & \cos\theta + u_z^2(1 - \cos\theta) - 1 \end{bmatrix} \begin{bmatrix} (x - x_0) \\ (y - y_0) \\ (z - z_0) \end{bmatrix} \frac{1}{\Delta t}$$

where $u_x = -\sin\phi$ and $u_z = \cos\phi$, where ϕ is the initial inclination of the tool.

5.3 Implementing Effective Mass Scaling to Reduce Computation Time

This section will discuss and analyse mass scaling (as described in the literature review) and its effects on FSP simulation.

5.3.1 The Limiting Condition on the Timestep

The Courant-Freidrichs-Lewy condition (CFL) [127] determines a limit on the critical time interval based on the time it takes for a stress or thermal wave to move from one cell or node to the next, thus it describes a timestep for accurately capturing evolution of field variables. It is shown in equation (5.13) below:

$$\Delta t = \frac{d}{c_d} \quad (5.13)$$

where d is the minimum cell size or distance between nodes, and c_d is the speed of the wave through the material. For an elastic material in MPM the stress wave speed, $c_{d, \text{stress}}$, is shown in equation 5.14.

$$c_{d, \text{stress}} = \sqrt{\frac{K + \frac{4G}{3}}{\rho}} \quad (5.14)$$

Using the definition in equation 5.13, it can be seen that decreasing the stress wave speed can reduce the restriction on the timestep. One way of doing this is to artificially increase the density. This is termed mass scaling and has been applied in the literature to a number of models in Friction Stir techniques. Some example mass scales used in previously published works include [152] which applied a scaling factor of 10^7 , [67] which applied 10^6 , and [153] which used 10^9 . This method slows down the stress wave propagation speed and while

allowing for larger time scales, can influence the dynamics of the material flow and the nature of the contact at the interface of the tool and workpiece.

Mass scaling can be implemented in NairnMPM in the following way. If we let χ_{ms} be the scaling factor applied to artificially increase the density, the specific heat capacity C_v is reduced by the same factor, as shown in equation (5.15). In this way the product of ρC_v is maintained and there is no effect on the dissipation of heat (as defined in Chapter 3).

$$C_{v_{ms}} = \frac{1}{\chi_{ms}} C_{v_{copper}} \text{ and } \rho_{ms} = \chi_{ms} \rho_{copper} \quad (5.15)$$

where $C_{v_{ms}}$ and ρ_{ms} are the adjusted specific heat capacity and density respectively for use in mass scaled simulations.

In NairnMPM a uniform cell size is assumed. As a result of this, the entirety of the copper workpiece will include the mass scaling factor, χ_{ms} . This will have the benefit of reducing computation time, however introduces the possibility of artificial inertial effects. To avoid this, the kinetic energy must be monitored carefully. The following sections will analyse the effects of mass scaling on the FSP model.

5.3.2 The Effect of Mass Scaling on the Kinetic Energy of the Workpiece

Figure 5.3 shows the total kinetic energy of the workpiece over the first 20 seconds of simulation at different mass scales, $\chi_{ms} = 10^4$ to $\chi_{ms} = 10^7$.

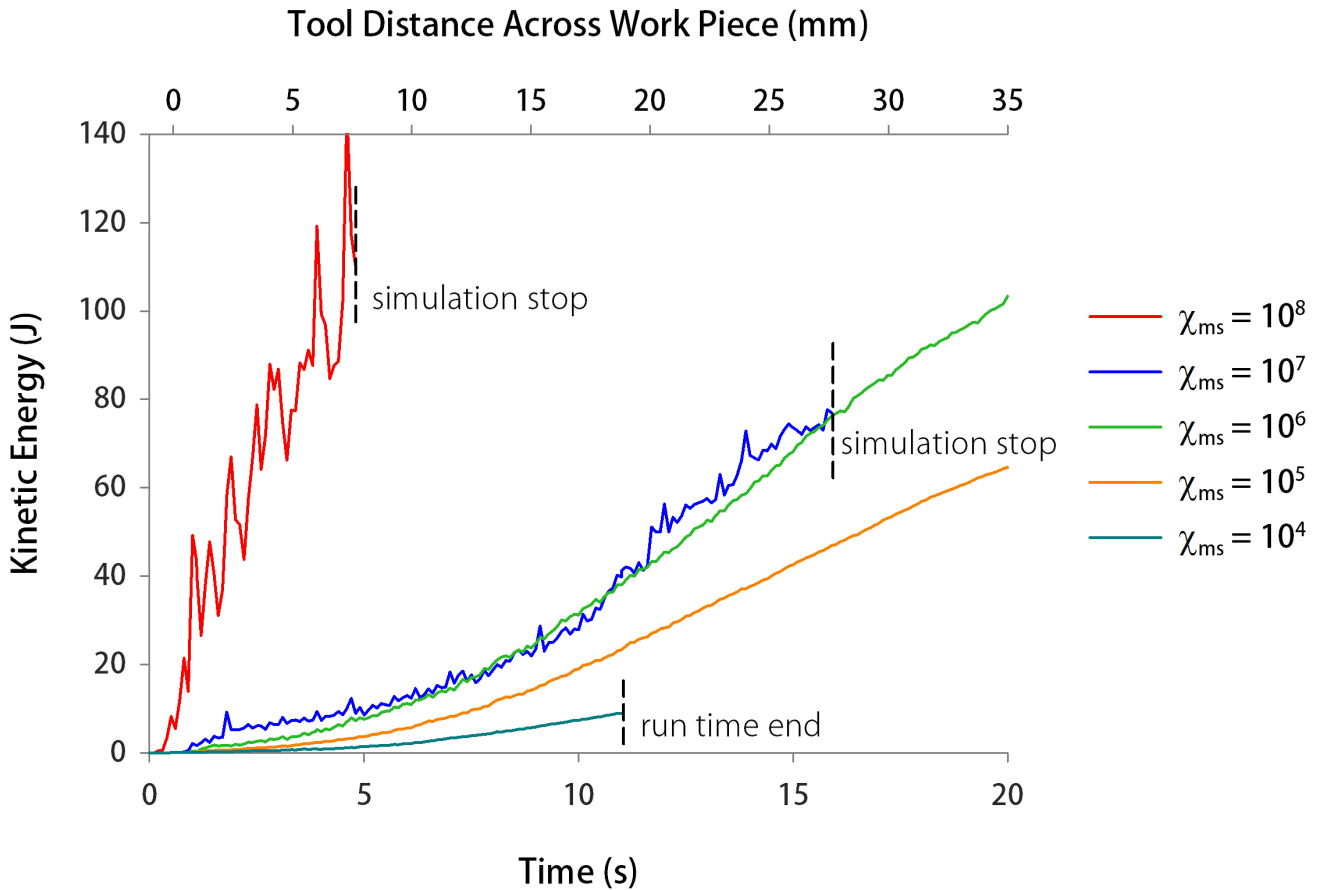


Figure 5.3: Kinetic energies over the first 20 seconds of simulation for $\chi_{ms} = 10^4$ to $\chi_{ms} = 10^7$.

It is clear that the amount of kinetic energy in the workpiece increases as the mass scaling factor, χ_{ms} , increases. The figure also shows that the simulation becomes unstable with mass scales of $\chi_{ms} = 10^7$ and above, indicated by the large fluctuations in kinetic energy. The 'simulation stop' refers to crashes resulting from this unstable kinetic energy. The 'run time end' indicates that the simulation was taking an impractical amount of time and was force stopped. In a number of articles [67, 71] it is argued that as long as the kinetic energy is below 1% of the internal energy, the mass scaling will not alter the mechanical portion of the solution.

$$\frac{\text{Kinetic Energy}}{\text{1\% Internal Energy}} < 1 \quad (5.16)$$

Figure 5.4 shows the kinetic energy and 1% of internal energy for mass scaling of $\chi_{ms} = 10^8$ and $\chi_{ms} = 10^7$. The plot shows that the kinetic energy is always above 1% of the internal energy for $\chi_{ms} = 10^8$ and below it for all but one point in $\chi_{ms} = 10^7$. Given the large instability in kinetic energy observed for $\chi_{ms} = 10^8$ this result seems consistent with the energy criteria, however for $\chi_{ms} = 10^7$ Figure 5.4 would indicate stability.

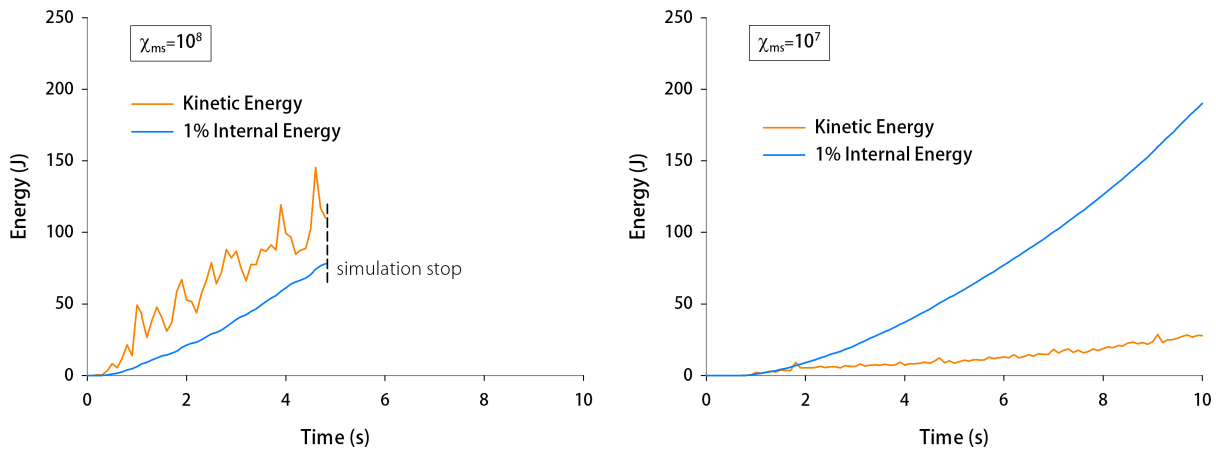


Figure 5.4: The kinetic energy and 1% of internal energy for mass scaling of (left) $\chi_{ms} = 10^8$, and (right) $\chi_{ms} = 10^7$.

To investigate this further, an additional region to consider is at the interface of the tool and workpiece. Figure 5.5 shows a plane section parallel to this interface on the material workpiece. The following sections will discuss the effect on this region for different parameters and mass scales for comparison of mass scale effects.

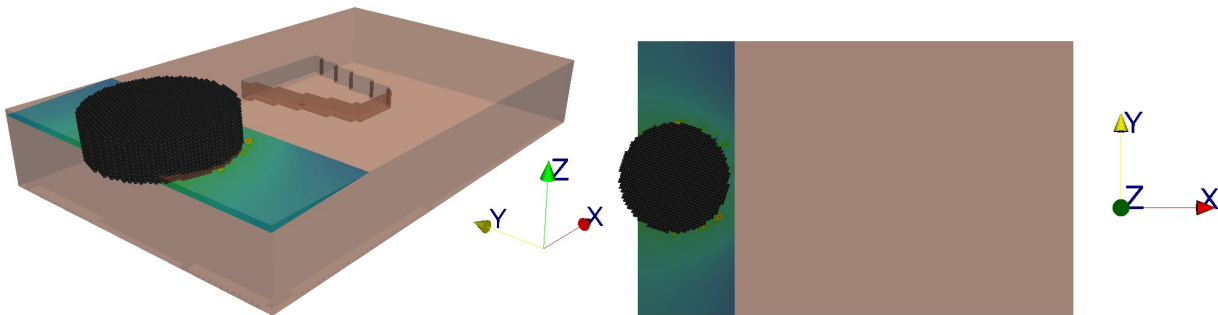


Figure 5.5: Plane section 10 seconds into simulation at the tool / workpiece interface. Axis orientation as shown for reference. Processing in the positive x-direction.

5.3.3 The Effect of Mass Scaling on Material Displacement in the Workpiece

Table 5.6 shows the material displacement around the tool 10 seconds into the simulation, in the x, y and z directions respectively. In the x and y directions, in general, there is an increased material flow as the mass scale increases, which is consistent with the increase in kinetic energy shown by Figure 5.3. In the z direction, the flow upward (out of the plate) increases as the mass scale increases, however the flow downward is reduced. The white sections, formed particularly for $\chi_{ms} = 10^7$, indicate regions where there are no material points, that is the material points have been pushed away leaving a numerical gap. These do not necessarily indicate a physical gap or cavity, but they are a problem for analysis due to the lack of data they represent.

A comparison of material flow at the surface can be observed in Figure 5.7, which shows that there is a very noticeable increase in material movement with increasing mass scale. Note that all these mass scales are within the energy criteria described by equation (5.16).

5.3.4 The Effect of Mass Scaling on the Temperature of the Workpiece

It has been argued that mass scaling does not alter the amount of heat generated from plastic dissipation and frictional slip [71]. However, Figure 5.8 shows the average plate temperature over time for the first 20 seconds of simulation. The plot shows that despite increasing kinetic energy as mass scaling increases, the temperature of the plate is greatest for the smallest mass scale, $\chi_{ms} = 10^4$. It looks as though $\chi_{ms} = 10^7$ is beginning to drop and would likely appear lower than $\chi_{ms} = 10^6$ at 20 seconds. In general it appears as though temperature is increasing as mass scale decreases, which itself is not an intuitive result. This dependence is further investigated below.

Table 5.9 shows the temperature distribution at the tool / workpiece interface. It shows that the greatest temperatures are reached when $\chi_{ms} = 10^7$, where the only areas of melting are produced. However the differences between $\chi_{ms} = 10^4$, $\chi_{ms} = 10^5$ and $\chi_{ms} = 10^6$ is less apparent. One observation is that the temperature seems to have the greatest homogeneity at $\chi_{ms} = 10^4$, with the temperature at the interface of the back half of the tool experiencing about 800-1000K. The trend toward higher equivalent stresses with greater mass scaling similarly suggests greater temperatures at the interface due to plastic dissipation. This table of results however, do not seem to correlate with Figure 5.8, where $\chi_{ms} = 10^4$ produces consistently greater plate temperature than the higher mass scales, in particular $\chi_{ms} = 10^7$.

To investigate this, Figure 5.10 shows three slices taken for an average value of temperature over time and area. The temperatures across the slice are averaged at each time step and plotted over time. The area was determined such that it be larger than the contact interface of the tool with the workpiece. The results are presented in Figure 5.11. It indicates that although higher temperatures are experienced on the surface at higher mass scaling, heat conducts through the plate more effectively at a lower mass scale. One explanation is that the large material movement attributed to the high mass scale, reduces the ability of the particles to conduct heat through to the rest of the plate. Again this can be highlighted by Figure 5.7 where more particles can be seen exiting the plate with increasing mass scale. Going back to Figure 5.8, the deviation for $\chi_{ms} = 10^7$ could be due to the movement of particles and lack of consistent heating of those material points.

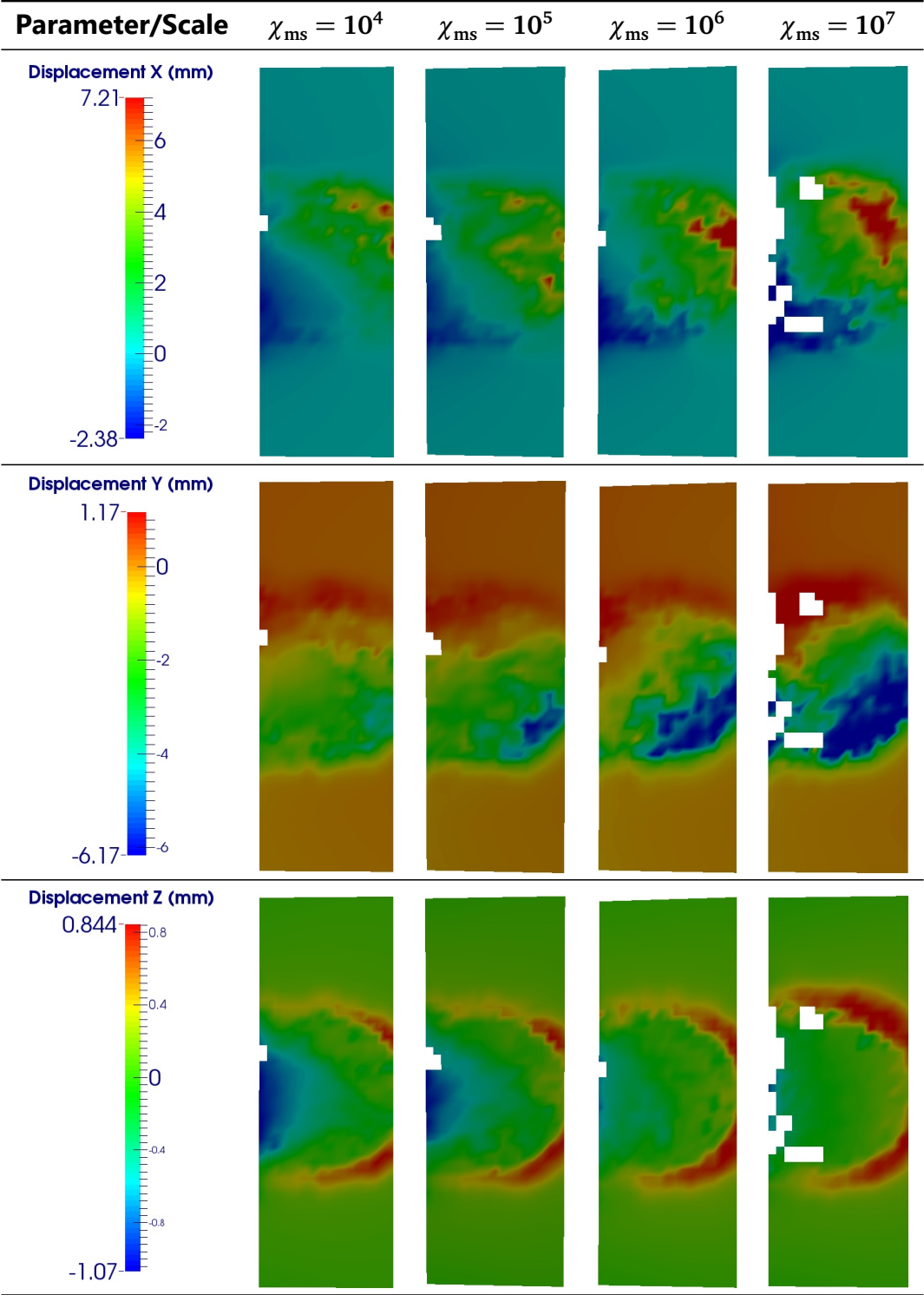


Figure 5.6: Material displacements at the tool/workpiece interface 10 seconds into the simulation for mass scaling factors of 10^4 , 10^5 , 10^6 and 10^7 .

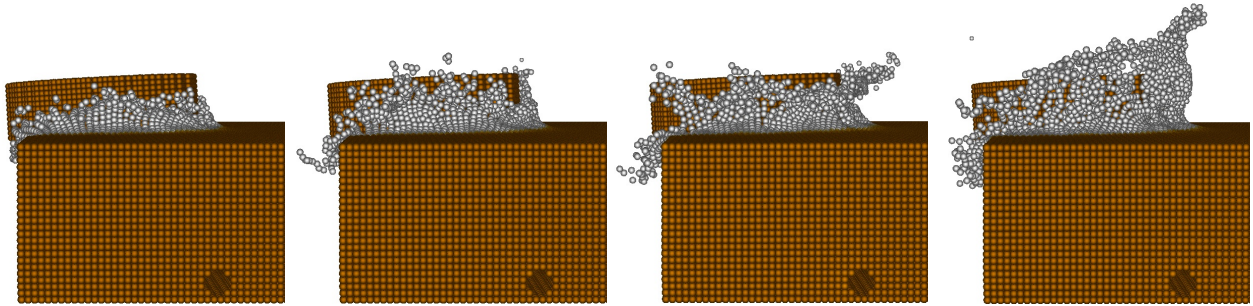


Figure 5.7: Material flow around the tool at a range of mass scaling factors (10 seconds into the simulation); from left to right, $\chi_{ms} = 10^4$, $\chi_{ms} = 10^5$, $\chi_{ms} = 10^6$ and $\chi_{ms} = 10^7$.

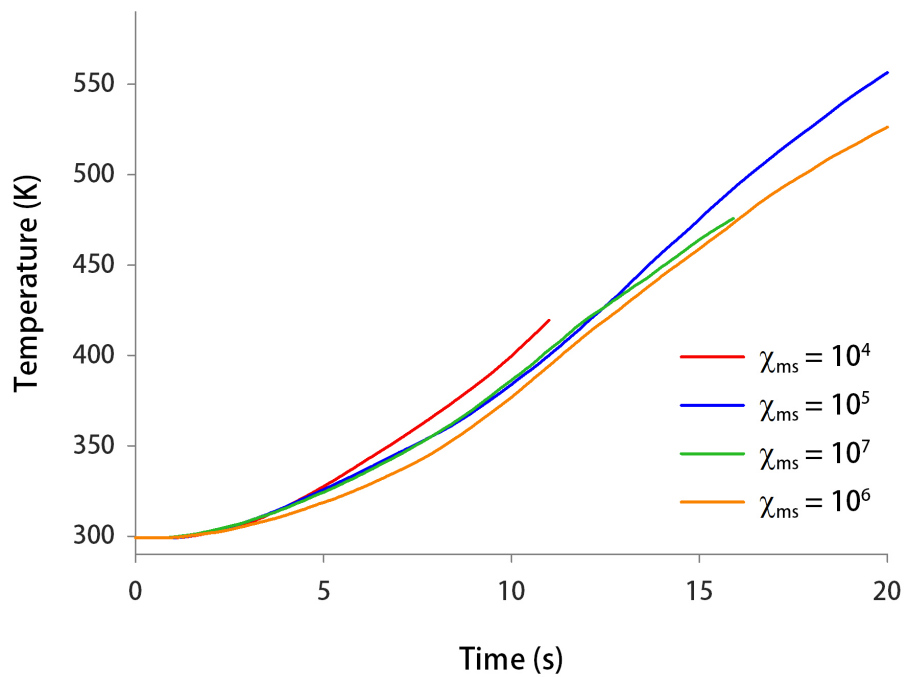


Figure 5.8: Average temperature for the copper plate over the first 20 seconds of simulation for $\chi_{ms} = 10^4$ to $\chi_{ms} = 10^7$.

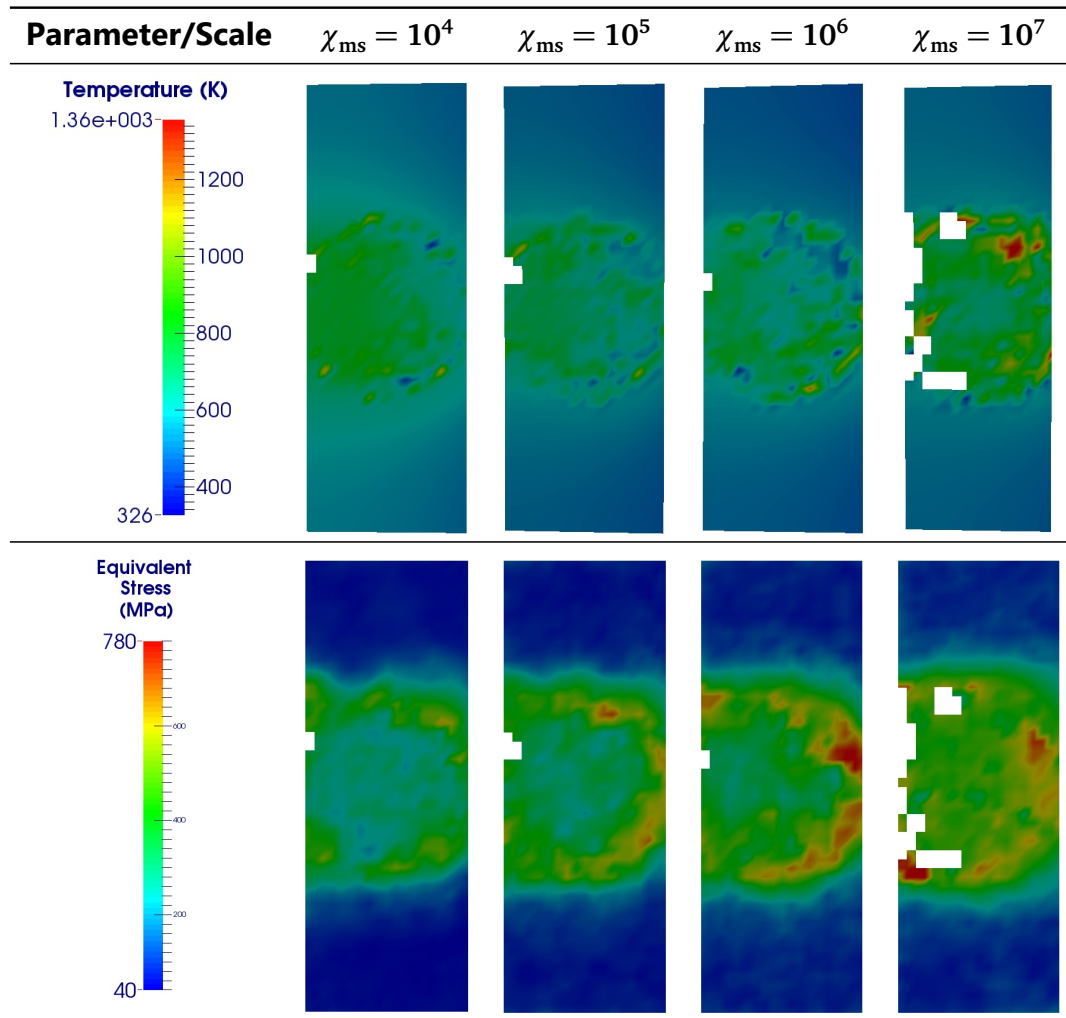


Figure 5.9: Temperature followed by equivalent stress at the tool/workpiece interface 10 seconds into the simulation for mass scaling factors of 10^4 , 10^5 , 10^6 and 10^7 .

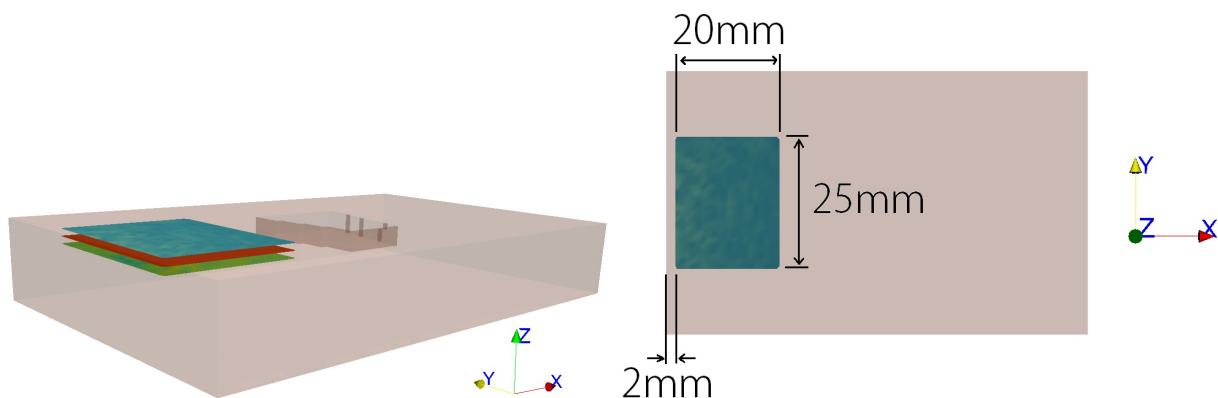


Figure 5.10: Surface area used for calculating the average temperature over both area and time, slices (blue, red, green) are 0mm, 1mm and 2mm from the surface, respectively.

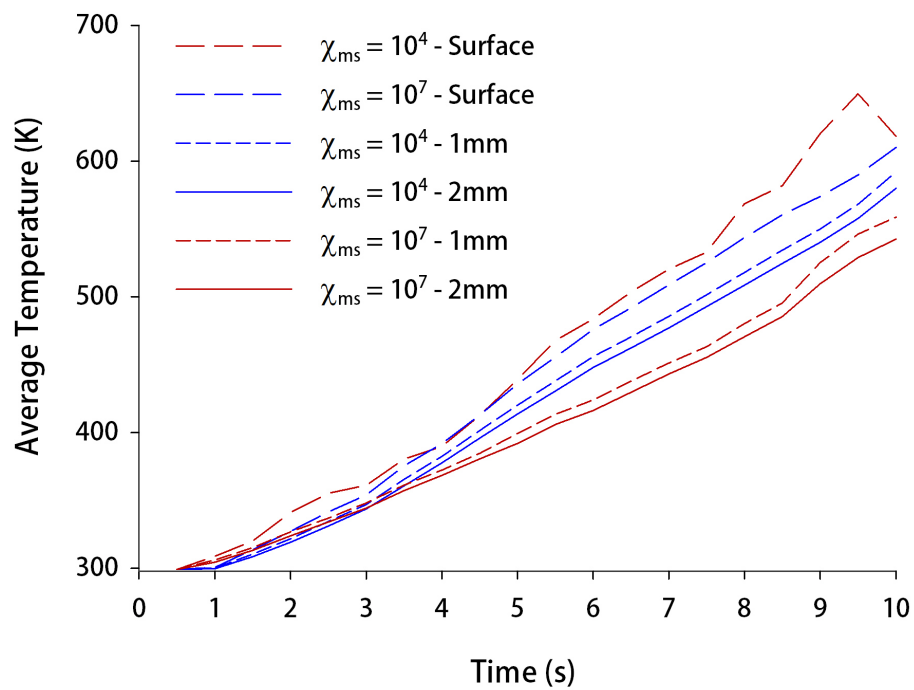


Figure 5.11: The average temperature over time and area for $\chi_{ms} = 10^4$ and $\chi_{ms} = 10^7$ at depths of 2mm, 1mm and at the surface of the copper plate.

5.3.5 Summarising the Effect of Mass Scaling on Simulation of FSP

The previous sections showed that at increased mass scales the kinetic energy of the workpiece increased. At $\chi_{ms} = 10^7$ and below the kinetic energy was under the given threshold applied in literature (1% of internal energy) however large variation was found in material flow. Further investigation showed larger material displacement and greater stresses at the tool / workpiece interface for greater mass scales. It also revealed that although greater temperatures are produced at greater mass scales, the increased material flow reduced the effectiveness of the thermal dissipation through the rest of the plate, resulting in greater localised heating and melting.

In order to balance the negative effects of mass scaling with the need for faster computation a compromise is required. In this case the compromise is $\chi_{ms} = 10^5$, which reduces the negative effects of mass scaling to an acceptable margin while allowing a reasonable time for computation. The next section will discuss the results acquired applying this mass scaling factor.

5.4 Comparison of Experiment with the Obtained Thermo-mechanical Model of FSP

5.4.1 Resulting Temperature Field

5.4.1.1 Comparison of Calculated Temperature Profile with the Experimental Result

Figure 5.12 shows the resulting temperature profiles for thermocouple positions T1, T2 and T3. The vertical dashed lines highlight notable positions of the tool relative to the plate during processing, linking them to the corresponding times that they occur.

The model predicts a drop in temperature as the tool passes over the cavity, and subsequent cooling after the tools leaves the workpiece. Compared against the experimental temperature readings shown in Figure 5.13, the overall trend is captured quite well at all three locations. The model reflects the drop in temperature for each thermocouple as the tool passes over the cavity. T1 (thermocouple 1) in red over-predicts the initial peak by about 11%, and under-predicts the secondary peak by approximately 8%. The rate of heat loss for T1 also compares well. In T2 there is again an over-prediction of the temperature (by about 5%) and an under-prediction of the secondary peak (of about 3%). T3 shows a less defined primary peak with the secondary peak error being approximately 8%. The trend to over-predict the initial temperature and under-predict the post cavity temperature seem to indicate that the heat generated by the tool is too high and that the heat loss through the backing plate is too aggressive. Although T3 may seem to have the reverse trend, the secondary peak is where the tool actually passes that thermocouple, and the over-prediction of heat is consistent with the previous analysis.

5.4.1.2 Analysis of Surface Temperature

Figure 5.14 shows the temperature along the three parallel lines across the plate at a depth of 1mm from the surface. The three lines represent areas corresponding to the advancing

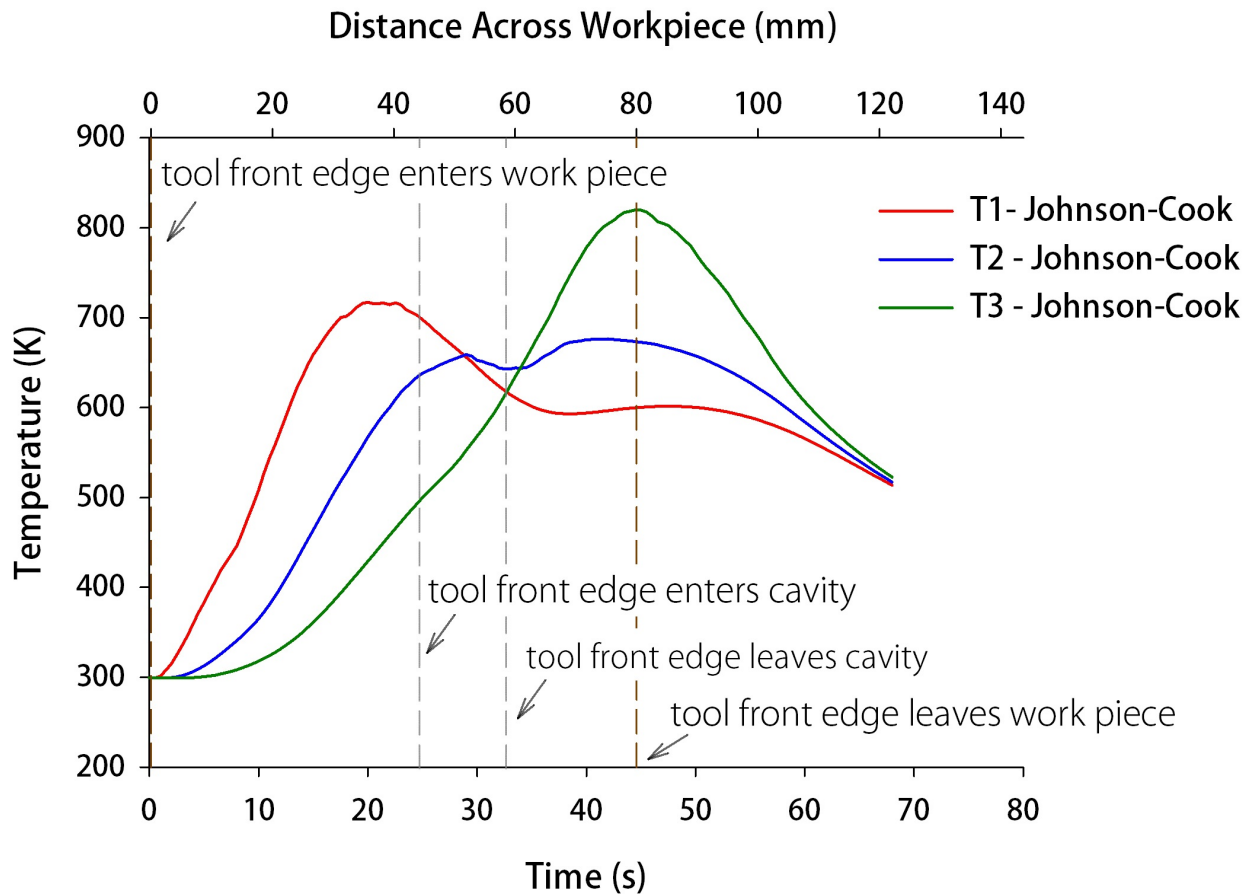


Figure 5.12: Temperature profile over time for thermocouple locations T1, T2 and T3.

side, retreating side and centre line. The advancing and retreating lines run along the edge of the tool, that is they are 10mm either side of the centre line of the plate.

The plots show the area bounded by the tool, and in each case the peak temperature is located close to or at the rear side of the tool in the centre of the plate. This makes sense as this plate area has been exposed to the tool surface for the longest. The addition of contact dependent heating gives the opportunity to observe differences between the advancing and retreating side temperatures. There is some evidence for a relationship between the front-half and back-half of the tool with the advancing and retreating side temperatures. Figure 5.14 a) shows that for the back-half of the tool the advancing side has greater temperatures, however moving toward the front of the tool, the retreating side becomes hotter. This behaviour is repeated in c). Figure 5.14 b) is interesting in that it represents the time the tool is entering the cavity. The trend is similar to c) albeit the large peak on the advancing side. This could be related to interaction between the material flow, tool and the cavity corner, which is where the peak is located. A higher temperature is expected on the advancing side due to the larger shearing rate, and has also been found in other simulations of FSP [63].

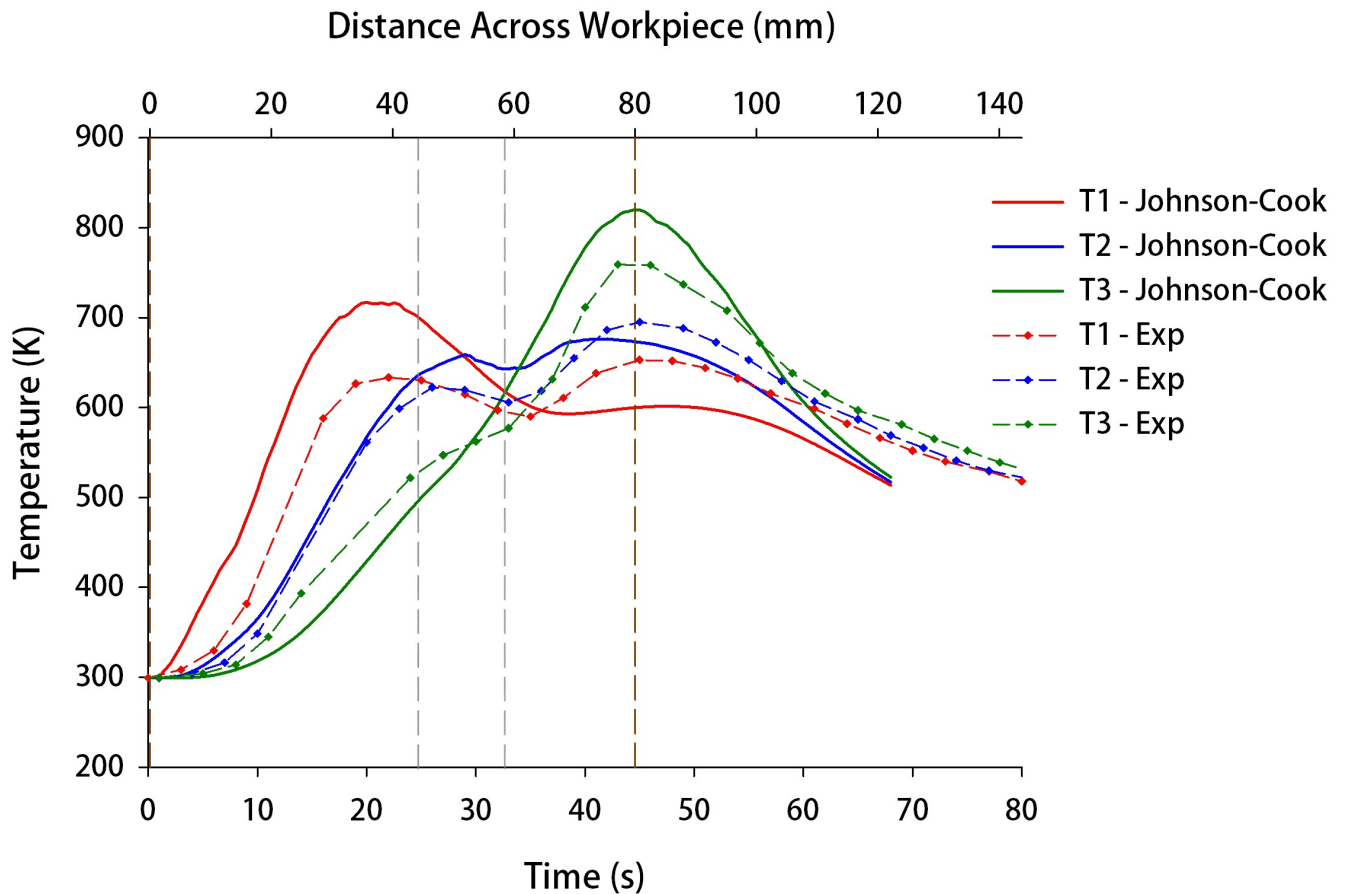


Figure 5.13: Temperature profile over time for thermocouple locations T1, T2 and T3 compared with experiment.

5.4.1.3 Comparison of the Thermal Field for the Thermo-mechanical Model and Thermal Model

Figure 5.15 shows the results obtained with the thermo-mechanical model overlaying the predicted thermal profile of the purely thermal model. As far as this author is aware, there has not been a direct comparison in the literature between a purely thermal model and a fully coupled thermo-mechanical model. A significant observation here is that the timing of the peaks is different, most noticeable for T1. Similarly, Figure 5.16 shows the thermal profiles grouped by thermocouple position for better comparison. It is clearer that the timing of the peaks for T1 and T2 is better achieved by the thermo-mechanical model, however the thermal model more accurately predicts the temperature drop over the cavity (shown by the larger inflection of T3 over the cavity region).

The difference in the peaks is probably due to the difference in the tool angle applied. The thermal model has none, meaning that the surface of the tool makes contact with the surface of the workpiece sooner and has no penetration into the surface. There may also be some effect from the addition of material flow in the thermo-mechanical model.

Figure 5.17 shows the comparison of surface line temperatures across the advancing side, retreating side, and the central line. Initially the temperatures are greatest in the thermal (stick) model, with the reverse as the tool progresses across the plate. This is likely due to a greater thermal softening in the thermal model due to the temperature dependent yield

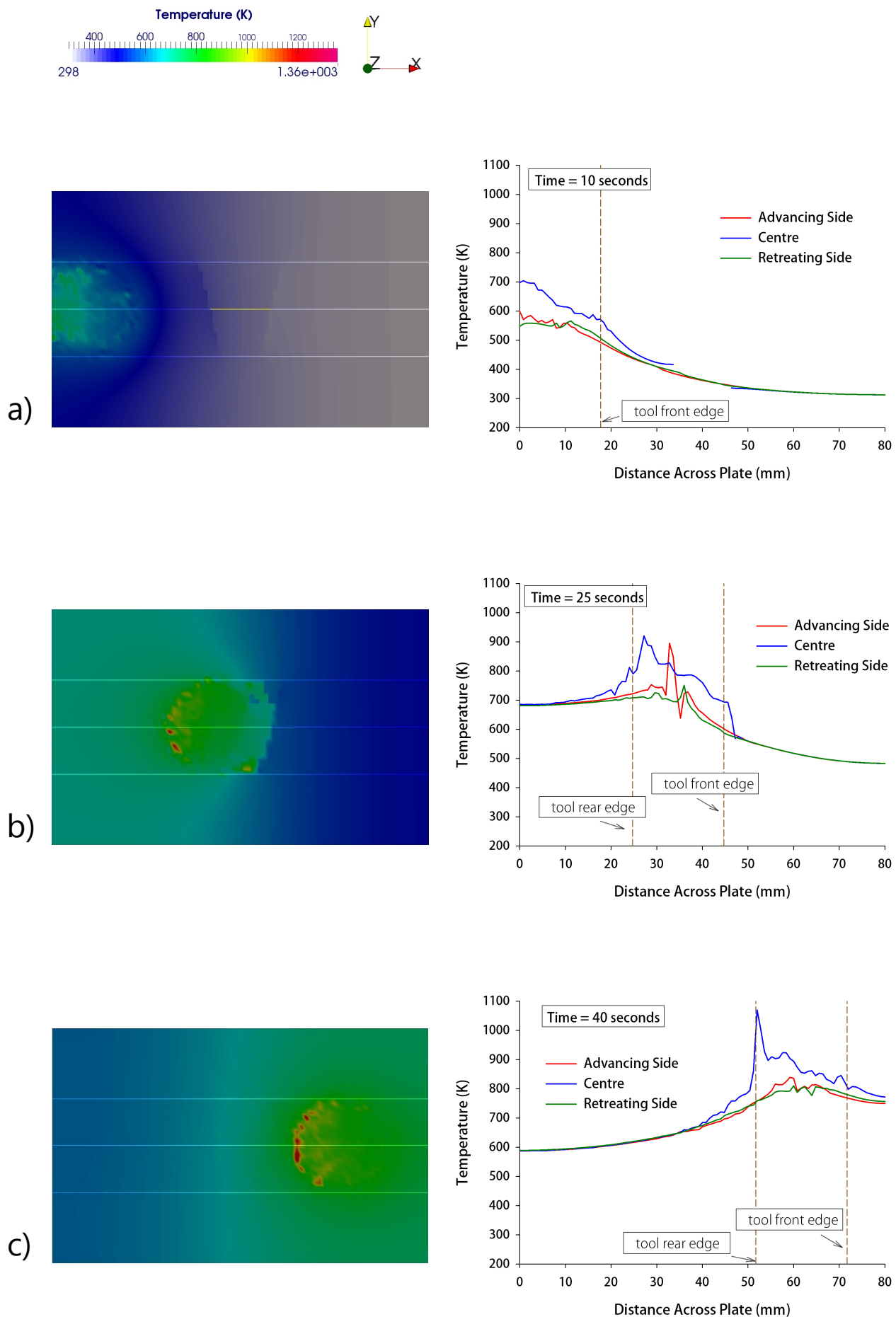


Figure 5.14: Temperature 1mm below the surface at times of a) 10s, b) 25s, c) 40s. Left image is the temperature across the slice, right is the temperature across each line on the advancing side, retreating side, and the central line.

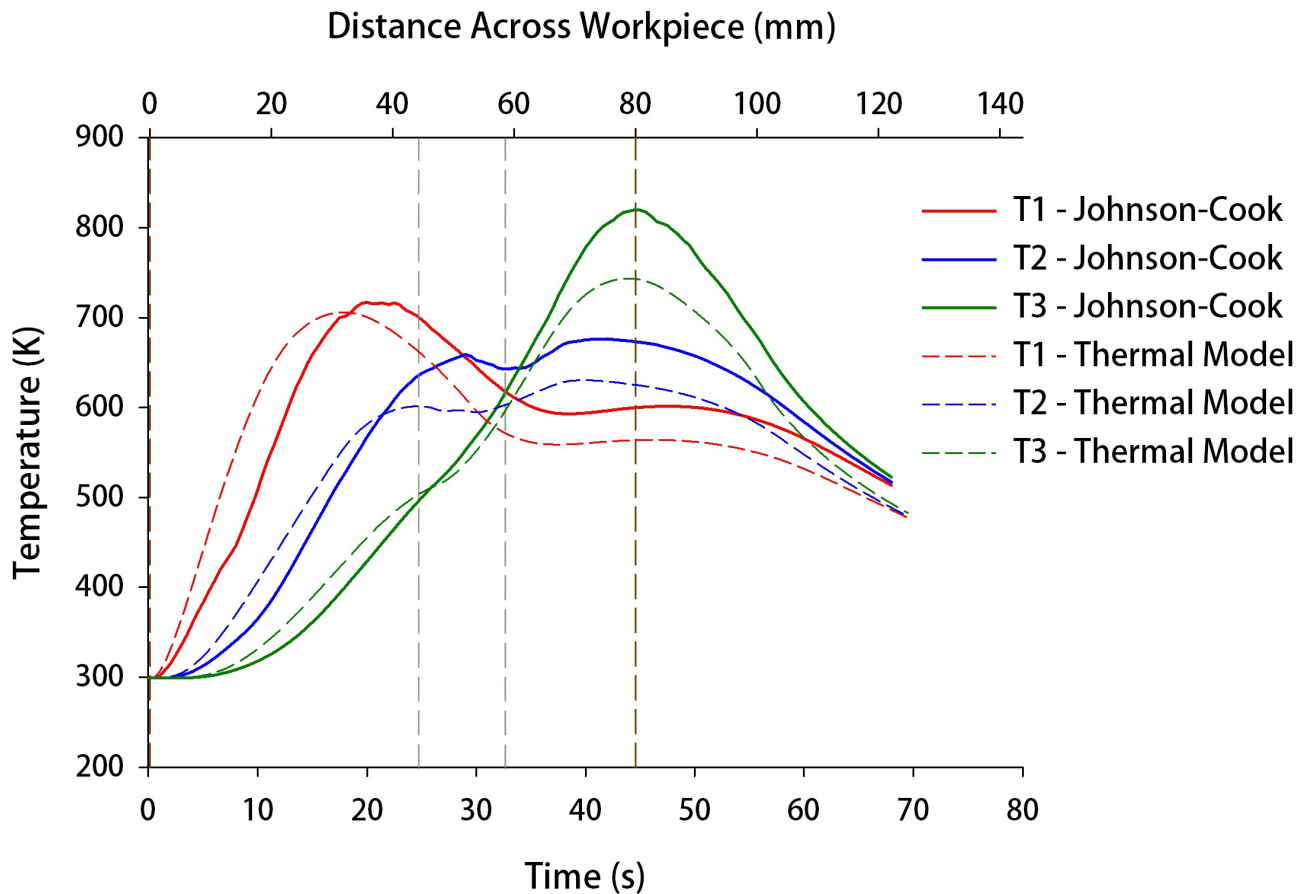


Figure 5.15: Comparison of temperature profiles over time for T1, T2 and T3 predicted by thermo-mechanical model and purely thermal model.

stress.

5.4.1.4 Summary of Temperature Analysis Using the Thermo-mechanical Model

Some over-prediction of temperature has been observed as discussed in the previous sections. To explain this, it is useful to note behaviour of the applied material model at high strains. The Johnson-Cook model accounts for thermal softening at high temperatures, however makes no provision for stress saturation at large strains. In FSP where deformation is very large, the flow stress as given by the JC model continues to increase beyond reasonable values as demonstrated by the following figures.

Figure 5.18 shows the tensile strength of copper with increasing temperature. The data was obtained from the ASM handbook [150], the tensile tests conducted as described in ASTM standards E8 and E21. The first temper is the same as the workpiece used in this work, C11000 H02, however the data is only available to about 700K. An approximate expected trend is shown by the O61 temper.

Figure 5.19 shows a small section of the workpiece in both (a) equivalent plastic strain, and b) the temperature field. The red section in b) gives an indication of the tool position at this time and is where the greatest temperature rise is noticed, generally $> 1000\text{K}$. Figure 5.19 a) shows an equivalent plastic strain value averaging around 30 for the same heated section.

With this in mind, Figure 5.18 also shows the flow stress determined by the Johnson-Cook model for this observed temperature (1000K) computed with the same strain rate as the tensile tests. It shows that the flow stress predicted at an equivalent plastic strain of 30 exceeds 250MPa, and is much greater than that shown experimentally, about 50 - 100MPa. An artificially high stress would result in higher than expected temperatures due to plastic dissipation (refer to equation 5.7). This can account for some of the higher than expected temperatures generated by the model. A constitutive model with both thermal softening and stress saturation is therefore recommended for future work (see next chapter).

Very high equivalent plastic strains should be expected in FSP, and have also been observed in previous works, as high as 135 in an ALE model of FSW of copper sheets [148], 160 in an Eulerian model [116], 132 in an ALE model [67], and 95 in an adaptive remeshing FEM model [154].

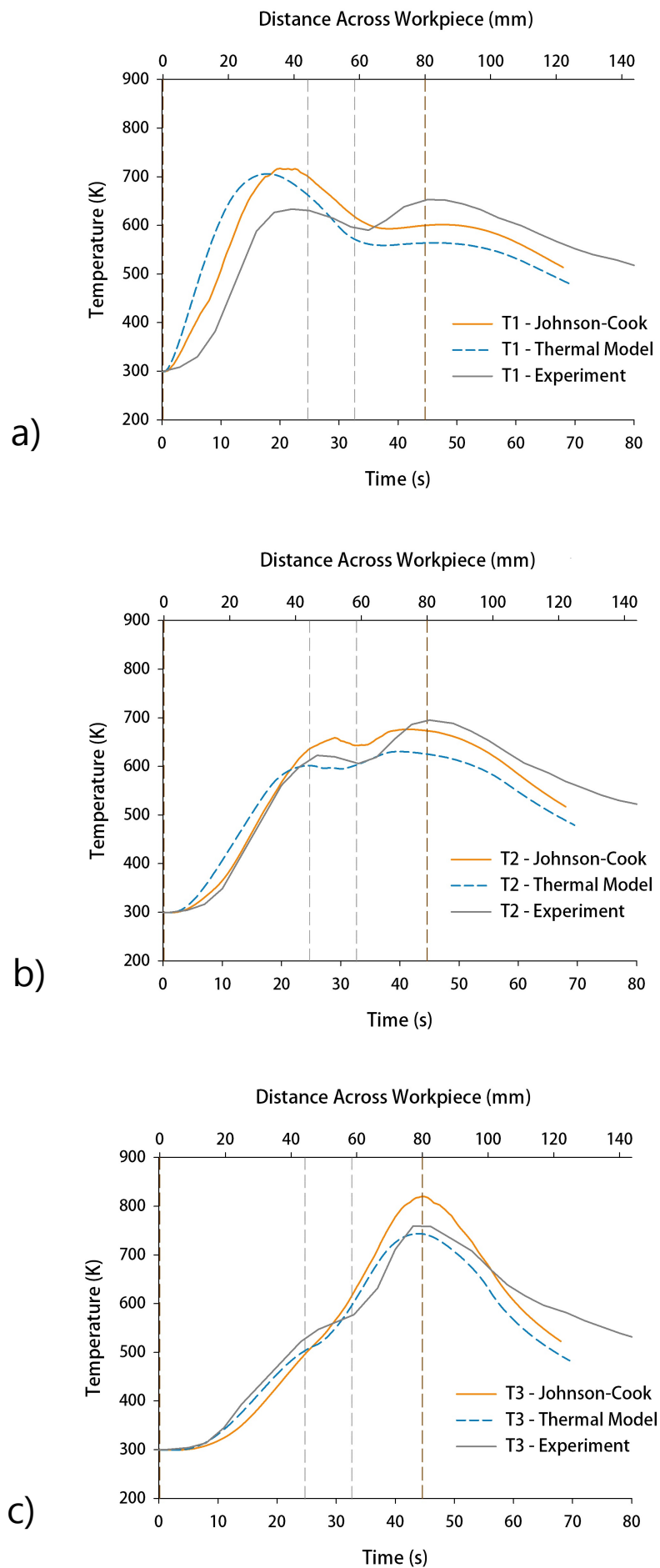


Figure 5.16: Comparison of temperature profiles over time predicted by the thermo-mechanical model (Johnson-Cook), purely thermal model and experiment for a) T1, b) T2 and c) T3.

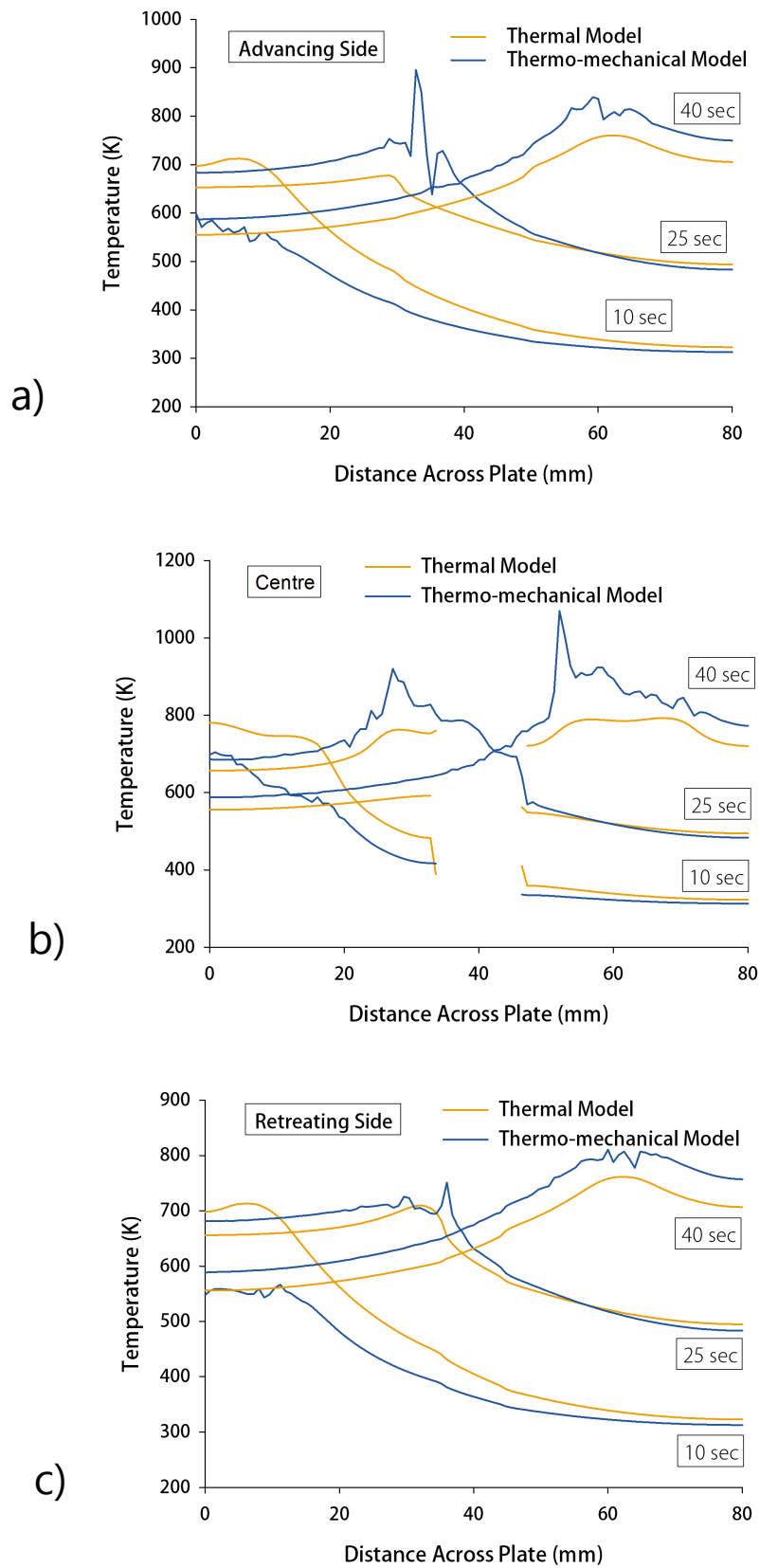


Figure 5.17: Temperature at locations 1mm below the surface across each line on the a) Advancing Side b) Centre Line, c) Retreating Side.

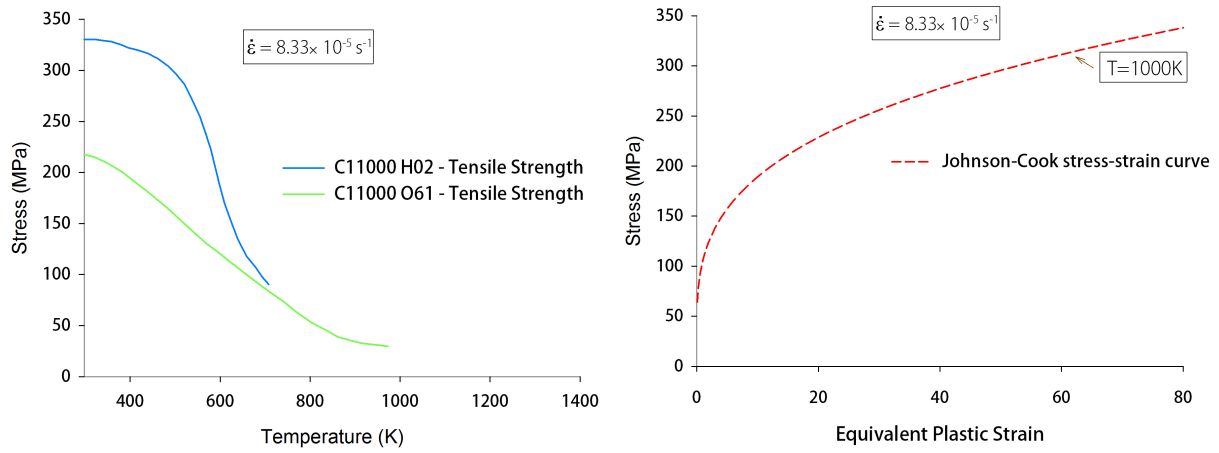


Figure 5.18: Left) Experimental tensile test data for yield stress vs. temperature for copper [150], Right) Johnson-Cook model for $T = 1000 \text{ K}$ and $\dot{\epsilon} = 8.33 \times 10^{-5} \text{ s}^{-1}$.

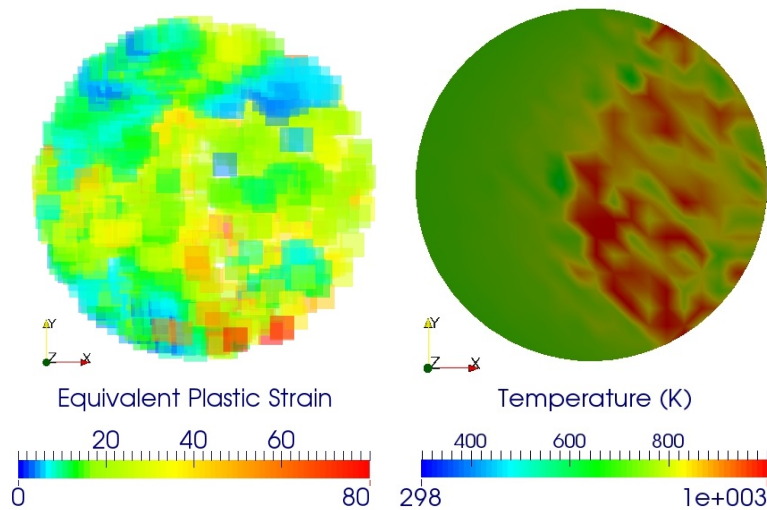


Figure 5.19: a) Strain map and b) temperature field for an area the size of the tool / workpiece interface as the tool passes across it ($t = 15$ seconds).

5.4.2 Resulting Material Flow

5.4.2.1 Flashing on the Surface of the Workpiece

The material flow is represented by the movement of the material points in MPM. Figure 5.20 shows the predicted flashing and is side by side with the experimental result. Figure 5.21 shows the overlaid experimental and simulated flash profiles. There is a small contrast between the advancing and retreating side flash volumes in the experimental results. This is reflected to a much greater extent in the simulation. The simulated flash reaches a maximum height of around 14 mm, while the experimental peak is about 8mm. Some qualitative agreement is observed in the reduction in flashing as the tool passes over the centre cavity in b), however this is not reflected in a) where there is a large amount of flash.

There are a couple of possible reasons for the over-estimation of the flash. One is to attribute it to the artificially increased kinetic energy in the system resulting from mass scaling. The second is that the friction coefficient applied is too high, or perhaps should not be assumed constant. In addition to these, the ability of MPM to resolve flashing is dependent on the particle size. Every particle in these simulations has a length of 0.5 mm, with the actual flashing thickness measuring at its thinnest approximately 0.1 of a millimetre. At this particle size the flashing determined is a rough approximation. One final reason is the use of the Johnson-Cook constitutive model: as it has been established in the summary of the temperature analysis above (section 5.4.1), this model does not represent the mechanical behaviour at high temperatures well.

ADVANCING SIDERETREATING SIDE

Figure 5.20: Copper flashing after processing (experimental and numerical) shown by a) Advancing side - Experiment (processing direction to the left), b) Advancing Side - Numerical, and c) Retreating side - Experiment (processing direction to the right), d) Retreating side - Numerical. Note that the thermocouple holes were machined on the other side to the simulation for this particular plate.

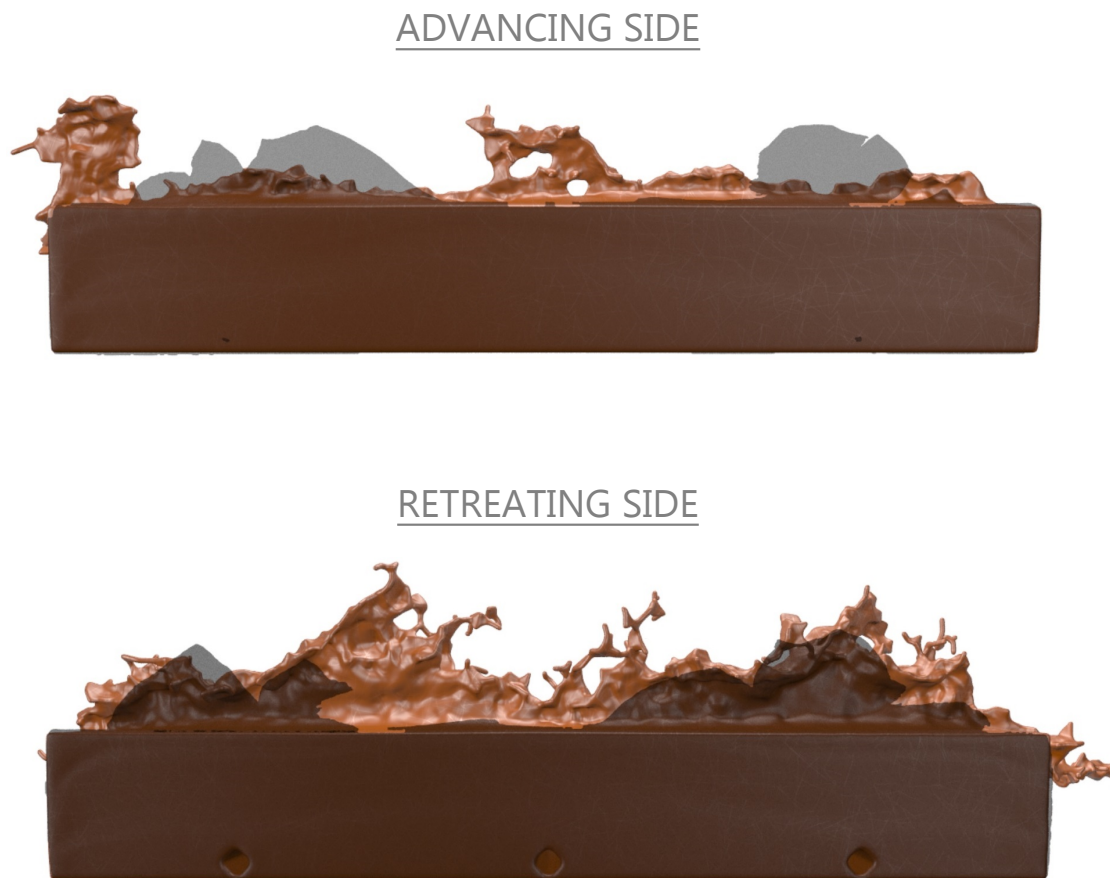


Figure 5.21: Overlaid images of simulation and experimental results according to processing side, top) advancing side flash, bottom) retreating side flash. The dark shadow shows the experimental flashing.

5.4.2.2 Surface Flow Visualization with Particle Pathlines

One of the advantages of MPM is the ability to track pathline histories for any material point. The following figures will investigate particle flow for areas of interest in FSP.

Figure 5.22 shows highlighted particles for pathline tracking. The regions selected represent workpiece particles in contact with i) the advancing side tool (red), ii) the centre of the tool (blue) and iii) the retreating side of the tool (green).

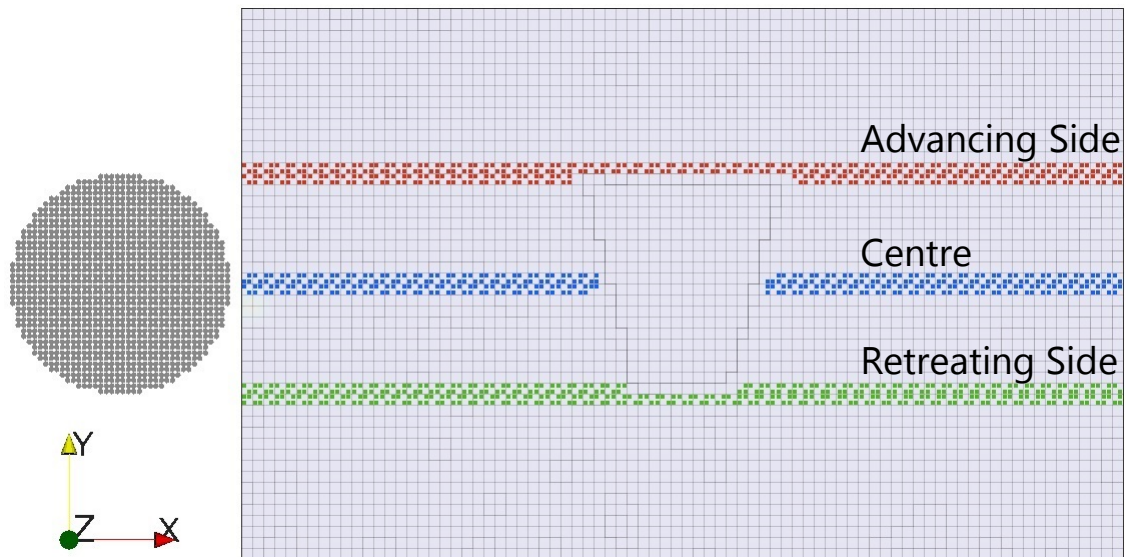


Figure 5.22: Series of particles used for tracking pathlines.

Figure 5.23 shows the complete paths of the particles selected. The particles at the outer edge of the tool tend to form flashing on their respective sides. The centre particles (blue) have much more diverse movement. Initially the particles rotated clockwise and back behind the tool, but as the tool progresses across the workpiece, it tends to push these particles forward and clockwise with its own rotation. The lower left image of Figure 5.23 reveals that many of the centre particles (blue) form part of the upper region of flash on the retreating side. The remaining particles have been rotated clockwise, but not enough to rejoin the centreline. Material flow was observed in a work of FSW, where a copper tracer was inserted through the middle of the tool pathline [60]. Tracer material was observed rotating from the centreline to the edge of the flashing or shear layer as they describe it. Another interesting region is just before the trapezoidal cavity, where the movement of the centre particles toward the retreating side shear layer or flash is reduced as the particles instead flow into the cavity.

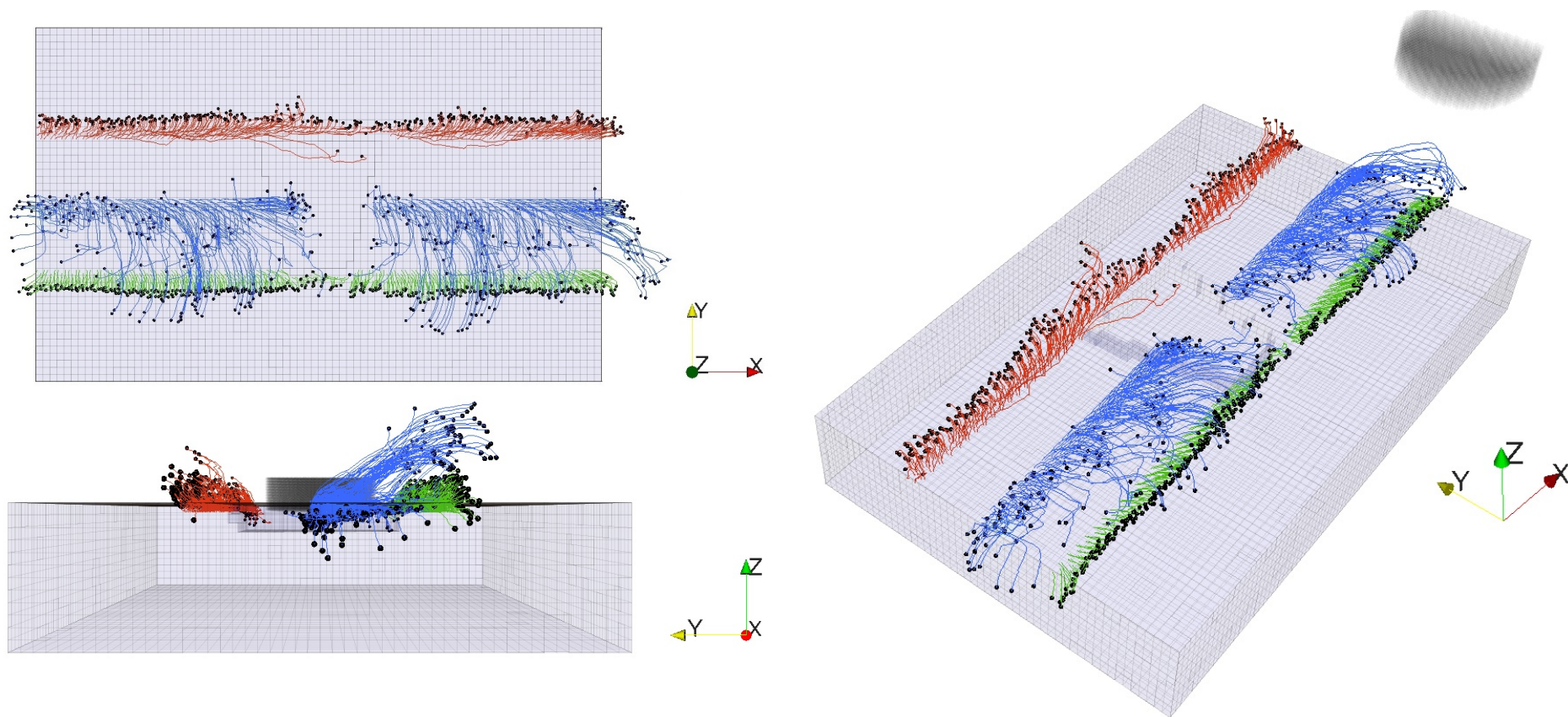


Figure 5.23: View of completed particle paths. Viewing angle clockwise from top left) top view (parallel projection), aerial view (perspective), processing direction view (perspective).

Figure 5.24 shows the side view of the plate with each of the individual particle lines. The centre particles show the most movement with large displacement in both z- and x-directions. This is in contrast to the advancing and retreating edge pathlines which show much smaller displacements.

Figure 5.25 shows another set of particles for pathline tracking. This time the particles are arranged in a rectangular box (10mm × 22mm × 1mm). The pages that follow show the flow of the particles at 10 second intervals. The particles are initially coloured by strata, but in the following pages the pathlines themselves take on the colour strata and the material points are presented as black points.

At t=10s the particles have been pushed either forward in front of the tool or have remained essentially where they started. Many of the particles have also been forced upward.

At t=20s, the particles that were originally positioned closer to the advancing or retreating sides have now formed part of the flashing on those respective sides and stopped moving. Those particles more toward the centre of the plate have either continued forward with the tool, or have been forced forward and clockwise to form flashing further along the retreating side of the plate.

At t=30s, the only remaining particles with the tool are the light blue and dark blue particles originally located about midway between the advancing side and centre line. Some have been forced into the cavity and the remaining ones are now moving toward the flashing areas on either side of the tool.

At t=40s all the mapped particles have found their final position.

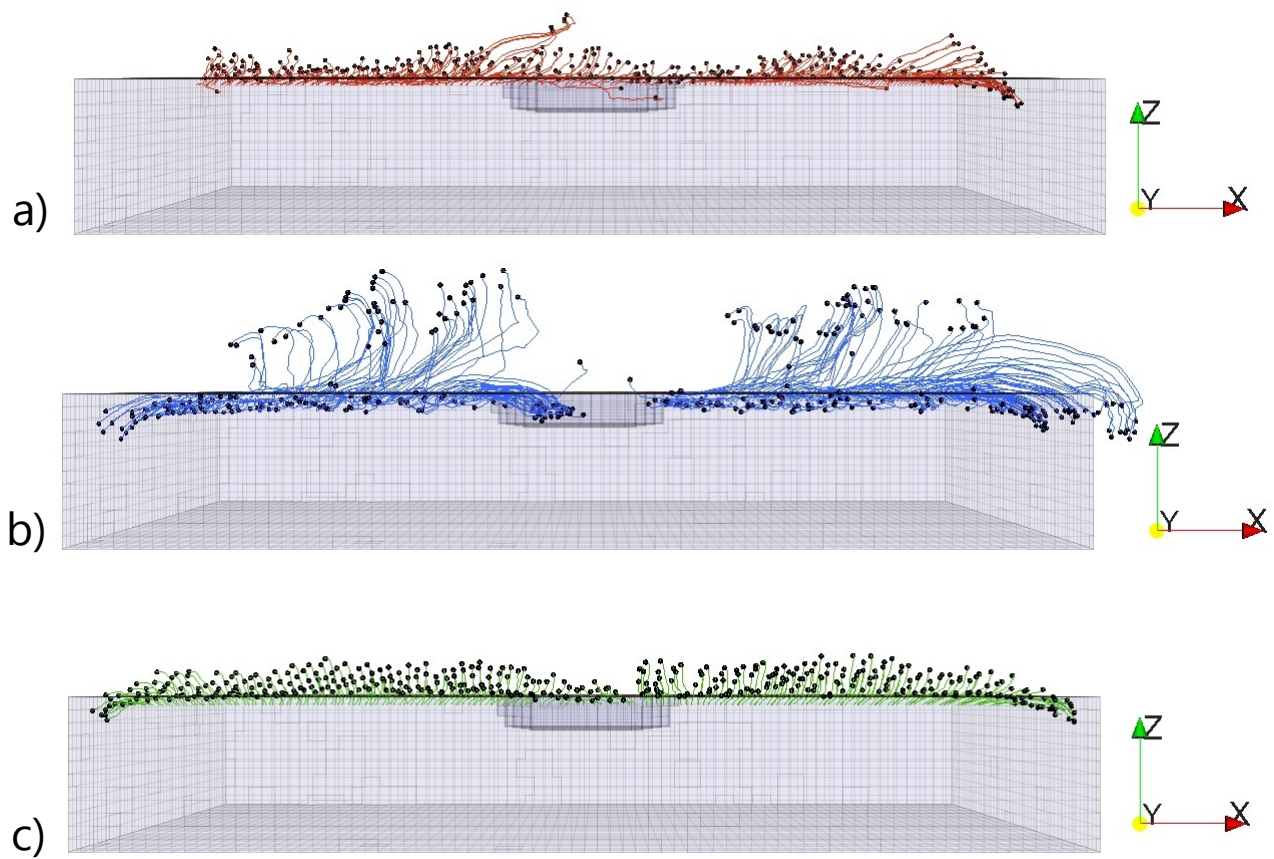
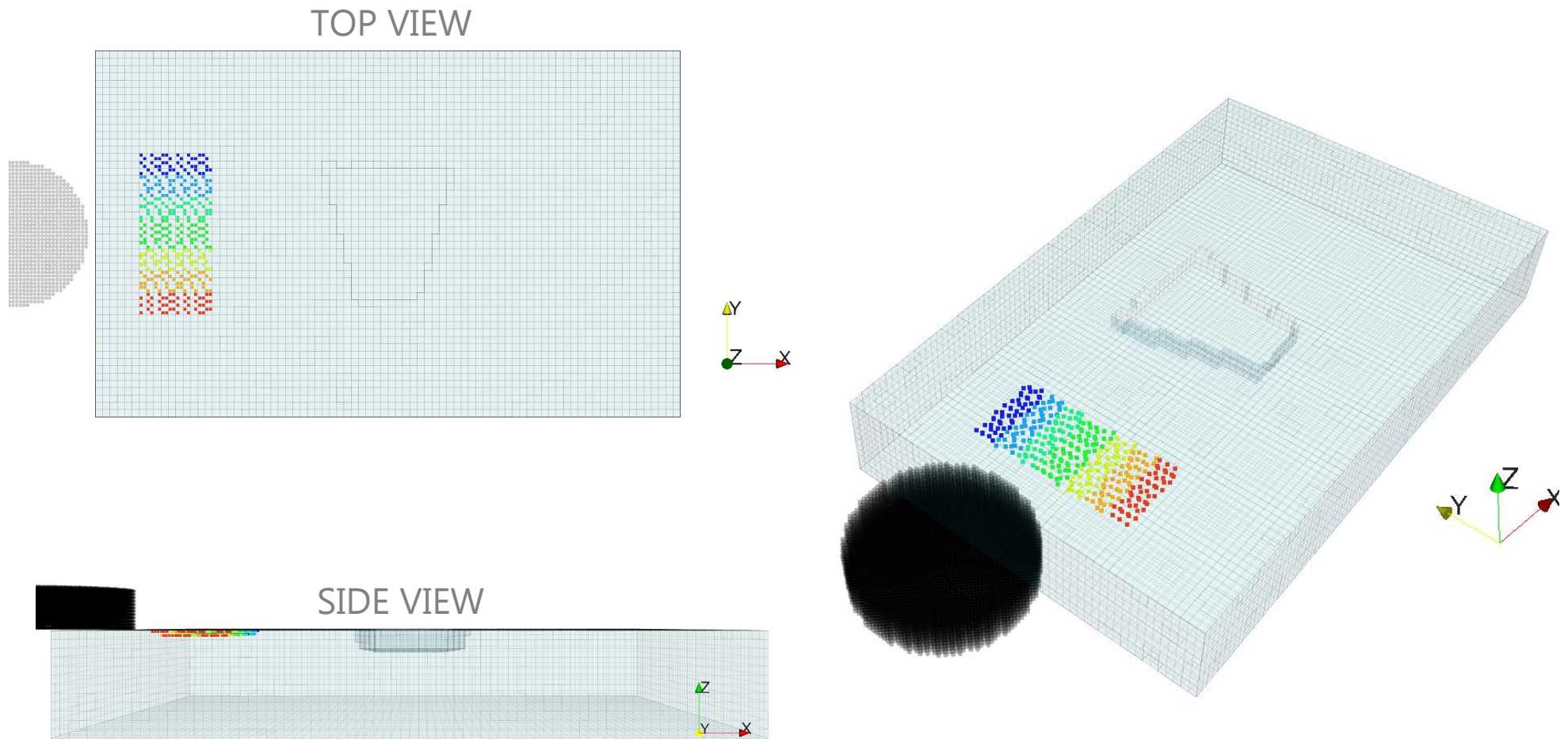
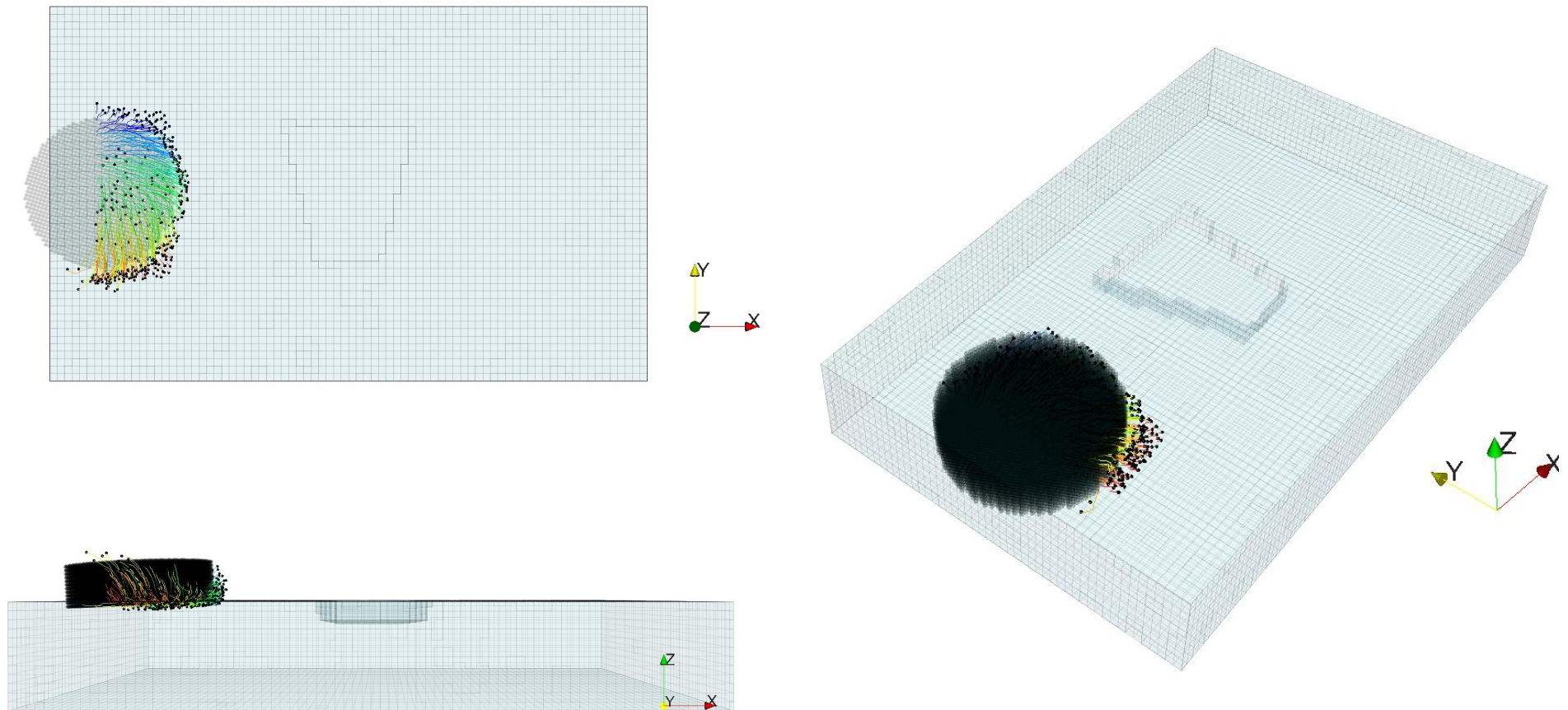


Figure 5.24: Side view (perspective) with each particle line shown individually. Processing direction indicated by positive x-direction.

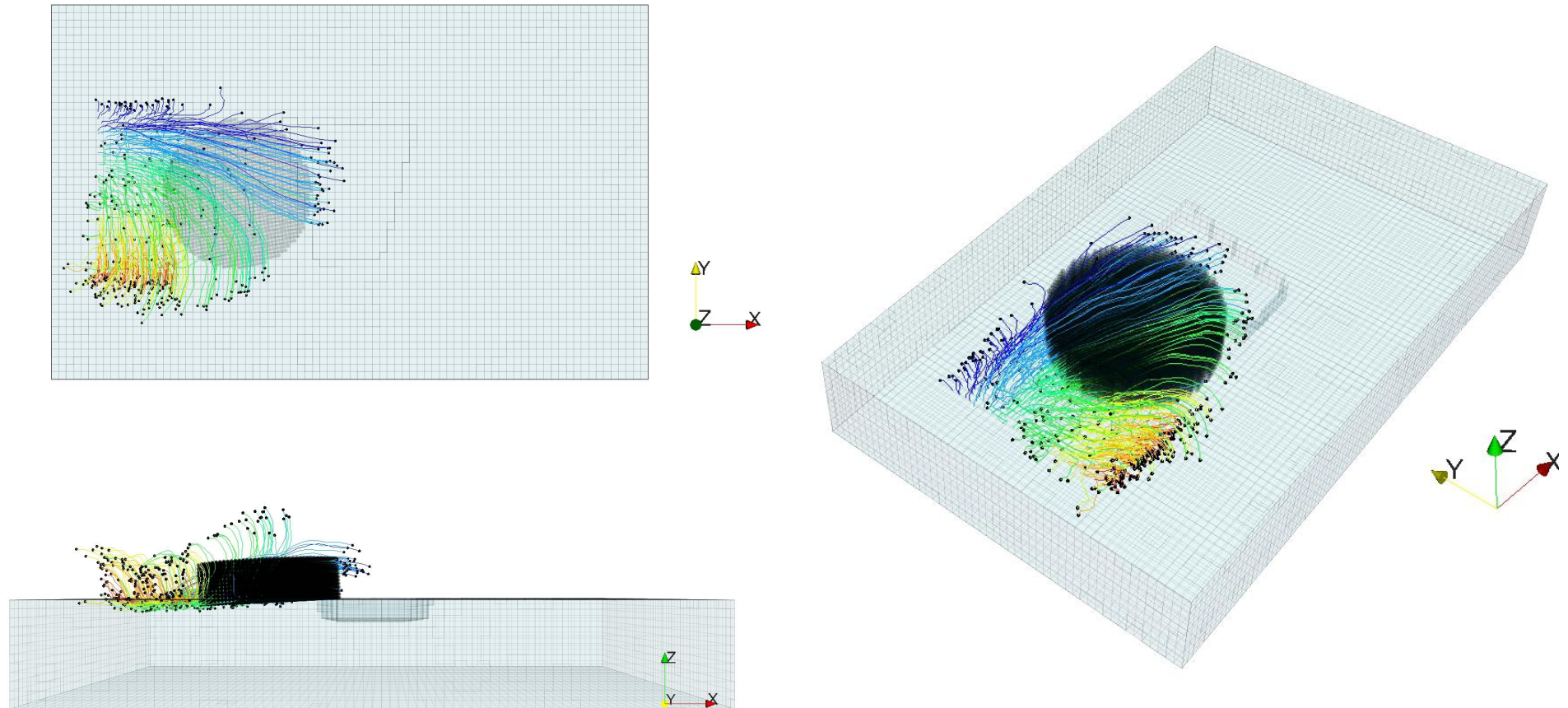


Time = 0 seconds

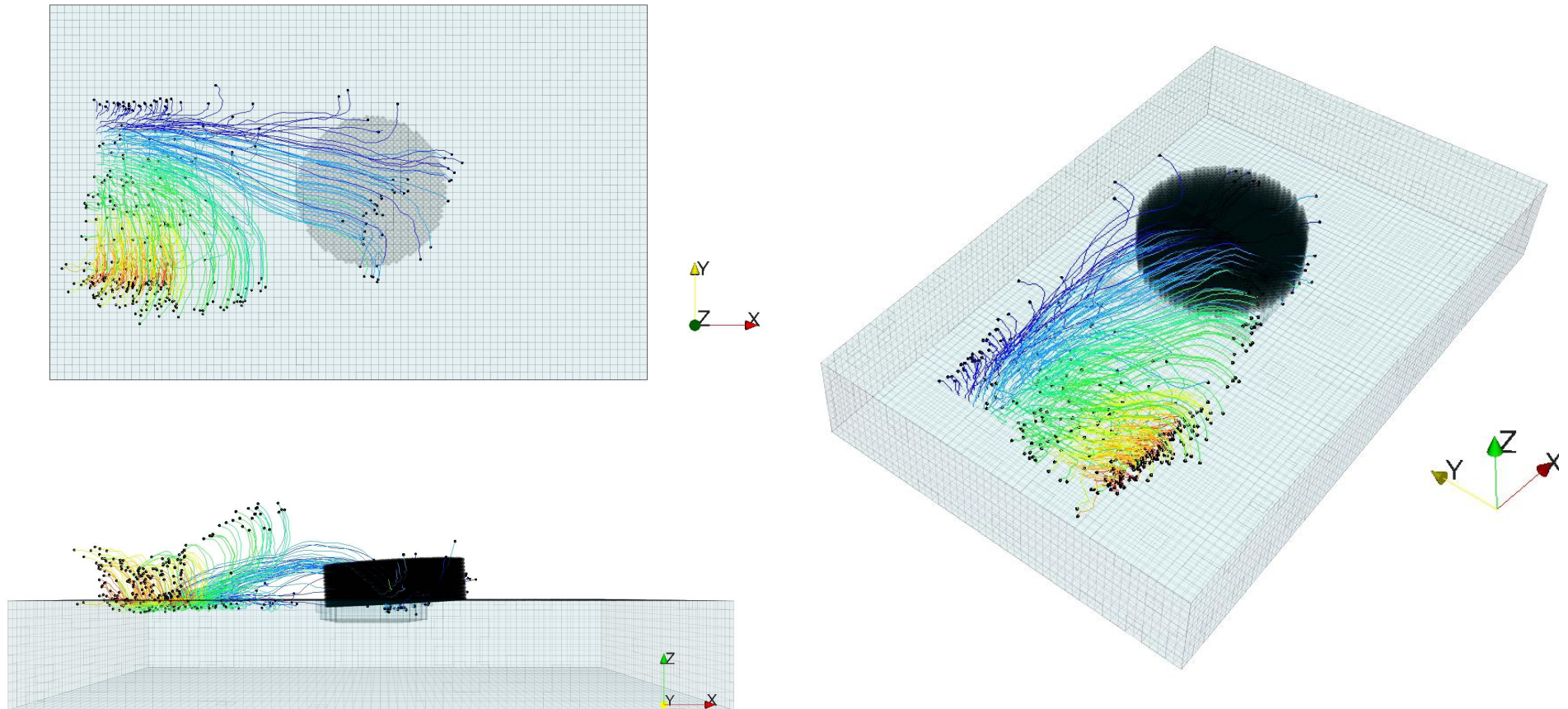
Figure 5.25: Initial set-up of simulation with seeded particles for pathline tracking (coloured by strata).



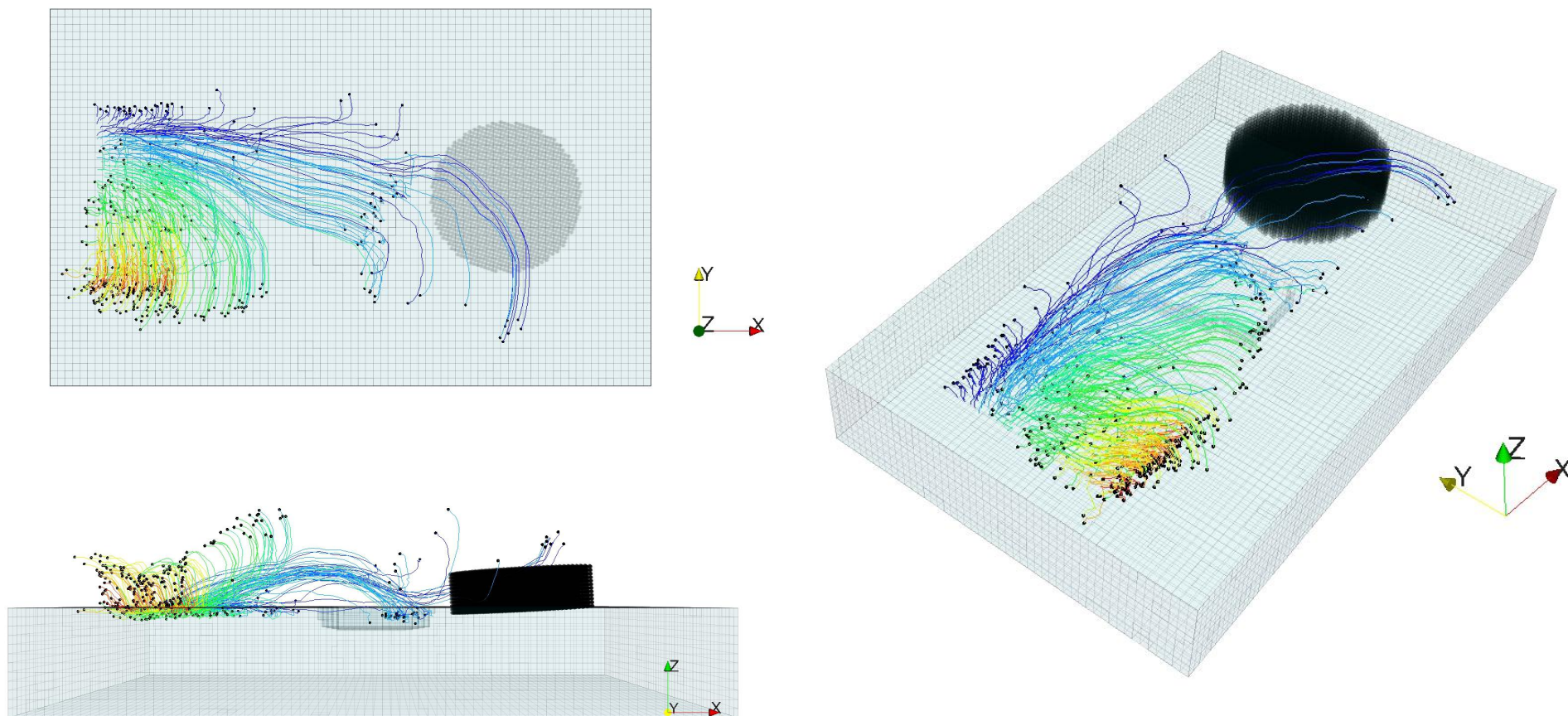
Time = 10 seconds



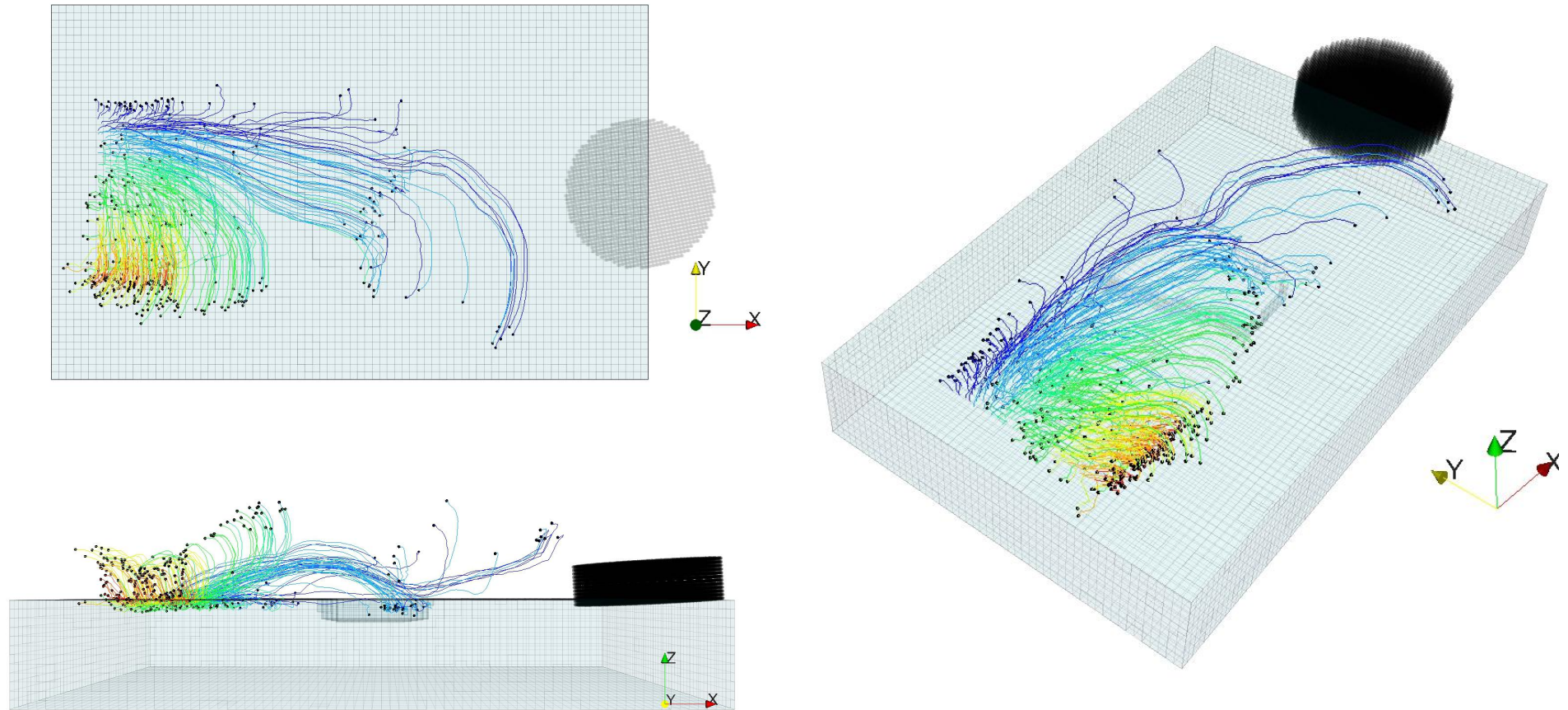
Time = 20 seconds



Time = 30 seconds



Time = 40 seconds



Time = 50 seconds

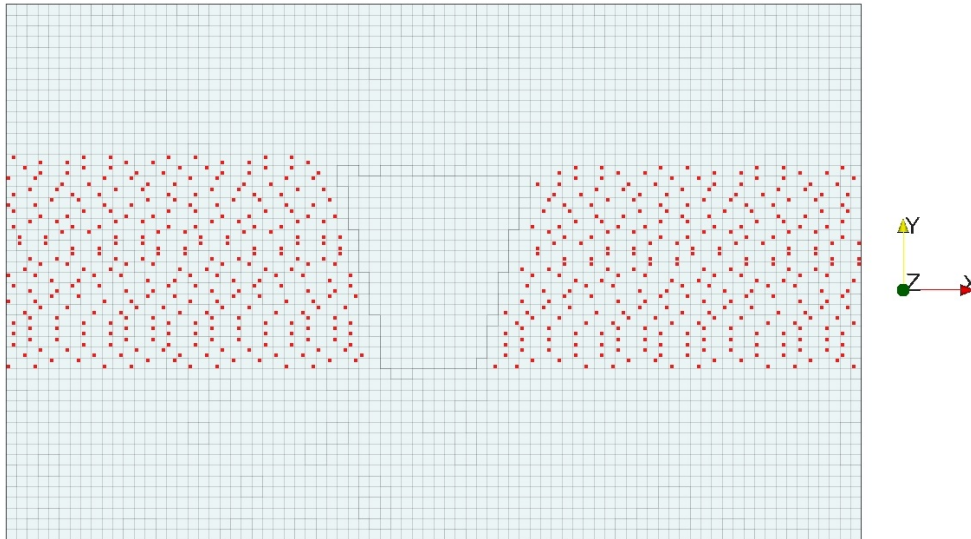


Figure 5.26: The initial state of particles for subsurface tracking at a depth of 1-2mm.

As a further analysis of material flow, the particle movement of the region between 1mm and 2mm from the surface is observed. The initial particle selection is shown by Figure 5.26. Figure 5.27 shows that much less movement occurs within this layer of material. This is in contrast to material flow typically observed with tools that have a pin [60, 155].

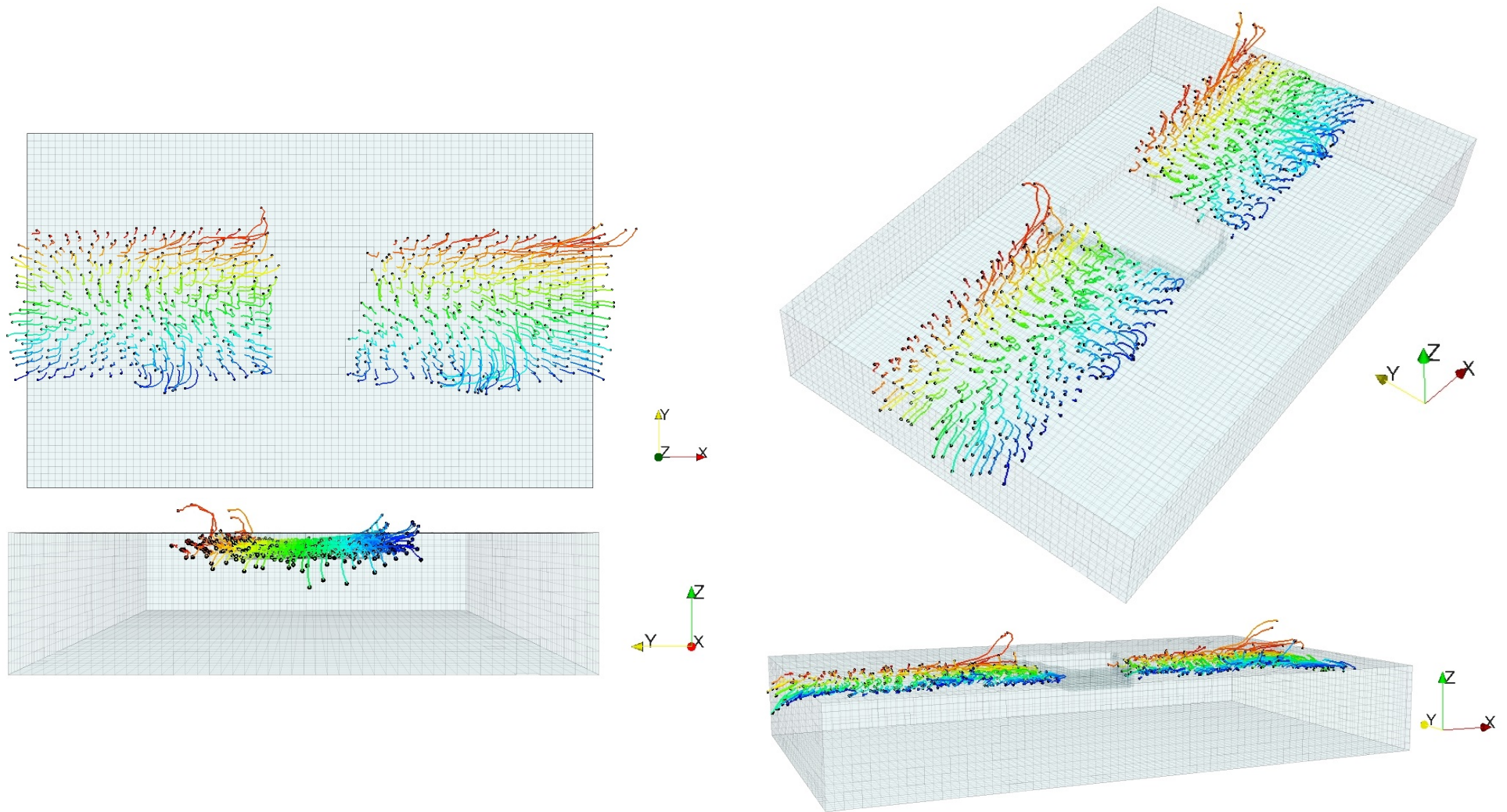


Figure 5.27: View of completed subsurface particle paths. Viewing angle clockwise from top left: top view (parallel projection), aerial views (perspective), processing direction view (perspective).

5.4.2.3 Material Filling of the Trapezoidal Cavities

The cavity machined into the plate surface allows for analysis of material flow into an empty space. Figure 5.28 shows the final material flow developed for cavity 1 in both the experiment and numerical model. Figure 5.29 highlights the experimental and numerical cavity flow for all cavities.

As a small aside, one note that should be made is that generating a surface for the cavity flow was less simple than for the flashing (figures 5.20 and 5.21). This is due to the way the surface generator distinguishes a surface among particles. It uses relative particle distances only; so if a material point has moved closer to the bottom of the cavity relative to the other material points that moved with it into the cavity, it will preferably form a surface with the particles on the bottom of the cavity. This can be seen clearly in Figure 5.29, where a small group of particles have formed an island within cavity 1. As such, parameters have been selected to represent the particle flow as accurately as possible, but the method is not perfect, and will be discussed further in the following chapter.

To continue, the experiments show that material generally flows in from the top left side, which is consistent with the tool rotation (clockwise viewed from the top). In general there is an over-prediction of the amount of material on the bottom section of each of the cavities.

Overall there is reasonable agreement between the experiment and the simulation based on the thermo-mechanical model. The material flow has a similar trend, typically filling from the top left side as in the experiment. There are consistent regions between both the experiment and model where no material is present.



Figure 5.28: Final material flow into cavity 1.

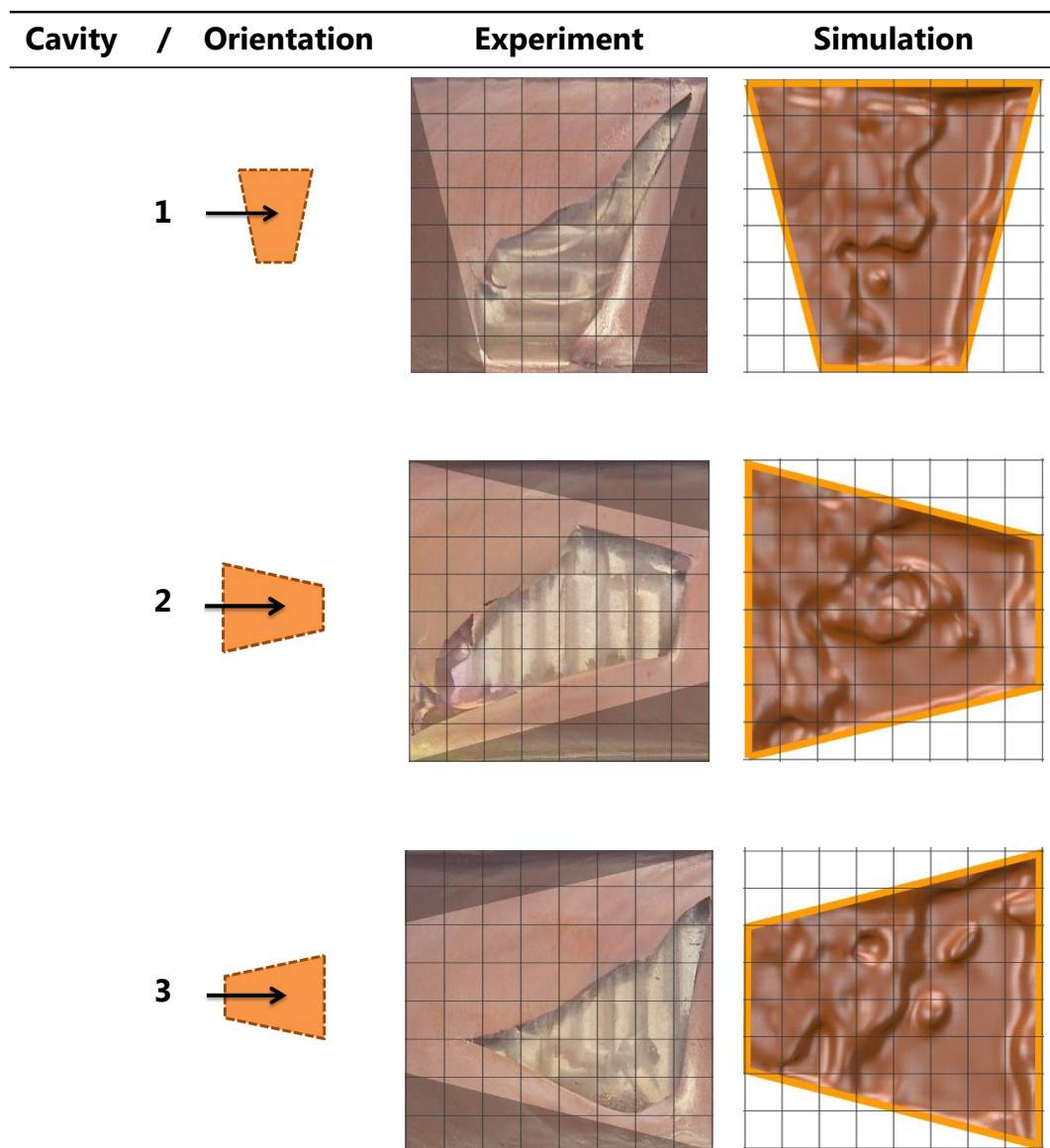


Figure 5.29: The three cavity orientations with material filling as shown for experiment and simulation.

5.4.2.4 Material Flow at the Tool Interface During FSP of Cu

Researchers have found a broad range of values for the velocity at the tool / workpiece interface [60, 61, 122, 148]. Figure 5.30 a) and b) show the interfacial velocities and displacements at 15 seconds and 40 seconds, respectively. The arrows are in the direction and coloured by magnitude of displacement, while the background circle is coloured according to the magnitude of the velocity. This simulation ran at 970rpm, giving a peak tool tangential velocity of 1m/s; the maximum observed material flow for this model is therefore $\sim 14\%$ of the maximum. Typical values at the interface however were between 5-25mm/s or 0.5-2.5% of the maximum tool speed.

In literature a range of velocities have been reported, for example 0-5% [148], 10-30% [60] and 35-100% [61], although some models do make the assumption of a sticking condition at the tool / workpiece interface resulting in greater material velocities. Wang et al. [122]

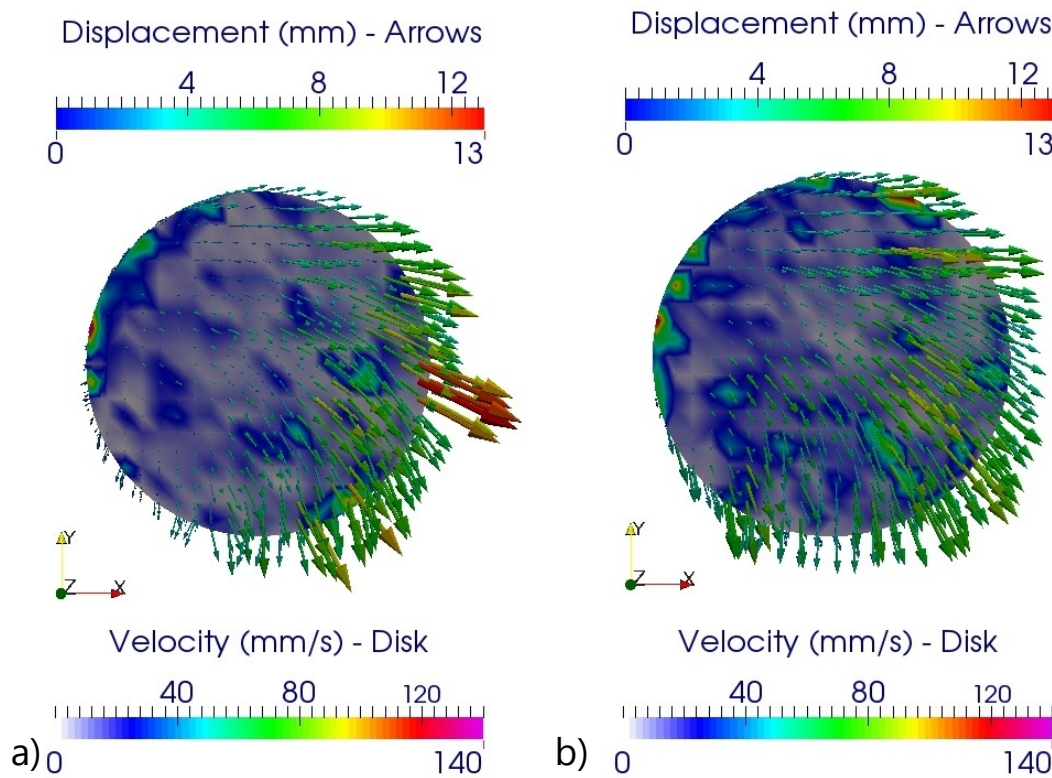


Figure 5.30: Material displacement and velocity at the tool interface for left) $t=15s$ and right) $t=40s$.

showed the difference this assumption makes in their work presenting velocities at the tool interface ranging, at a maximum 55-88% for the sticking condition and 6.1-9% for the sliding condition. The velocities reported in this work are reasonably consistent with those reported for the sliding models.

5.5 Conclusion

In this chapter, the model was developed into a fully-coupled thermo-mechanical model of FSP. It has been shown that a meshless numerical method can be successfully applied to modelling FSP, with the advantage of history tracking of field variables such as plastic strain and without the drawback of mesh entanglement associated with finite element methods. Applying the well tested Johnson-Cook constitutive model, the temperature and material flow were determined with reasonable accuracy (within 15%) for the experimental conditions.

Material flow was analysed through particle tracking inherent to particle methods. Flashing and cavity flow were compared against experiment with reasonable agreement and explainable error.

In addition, the effect of mass scaling was investigated. The limit for mass scaling often applied in literature was found to be inadequate. The temperature, displacement and stress fields were analysed and showed significant variation in results at the tool/workpiece interface at different mass scales, despite kinetic energy being below 1% of internal energy.

The temperatures were seen to increase in general as the mass scale was reduced. This was due to improvement in particle-particle contact and conduction as kinetic effects were reduced. The over-estimation of the temperature field can also be attributed to over-prediction

of the stress by the Johnson-Cook flow model.

The results have highlighted some of the limitations of the Johnson-Cook material model and mass scaling applied to FSP. The next chapter will attempt to improve on this by adding a more sophisticated material model able to capture the evolution of the underlying dislocation cell or subgrain structure in order to determine the material response.

Chapter 6

Modelling of FSP with a Dislocation-Density Based Material Model

6.1 Introduction

In the previous chapter, the model was developed into a fully-coupled thermo-mechanical model of FSP. In this chapter, the Johnson-Cook constitutive law is replaced by a dislocation-density based material model (referred to here as the two-phase model), which was developed [101] to describe the microstructure evolution in dislocation cell-forming materials. In addition to calculation of stress as a result of deformation conditions and temperature, additional dependence is enabled via evolution equations for the dislocation density. This also allows for local history tracking of the grain size.

In addition to the copper workpiece that has been previously modelled, this chapter will introduce aluminium alloy 5005. Rather than presenting the complete results alongside the copper material, the AA5005 is used for the purpose of further validation of the predicted microstructure evolution only.

As a general introduction and for the purpose of completeness, what follows is a very brief description of material microstructure related to deformation. For further information the reader is referred to the work of Humphreys and Hatherly [156].

6.2 Dislocation-Density Based Microstructure Model

6.2.1 Brief Description of the Model

During deformation or processing, most of the expended work energy is released as heat, with a small amount stored mainly in the form of dislocations. The difference in energy between the deformed and the annealed state is the dislocation content and arrangement. This stored energy provides the driving force for all the property changes that can take place during or after processing. This is why modelling of microstructure during deformation should be through the density, distribution and arrangement of dislocations.

In a simple model of a polycrystal, it is made up of three main components:

1. High angle grain boundaries.

2. Dislocation cells or subgrains, which are typically micron size volumes bounded by dislocation walls. The walls can be tangled or fraying (cells) or well-ordered low angle boundaries (subgrains).
3. Dislocations other than those comprising the cell/subgrain boundaries.

It is the dislocations themselves that define the microstructure, and with applied deformation, order in the arrangement of these dislocations is established through various mechanisms. One such set of mechanisms commonly experienced during deformation is called dynamic recovery. It can occur in plastically deformed material at high temperatures and is not a single microstructural change but a series of events. It generally follows the form outlined below.

1. Dislocation tangles are formed through deformation.
2. Cells are formed through movement of dislocations (cell walls and interiors formed).
3. Annihilation of dislocations within cells (mostly interior).
4. Dislocations become more ordered in walls, cells become subgrains with low angle grain boundaries (LAGB).
5. Subgrains grow.

Some of these can occur after deformation as static recovery and significant overlap can occur for each of these processes.

These can be summarised into three components: dislocation annihilation, dislocation rearrangement and subgrain growth. The model applied in this work considers the first two, the latter generally being a post-process phenomena. With that in mind, what follows are the equations of the dislocation-density based constitutive model developed by Kocks, Mecking and Estrin [101, 157], referred to here as the two-phase model.

6.2.2 Flow Stress According to the Two-Phase Model

In this model dislocation cells or subgrains, which we shall collectively refer to as subgrains, are divided into two components, the subgrain walls and subgrain interiors, each with their own dislocation density and related mechanical condition. The shear stress within each subgrain interior τ_c^r and subgrain wall τ_w^r can be given according to equation (6.1) and (6.2).

$$\tau_c^r = \alpha G b \sqrt{\rho_c} \left(\frac{\dot{\gamma}_c^r}{\dot{\gamma}_0^r} \right)^{\frac{1}{m}} \quad (6.1)$$

$$\tau_w^r = \alpha G b \sqrt{\rho_w} \left(\frac{\dot{\gamma}_w^r}{\dot{\gamma}_0^r} \right)^{\frac{1}{m}} \quad (6.2)$$

where the superscript, r , refers to the resolved shear stress along the slip plane, α is a constant, G is the shear modulus, b is the magnitude of the Burgers vector (a constant dependent on the crystal structure of the metal, i.e. fcc, hpc, bcc), ρ_w and ρ_c are the dislocation densities in the subgrain wall and interior respectively, $\dot{\gamma}_0^r$ is a reference shear strain rate, $\dot{\gamma}_c^r$ is the shear strain rate of the subgrain interior, $\dot{\gamma}_w^r$ is the shear strain rate of the subgrain wall, and $1/m$ is the strain rate sensitivity parameter, where m is inversely proportional to the absolute temperature:

$$m = \frac{A}{T} \quad (6.3)$$

where A is a constant. The overall behaviour of the composite structure, described with two dislocation densities, is defined by the scalar quantity obtained using the rule of mixtures below.

$$\tau^r = f\tau_w^r + (1-f)\tau_c^r \quad (6.4)$$

where f is the volume fraction of the dislocation density within the subgrain walls. The evolution equations for the dislocation density in the subgrain interior and subgrain wall are given below. Their evolution rate is a function of addition, subtraction and annihilation of dislocations. The growth of the dislocation density can be attributed to Frank-Read sources at the subgrain wall or interior interface. The loss of grain interior dislocations can be attributed to the movement from grain interior dislocations into the grain wall through glide and also by annihilation within the subgrain involving cross-slip. The annihilation of subgrain dislocations is governed by climb-controlled annihilation of dislocations. This is the last term in each equation.

The set of coupled differential equations, which describe the evolution of the two dislocation densities defined in the two-phase model is as follows:

$$\dot{\rho}_c = \alpha^* \frac{1}{\sqrt{3}} \frac{\sqrt{\rho_w}}{b} \dot{\gamma}_w - \beta^* \frac{6\dot{\gamma}_c}{bd(1-f)^{\frac{1}{3}}} - k_o \left(\frac{\dot{\gamma}_c}{\dot{\gamma}_0} \right)^{-\frac{1}{n}} \dot{\gamma}_c \rho_c \quad (6.5)$$

$$\dot{\rho}_w = \frac{6\beta^* \dot{\gamma}_c (1-f)^{\frac{2}{3}}}{bdf} + \frac{\sqrt{3}\beta^* \dot{\gamma}_c (1-f) \sqrt{\rho_w}}{fb} - k_o \left(\frac{\dot{\gamma}_w}{\dot{\gamma}_0} \right)^{-\frac{1}{n}} \dot{\gamma}_w \rho_w \quad (6.6)$$

where β^*, α^*, k_o are constants, and $1/n$ is the strain rate sensitivity parameter, where n is inversely proportional to the absolute temperature:

$$n = \frac{B}{T} \quad (6.7)$$

where B is a constant. To maintain strain compatibility at the subgrain interior and wall interface, the resolved shear strain rate is equal within each phase of the composite structure.

$$\dot{\gamma}_c^r = \dot{\gamma}_w^r = \dot{\gamma}^r \quad (6.8)$$

The total dislocation density is made up of these two variables added together via a rule of mixtures:

$$\rho_t = f\rho_w + (1-f)\rho_c \quad (6.9)$$

where ρ_t is the total dislocation density. The subgrain size is determined as proportional to the inverse of the square root of the total dislocation density:

$$d = \frac{K}{\sqrt{\rho_t}} \quad (6.10)$$

where d is the average subgrain size and K is a proportionality constant. The relation for volume fraction of the dislocation density in the subgrain walls, f , is associated with the shear strain rate, $\dot{\gamma}^r$, the saturation value of f at large strains, f_{∞} , and the initial volume fraction, f_0 , which are constants. Finally, $\dot{\gamma}^r$ is the rate of variation of f with resolved shear strain, γ^r [157].

$$f = f_{\infty} + (f_0 - f_{\infty})e^{-\frac{\gamma^r}{\dot{\gamma}^r}} \quad (6.11)$$

The resolved shear strain rate can be determined from the following relationship.

$$\dot{\gamma}^r = M_T \dot{\epsilon}_p \quad (6.12)$$

where M_T is the Taylor factor, which for simplicity is assumed to be constant. Lastly the resultant equivalent flow stress can be related to the calculated resolved shear stress:

$$\sigma = \sigma_0 + M_T \tau^r \quad (6.13)$$

The strength of this physically-based microstructure model is that it can be incorporated into a numerical model that operates at the continuum level, and through the material constitutive behaviour provide information at a microscopic level (microstructure). The thermal coupling allows for temperature effects and is introduced through the strain rate sensitivity parameters m and n , shown in equations 6.3 and 6.7. This couples the thermal solution to the mechanical solver.

6.2.3 Calibration of the Two-Phase Model to FSP Conditions for Copper and AA5005

The original material parameters chosen for the model were developed for Equal-Channel Angular Pressing (ECAP), which although a severe deformation process, is carried out at low strain rate often at room temperature. One of the challenges of FSP is the high strain rate and high temperatures experienced, and some adjustment needs to be made to account for these conditions. The following sections calibrate the two-phase model to FSP conditions for copper and aluminium alloy 5005.

6.2.3.1 Copper

In the following analysis, the original parameters have been used for the material properties for copper [157], see Table 6.1. The graphs below represent the stress-strain relationship predicted by the two-phase model; they include temperature rises due to dissipation of mechanical work of plastic deformation.

As shown in Figure 6.1, the fit is very good for low strain rate, room temperature conditions [157, 158].

Note that the reference shear strain rate, $\dot{\gamma}_0$, must be higher than the imposed shear strain rate, hence this is adjusted according to the expected experimental conditions. Figure 6.2 shows that at higher temperatures and moderate strain rates, the model becomes less robust. For the imposed strain rate of $\dot{\epsilon} = 1s^{-1}$ and given range of temperatures, the stress ranges over about 300 MPa for the experimental conditions, but the model predicts only

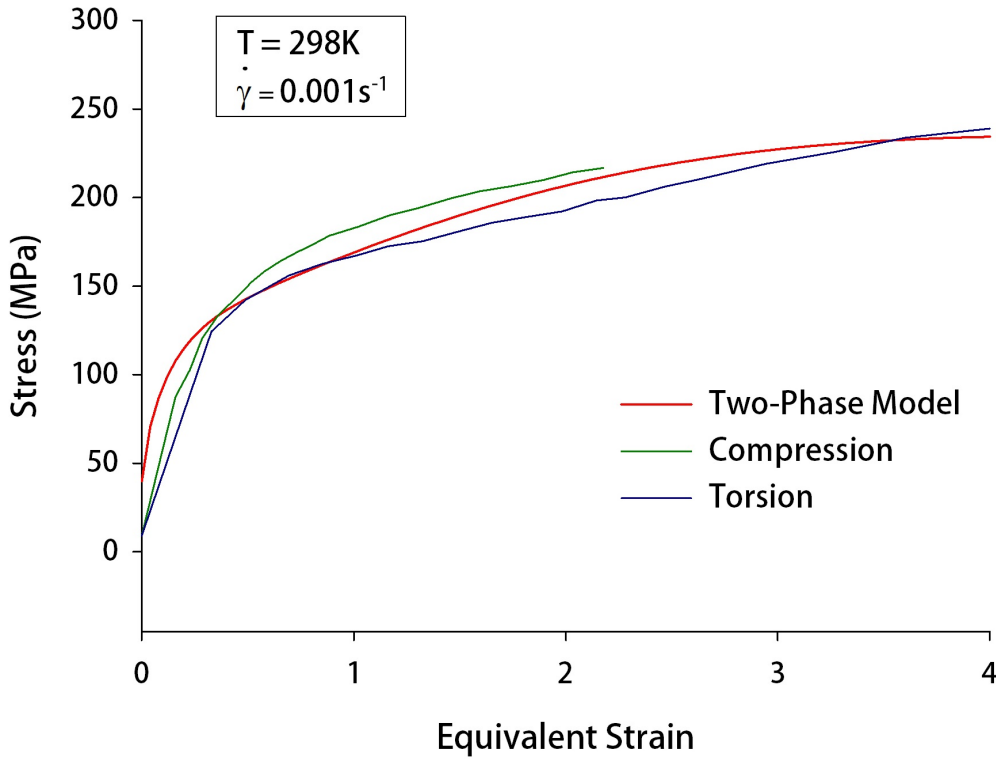


Figure 6.1: Flow stress response for two-phase model at low strain rate and room temperature compared against experiment (in compression and torsion) [157, 158].

small change with variation in temperature. The model shows a reduction of stress as temperature increases, which is consistent with the experiments, however the current temperature dependence through the exponents m and n is not accurate enough.

One solution is to incorporate an additional temperature dependence through the free parameter α^* . Appropriate values for α^* were determined through best-fit to the experimental data, and a least squares regression analysis applied to determine an appropriate function. The calibrated values of α^* are shown in Figure 6.3 by the red circle markers, against the fitted function. The parameters for the fitted function are given in equation (6.14). At the outer limits of the temperature range, the temperature dependence is replaced by constant values for α^* . This ensures α^* is never negative and not excessively high.

$$\alpha^*(T) = \begin{cases} 0.216 & : T < 298 \\ \frac{600}{T+885.6} - 0.3 & : T \in \{298 \rightarrow 1100\} \\ 0.002 & : T > 1100 \end{cases} \quad (6.14)$$

Here the temperatures are given in kelvin. Figure 6.4 shows the resulting stress-strain curves with $\alpha^*(T)$ replacing the initial constant value α^* . With this replacement the prediction from the two-phase model is much improved. The correlation for all four temperatures is much better and fairly consistent. At a temperature of 773K and 1123K the experimental curves exhibit flow softening due to dynamic recrystallization [160]; the current model does not take this phenomenon into account, however the fit is still quite reasonable.

Figure 6.5 shows the softening that is induced by the temperature dependent α^* . As the temperature increases due to plastic deformation, softening occurs due to the reduction of α^* . Without this temperature dependence, the stress tends to saturate at high values despite near melting temperatures. This softening can be seen as an added bonus of the temper-

Parameter	Copper
Density, ρ (kg/m ³)	8960
Young's modulus, E (GPa)	124
Poisson's ratio, ν	0.34
dislocation density in subgrain walls, ρ_w (m ⁻²)	10^{13}
dislocation density in subgrain interiors, ρ_c (m ⁻²)	10^{12}
initial volume fraction, f_0	0.25
saturated volume fraction, f_∞	0.06
rate of decrease of f , $\bar{\gamma}^T$	3.2
α	0.25
K	10
α^*	0.03
β^*	0.0018
k_0	4.6
A	30000
B	14900
Taylor factor, M_T	3.06
Burgers vector, b	2.56×10^{-10}
Reference shear strain rate, $\dot{\gamma}_0$ (s ⁻¹)	1000

Table 6.1: Model parameters for Copper [101, 157].

ature dependent α^* , and will be an important part of modelling FSP, where near melting temperatures arise at the interface of the tool and workpiece.

The following Figures 6.6 and 6.7 show the flow stress response at higher temperatures (773K and 1123K) for different strain rates (1s⁻¹-100s⁻¹). The figures show an improved accord between the model and the experimental data. Figure 6.6 shows material softening, indicated by a drop in flow stress with increasing strain, not predicted without temperature dependent α^* .

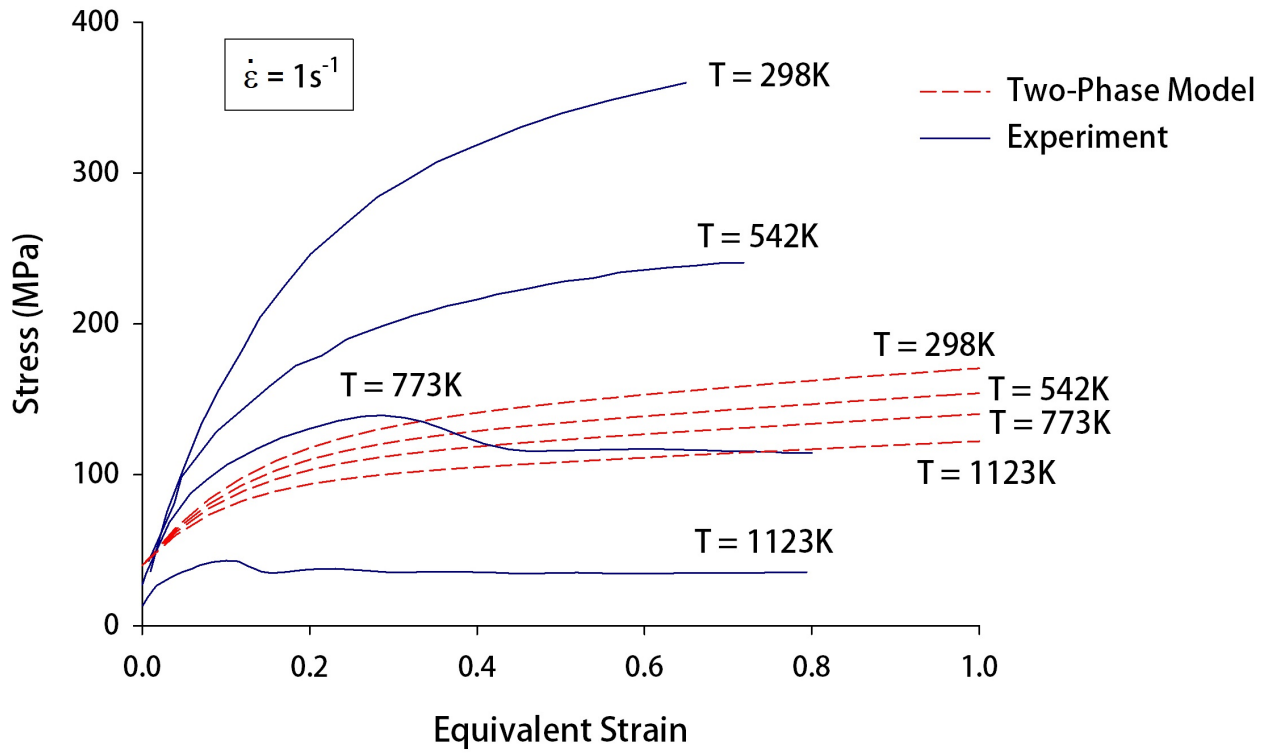


Figure 6.2: Flow stress response for original model at various temperatures and a strain rate of $\dot{\epsilon} = 1 \text{ s}^{-1}$. Experimental data sourced from $T=298\text{K}, 542\text{K}$ [159], $T=773\text{K}, 1123\text{K}$ [160].

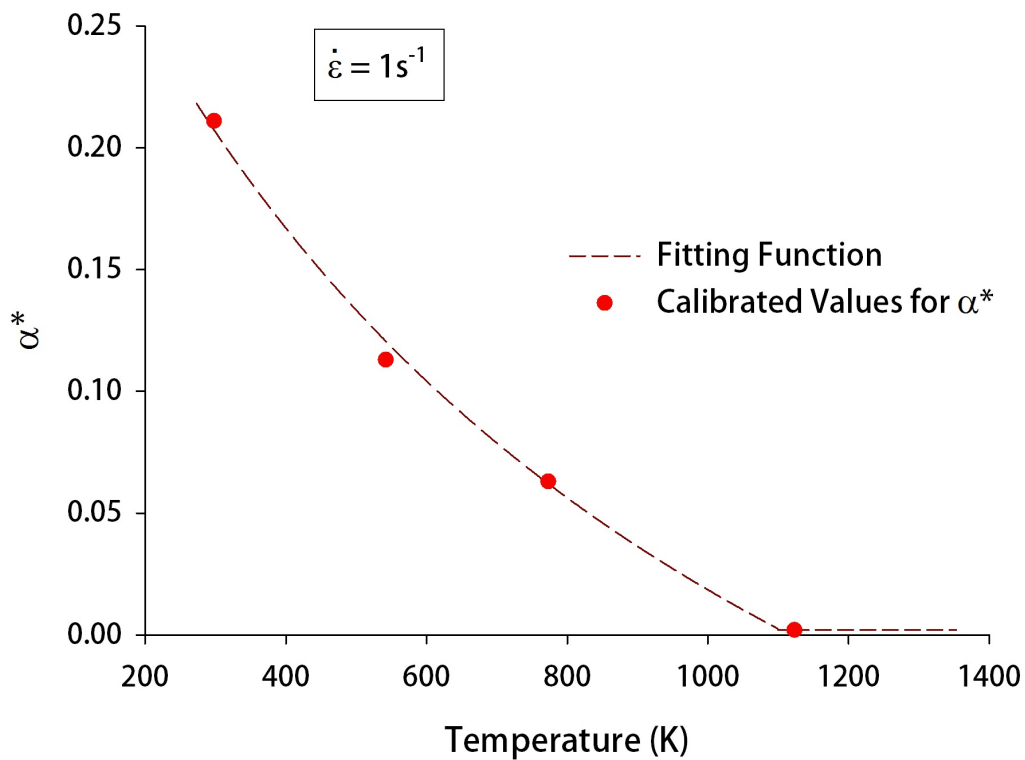


Figure 6.3: Fitted curve for calibration of temperature dependent α^* .

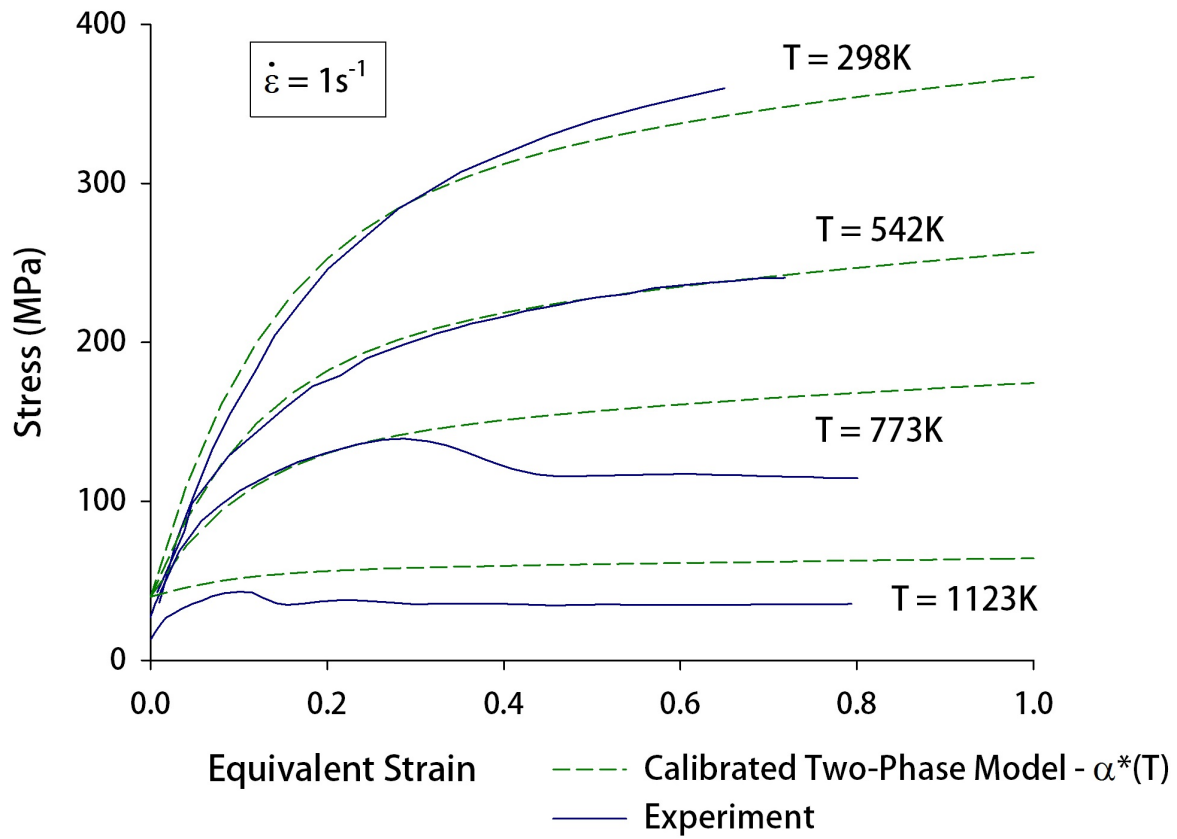


Figure 6.4: Flow stress response for calibrated two-phase model at various temperatures and a strain rate of $\dot{\epsilon} = 1 \text{ s}^{-1}$.

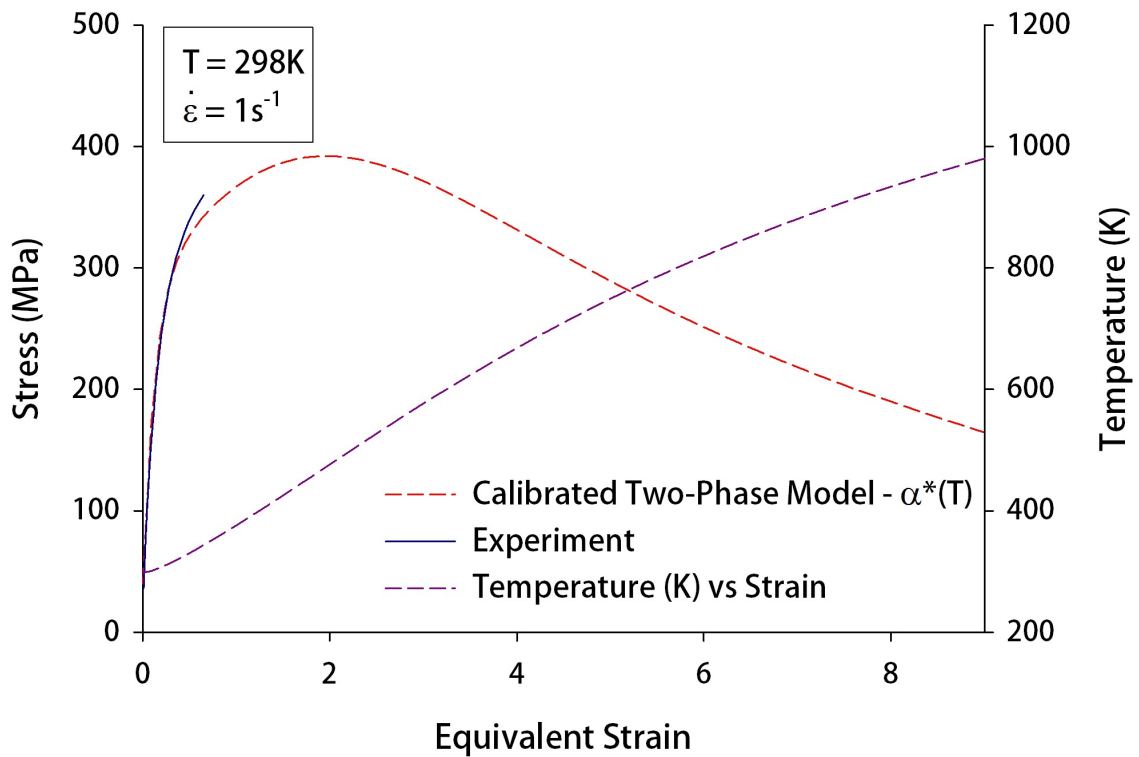


Figure 6.5: Flow stress and temperature response at T=298K and $\dot{\epsilon} = 1 \text{ s}^{-1}$.

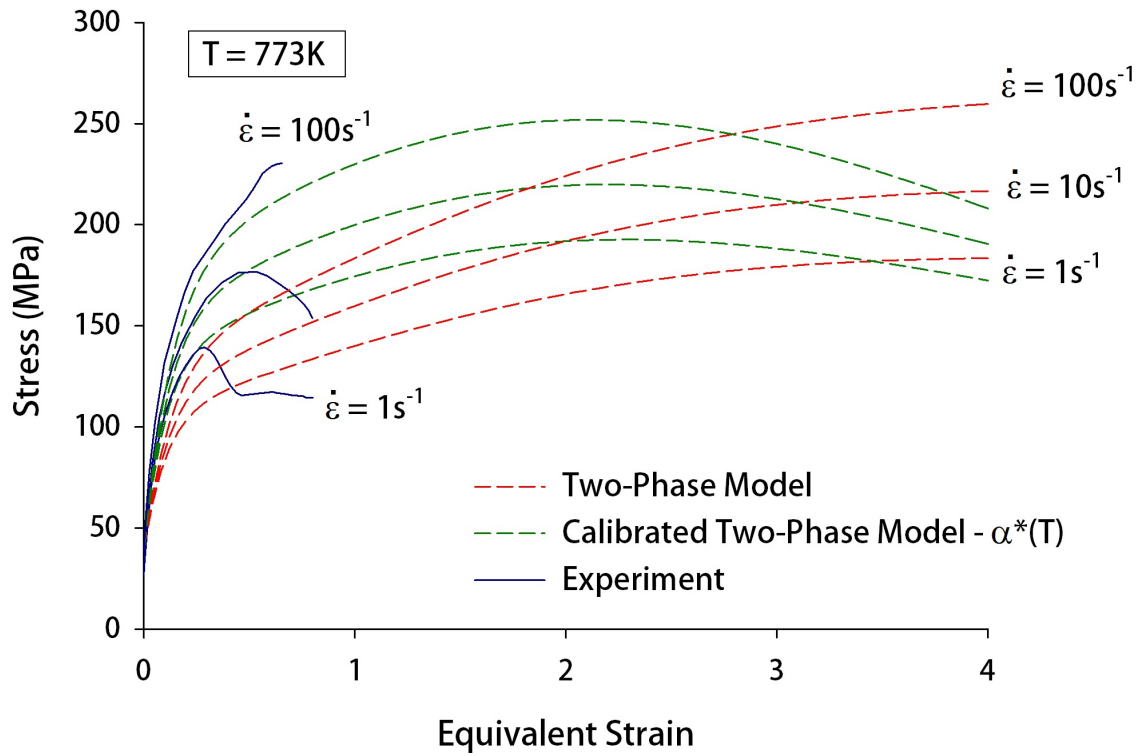


Figure 6.6: Comparison of both models to experimental compression tests at 773K. Experimental data sourced from [160].

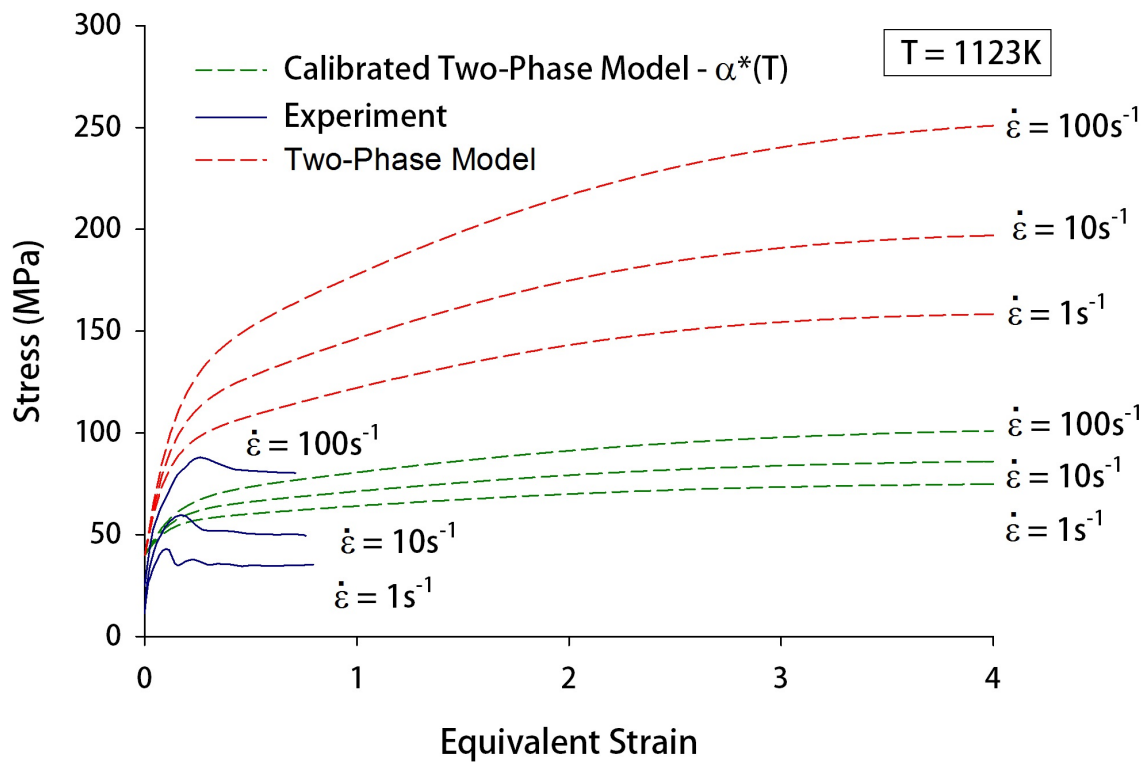


Figure 6.7: Comparison of both models to experimental compression tests at 1123K. Experimental data sourced from [160].

6.2.3.2 Aluminium Alloy 5005

As this material has not been calibrated for previously, β^* and k_0 must be determined in addition to α^* . A starting point is the original parameters determined for pure aluminium [105].

Applying the same method as explained above for copper, a fitting function is applied to determine the appropriate level of temperature dependence for α^* . The calibrated values are shown in Figure 6.8 by the red circle markers. The fitted function is displayed in dark red. The parameters for the fitted function are shown in equation (6.15).

$$\alpha^*(T) = \begin{cases} 0.22 & : T < 293 \\ \frac{46}{T-139.56} - 0.08 & : T \in \{293 \rightarrow 700\} \\ 0.001 & : T > 700 \end{cases} \quad (6.15)$$

The values for β^* and k_0 are 0.001 and 2.7 respectively.

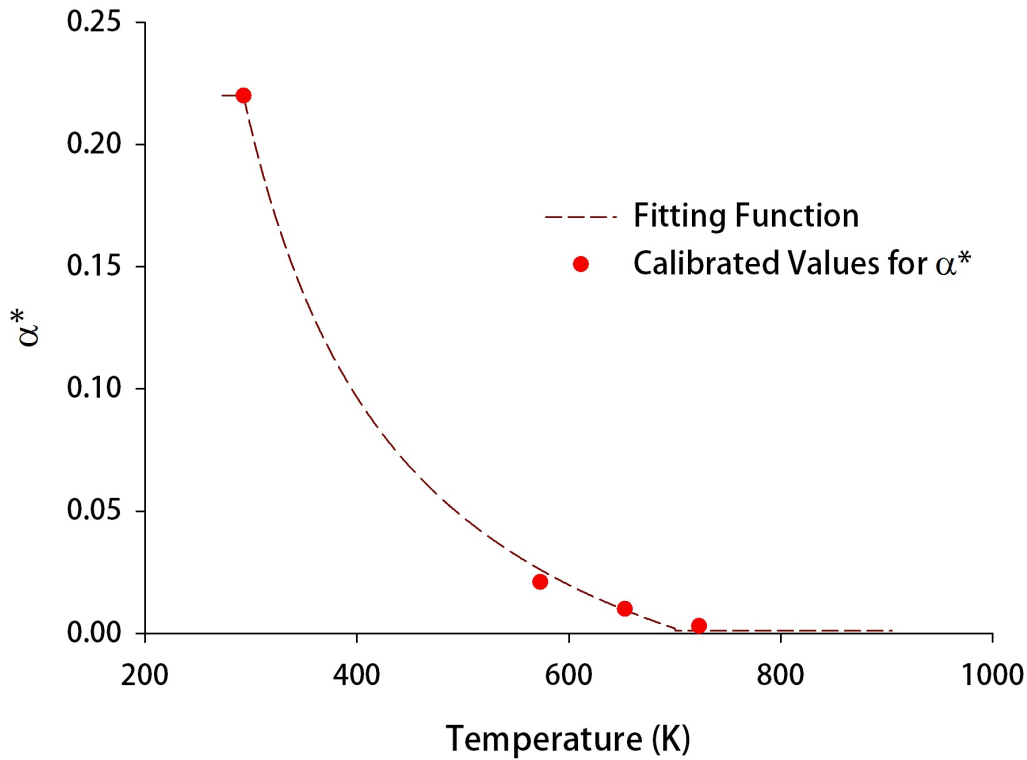


Figure 6.8: Fitted curve for calibration of temperature dependent α^* for aluminium alloy 5005.

Figure 6.9 shows the calibrated two-phase model against experimental tests carried out at $0.25\text{-}1\text{s}^{-1}$ and temperatures ranging from 293K-723K. The correlation is quite good, particularly at larger strain which is the region of interest for FSP.

Figure 6.10 shows the softening induced by the temperature dependent α^* . As the temperature increases due to plastic deformation, softening occurs due to the reduction of α^* . Without this temperature dependence, the stress tends to saturate despite high and near melting temperatures.

The following Figures 6.11, 6.12 and 6.13 show the flow stress response at higher temperatures (573K, 653K and 723K) for different strain rates (0.25s^{-1} - 25s^{-1}). There is some discrepancy at low strain, however the two-phase model tends to approach the experimental values at higher strains, which is reasonable in this application as high strains are expected in FSP.

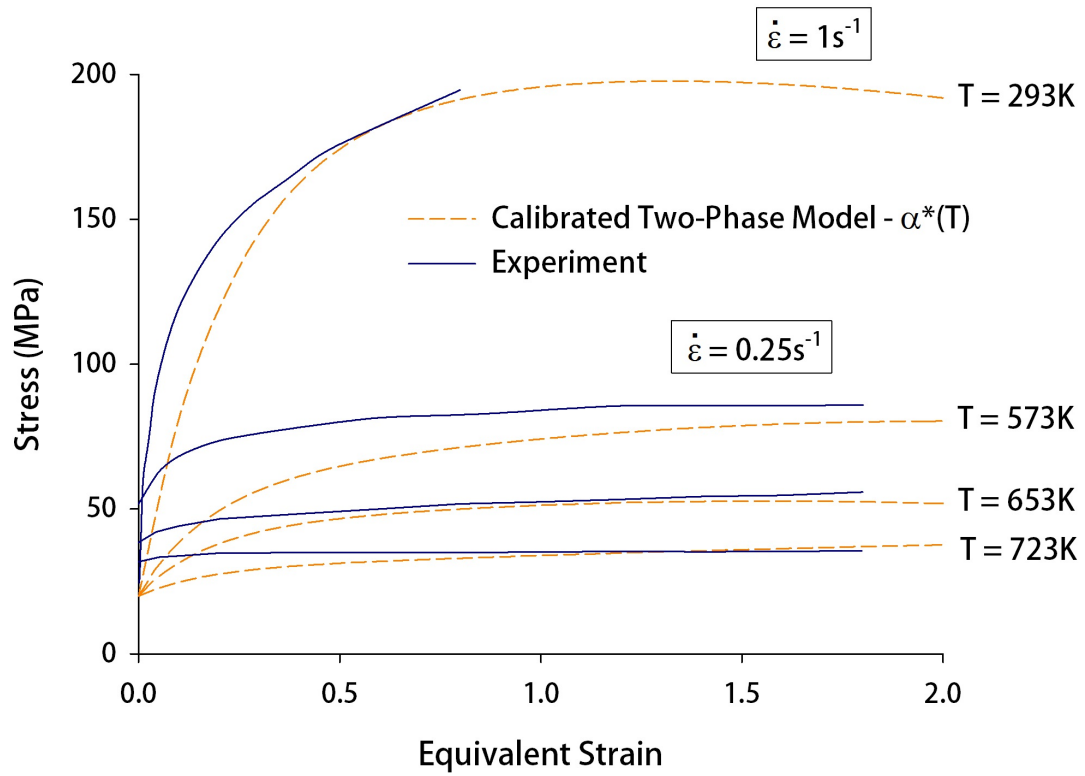


Figure 6.9: Flow stress response for calibrated two-phase model at a range of temperatures and strain rates of $\dot{\epsilon} = 0.25s^{-1}$ and $\dot{\epsilon} = 1s^{-1}$. Experimental data sourced from: $\dot{\epsilon} = 0.25s^{-1}$ [161] and $\dot{\epsilon} = 1s^{-1}$ [162].

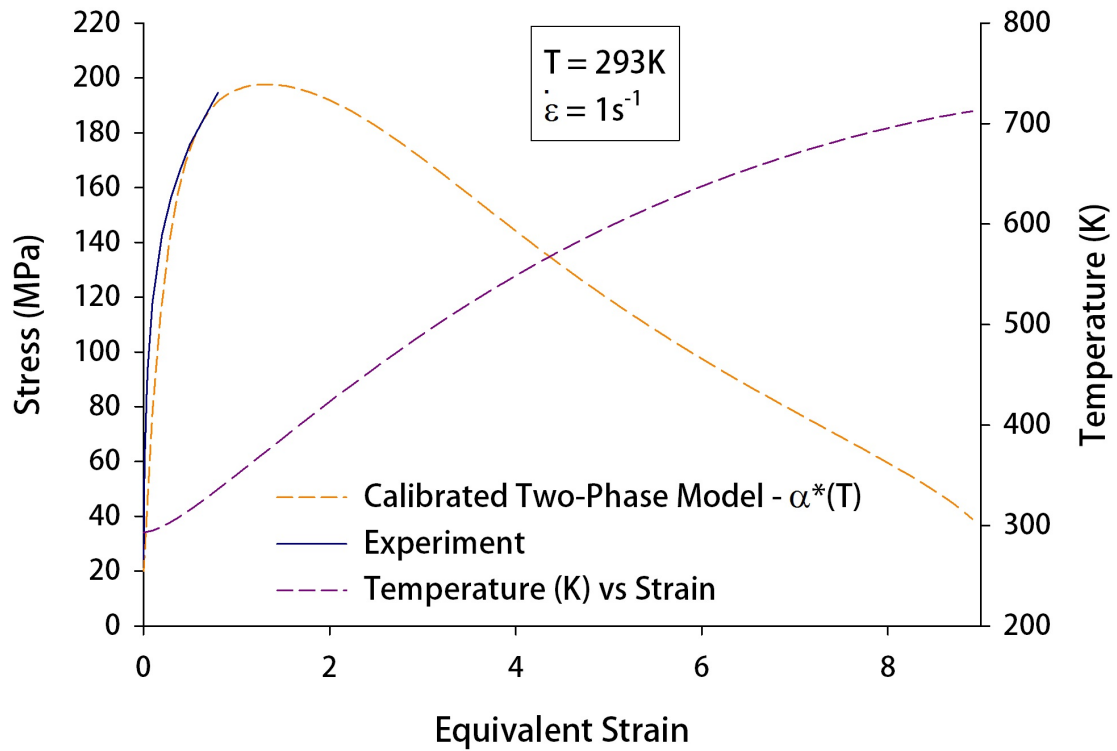


Figure 6.10: Flow stress and temperature response at $T = 293K$ and $\dot{\epsilon} = 1s^{-1}$.

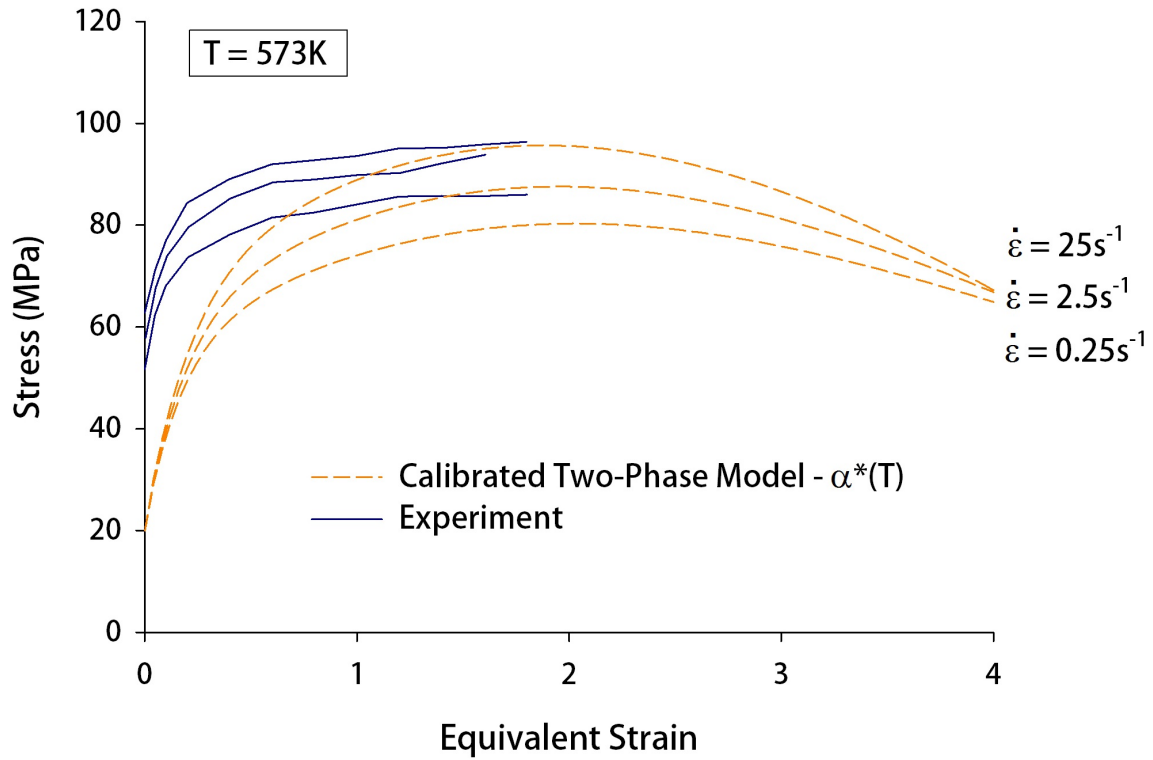


Figure 6.11: Comparison of two-phase model to experimental compression tests at 573K. Experimental data sourced from [161].

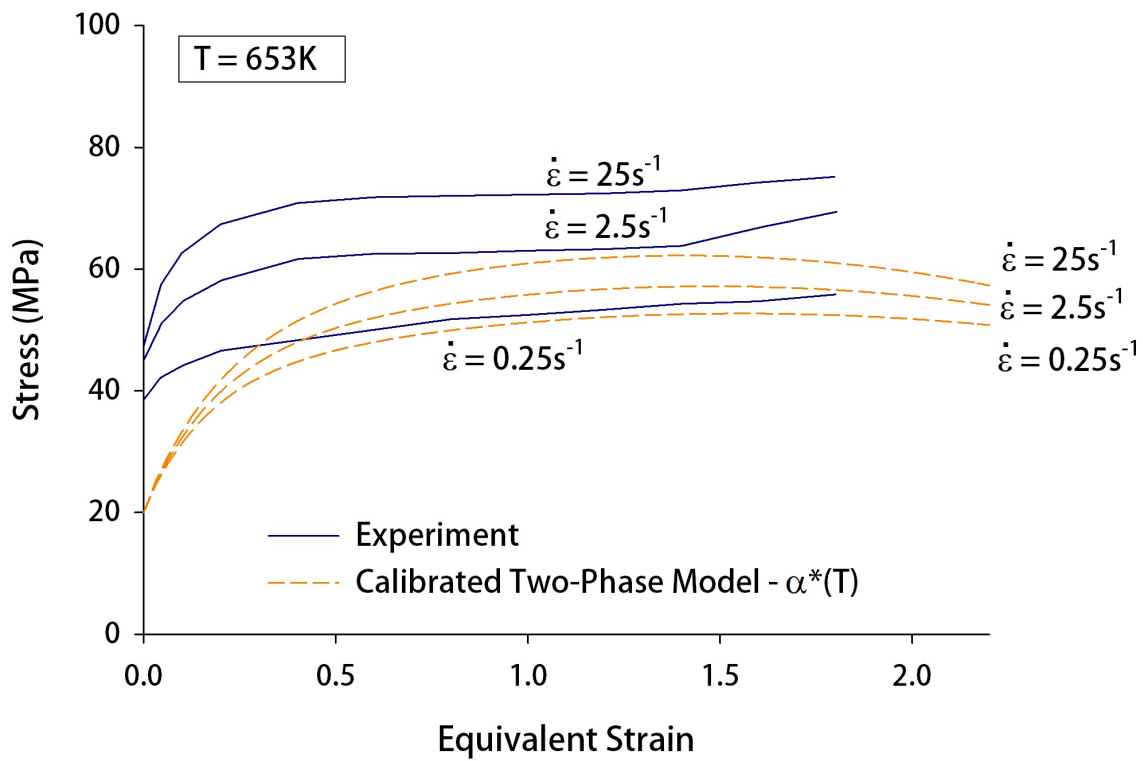


Figure 6.12: Comparison of two-phase model to experimental compression tests at 653K. Experimental data sourced from [161].

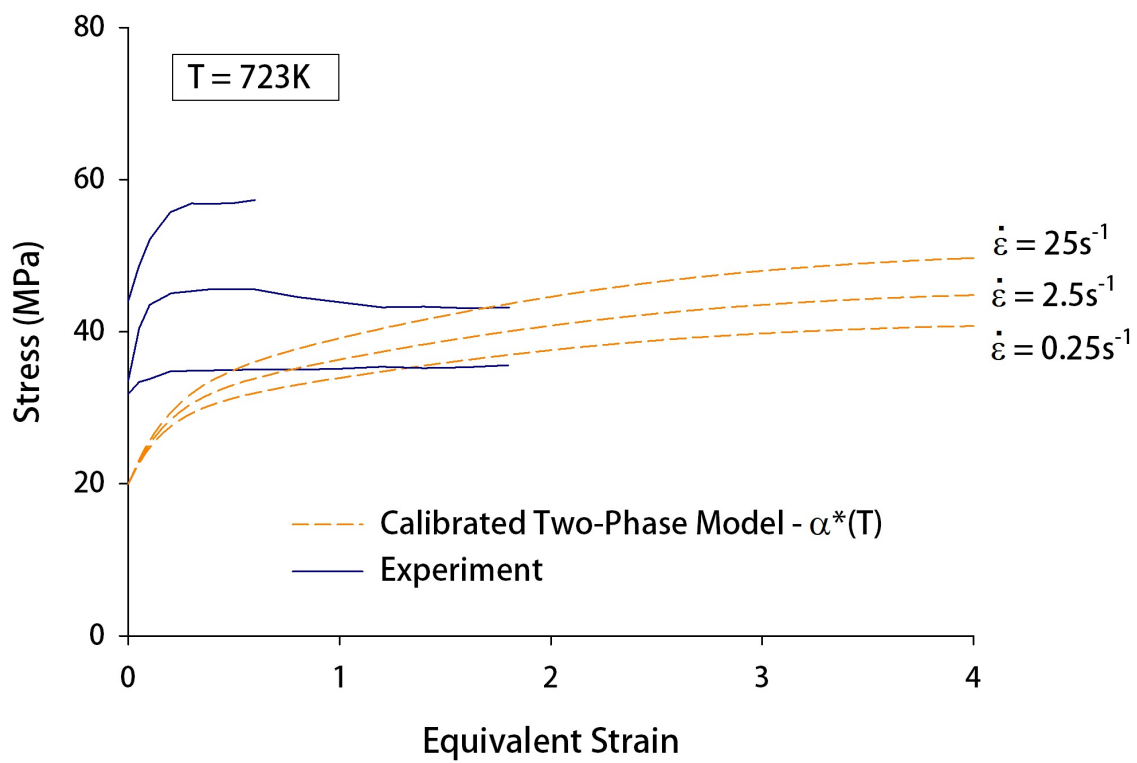


Figure 6.13: Comparison of two-phase model to experimental compression tests at 723K. Experimental data sourced from [161].

6.3 Establishing the Boundary Conditions for the Microstructure FSP Model

6.3.1 Thermal Loss to the Backing Plate and Surrounding Air

As mentioned in chapter 4, this model will use an improved method to determine thermal losses to the backing plate, which is via fitting an exponential decay curve to the thermal data in the cooling phase. This provides a more consistent relationship between dT/dt and $(T_{\text{room}} - T_{\text{body}})$. The fitted curve is shown in equation (6.16) and plotted against the thermocouple cooling phase data in Figure 6.14. The relationship dT/dt vs $(T_{\text{room}} - T_{\text{body}})$ is plotted in Figure 6.15 with the least squares regression applied for a linear polynomial fit. The plot shows a much more consistent fit than the previous methodology. Note that again cooling phase data is taken from 65 seconds on, which is when the rear of the tool is well past the edge of the plate.

$$T = 323 + 564e^{-0.0137t} \quad (6.16)$$

where T is the temperature (K) and t is the time (s).

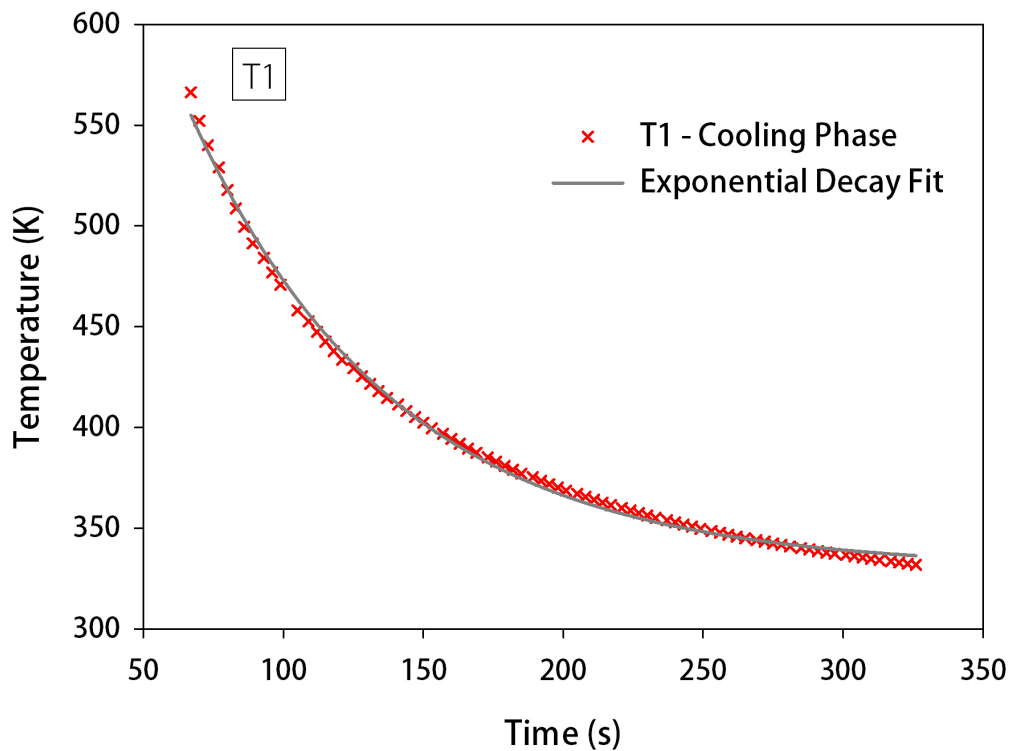


Figure 6.14: Experimental cooling phase (for the copper workpiece) plotted with a fitted exponential decay curve, equation (6.16).

Applying this improved fitting to the measurements obtained with thermocouples T1, T2, T3 yields gradients of -0.0137, -0.0144, -0.0138 respectively, and thus an average value of -0.0140. This slope is substituted into Equation (4.10) to determine the new global value for \bar{h}_c , namely 560 W/m²K. The values used to determine \bar{h}_c can be found in Table 6.2.

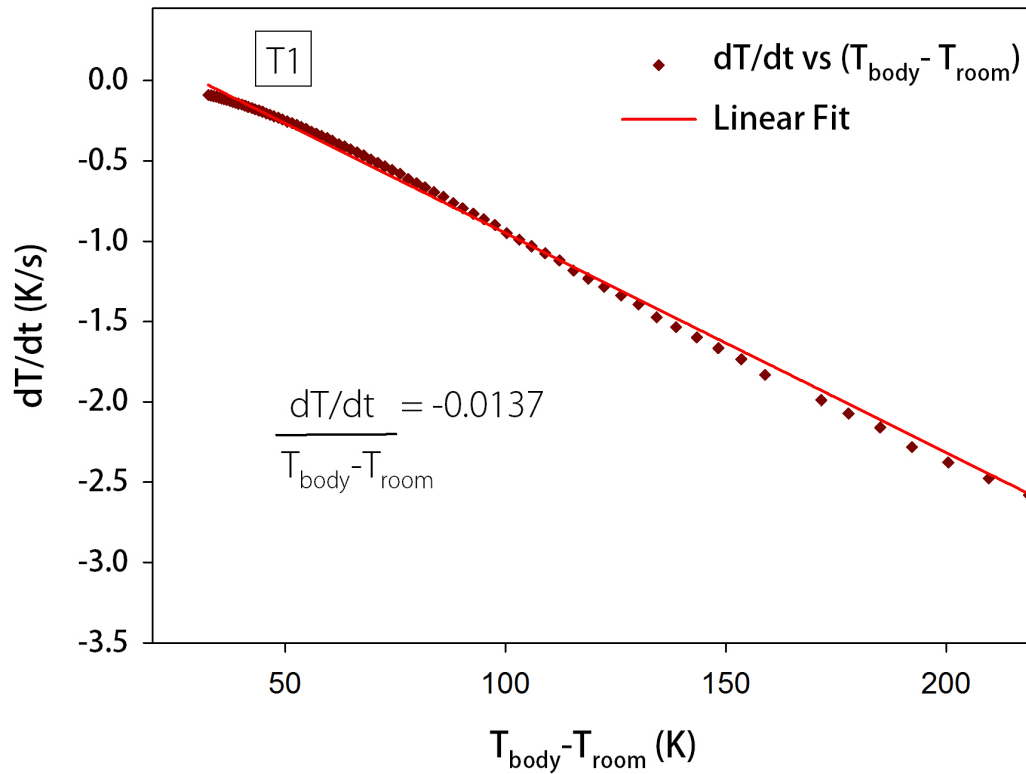


Figure 6.15: Plot of dT/dt vs $(T_{\text{room}} - T_{\text{body}})$ to determine the rate of change for substitution into equation (4.10).

ρ (kg/m ³)	C_p (J/kg-K)	V (m ³)	S (m ²)	$(dT/dt)/(T_{\text{body}} - T_{\text{room}})$	\bar{h}_c (W/m ² K)
8960	386	4.671×10^{-5}	0.004	-0.0140	560

Table 6.2: Values used for calculation of global convective coefficient, \bar{h}_c , for copper.

The same analysis undertaken for AA5005 yields the data in Table 6.3.

ρ (kg/m ³)	C_p (J/kg-K)	V (m ³)	S (m ²)	$(dT/dt)/(T_{\text{body}} - T_{\text{room}})$	\bar{h}_c (W/m ² K)
2700	900	2.576×10^{-5}	0.004	-0.0127	200

Table 6.3: Values used for calculation of global convective coefficient, \bar{h}_c , for AA5005.

6.3.2 Friction Coefficient Between Tool and Workpiece - AA5005

The same methodology is used as described in Chapter 5 to determine the friction coefficient. The result for about 6 seconds of runtime for a pin translation speed of 120mm/min is shown in Figure 6.16.

Temporal averages of the friction coefficient for each run are shown in Table 6.4.

The average friction coefficient is 0.28 to two decimal points, and the coefficient applied in this work was 0.3. An investigation into friction in FSW of aluminium found 0.3 to be the best

calibrated value from a range of values and alternative friction laws [163] and has also been used in other work [114].

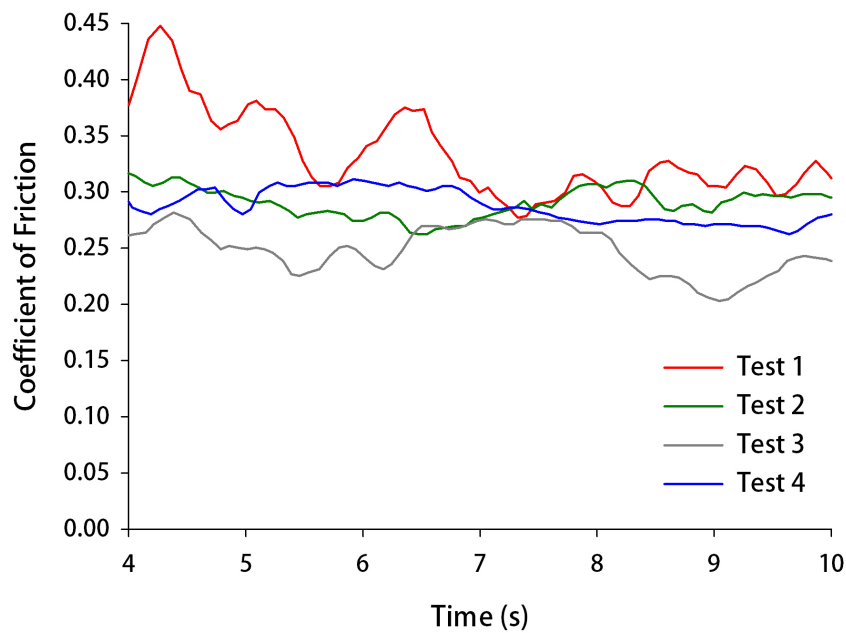


Figure 6.16: Plot of experimentally determined coefficient of friction over time (~4s) for a translation speed of 120mm/min for AA5005.

Speed	Test 1	Test 2	Test 3	Test 4	Test 5	Test 6	Average
120mm/min	0.31	0.25	0.25	0.26	0.29	0.29	0.28

Table 6.4: Temporal averages of the friction coefficient for Tests 1-6 at speeds of 120mm/min for AA5005.

6.4 Comparison of Experiment with the Obtained Dislocation-Density Based Model of FSP

6.4.1 Resulting Temperature Field

6.4.1.1 Comparison of Calculated Temperature Profile with the Experimental Result

Figure 6.17 shows the physically-based model is predicting the peaks quite well, T1 within 7% and 10% respectively, T2 within 1% and 7%, and T3 within 3%. This is a consistent improvement on the Johnson-Cook model predictions. One thing to note is the decrease in accuracy for the latter temperatures of T1 and T2. This is surprising as the trend in heat loss is quite good and the initial peaks for all three thermocouples are also reasonably accurate.

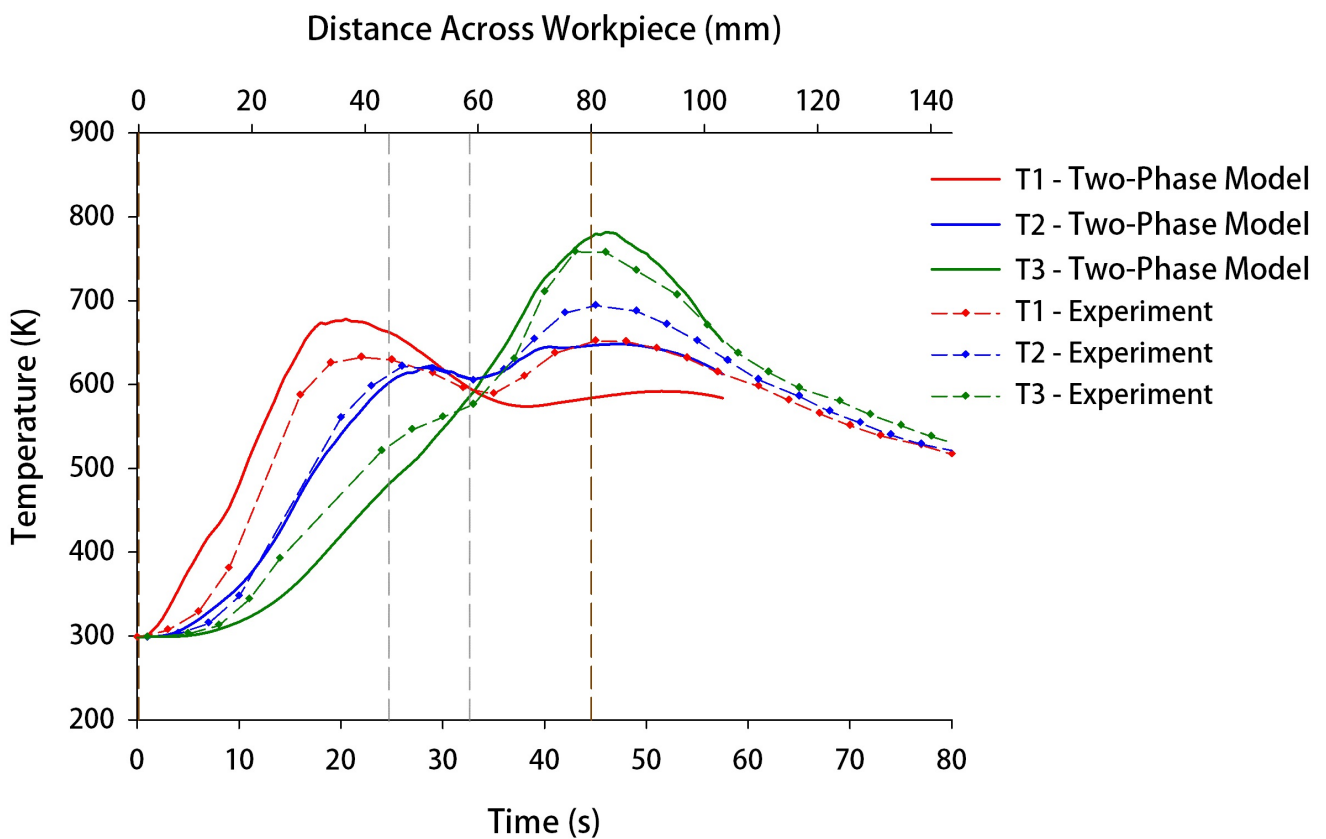


Figure 6.17: Temperature profiles over time with the Dislocation-Density based material model, for T1, T2 and T3 compared against experiment (for the copper workpiece).

6.4.1.2 Analysis of Surface Temperature

Figure 6.18 shows the surface temperatures across the workpiece at 10s, 25s and 40s. All three models give a satisfactory description of the temperature profiles.

6.4.1.3 Comparison of the Thermal Field for All Models

Figure 6.19 shows the dislocation-based two-phase model compared against both the thermal model and Johnson-Cook thermo-mechanical model for the thermocouple temperatures

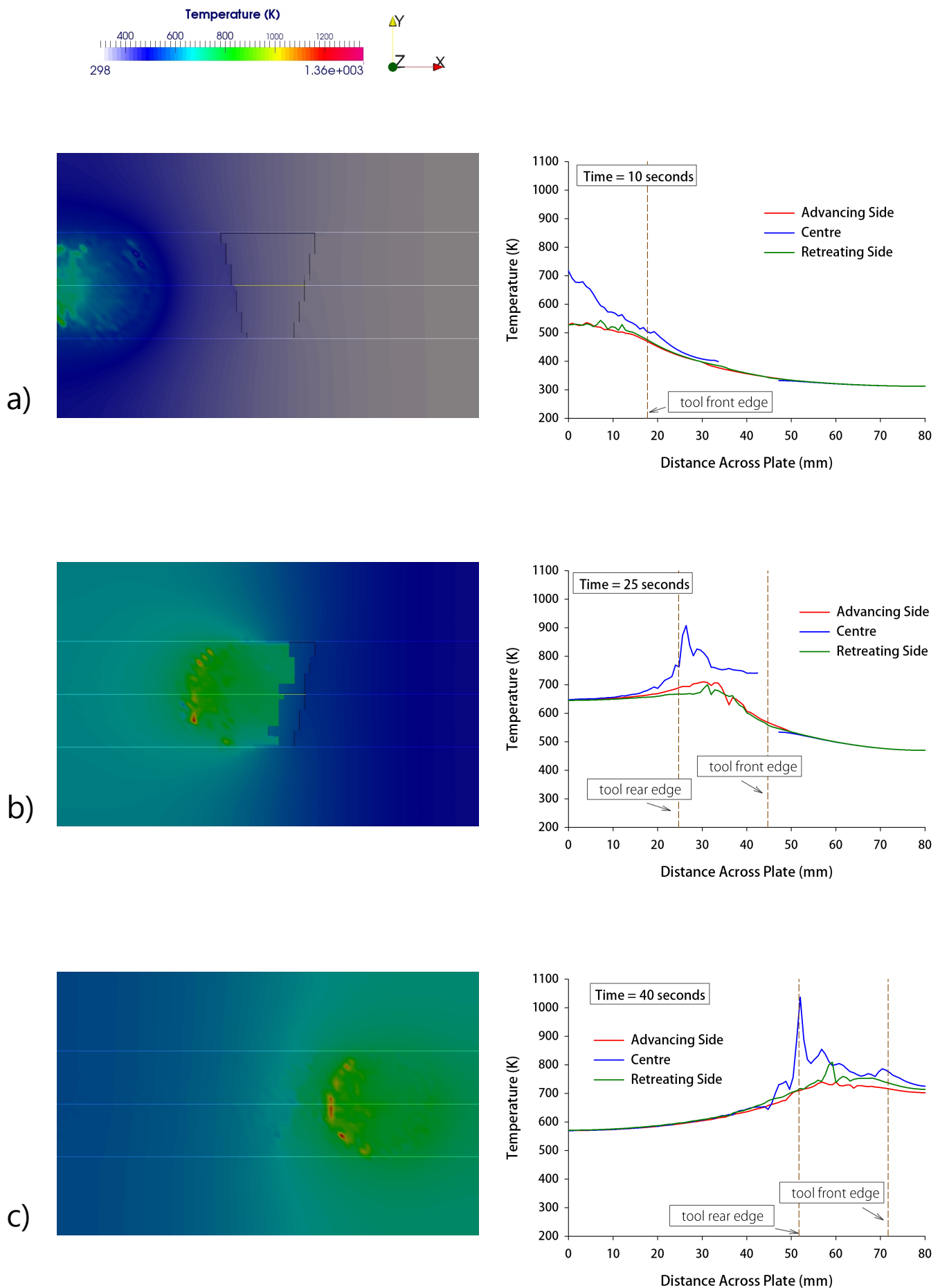


Figure 6.18: Temperature 1mm below the surface at times of a) 10s, b) 25s, c) 40s. Left image is the temperature across the slice, right is the temperature across each line on the advancing, centre and retreating sides (for the copper workpiece).

over time. The thermal model prediction is initially higher, but lower towards the end of the plate. It is a similar trend to that between the JC model and the thermal model, likely for the same reason, that the softening induced by the applied yield stress vs temperature curve is quite strong at higher temperatures. The comparison to the JC model reveals that in general the two-phase model predicts a lower temperature throughout. Again probably due to the stronger softening in the two-phase model. The different rate of cooling after the tool leaves the plate is due to the reduced backing plate convection coefficient applied in the two-phase model.

Figure 6.20 isolates the thermocouples for better comparison between the models and experiment. As the thermal and JC models have been analysed in the previous chapter, the focus here will be on the two-phase model. For T1, the two-phase model more accurately predicts the first peak but similar to the other models fails to gain the required temperature for the secondary peak. In T2, the two-phase model presents an excellent comparison for heat loss as the tool traverses the cavity, but again fails to regain the required temperature to match the secondary peak. For T3, the inflection as the tool travels over the cavity is improved over the JC model, but the trend is still not as accurate as the thermal model. All in all, a reasonably good performance of the dislocation-based model was demonstrated. Thus, the benefits of the model in terms of its ability to predict microstructure evolution are achieved without sacrificing its predictive capability with respect to the thermal aspect of the problem.

Figure 6.21 shows the comparison of surface line temperatures across the advancing side, centre line and retreating side, respectively. The temperature predicted by the dislocation-based two-phase model is consistently lower than the other two models, likely due to the improved temperature dependence and softening. For all three sides, the temperature is initially similar to the Johnson-Cook model, and as the simulation progresses, the improved softening reduces the temperature down to that predicted by the thermal model.

6.4.1.4 Source of Thermal Energy During FSP

Figure 6.22 shows the source of energy for thermal changes in the workpiece. It demonstrates that the vast majority is from friction, contributing between 95-98% of the total thermal energy in the system. This is similar to results by Hamilton et al. [121] who found friction contributed 98% of the thermal energy in the system.

6.4.1.5 Summary of Temperature Analysis Using the Two-Phase Model

The thermal field predicted by the two-phase model compares favourably with the experimental results, within 10% for the thermocouple predictions. The model also improves upon the prediction of the Johnson-Cook constitutive model, although some discrepancy may lie in the corrected backing plate convection coefficient.

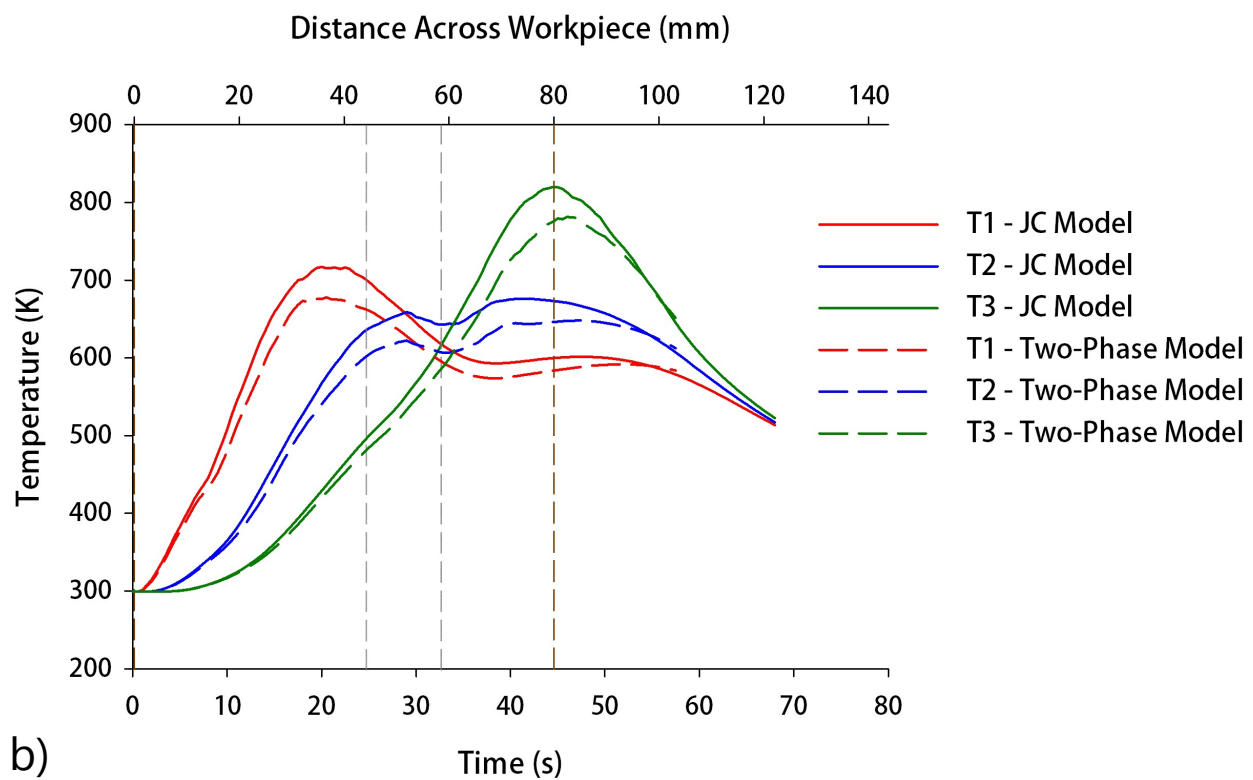
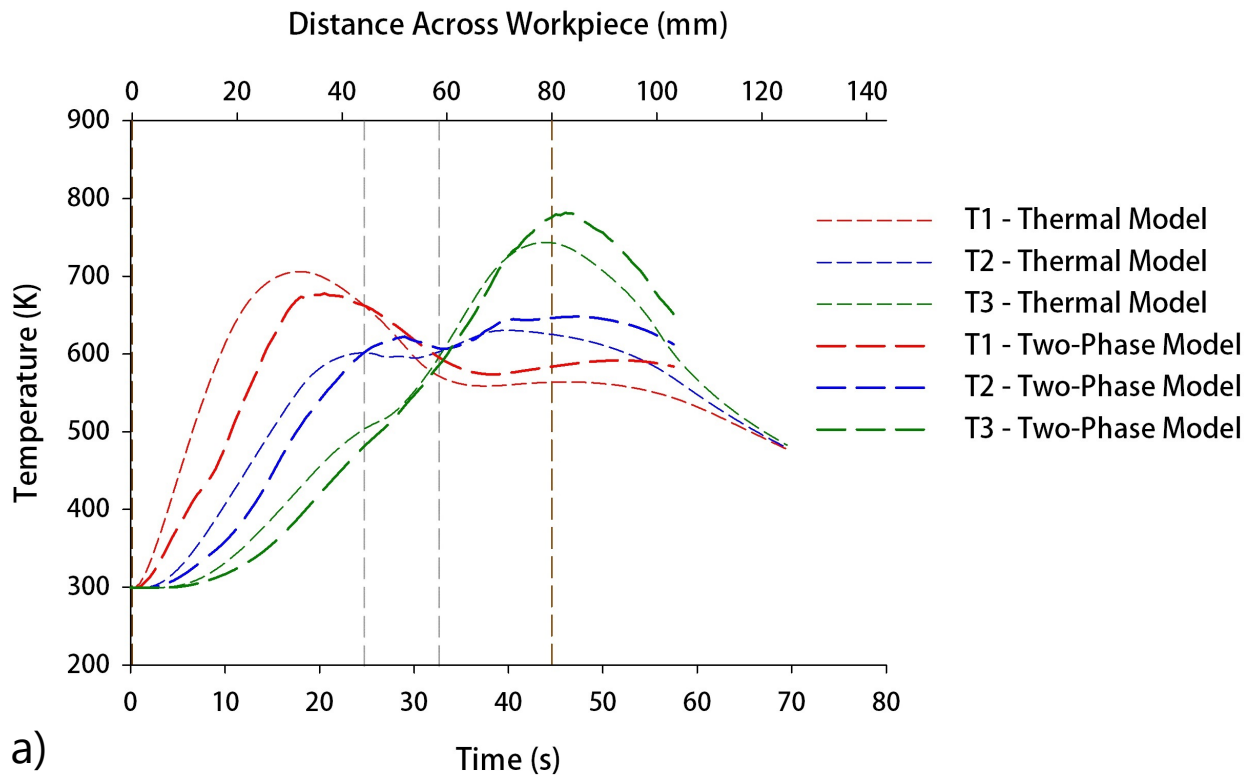


Figure 6.19: Comparison of temperature profiles over time for T1, T2 and T3 predicted by all three developed models a) two-phase and thermal model, b) two-phase and Johnson-Cook thermo-mechanical model (for the copper workpiece).

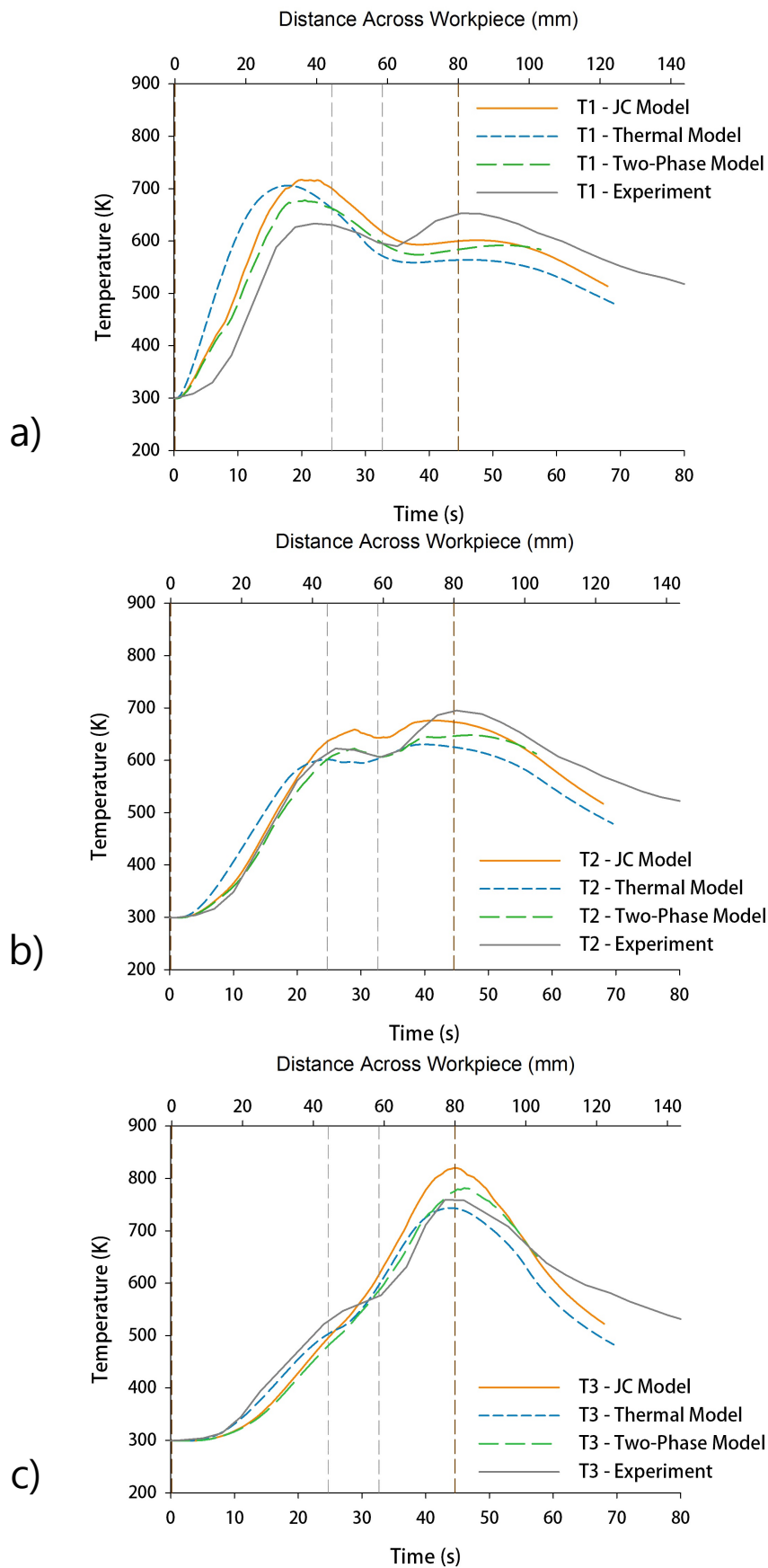


Figure 6.20: Comparison of temperature profiles over time predicted by the two-phase model, Johnson-Cook model, thermal model and experiment for a) T1, b) T2 and c) T3 (for the copper workpiece).

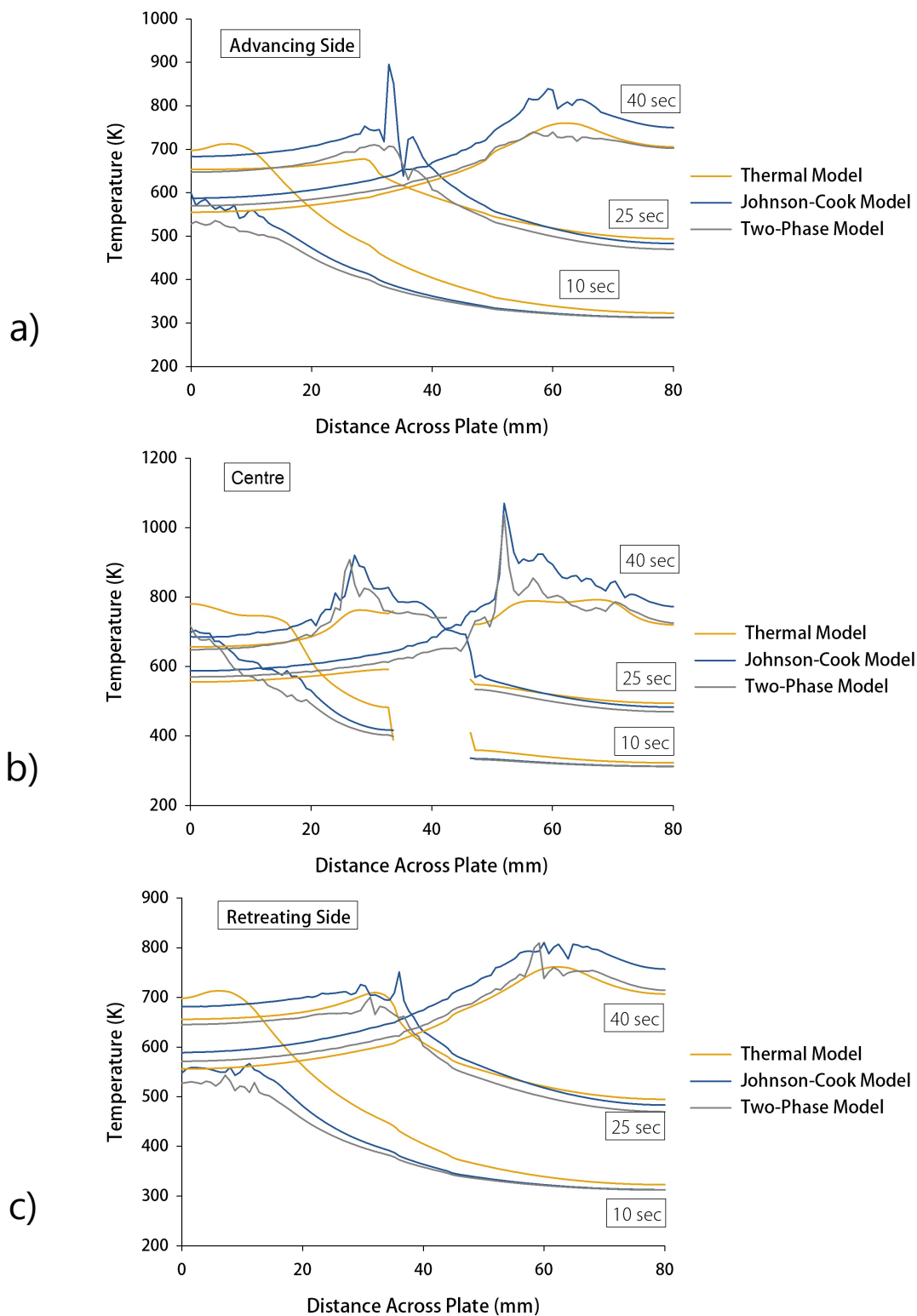


Figure 6.21: Temperature 1mm below the surface across each line on the a) Advancing Side b) Centre Line, c) Retreating Side for all three models (for the copper workpiece).

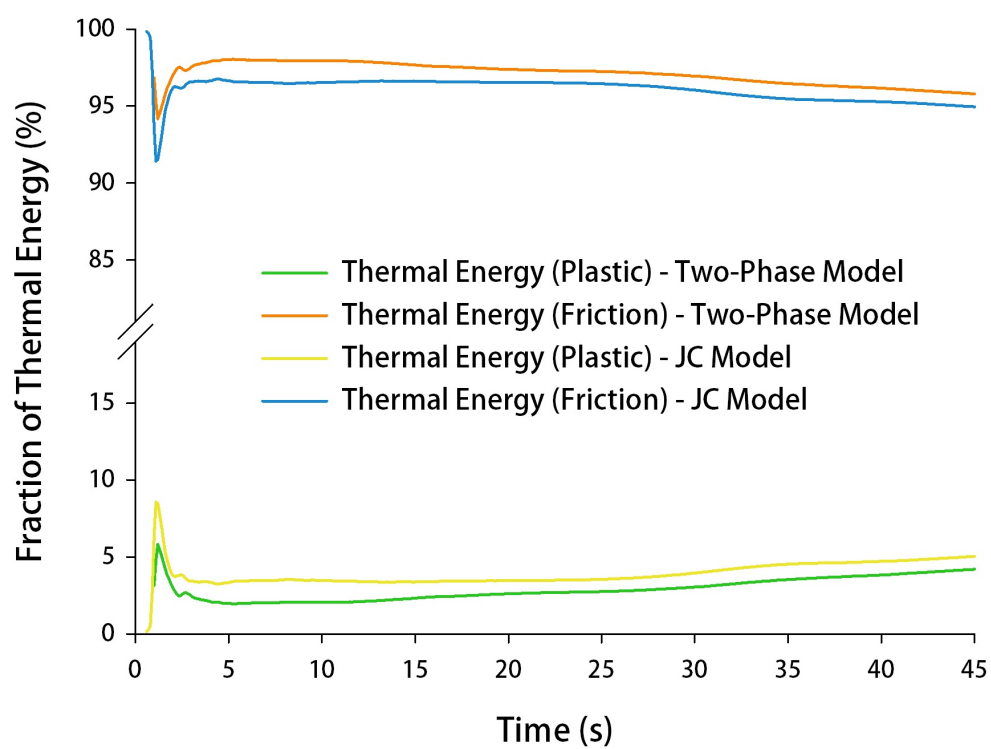


Figure 6.22: Source of thermal energy (%) in FSP of copper for the two-phase model and the Johnson-Cook thermo-mechanical model.

6.4.2 Resulting Material Flow

6.4.2.1 Flashing on the Surface of the Workpiece

Figure 6.23 shows a comparison of the numerical flashing to the experimental flashing for cavity 1. The two-phase model displays similar behaviour to the Johnson-Cook model in that the retreating side attracts a greater amount of material, consistent with the tool rotation. Observing Figure 6.24, the shape and spread of material seems reasonably consistent with the experiment, noting similar height and triangular shape. In general there is more flashing (similar to the JC model), and to some degree this can be attributed to mass scaling and possibly an insufficient resolution for this particular region. In comparison to the Johnson-Cook result (Figure 5.21), the retreating side flash has a more consistent height with less over-prediction compared to the experiment.

6.4.2.2 Surface Flow Visualization with Particle Pathlines

In general these series of results are similar to the Johnson-Cook model with less drastic deformation in some areas. It is hard to determine which is more accurate however. The overriding factor in the material flow may in fact be the mass scaling factor applied, rather than the material law, although some differences are noticed.

Figure 6.25 shows the particles along the processing path at the surface and have great similarity to the Johnson-Cook prediction. There is little difference to note in this case.

ADVANCING SIDERETREATING SIDE

Figure 6.23: Copper flashing after processing (experimental and numerical) shown by a) Advancing side - Experiment (processing direction to the left), b) Advancing Side - Numerical, and c) Retreating side - Experiment (processing direction to the right), d) Retreating side - Numerical. Note that the thermocouple holes were machined on the other side to the simulation for this particular plate.

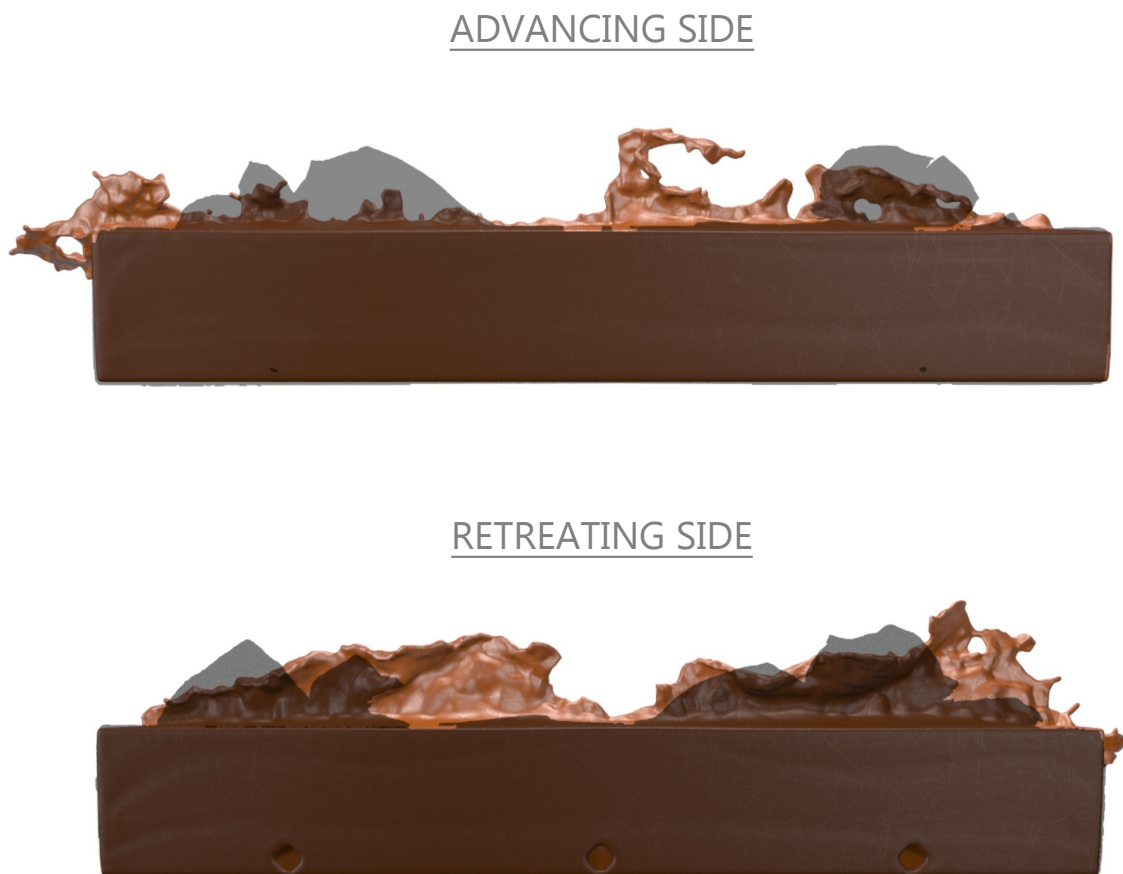


Figure 6.24: Overlaid images of simulation and experimental results according to processing side, top) advancing side flash, bottom) retreating side flash. The dark shadow shows the experimental flashing.

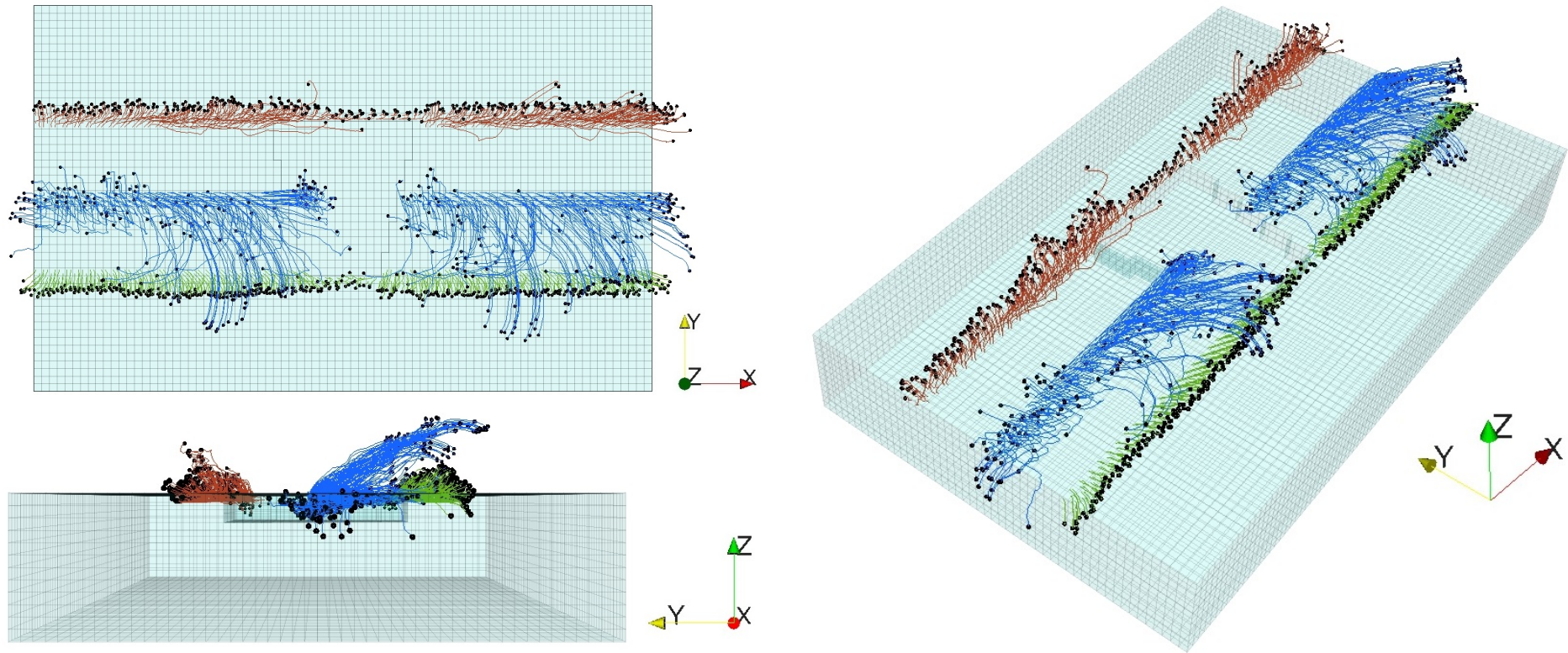
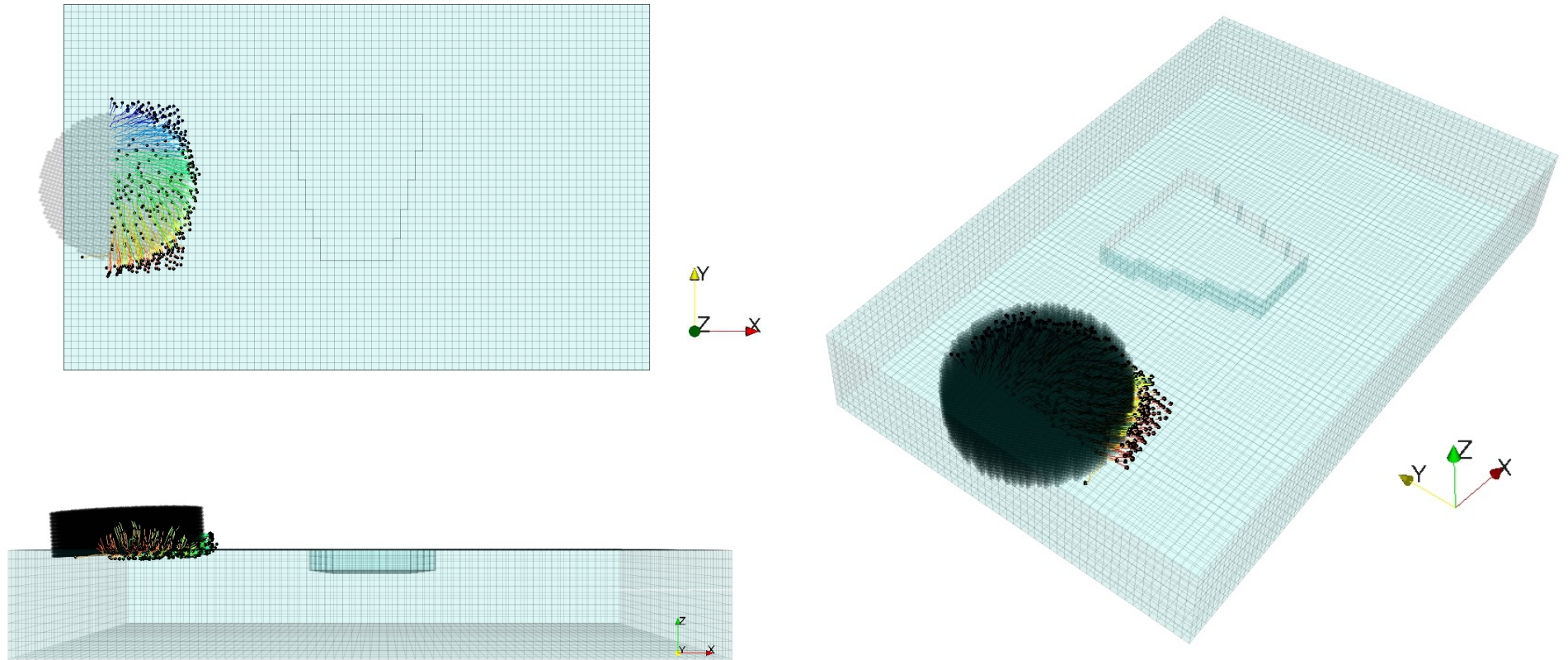
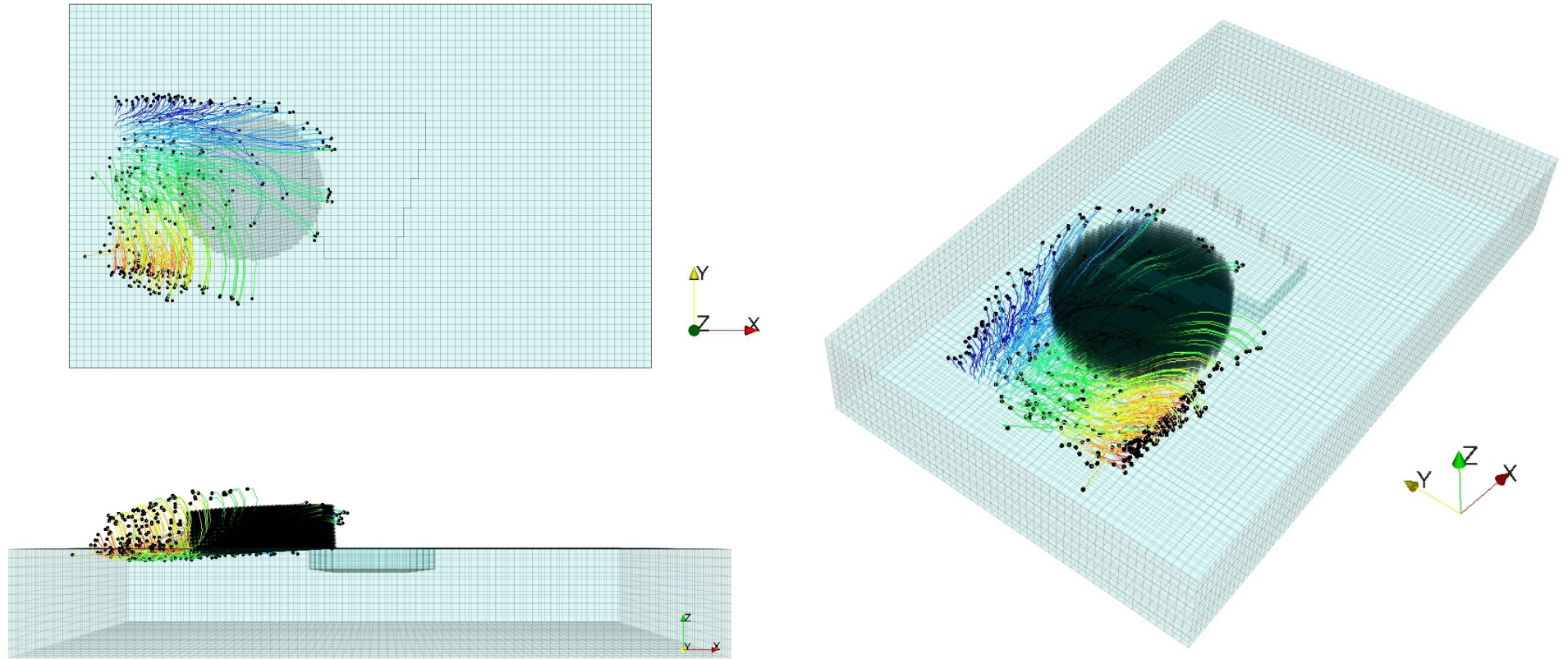


Figure 6.25: View of completed particle paths. Viewing angle clockwise from top left) top view (parallel projection), aerial view (perspective), processing direction view (perspective).

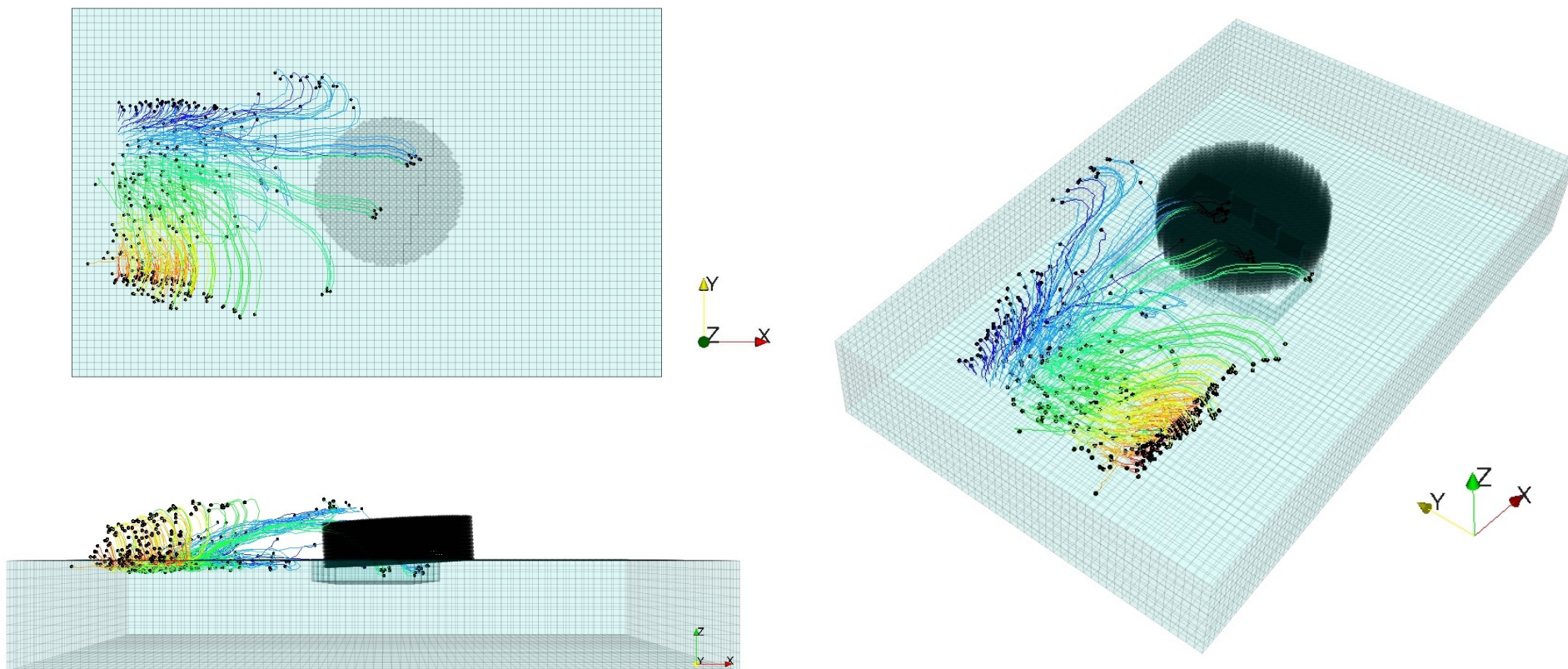
The following figures show the particle flow for a box on the surface. The deformation pattern is similar to that previously noted (section 5.4.2.2), with particles flowing clockwise with the tool rotation. A smaller deformation field is noticed however, with a reduction in the number of particles pushed forward and the distance of those that do.



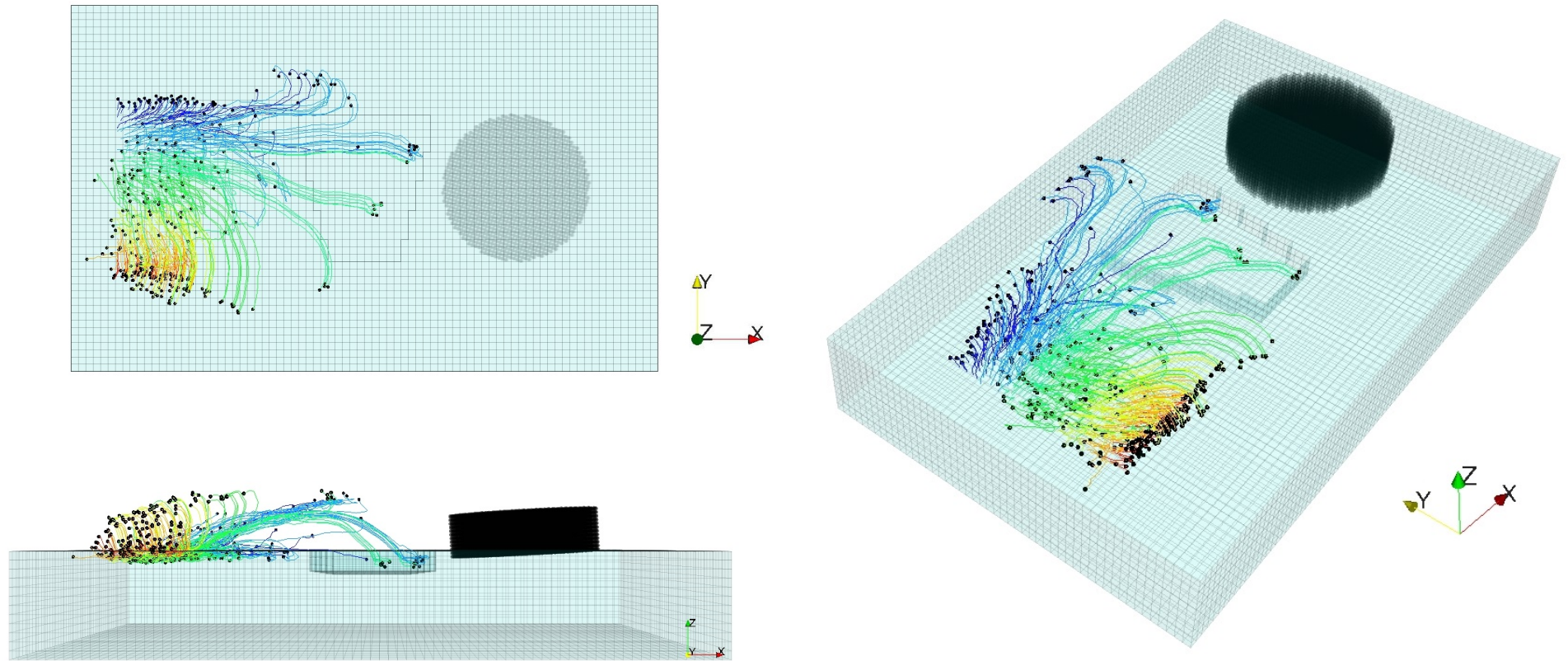
Time = 10 seconds



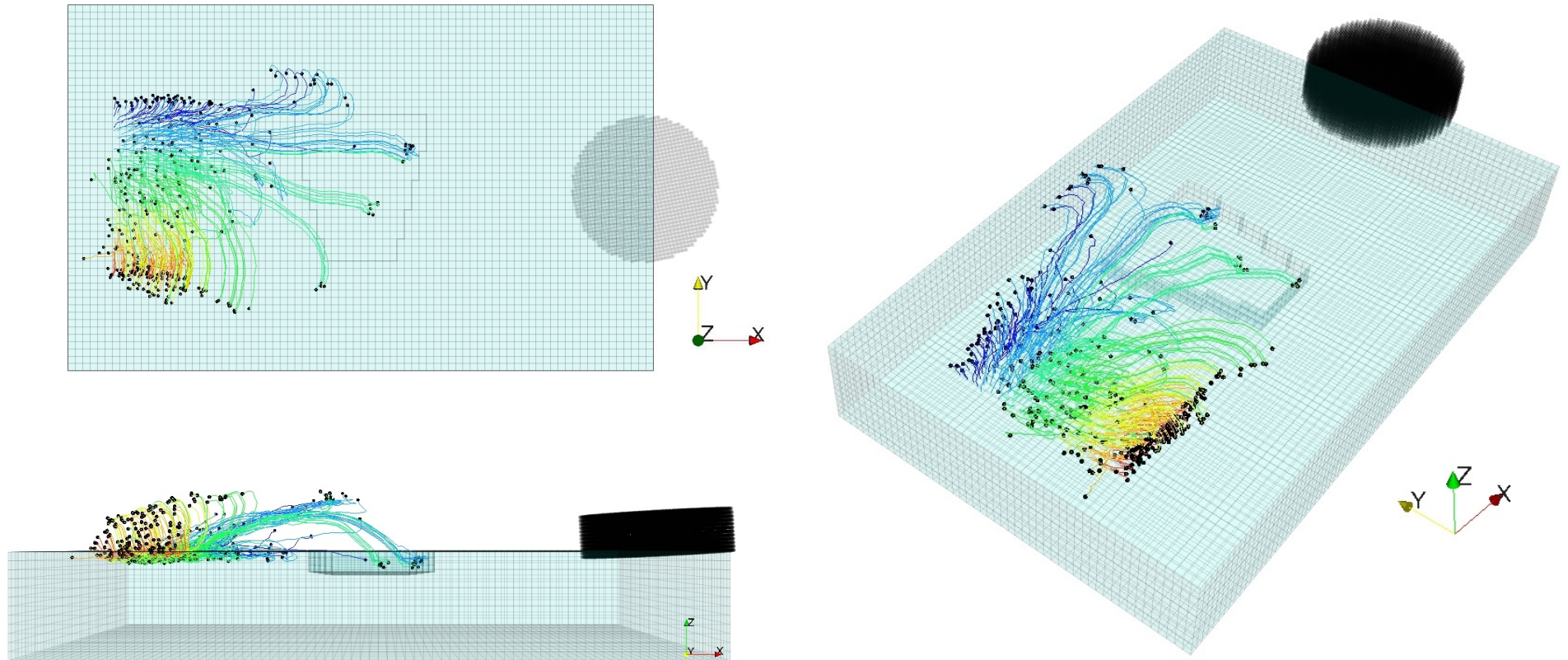
Time = 20 seconds



Time = 30 seconds



Time = 40 seconds



Time = 50 seconds

6.4.2.3 Material Filling of the Trapezoidal Cavities

Figure 6.27 shows the final material flow developed for cavity 1 in both the experiment and numerical models. Figure 6.28 highlights the experimental and numerical material flow for all cavities.

In general, the surface is more consistent in the two-phase model with less holes and "islands" as compared to the JC surfaces. Both models predict the flow of material into the cavity from the top left, which coincides with the rotation of the tool. The most accurate surface is achieved with the two-phase model for cavity 3 - it accurately captures the filling of material from the top left leaving a triangular shaped region free of material. The hole is smaller but the shape is quite consistent. The simulation also displays a good approximation of the reverse flow of material at the bottom right side of the cavity, where the tool rotates material into the cavity as it exits.

Table 6.5 shows a comparison of the filling percentage (via grid volume approximation) to give an indication of relative model accuracy. Note that this does not take into account correctness of filling shape. The two-phase model shows a filling percentage closest to the experiment for cavity 1 and 3, within 5% and 8% respectively, while the Johnson-Cook model gives an excellent result for cavity 2, within approximately 0.5%.

To demonstrate more accurately the difference in the particle distribution, Figure 6.26 shows the material particles in cavity 3 with the surface generated for both the JC and two-phase models. For the JC model, the region outside of the surface still maintains a large number of particles. As discussed in section 5.4.2.3, this is a consequence of the reliance on particle separation to generate the surface. The surface generated for the two-phase model is more representative of the particles and also a better match to experiment. The excess material flow observed in both numerical models could be due to the effect of mass scaling and insufficient resolution.

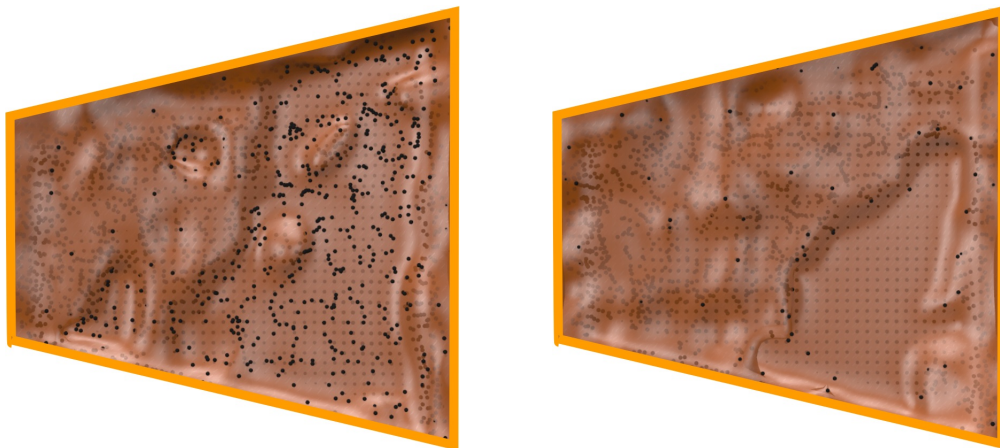


Figure 6.26: Overlay of material particles (black) and the generated surfaces for the JC model and two-phase model (cavity 3).

Cavity	Experiment	Simulation - JC		Simulation - Two-Phase	
	%Fill	%Fill	%Error	%Fill	%Error
1	68	61	7	66	5
2	59	59	0.5	80	21
3	69	53	16	77	8

Table 6.5: Approximate percentage of material filling for each cavity in the experiment and both thermo-mechanical models, Johnson-Cook and two-phase (to two significant figures).



Figure 6.27: Final material flow into cavity 1.

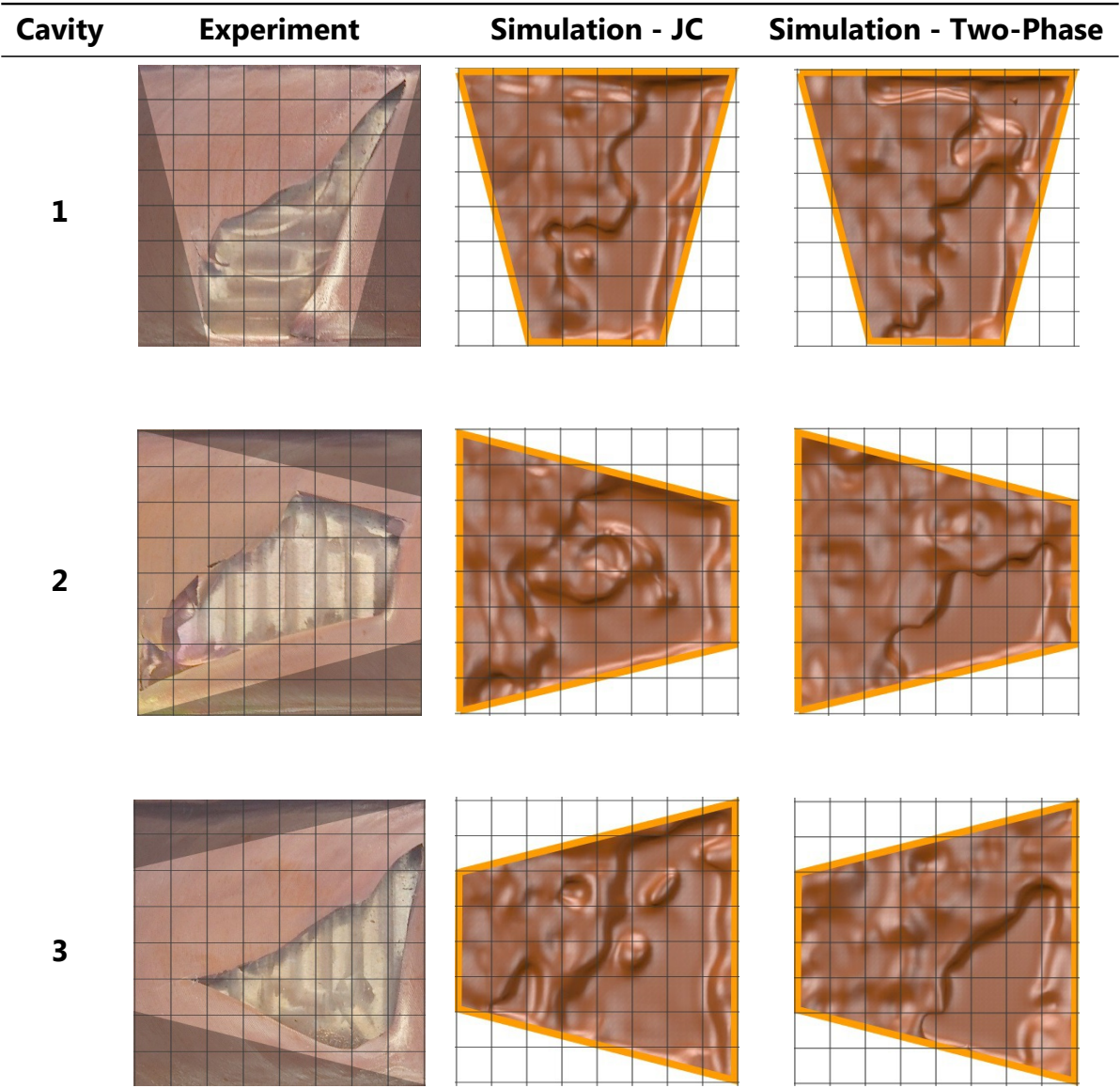


Figure 6.28: Cavity filling for the experiment and both thermo-mechanical models, Johnson-Cook and two-phase.

6.4.2.4 Cross-Section Material Flow During FSP of Cu

Figure 6.29 shows material flow for tracer material (black coloured copper particles) placed in the cross section, similar to experiments carried out in literature [60, 155]. The major difference in this numerical simulation is the absence of a pin. The pin (or lack of) has significant effects on the material flow in subsurface layers, as noted in section 5.4.2.2 (on subsurface particle flow). As a consequence, Figure 6.29 displays limited flow of tracer material forward along the tool path. The figure also shows particles distributed up to $1.5\times$ the tool diameter along the tool path, roughly 56% deposited on the advancing side of the workpiece. In general, this processing behaviour is consistent with a surface processing technique and use of a pinless tool. The lack of subsurface flow is also what makes this type of pinless tool ideal for use in FSF, where subsurface deformation must be avoided to ensure no damage to an interlocking material.

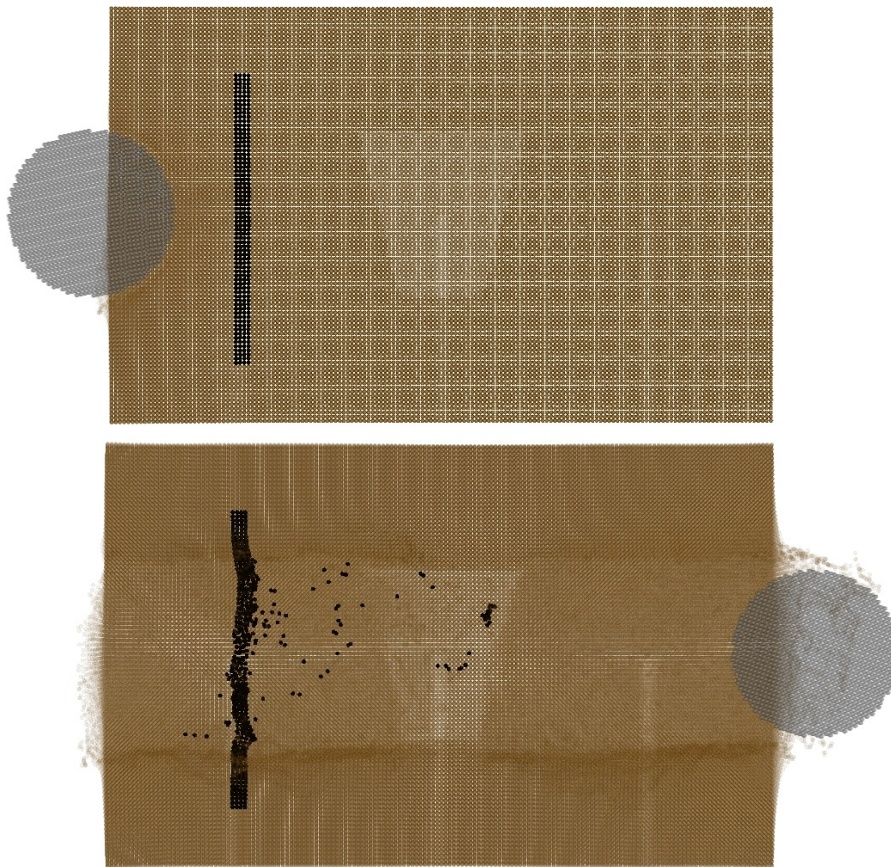


Figure 6.29: Cross-section material flow analysis.

6.4.2.5 Material Flow at the Tool Interface During FSP of Cu

Figure 6.30 shows the material flow and velocity at the tool interface 15s and 40s into processing. In contrast to the previous material flow predicted via the Johnson-Cook flow model, greater displacement occurs at 40s with the dislocation-based two-phase model. Otherwise the response is very similar. This shows that material flow at the tool-interface is reasonably consistent between the two material models.

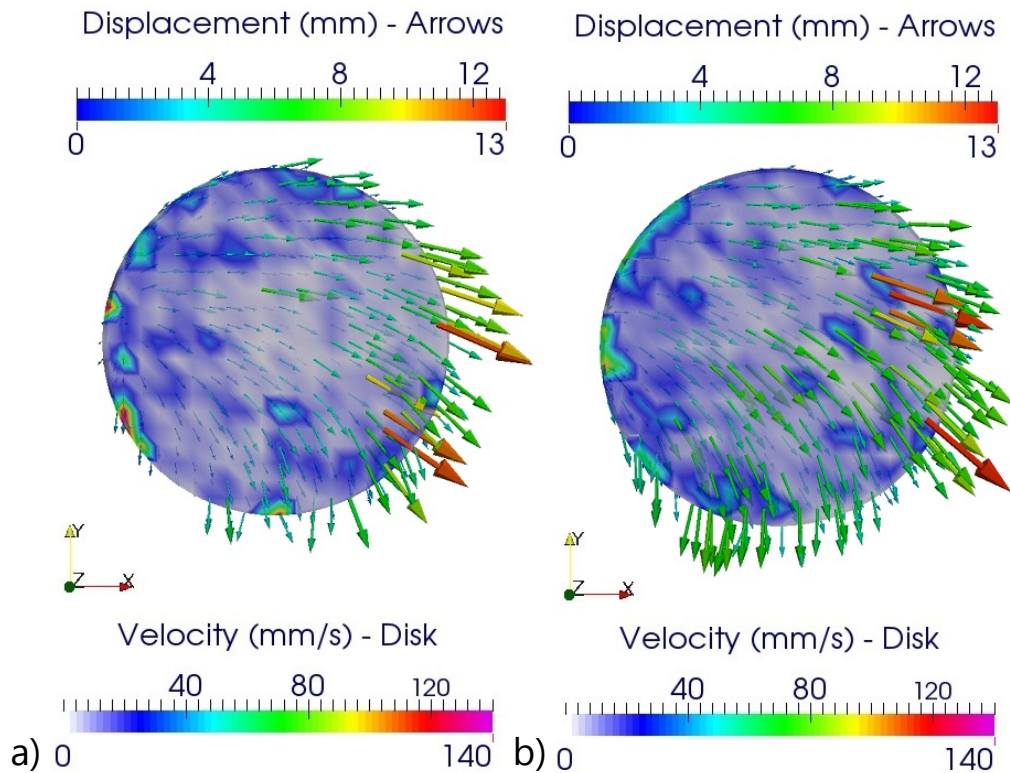


Figure 6.30: Material displacement and velocity at the tool interface for left) $t=15s$ and right) $t=40s$.

6.4.3 Resulting Microstructure

This section will explore the effect of FSP on the final microstructure. It is this aspect of modelling that constitutes the strength of the dislocation-based approach and its superior predictive capability.

6.4.3.1 Calculated Microstructure Across a Section of the Workpiece Using the Two-Phase Model

Figure 6.31 shows the numerical cross-sectional grain structure of both copper and aluminium alloy 5005. Note that the AA5005 workpiece has the same dimensions as the copper workpiece albeit with a reduced plate height (6.5mm rather than 12mm). The reader is referred to Appendix - B for the complete AA5005 plate dimensions.

The left side of Figure 6.31 shows the numerical cross-section at 65mm into each plate (in the processing direction); particles are coloured by average grain size. The right side of Figure 6.31 shows the average grain size for the copper workpiece on the advancing and retreating sides, as well as in the middle of the workpiece, where the data is measured in a direct line from the surface to the bottom of the plate. The stir zone represents the region with the most severe deformation, here it has been identified by an equivalent plastic strain greater than 1 ($\epsilon^p > 1$). In the plot, the end of this region is marked by horizontal lines, which show where the equivalent plastic strain is equal to 1 for the advancing and retreating sides, as well as in the middle of the workpiece. It should be noted that the predicted grain size is identified with the dislocation cell or subgrain size, as the subgrain structure transforms to a new grain structure with accumulation of misorientations for large strains. Thus the microstructure prediction by

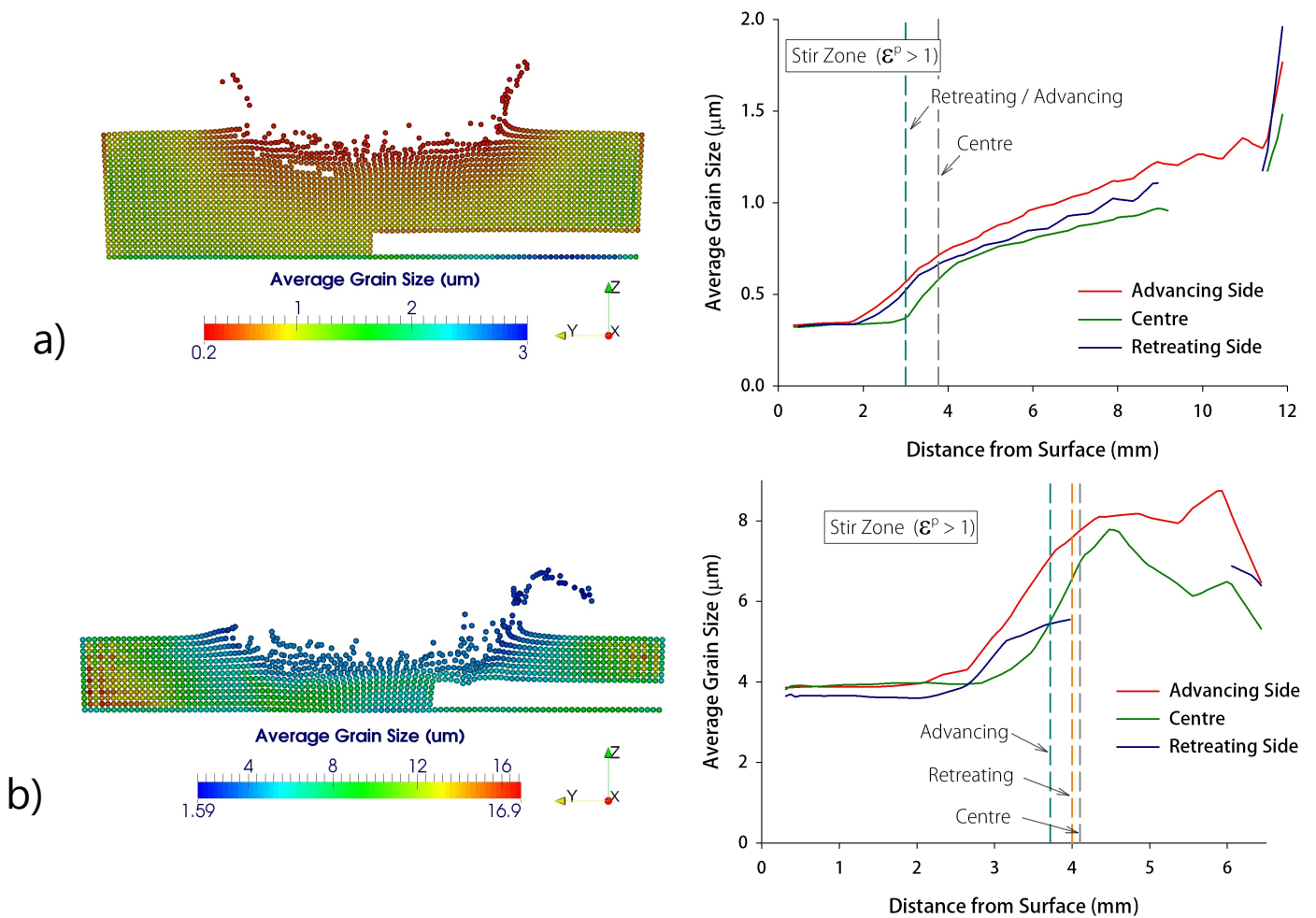


Figure 6.31: Average grain size at a slice 65mm into the plate (parallel to processing direction) for a) Copper and b) AA5005. Points on the advancing side, centre and retreating side are plotted against their distance from the bottom.

the two-phase model is appropriate for the identified stir zone, typically of the most interest in FSP.

The predicted grain size refinement is greatest for copper, at the surface reaching around 350nm. The aluminium alloy refines to just 3-4 μ m at the surface. At the edge of the stir zone, a larger average grain size is observed, around 600nm in copper. For AA5005, the average grain size at the edge of the stir zone varies between around 5.5 μ m and 7 μ m. Also noticed in the AA5005 is a reduction in average grain size moving from the middle region of the workpiece to the bottom. This may be a numerical artefact due to a combination of the applied boundary conditions and resolution producing over-prediction in deformation and grain refinement. Some error can be expected along the bottom of the workpiece as this is where the fixed boundary condition is applied - a greater resolution would likely reduce the BCs influence on the rest of the plate.

6.4.3.2 Comparison of the Calculated Microstructure with the Experimental Results

Figure 6.32 shows the inverse pole figure EBSD map for the copper workpiece. The section of the plate used for EBSD imaging is shown to the left, and is cut from the retreating side of the plate. The image is taken up to 100 μ m from the surface and thus lies within the stir

zone. The base material had an initial average grain size of $51.28\mu\text{m}$.

The figure shows a thin nano-sized layer is formed on the surface of the copper plate. In addition, smaller pockets of ultra-fine grains are present; one such region is highlighted. The surface layer in closer detail reveals an approximate thickness of 500nm . The close-up of the ultra-fine grains within the general structure shows subgrains averaging around 300nm in diameter, varying from $\sim 100\text{nm}$ - 800nm . The measured subgrains compare very favourably to the prediction of the two-phase model. The larger grains of the microstructure typically range from 20 - $50\mu\text{m}$. This contrast between the small nano-sized grains and larger grains is likely formed due to processes of recrystallisation and subgrain growth after processing. This is discussed further below.

Figure 6.32 also shows the microstructure of the AA5005 sample with both an inverse pole figure orientation map and band contrast map. The band contrast map is able to reveal a threshold misorientation between neighbouring grains, highlighting low angle grain boundaries (LAGB) in black ($<2^\circ$) and high angle grain boundaries in red ($<15^\circ$). The initial grain size of the AA5005-H34 plate was approximately $192\mu\text{m}$. It shows that for LAGB, the grain size varies between about 830nm and $6.7\mu\text{m}$, with an average grain size of around $2.5\mu\text{m}$. The average grain size predicted by the two-phase model (on the retreating side) is $3.65\mu\text{m}$, which gives a very reasonable comparison to the experimental data. Table 6.6 shows the comparison of subgrains within each workpiece to the prediction of the two-phase model.

Stir Zone	Exp. (Range)	Exp. (Average)	Retreating	Centre	Advancing
d (Cu)	100 nm - 800 nm	300 nm	326 nm	323 nm	331 nm
d (AA5005)	830 nm - $6.7\mu\text{m}$	$2.5\mu\text{m}$	$3.65\mu\text{m}$	$3.82\mu\text{m}$	$3.87\mu\text{m}$

Table 6.6: Comparison of the resulting grain size in the SZ for the experiment and two-phase model. Note that the experimental data is taken from the retreating side of the workpiece, and the two-phase model predicts an average grain size.

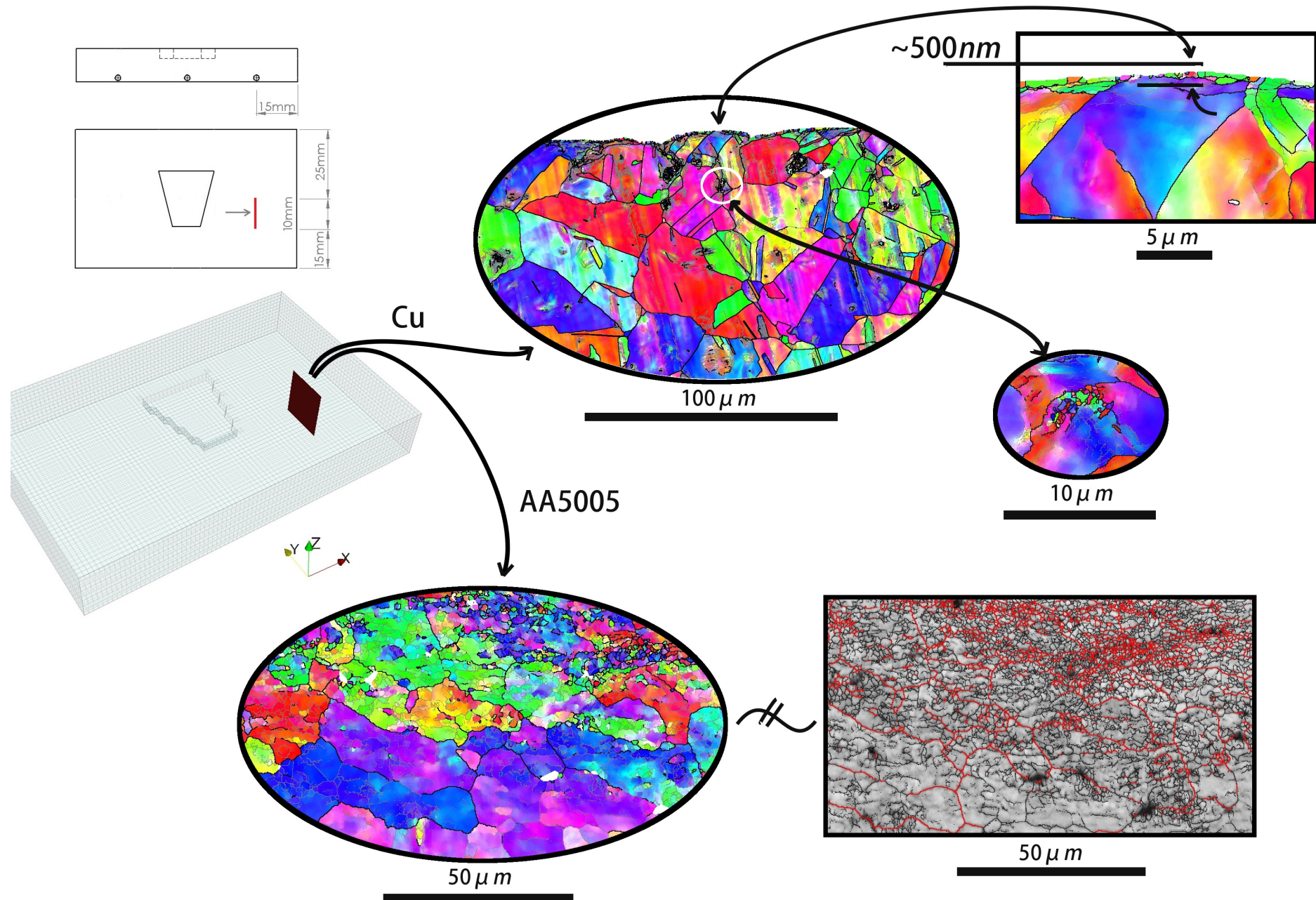


Figure 6.32: Cross-section EBSD data for copper and AA5005.

Figure 6.33 shows the region of the copper plate where the equivalent plastic strain is greater than 1, and is coloured by the average grain size. It shows a nano-sized surface layer is produced. Figure 6.34 shows the corresponding depth of the stir zone from the surface, in this case varying between 3-4mm. Notice that the stir zone is reasonably flat, consistent with pinless tool stir zones in literature [4].

Although the model predicts very fine grain size, it does not take into account grain growth due to the processes of recovery or static recrystallisation that follows FSP processing. As such some deviation can be expected from the experimental results. The stored energy of a recovered substructure is large compared to that of the fully recrystallised material. It can be lowered by coarsening of the substructure, which leads to a reduction in the total area of low angle grain boundaries. Thus the refined (subgrain) microstructure can be consumed during post-process cooling, if initially at high enough temperature [156].

It has been shown in the literature that immediate application of coolant can significantly reduce the amount of grain growth after processing for copper [164, 165]. In a study by Deghani et al. [4], nanosized grains were observed in pinless FSP of copper in the range of 50-200nm at a depth of up to 90 μ m. In a study by Xu et al. liquid CO₂ was applied to FSW of copper plates [164], with a reported average grain size of 17 μ m reduced to 1.8 μ m. This seems to indicate that post process grain growth plays a significant role for FSP of copper. Thus the nano-sized grains in Figure 6.32 likely represent the developed grain size produced by FSP prior to post-process grain growth. Dynamic recrystallisation (DRX) may also play a role in FSP of copper, whereby subgrain formation (nucleation) and subgrain growth occur during processing, similarly leading to large variation in grain size. Although the previous cited works seem to indicate a post-process (static) grain growth is the more dominant regime in this case.

As a general guide, the annealing temperature for copper C11000 is 748K [150]. Figure 6.35 shows the region of the copper plate that experiences temperatures of 748K and above during the simulation. The region encompasses most of the stir zone, highlighted by Figure 6.36, and a significant portion of the end of the plate. The region taken for the EBSD image is also shown for reference in Figure 6.35.

This result indicates that in order to maintain and observe the developed ultrafine-grained microstructure, immediate application of coolant may be necessary.

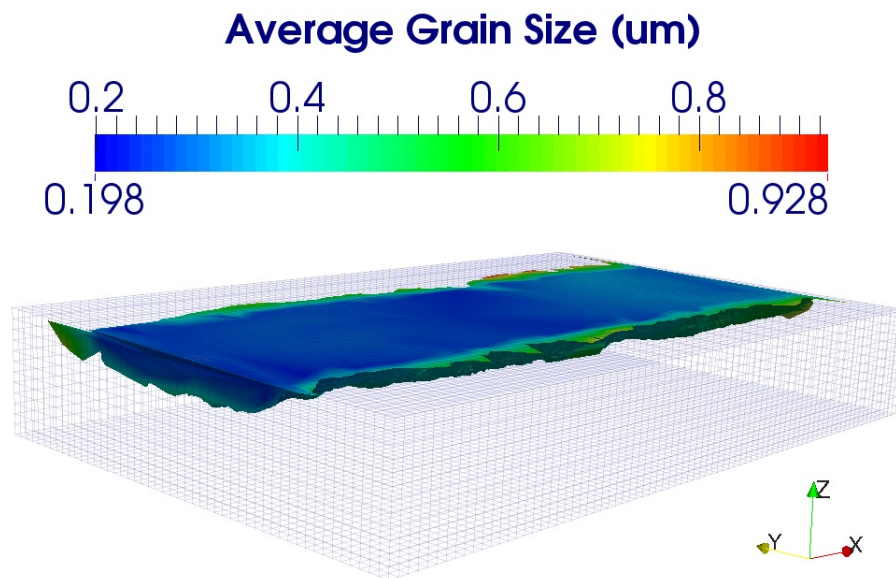


Figure 6.33: Stir zone of the processed copper coloured by average grain size.

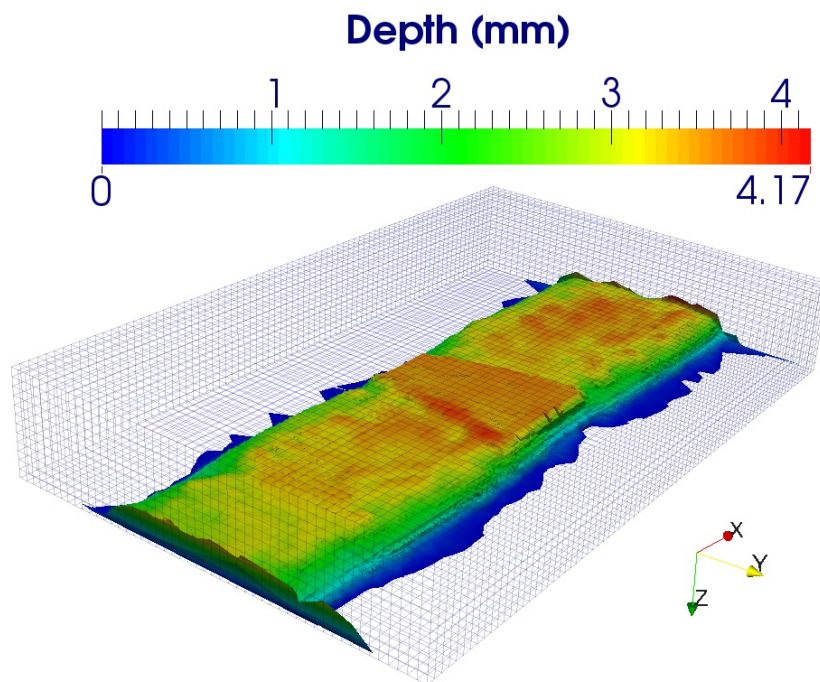


Figure 6.34: The inverted copper workpiece, which combined with the scale shows the depth of the stir zone from the surface.

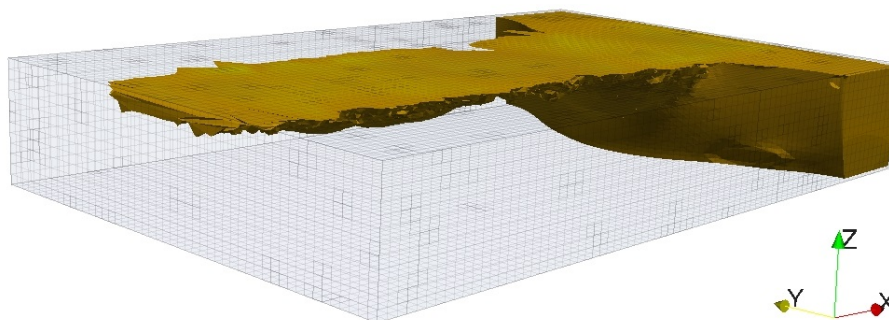


Figure 6.35: Processed copper that experiences temperatures greater than 748K during processing.

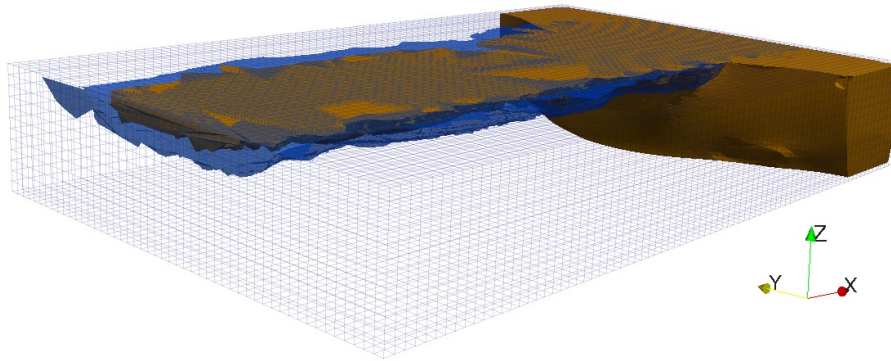


Figure 6.36: The stir zone of the processed copper (transparent blue) compared to the region that experiences temperatures greater than 748K (orange).

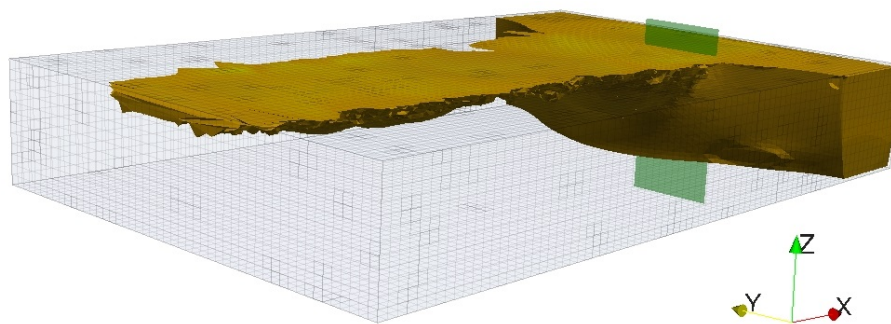


Figure 6.37: EBSD plane (green) lies in the region experiencing annealing temperatures (yellow).

6.4.4 Conclusion

The addition of the dislocation-density based material model improved the prediction of the thermocouple temperatures, compared to the previous Johnson-Cook material model. The predicted material flow was found to be reasonably consistent with the experiment where comparison was possible, with good prediction of flashing and material flow into the cavities. Improvement over the Johnson-Cook model was noticed in consistency of the surface generated and shape of the generated surface in the cavities.

The two-phase dislocation-based model is the only fully-coupled model currently available that makes it possible to predict the grain size produced by FSP. The prediction for the aluminium alloy 5005 is reasonably consistent with the average grain size observed in the experimental results. The retained subgrain structure in copper, maintained after part of the microstructure underwent grain coarsening, is consistent with the predictions of the model, which can be seen as its validation. It is noted that the model would better reflect the average grain size for copper in experiments involving application of immediate post-process cooling or quenching. Further extension of the dislocation-based model should include a provision for complete dynamic and static recovery and grain coarsening.

The contribution of this chapter is the development of an FSP model capable of predicting subgrain microstructure within the framework of a particle method. The next and final chapter will present a more detailed conclusion and discuss the significance of this overall work to the field of friction stir modelling. It will also explore possibilities for further work.

Chapter 7

Conclusions and Future Work

7.1 Conclusions

The aim of this work was to develop a computational tool able to relate external processing parameters of FSP, such as tool rotation and penetration depth, to the final condition of processed FCC material. This was accomplished using a particle method implementing a physically based constitutive model. A comparative analysis of the final model with alternative models (including a thermal model and thermo-mechanical model using an alternative constitutive law) is also achieved.

The final constitutive behaviour was based on the strain hardening model proposed by Estrin et al. including calibration for FSP conditions. This new model has been implemented in the open-source MPM software, NairnMPM.

A purely thermal model was established. It was compared against experimental results using three thermocouples to model the thermal profile at different locations. The results compared well to the experiment, the predicted curves were within 14% of the experimental data. From this model it was concluded that the air convection coefficient can be effectively accounted for by adjusting the backing plate convection coefficient with minimal change in the resulting temperature field. However, the inability to determine thermal differences on the advancing and retreating side of the FSP processed plate, and of course analyse material flow, drove the need for a full thermo-mechanical model.

A fully coupled thermo-mechanical model requires the use of a constitutive law to relate the deformation to resulting stresses. The Johnson-Cook model was the initial constitutive law applied. Analysis of material flow was conducted through comparison to experimental material flow into specimens with a cavity. Various trapezoidal cavity orientations were used and general material flow behaviour was in agreement. In addition thermal differences were noted on the advancing and retreating sides in correlation to experimental observations in literature, and predicted thermocouple temperatures were within 11% of the experimental results.

The non-saturation of stress at high strains however, was determined to be a weakness of the JC constitutive model, as FSP induces very large deformation, which in turn contributes to over-prediction of the thermal field. A natural way to overcome the difficulties of the phenomenological models of the JC type was seen in the use of a dislocation-based constitutive approach that goes back to the work by Kocks, Mecking and Estrin. More specifically, a two-phase model [101] was adopted.

The final complete thermo-mechanical model was able to predict the evolution of the Cu and AA5005 microstructure, in addition to their temperature and material flow, using the experimental FSP processing parameters. The thermal prediction was good for all three models (the thermal model, Johnson-Cook model and two-phase model), however the two-phase model presented the closest result, within 10% of the experimental results.

The flashing formed during processing was found to be improved using the two-phase model, with a reduction in over-prediction of the height. Similarly, material flow into the cavities produced more regular surfaces. Although the general material flow showed small improvements, an important and key factor, is that the two-phase model was able to introduce a predictive capability for the microstructure, with no loss in accuracy for the macroscopic predictions of temperature and material flow.

The determined microstructure of Cu and AA5005 was validated against experimental results using EBSD images. The subgrain size in the stir zone of copper was observed to be approximately 300nm, which compared very favourably with the numerical result of 326nm. Similarly an average grain size of approximately $2.5\mu\text{m}$ in AA5005 compared well to the numerical prediction of $3.65\mu\text{m}$.

Numerical problems which were encountered during the course of this research were discussed and the need for a more complete threshold for mass scaling was identified. The criteria that the kinetic energy be less than 1% of the internal energy was found to be inadequate due to significant increases in material flow and temperature at the tool/workpiece interface.

As a final conclusion, the model which has been developed allows very sophisticated analysis of temperature, material flow and microstructure. The combined effect is a very powerful tool which enables the design of the next generation of FSP processing tools and processing techniques. The focus of the applied model has been validation in this work, however there is a great deal of numerical experimentation, investigation and observation that can potentially be undertaken. In addition, a numerical model that covers all aspects of microstructure evolution is a continuous work, which will evolve as the understanding of microstructure evolution itself develops. Implementation of a material model based on the dislocation density evolution within a particle based numerical method is a promising approach, which can be used to further observe and investigate the effects of FSP and similar processes.

7.2 Outlook

Implementation within a particle method enabled the modelling of very large material deformation, challenging for the typical methods applied for FSP. The combination of a particle based method and a physically based constitutive model represent a unique contribution to the FSP and FSW modelling community. There are however, clear and identifiable avenues of investigation for future improvements to this computational tool.

Although more robust with large deformation problems, particle methods in general are known to be more computationally expensive compared to solid mechanics based FEA. Implicit schemes could lead to faster computation time. In computer animation, where efficient computation is a necessity, Disney Animation developed a semi-implicit time integration scheme for MPM [166].

The use of a mass scaling factor is necessary for the explicit method used here, but more investigation is required. Reducing the necessary mass scaling, whether by increased com-

putational efficiency or through some other means would be a significant contribution, as the compromise does introduce error which is difficult to isolate and quantify.

With further computational efficiency, the MPM model could also be implemented with convected particle domain interpolation (CPDI), a more accurate scheme for capturing shear and rotation of particles. For example with shear deformation, the particle domains should become parallelograms. However the computational cost involved in the CPDI technique was found to be too great to implement in the current model. Balancing computational efficiency, introducing CPDI may be preferred to further mesh refinement as the latter has actually been shown to reduce numerical accuracy due to the assumption of a constant regular particle domain [167].

A more sophisticated model for the friction condition could go some way to improve the model, particularly the thermal predictions. The challenge there lies in finding a way to accurately study it. Understanding the mechanisms involved could lead to further understanding of both the nature of the microstructure evolution and the contact condition at the tool/workpiece interface, for example experimental research suggests the contact condition between the tool and the workpiece generates micron size banding due to variation in strain rates. A variable friction coefficient based on the particle state could be an interesting addition.

The model that was developed is appropriate for predicting microstructure during processing, however due to its dynamic formulation, will not predict any change in microstructure post deformation. With a relatively small modification however it could account for static grain coarsening. There are analytical relationships based on dislocation density and time that could be applied. Another alternative would be to include a model for full dynamic recrystallisation within the current microstructure model. These models have been attempted before in the materials field and generally rely on a volume fraction of recrystallised versus un-recrystallised grains. In addition, a growth rate for the recrystallised volume fraction and a nucleation rate are needed. With current understanding of nucleation however, the latter would still rely on calibration, but could help to improve the prediction of the microstructure for a larger selection of materials and processing conditions.

This model of FSP was developed as part of an ongoing work to simulate the formation of hybrid composites through FSF. The addition of secondary materials, and the interaction of the surfaces of these materials during processing, will need to be examined in future work.

Bibliography

1. Australian Bureau of Statistics. Manufacturing Statistics <www.abs.gov.au> (2015).
2. Mishra, R., Mahoney, M., McFadden, S., Mara, N. & Mukherjee, A. High strain rate superplasticity in a friction stir processed 7075 Al alloy. *Scripta Materialia* **42**, 163–168 (2000).
3. Ahuja, Y., Ibrahim, R., Paradowska, A. & Riley, D. Friction stir forming to fabricate copper - tungsten composite. *Journal of Materials Processing Technology* **26**, 222–231 (2015).
4. Dehghani, K. & Mazinani, M. Forming nanocrystalline surface layers in copper using friction stir processing. *Materials and Manufacturing Processes* **26**, 922–925 (2011).
5. Ma, Z. Friction stir processing technology: a review. *Metallurgical and Materials Transactions A* **39A** (2008).
6. Schneider, J. in *Friction Stir Welding and Processing* (eds Mishra, R. & Mahoney, M.) p.37–50 (ASM International, 2007).
7. Akramifard, H., Shamanian, M., Sabbaghian, M. & Esmailzadeh, M. Microstructure and mechanical properties of Cu/SiC metal matrix composite fabricated via friction stir processing. *Materials and Design* **54**, 838–844 (2014).
8. Savolainen, K., Saukkonen, T. & Hänninen, H. Banding in copper friction stir weld. *Science and Technology of Welding and Joining* **17**, 111–115 (2012).
9. Fagan, T., Lemiale, V., Ibrahim, R. & Estrin, Y. A Thermal Model of Friction Stir Processing Using a Particle Based Method in *Proceedings of the 4th International Conference on Computational Methods* (2012).
10. in. *Friction Stir Welding and Processing* (eds Mishra, R. & Mahoney, M.) p.40 (ASM International, 2007).
11. Zeng, K. et al. Removing approach for flashes of friction stir spot welds. *Journal of Materials Processing Technology* **213**, 1725–1733 (2013).
12. Mishra, R. & Mahoney, M. Friction Stir Processing: A new grain refinement technique to achieve high strain rate superplasticity in commercial alloys. *Materials Science Forum* **357-359**, 507–514 (2001).
13. Ma, Z., Mishra, R., Mahoney, M. & Grimes, R. High strain rate superplasticity in friction stir processed Al-Mg-Zr alloy. *Materials Science and Engineering A* **351**, 148–153 (2003).
14. Ma, Z., Mishra, R. & Mahoney, M. Superplastic deformation behaviour of friction stir processed 7075Al alloy. *Acta Materialia* **50**, 4419–4430 (2002).
15. Pradeep, S. & Pancholi, V. Superplastic forming of multipass friction stir processed aluminium-magnesium alloy. *Metallurgical and Materials Transactions A* **45A**, 6207–6216 (2014).
16. Kato, H., Suzuki, T., Annou, Y. & Kageyama, K. Nondestructive detection of cold flakes in aluminium alloy die-cast plate with ultrasonic measurement. *Materials Transactions* **45**, 2403–2409 (2004).

17. Ma, Z., Sharma, S. & Mishra, R. Effect of friction stir processing on the microstructure of cast A356 aluminium. *Materials Science and Engineering A* **433**, 269–278 (2006).
18. Nakata, K., Kim, Y., Fujii, H., Tsumara, T. & Komazaki, T. Improvement of mechanical properties of aluminium die casting alloy by multi-pass friction stir processing. *Materials Science and Engineering A* **437**, 274–280 (2006).
19. Kapoor, R., Kandasamy, K., Mishra, R., Baumann, J. & Grant, G. Effect of friction stir processing on the tensile and fatigue behaviour of a cast A206 alloy. *Materials Science and Engineering A* **561**, 159–166 (2013).
20. Mahmoud, T. Surface modification of A390 hypereutectic Al-Si cast alloys using friction stir processing. *Surface and Coatings Technology* **228**, 209–220 (2013).
21. Image Source <http://static-hp.com/store2/images/uploads/hemi_6_pistons_img_7257_small.jpg>.
22. Image Source <<http://www.speednik.com/files/2012/10/Dart-LS-Next-Block-3qtr-view.jpg>>.
23. Cao, Y. & Lados, D. Friction stir processing in wrought and cast aluminium alloys. *Materials Science Forum* **765**, 741–745 (2013).
24. Weglowski, M. An experimental study on the friction stir processing process of aluminium alloy. *Key Engineering Materials* **554-557**, 1787–1792 (2013).
25. Song, Q., Zheng, Y., Ni, D. & Ma, Z. Corrosion and cavitation erosion behaviours of friction stir processed ni-al bronze: effect of processing parameters and position in the stirred zone. *Corrosion* **70**, 261–270 (2014).
26. Oh-ishi, K., Zhilyaev, A. & McNelley, T. Enhancement of ductility and strength through microstructural refinement by FSP of nickel aluminium bronze. *Materials Science Forum* **503-504**, 161–168 (2006).
27. Fujii, H., Yamaguchi, Y., Kikuchi, T., Kiguchi, S. & Nogi, K. Surface hardening of two cast irons by friction stir processing. *Journal of Physics: Conference Series* **165**, 1–4 (2009).
28. Imagawa, K., and Y. Morisada, H. F., Hashimoto, T., Yamaguchi, Y. & Kiguchi, S. Surface hardening of ferritic flake graphite cast iron by friction stir processing. *Materials Transactions* **54**, 1938–1943 (2013).
29. Mishra, R., Ma, Z. & Charit, I. Friction stir processing: a novel technique for fabrication of surface composite. *Materials Science and Engineering A* **341**, 307–310 (2003).
30. Mahmoud, E., Ikeuchi, K. & Takahashi, M. Fabrication of SiC particle reinforced composite on aluminium surface by friction stir processing. *Science and Technology of Welding and Joining* **13**, 607–618 (2008).
31. Asadi, P., Faraji, G. & Besharati, M. Producing of AZ91/SiC composite by friction stir processing (FSP). *International Journal of Advanced Manufacturing Technology* **51**, 247–260 (2010).
32. Zahmatkesh, B. & Enayati, M. A novel approach for development of surface nanocomposite by friction stir processing. *Materials Science and Engineering A* **527**, 6734–6740 (2010).
33. Anvari, S., Karimzadeh, F. & Enayati, M. A novel route for development of Al-Cr-O surface nano-composite by friction stir processing. *Journal of Alloys and Compounds* **562**, 48–55 (2013).
34. Li, B., Shen, Y., Luo, L. & Hu, W. Fabrication of TiCp/Ti-6Al-4V surface composite via friction stir processing (FSP): Process optimization, particle dispersion-refinement behavior and hardening mechanism. *Materials Science and Engineering A* **574**, 75–85 (2013).
35. Heydarian, A., Dehghani, K. & Slamkish, T. Optimizing powder distribution in production of surface nano-composite via friction stir processing. *Metallurgical and Materials Transactions B* **45B**, 821–826 (2014).

36. Huang, Y., Wang, T., Guo, W., Wan, L. & Lv, S. Microstructure and surface mechanical property of AZ31 Mg/SiCp surface composite fabricated by friction stir processing. *Materials and Design* **59**, 274–278 (2014).
37. Sathiskumar, R., Murugan, N., Dinaharan, I. & Vijay, S. Prediction of mechanical and wear properties of copper surface composites fabricated using friction stir processing. *Materials and Design* **55**, 224–234 (2014).
38. Sun, N. & Apelian, D. Friction Stir Processing of aluminium cast alloys for high performance applications. *JOM* **63**, 44–50 (2011).
39. Kang, S. et al. Relationship between formability and microstructure of Al alloy sheet locally modified by friction stir processing. *Scripta Materialia* **57**, 17–20 (2007).
40. in. *Friction Stir Welding and Processing* (eds Mishra, R. & Mahoney, M.) p.309–350 (ASM International, 2007).
41. Venkateswarlu, G., Davidson, M. & Tagore, G. Modelling studies of sheet metal formability of friction stir processed Mg AZ31B alloy under stretch forming. *Materials and Design* **40**, 1–6 (2012).
42. Hütsch, L., Hütsch, J., Herzberg, K., dos Santos, J. & Huber, N. Increased room temperature formability of Mg AZ31 by high speed friction stir processing. *Materials and Design* **54**, 980–988 (2014).
43. Tagore, G., Venkateswarlu, G. & Davidson, M. Formability studies of friction stir processed Mg AZ31B alloy in plain-stretch forming. *Applied Mechanics and Materials* **325–326**, 16–21 (2013).
44. Liu, Z., Xiao, B., Wang, W. & Ma, Z. Singly dispersed carbon nanotube/aluminium composites fabricated by powder metallurgy combined with friction stir processing. *CARBON* **50**, 1843–1852 (2012).
45. Liu, Z., Xiao, B., Wang, W. & Ma, Z. Tensile strength and electrical conductivity of carbon nanotube reinforced aluminium matrix composites fabricated by powder metallurgy combined with friction stir processing. *Journal of Materials Science and Technology* **30**, 649–655 (2014).
46. Izadi, H. et al. Friction stir processing of Al/SiC composites fabricated by powder metallurgy. *Journal of Materials Processing Technology* **213**, 1900–1907 (2013).
47. Zhang, Q., Xiao, B., Xue, P. & Ma, Z. Microstructural evolution and mechanical properties of ultrafine grained Al3Ti/Al-5.5Cu composites produced via hot pressing and subsequent friction stir processing. *Materials Chemistry and Physics* **134**, 294–301 (2012).
48. Tutunchilar, S., Haghpanahi, M., Givi, M. B., Asadi, P. & Bahemmat, P. Simulation of material flow in friction stir processing of a cast Al-Si alloy. *Materials and Design* **40**, 415–426 (2012).
49. Balasubramanian, N., Mishra, R. & Krishnamurthy, K. Friction stir channeling: characterization of the channels. *Journal of Materials Processing Technology* **209**, 3696–3704 (2009).
50. Balasubramanian, N., Mishra, R. & Krishnamurthy, K. Development of a mechanistic model for friction stir channeling. *Journal of Manufacturing Science and Engineering* **132** (2010).
51. Balasubramanian, N., Mishra, R. & Krishnamurthy, K. Process forces during friction stir channeling in an aluminum alloy. *Journal of Materials Processing Technology* **211**, 305–311 (2011).
52. in. *Friction Stir Welding and Processing* (eds Mishra, R. & Mahoney, M.) p.235–272 (ASM International, 2007).
53. Liu, G. *Mesh free methods: moving beyond the finite element method* (CRC Press, 2nd ed. 2010).

54. Liu, G. & Liu, M. Smoothed particle hydrodynamics: a meshfree particle method (World Scientific, 2003).
55. Reynolds, A. Flow visualization and simulation in FSW. *Scripta Materialia* **58**, 338–342 (2008).
56. Shi, Q.-Y., Sun, K., Wang, W. & Chen, G. Flow behaviour of SiC particles as tracer material during the fabrication of MMCs by friction stir processing in Friction Stir Welding and Processing VII - Held During the TMS 2013 Annual Meeting and Exhibition (2013).
57. Colligan, K. Material flow behaviour during friction stir welding of aluminium. *Welding Research Supplement*, 229–s–237–s (1999).
58. Seidel, T. & Reynolds, A. Visualization of the material flow in AA2195 friction-stir welds using a marker insert technique. *Metallurgical and Materials Transactions A* **32A**, 2879–2884 (2001).
59. Guerra, M., Schmidt, C., McClure, J., Murr, L. & Nunes, A. Flow patterns during friction stir welding. *Materials Characterization* **49**, 95–101 (2003).
60. Schmidt, H., Dickerson, T. & Hattel, J. Material flow in butt friction stir welds in AA2024-T3. *Acta Materialia* **54**, 1199–1209 (2006).
61. Aljoaba, S., Jawahir, I., Jr, O. D., Ali, M. & Khraisheh, M. Modeling of friction stir processing using 3D CFD analysis. *Int J Mater Form* **2**, 315–318 (2009).
62. Aljoaba, S., Jr, O. D., Khraisheh, M. & Jawahir, I. Modeling the effects of coolant application in friction stir processing on material microstructure using 3D CFD analysis. *Journal of Materials Engineering and Performance* **21(7)**, 1141–1150 (2012).
63. Nassar, H. & Khraisheh, M. Simulation of material flow and heat evolution in friction stir processing incorporating melting. *Journal of Engineering Materials and Technology* **134** (2012).
64. Yu, Z., Zhang, W., Choo, H. & Feng, Z. Transient heat and material flow modeling of friction stir processing of magnesium alloy using threaded tool. *Metallurgical and Materials Transactions A* **43A**, 724–737 (2012).
65. Colegrove, P. & Shercliff, H. 3-Dimensional CFD modelling of flow round a threaded friction stir welding tool profile. *Journal of Materials Processing Technology* **169**, 320–327 (2005).
66. Colegrove, P. & Shercliff, H. CFD Modelling of friction stir welding of thick plate 7449 aluminium alloy. *Science and Technology of Welding and Joining* **11**, 429–441 (2006).
67. Schmidt, H. & Hattel, J. A local model for the thermomechanical conditions in friction stir welding. *Modelling and Simulation in Materials Science and Engineering* **13**, 77–93 (2005).
68. Zhang, H., Zhang, Z. & Chen, J. The finite element simulation of the friction stir welding process. *Materials Science and Engineering A* **403**, 340–348 (2005).
69. Mukherjee, S. & Gosh, A. Flow visualization and estimation of strain and strain-rate during friction stir process. *Materials Science and Engineering A* **527**, 5130–5135 (2010).
70. Zhang, Z. & Zhang, H. A fully coupled thermo-mechanical model of friction stir welding. *International Journal of Advanced Manufacturing Technology* **37**, 279–293 (2008).
71. Grujicic, M. et al. Fully coupled thermomechanical finite element analysis of material evolution during friction-stir welding of AA5083. *Proc. IMechE Part B: J. Engineering Manufacture* **224** (2009).
72. Grujicic, M. et al. Modeling of AA5083 material-microstructure evolution during butt friction-stir welding. *Journal of Materials Engineering and Performance* **19(5)** (2010).
73. Grujicic, M. et al. Computational analysis of material flow during friction stir welding of AA5059 aluminum alloys. *Journal of Materials Engineering and Performance* (2011).

74. Zhang, P. et al. Plastic deformation behaviour of the friction stir welded AA2024 aluminum alloy. *International Journal of Advanced Manufacturing Technology* **74**, 673–679 (2014).
75. Tartakovsky, A., Grant, G., Sun, X. & Khaleel, M. Modeling of friction stir welding (FSW) process with smoothed particle hydrodynamics (SPH) in 2006 SAE world Congress (2006).
76. Gingold, R. & Monaghan, J. Smoothed particle hydrodynamics: theory and application to non-spherical stars. *Royal Astronomical Society* **181**, 375–389 (1977).
77. Monaghan, J. An introduction to SPH. *Computer Physics Communications* **48**, 89–96 (1988).
78. Libersky, L., Petschek, A., Carney, T., Hipp, J. & Allahdadi, F. High strain lagrangian hydrodynamics: A three-dimensional SPH code for dynamic material response. *Journal of Computational Physics* **109**, 67–75 (1993).
79. Pan, W., Li, D., Tartakovsky, A., Ahzi, S. & Khraisheh, M. A new smoothed particle hydrodynamics non-Newtonian model for friction stir welding: process modeling and simulation of microstructure evolution in a magnesium alloy. *International Journal of Plasticity* **48**, 189–204 (2013).
80. Yoshikawa, G., Miyasaka, F., Hirata, Y., Katayama, Y. & t. Fuse. Development of numerical simulation model for FSW employing particle method. *Science and Technology of Welding and Joining* **17**, 255 (2012).
81. Miyasaka, F., Yoshikawa, G. & Matsuzawa, S. Numerical simulation model for FSW employing particle method - effect of tool angle on fluid motion. *Materials Science Forum* **783-786**, 1765–1769 (2014).
82. Hirasawa, S., Badarinarayan, H., Okamoto, K., Tomimura, T. & Kawanami, T. Analysis of effect of tool geometry on plastic flow during friction stir spot welding using particle method. *Journal of Materials Processing Technology* **210** (2010).
83. Belytschko, T., Lu, Y. & Gu, L. Element-free galerkin methods. *International Journal for Numerical Methods in Engineering* **37**, 229–256 (1994).
84. Machado, G., Alves, M., Rossi, R. & Jr., C. S. Numerical modeling of large strain behaviour of polymeric crushable foams. *Applied Mathematical Modelling* **35**, 1271–1281 (2011).
85. Atluri, S. & Zhu, T. A new meshless local petrov-galerkin (MLPG) approach in computational mechanics. *Computational Mechanics* **22**, 117–127 (1998).
86. Wieckowski, Z. The material point method in large strain engineering problems. *Computational Methods in Applied Mechanics and Engineering* **193**, 4417–4438 (2004).
87. SPH Projects and Codes Spheric. <https://wiki.manchester.ac.uk/spheric/index.php/SPH_Projects_and_Codes> (2014).
88. Nairn, J. Computational mechanics software originating from John A. Nairn's research group at Oregon State University <<http://code.google.com/p/nairn-mpm-fea/>>.
89. Uintah University of Utah Scientific Computing and Imaging Institute. <<http://www.sci.utah.edu/software/65/528-uintah.html>> (2014).
90. Ma, S., Zhang, X. & Qiu, X. Comparison study of MPM and SPH in modeling hypervelocity impact problems. *International Journal of Impact Engineering* **36**, 272–282 (2009).
91. Lemiale, V., Nairn, J. & Hurmane, A. Material point method simulation of equal channel angular pressing involving large plastic strain and contact through sharp corners. *Computer Modeling in Engineering and Sciences* **70**, 41–66 (2010).
92. Yazdipour, A., Shafiei, A. & Dehghani, K. Modeling the microstructural evolution and effect of cooling rate on the nanograins formed during the friction stir processing of Al5083. *Materials Science and Engineering A* **527**, 192–197 (2009).

93. Hofmann, D. & Vecchio, K. Thermal history analysis of friction stir processed and submerged friction stir processed aluminium. *Materials Science and Engineering A* **465**, 165–175 (2007).
94. Fratini, L. & Buffa, G. CDRX modelling in friction stir welding of aluminium alloys. *International Journal of Machine Tools and Manufacture* **45**, 1188–1194 (2005).
95. Fratini, L. & Buffa, G. Continuous dynamic recrystallization phenomena modelling in friction stir welding of aluminium alloys: a neural-network-based approach. *Journal of Engineering Manufacture* **221**, 857–864 (2006).
96. Buffa, G., Fratini, L. & Shivpuri, R. CDRX modelling in friction stir welding of AA7075-T6 aluminum alloy: Analytical approaches. *Journal of Materials Processing Technology* **191**, 356–359 (2007).
97. Simar, A. et al. Integrated modeling of friction stir welding of 6xxx series Al alloys: Process, microstructure and properties. *Progress in Materials Science* **57**, 95–183 (2011).
98. Robson, J. & Campbell, L. Model for grain evolution during friction stir welding of aluminium alloys. *Science and Technology of Welding and Joining* **15**, 171–176 (2010).
99. Gao, Z. et al. FE modelling of microstructure evolution during friction stir spot welding in AA6082-T6. *Weld World* **57**, 895–902 (2013).
100. Estrin, Y. & Vinogradov, A. Extreme grain refinement by severe plastic deformation: A wealth of challenging science. *Acta Materialia* **61**, 782–817 (2013).
101. Toth, L., Molinari, A. & Estrin, Y. Strain hardening at large strains as predicted by dislocation based polycrystal plasticity model. *Journal of Engineering Materials and Technology* **124** (2002).
102. Yadav, D. & Bauri, R. Effect of friction stir processing on microstructure and mechanical properties of aluminium. *Materials Science and Engineering A* **539**, 85–92 (2012).
103. Fonda, R., Knipling, K. & Bingert, J. Microstructural evolution ahead of the tool in aluminium friction stir welds. *Scripta Materialia* **58**, 343–348 (2007).
104. Baik, S., Hellmig, R., Estrin, Y. & Kim, H. Modeling of deformation behaviour of copper under equal channel angular pressing. *Z. Metallkd.* **94**, 754–760 (2003).
105. Baik, S., Estrin, Y., Kim, H. & Hellmig, R. Dislocation density-based modeling of deformation behaviour of aluminium under equal channel angular pressing. *Materials Science and Engineering A*, 86–97 (2003).
106. Zhang, Z., Chen, T., Zhang, Z. & Zhang, H. Coupled thermo-mechanical model based comparison of friction stir welding process of AA2024-T3 in different thicknesses. *Journal of Materials Science* **46**, 5815–5821 (2011).
107. Zhang, Z. & Chen, J. Computational investigations on reliable finite element-based thermomechanical-coupled simulations of friction stir welding. *International Journal of Advanced Manufacturing Technology* **60**, 959–975 (2012).
108. Vilaca, P., Quintino, L., dos Santos, J., Zettler, R. & Sheikhi, S. Quality assessment of friction stir welding joints via an analytical thermal model, iSTIR. *Materials Science and Engineering A* **445-446**, 501–508 (2007).
109. Ferro, P. & Bonollo, F. A semianalytical thermal model for friction stir welding. *Metallurgical and Materials Transactions A* (2009).
110. Nguyen, N., A.Ohta, Matsuoka, K., Suzuki, N. & Y.Maeda. Analytical solutions for transient temperature of semi-infinite body subjected to 3-D moving heat sources. *Welding Research* (1999).
111. Hou, Z. & Komanduri, R. General solutions for stationary/moving plane heat source problems in manufacturing and tribology. *International Journal of Heat and Mass Transfer* **43**, 1679–1698 (2000).

112. Haghpanahi, M., Salimi, S., Bahemmat, P. & Sima, S. 3-D transient analytical solution based on Green's function to temperature field in friction stir welding. *Applied Mathematical Modelling* (2013).
113. Colegrove, P., Painter, M., Graham, D. & Miller, T. in 2nd International Symposium on Friction Stir Welding (2000).
114. Schmidt, H., Hattel, J. & Wert, J. An analytical model for the heat generation in friction stir welding. *Modelling and Simulation in Materials Science and Engineering* **12**, 143–157 (2004).
115. Khandkar, M., Khan, J. & Reynolds, A. Prediction of temperature distribution and thermal history during friction stir welding: input torque based model. *Science and Technology of Welding and Joining* **8(3)**, 165–174 (2003).
116. Zhang, Z. & Zhang, H. Solid mechanics-based Eulerian model of friction stir welding. *International Journal of Advanced Manufacturing Technology* (2014).
117. Cao, F. Heat Modeling for Friction Stir Welding. *Applied Mechanics and Materials* **467**, 385–391 (2014).
118. Nandan, R., Roy, G., Lienert, T. & Debroy, T. Three-dimensional heat and material flow during friction stir welding of mild steel. *Acta Materialia* **55**, 883–895 (2007).
119. Jabbari, M. Elucidating of rotation speed in friction stir welding of pure copper: Thermal modeling. *Computational Materials Science* **81**, 296–302 (2014).
120. Darvazi, A. & Iranmanesh, M. Prediction of asymmetric transient temperature and longitudinal residual stress in friction stir welding of 304L stainless steel. *Materials and Design* **55**, 812–820 (2014).
121. Hamilton, R., MacKenzie, D. & Li, H. Multi-physics simulation of friction stir welding process. *Engineering Computations: International Journal for Computer-Aided Engineering and Software* **27**, 967–985 (2010).
122. Wang, H., Colegrove, P. & dos Santos, J. Numerical investigation of the tool contact condition during friction stir welding of aerospace aluminium alloy. *Computational Materials Science* (2013).
123. Arora, A., Nandan, R., Reynolds, A. & Debroy, T. Torque, power requirement and stir zone geometry in friction stir welding through modeling and experiments. *Scripta Materialia* **60**, 13–16 (2009).
124. Frigaard, O., Grong, O. & Midling, O. A process model for friction stir welding of age hardening aluminium alloys. *Metallurgical and Materials Transactions A* **32A**, 1189–1200 (2001).
125. Moraitis, G. A. & Labeas, G. N. Investigation of friction stir welding process with emphasis on calculation of heat generated due to material stirring. *Science and Technology of Welding and Joining* **15**, 177–184 (2010).
126. Ulysse, P. Three-dimensional modeling of the friction stir-welding process. *International Journal of Machine Tools and Manufacture* **42**, 1549–1557 (2002).
127. Courant, R., Freidrichs, K. & Lewy, H. On the partial difference equations of mathematical physics. *IBM Journal* **11**, 215–234 (1967).
128. Brackbill, J. & Ruppel, H. FLIP: a low-dissipation, particle-in-cell method for fluid flows in two-dimensions. *Journal of Computational Physics* **65**, 314–343 (1986).
129. Sulsky, D., Chen, Z. & Schreyer, H. A particle method for history-dependent materials. *Computer Methods in Applied Mechanics and Engineering* **118**, 179–196 (1994).
130. Sulsky, D., Zhou, S. & Schreyer, H. Application of a particle-in-cell method to solid mechanics. *Computer Physics Communications* **87**, 236–252 (1995).
131. Sulsky, D. & Schreyer, H. Axisymmetric form of the material point method with applications to upsetting and Taylor impact problems. *Computer Methods in Applied Mechanics and Engineering* **139**, 409–429 (1996).

132. Nairn, J. A. Home page of Professor John A. Nairn <<http://www.cof.orst.edu/cof/wse/faculty/Nairn/>>.
133. Bardenhagen, S. & Kober, E. The generalized interpolation material point method. *Computer Modeling in Engineering* **5**, 477–495 (2004).
134. Sadeghirad, A., Brannon, R. & Burghardt, J. A convected particle domain interpolation technique to extend applicability of the material point method for problems involving massive deformations. *International Journal for Numerical Methods in Engineering* **86**, 1435–1456 (2011).
135. Sadeghirad, A., Brannon, R. & Guilkey, J. Second order convected particle domain interpolation (CPDI2) with enrichment for weak discontinuities at material interfaces. *International Journal for Numerical Methods in Engineering* **95**, 928–952 (2013).
136. Nairn, J. & Guilkey, J. Axisymmetric form of the generalized interpolation material point method. *International Journal for Numerical Methods in Engineering* (2012).
137. Simo, J. & Hughes, T. *Computational Inelasticity* (Springer, 2nd Ed. 2000).
138. Moler, C. & Loan, C. V. Nineteen dubious ways to compute the exponential of a matrix, 25 years later. *Society for Industrial and Applied Mathematics Publications* **45**, 3–49 (2003).
139. Aimene, Y. & Nairn, J. Simulation of transverse wood compression using a large-deformation, hyperelastic-plastic material model. *Wood Science Technology* **49**, 21–39 (2015).
140. Nairn, J. Modeling imperfect interfaces in the material point method using multimaterial methods. *Computer Modeling in Engineering and Sciences* **1**, 1–15 (2013).
141. Bardenhagen, S. et al. An improved contact algorithm for the material point method and application to stress propagation in granular material. *Computer Modeling in Engineering and Sciences* **2**, 509–522 (2001).
142. Bardenhagen, S., Brackbill, J. & Sulsky, D. The material-point method for granular materials. *Computer Methods in Applied Mechanics and Engineering* **187**, 529–541 (2000).
143. Nairn, J. Material Point Method Calculations with Explicit Cracks. *Computer Modeling in Engineering and Sciences* **4**, 649–663 (2003).
144. Bardenhagen, S. Energy conservation error in the material point method for solid mechanics. *Journal of Computational Physics*, 383–403 (2002).
145. Selvaraj, M., Murali, V. & Rao, S. Thermal model for friction stir welding of mild steel. *Multidiscipline Modeling in Materials and Structures* **9(1)**, 49–61 (2013).
146. Schmidt, H. & Hattel, J. Thermal modelling of friction stir welding. *Scripta Materialia* **58**, 332–337 (2008).
147. Albakri, A., Mansoor, B., Nassar, H. & Khraisheh, M. Simulation of friction stir processing with internally cooled tool. *Advanced materials research* **445**, 560–565 (2012).
148. Pashazadeh, H., Teimournezhad, J. & Masoumi, A. Numerical investigation on the mechanical, thermal, metallurgical and material flow characteristics in friction stir welding of copper sheets with experimental verification. *Materials and Design* **55**, 619–632 (2013).
149. Carslaw, C. & Jaeger, J. in *Conduction of heat in solids* 2nd edition (Oxford: Clarendon Press, 1959).
150. ASM International Handbook Committee. in *ASM Handbook: Volume 2, Properties and Selection: Nonferrous Alloys and Special-Purpose Materials* (1990).
151. Johnson, G. & Cook, W. A constitutive model and data for metals subjected to large strains, high strain rates and high temperatures in *Proceedings of the 7th International Symposium on Ballistics* (The Hague, The Netherlands, 1983), 541–547.
152. Zhang, Z. & Zhang, H. Numerical studies on the effect of traverse speed in friction stir welding. *Materials and Design* **30**, 900–907 (2009).

153. Riahi, M. & Nazari, H. Analysis of transient temperature and residual thermal stresses in friction stir welding of aluminum alloy 6061-T6 via numerical simulation. *International Journal of Advanced Manufacturing Technology* **55**, 143–152 (2010).
154. Zhang, Z. & Wan, Z. Predictions of tool forces in friction stir welding of AZ91 magnesium alloy. *Science and Technology of Welding and Joining* **17**, 495–500 (2012).
155. Lorrain, O., Favier, V., Zahrouni, H. & Lawrjaniec, D. Understanding the material flow path of friction stir welding process using unthreaded tools. *Journal of Materials Processing Technology* **210**, 603–609 (2010).
156. Humphreys, F. & Hatherly, M. Second Edition (2004).
157. Estrin, Y., Toth, L., Molinari, A. & Brechet, Y. A dislocation based model for all hardening stages in large strain deformation. *Acta Materialia* **46**, 5509–5522 (1998).
158. Zehetbauer, M. & Seumer, V. Cold work hardening in stages IV and V of F.C.C metals - I. Experiments and interpretation. *Acta Metallurgica Materialia* **41**, 577–588 (1993).
159. Tanner, A. & McDowell, D. Deformation, temperature and strain rate sequence experiments on OFHC Cu. *International Journal of Plasticity* **15**, 375–399 (1999).
160. Prasad, Y. & Rao, K. Mechanisms of high temperature deformation in electrolytic copper in extended ranges of temperature and strain rate. *Materials Science and Engineering A* **374**, 335–341 (2004).
161. Shi, H., McLaren, A., Sellars, C., Shahani, R. & Bolingbroke, R. Constitutive equations for high temperature flow stress of aluminium alloys. *Materials Science and Technology* **13**, 210–216 (1997).
162. Marthinsen, K. & Nes, E. Modelling strain hardening and steady state deformation of Al-Mg alloys. *Materials Science and Technology* **17**, 376–388 (2001).
163. Assidi, M., Fourment, L., s. Guerdoux & Nelson, T. Friction model for friction stir welding process simulation: calibrations from welding experiments. *International Journal of Machine Tools and Manufacture* **50**, 143–155 (2010).
164. Xu, N., Ueji, R., Morisada, Y. & Fujii, H. Modification of mechanical properties of friction stir welded Cu joint by additional liquid CO₂ cooling. *Materials and Design* **56**, 20–25 (2014).
165. Su, J.-Q, Nelson, T., McNelley, T. & Mishra, R. Development of nanocrystalline structure in Cu during friction stir processing (FSP). *Materials Science and Engineering A* **528**, 5458–5464 (2011).
166. Stomakhin, A., Schroeder, C., Chai, L., Teran, J. & Selle, A. A material point method for snow simulation. *ACM Transactions on Graphics* **32**, article 102 (2013).
167. Wallstedt, P. & Guilkey, J. An evaluation of explicit time integration schemes for use with the generalized interpolation material point method. *Journal of Computational Physics*, 9628–9642 (2008).

Appendices

A Full Resolution EBSD Images

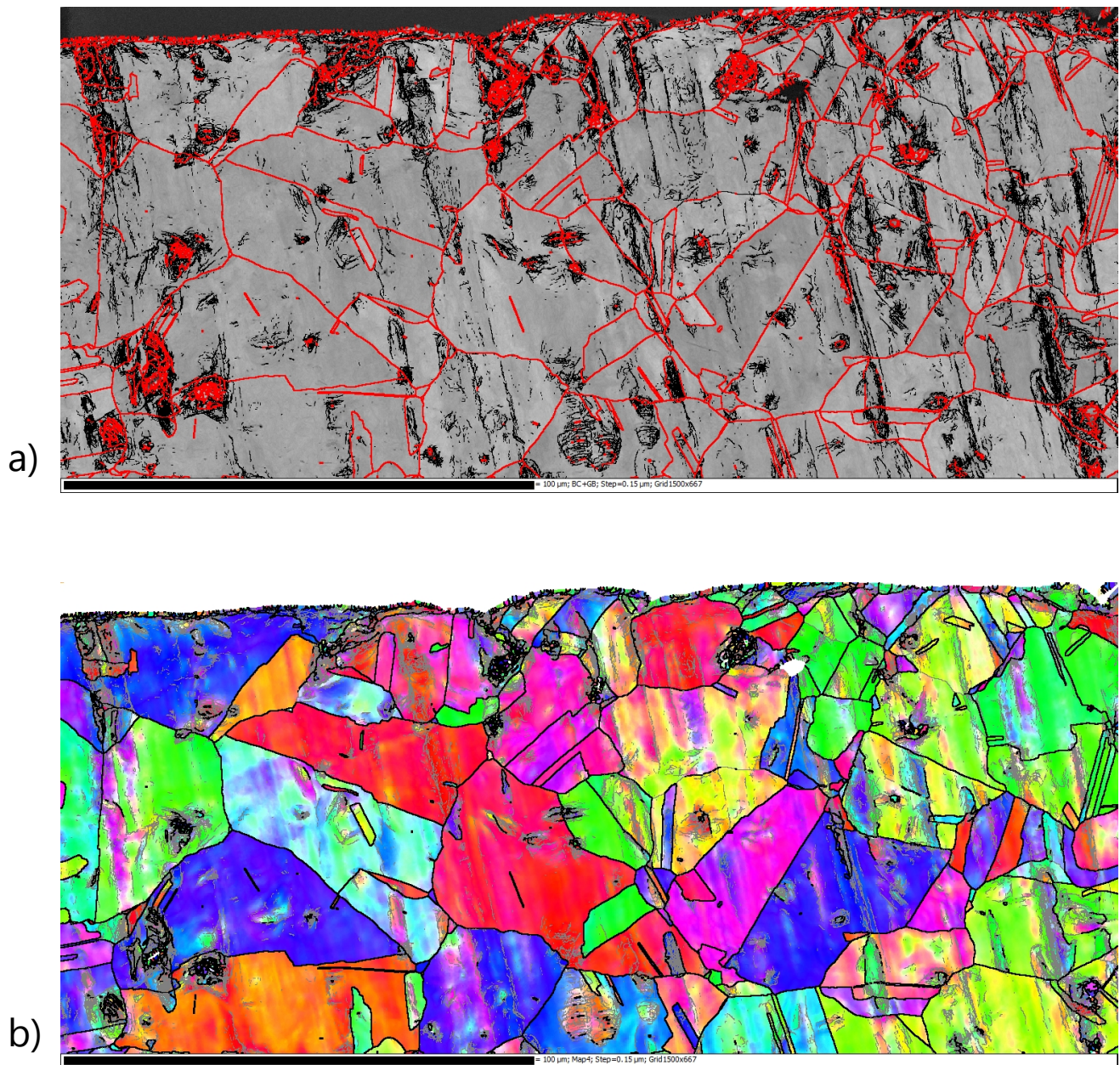


Figure 1: Copper workpiece at a slice 65mm into the plate (parallel to processing direction); a) Band contrast map - high angle boundaries ($>15^\circ$) in red, LAGB in black ($>2^\circ$); b) Inverse pole figure orientation map - high angle grain boundaries ($>15^\circ$) in black, LAGB in grey ($>2^\circ$).

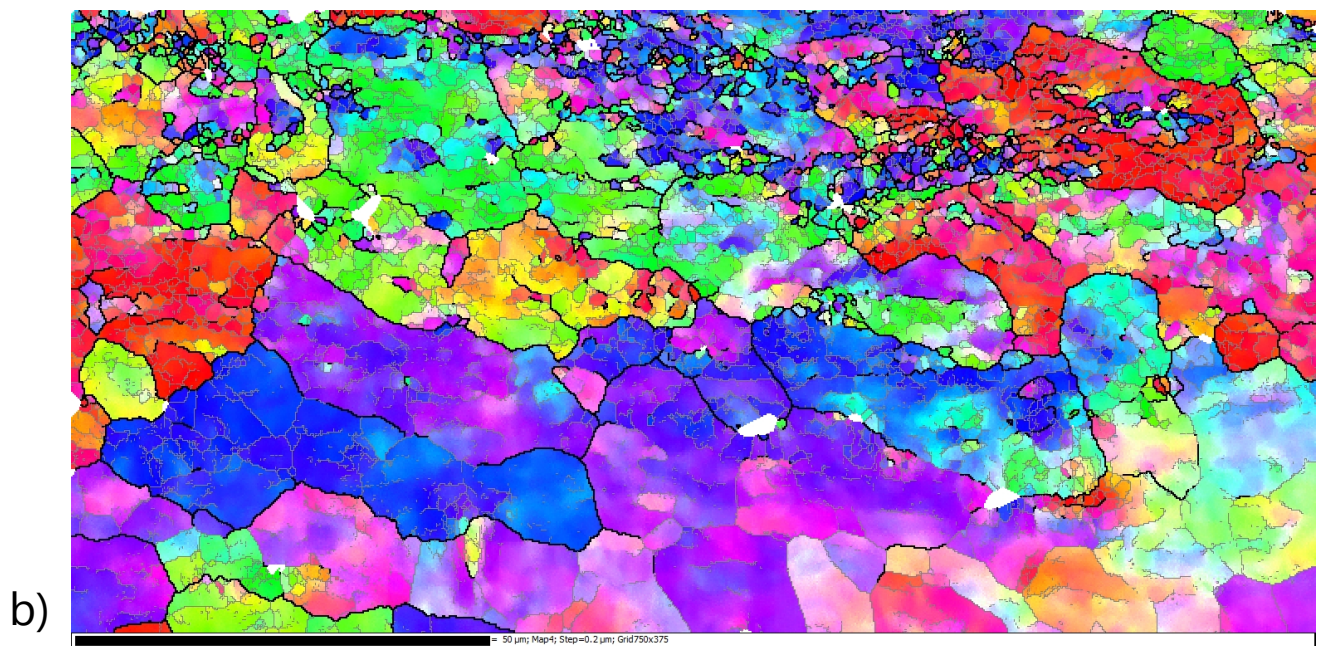
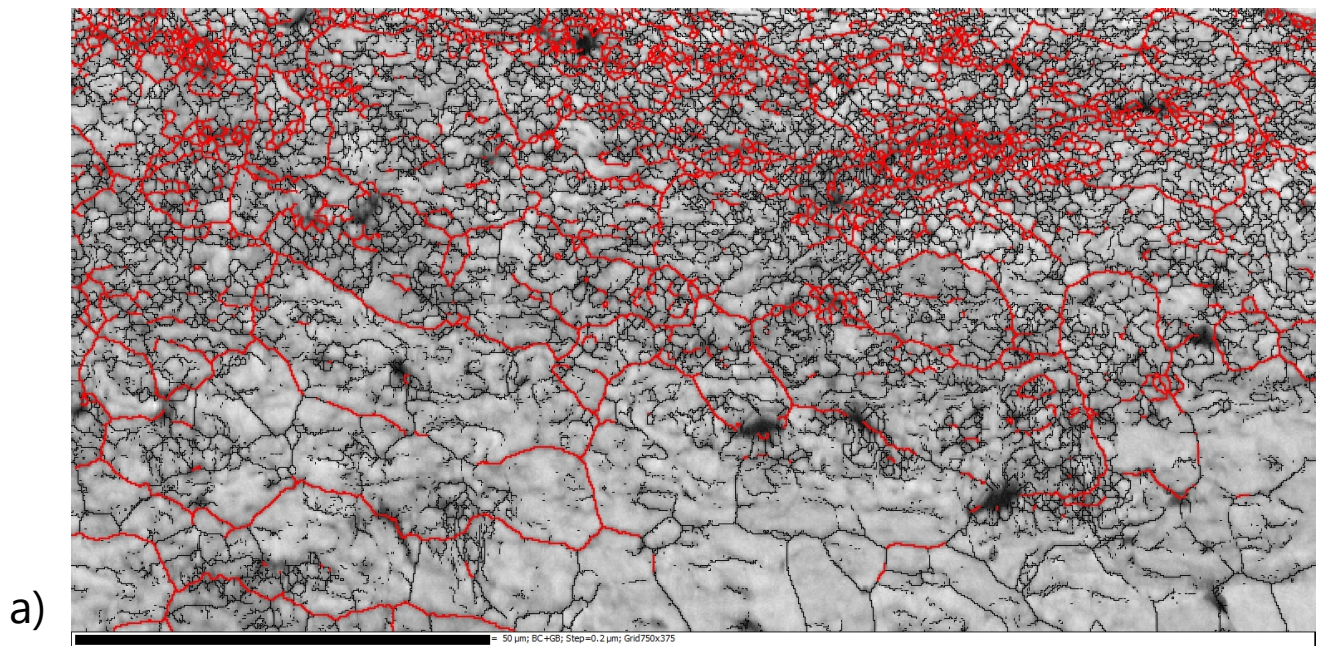


Figure 2: AA5005 workpiece at a slice 65mm into the plate (parallel to processing direction); a) Band contrast map - high angle boundaries ($>15^\circ$) in red, LAGB in black ($>2^\circ$); b) Inverse pole figure orientation map - high angle grain boundaries ($>15^\circ$) in black, LAGB in grey ($>2^\circ$).

B Aluminium Alloy 5005 Workpiece Dimensions and Properties

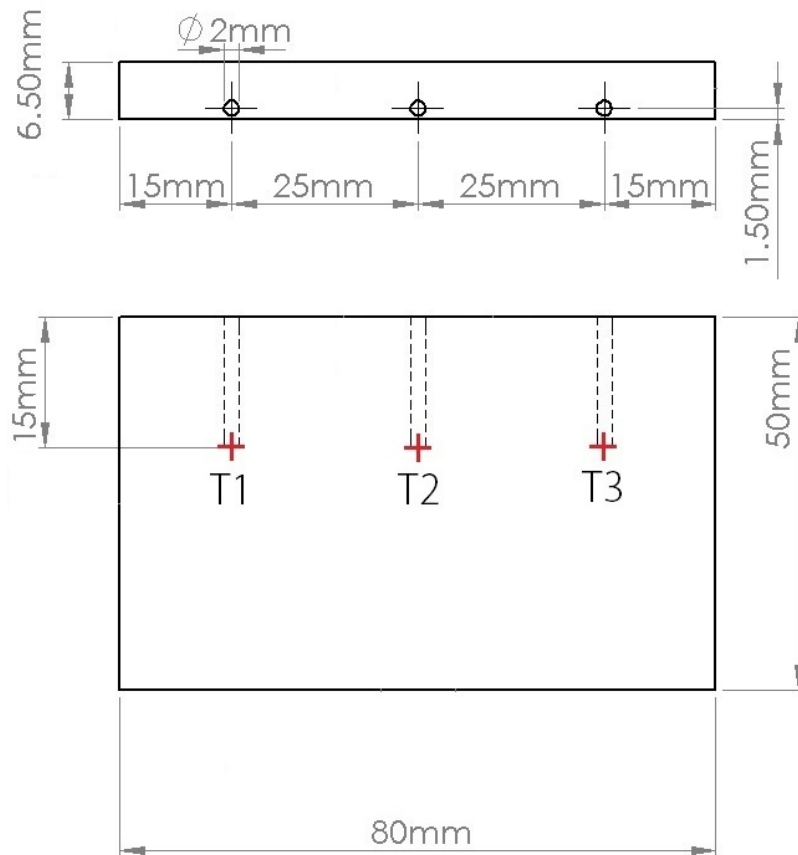


Figure 3: Schematic of AA5005 plate with marked (+) thermocouple positions, T1-T3, although note that the thermocouple results for AA5005 are not reported in this thesis.

Parameter	AA5005
Density, ρ (kg/m ³)	2700
Specific heat capacity, C_p (J/Kg-K)	900
Thermal conductivity, k (W/m-K)	200
Coefficient of thermal expansion, α_t (ppm/K)	25.6
Young's modulus, E (GPa)	68.9
Poisson's ratio, ν	0.33
Initial yield strength, σ_o (MPa)	20
dislocation density in subgrain walls, ρ_w (m ⁻²)	7.512×10^{10}
dislocation density in subgrain interiors, ρ_c (m ⁻²)	7.512×10^9
initial volume fraction, f_o	0.25
saturated volume fraction, f_∞	0.06
rate of decrease of f , $\bar{\gamma}^r$	3.2
α	0.25
K	30
α^*	(see equation 6.15)
β^*	0.001
k_0	2.7
A	30000
B	14900
Taylor factor, M_T	3.06
Burgers vector, b	2.86×10^{-10}
Reference shear strain rate, $\dot{\gamma}_0$ (s ⁻¹)	1000

Table 1: Two-phase model parameters for AA5005.